# A quantum gas of polar molecules in an optical lattice

by

**Steven A. Moses**

B.S., University of Michigan, 2010

M.S., University of Colorado, 2013

A thesis submitted to the

Faculty of the Graduate School of the

University of Colorado in partial fulfillment

of the requirements for the degree of

Doctor of Philosophy

Department of Physics

2016

This thesis entitled:
A quantum gas of polar molecules in an optical lattice
written by Steven A. Moses
has been approved for the Department of Physics

_____

Jun Ye

_____

Deborah S. Jin

Date _____

The final copy of this thesis has been examined by the signatories, and we find that both the content and the form meet acceptable presentation standards of scholarly work in the above mentioned discipline.

Moses, Steven A. (Ph.D., Physics)

A quantum gas of polar molecules in an optical lattice

Thesis directed by Prof. Jun Ye

Ultracold polar molecules, because of their long-range, spatially anisotropic interactions, are a new quantum system in which to study novel many-body phenomena. In our lab, we have produced the first quantum gas of $^{40}K^{87}Rb$ polar molecules. These molecules were found to undergo exothermic chemical reactions, and this led to interesting studies of chemistry near absolute zero. By creating the molecules at individual sites of a 3D optical lattice, we completely suppress these chemical reactions, and the polar molecule gas becomes stable and lives for tens of seconds. This thesis documents our efforts to explore coherent, many-body phenomena resulting from long-range dipolar interactions in the lattice. By encoding a spin-1/2 system in the rotational states of the molecules, we were able to realize spin-exchange interactions based on a spin Hamiltonian, which is one of the first steps in studying quantum magnetism with polar molecules. While this study was the first realization of such coherent dipolar interactions with polar molecules in a lattice, its full potential was limited by the low lattice filling fractions. Using our ability to exquisitely control the initial atomic gas mixture, we loaded a Mott insulator of Rb and a band insulator of K into the lattice. This quantum synthesis approach led to significantly higher molecular filling fractions and represents the first fully connected system of polar molecules in an optical lattice. This low-entropy quantum gas of polar molecules opens the door to interesting quantum simulations, which should be attainable in the next generation of the experiment.

Note: This work was jointly supervised by Prof. Deborah Jin.

## Dedication

To my family, for their constant love and support.

## Acknowledgements

My interest in physics started pretty early in life. I had several great professors in college who were very influential in my decision to go to graduate school. In particular, I would like to thank Jean Krisch, Ctirad Uher, Georg Raithel, and Aaron Leanhardt. It was while I was an REU summer student with James Thompson at JILA in 2008 that I developed my interest in atomic physics, and I realized that Boulder was a very special place. I liked it so much that I came back to JILA for grad school!

My time at JILA has been an adventure, and there are many people I would like to thank for making my time here a great experience. First, I am grateful for having the opportunity to work with Jun and Debbie. They have been incredible leaders. Debbie's patience and positive attitude are incredible, and among the many things that I've learned from her are how to ask the right questions and how to break hard problems into the simplest, most important pieces. Jun has an incredible passion for physics, and his infectious optimism consistently kept my spirits high, even when it seemed like the experimental progress had come to a screeching halt. I also want to thank Eric Cornell, who gave us many useful suggestions over the years. I'm continually amazed by his intuition for experimental physics and his ability to find creative solutions to problems that might initially sound crazy, but almost always work!

When I first came to the lab, I worked with Brian Neyenhuis, Amodsen Chotia, and Marcio de Miranda, who taught me the nuts and bolts of the experiment. I also overlapped briefly with Dajun Wang and Silke Ospelkaus, and I have kept in contact with them from time to time as they're setting up their own polar molecule experiments. After my first year, I met Kang-Kuen

Ni, and since then I've had many fruitful physics discussions with her. Around the same time, Bo Yan joined the project as a postdoc and Jake Covey joined as a grad student. A year later, Bryce Gadway arrived. Bo had an amazing work ethic and could fix anything. Bryce had an encyclopedic knowledge of atomic physics, was an expert at Mathematica, and could always get interesting data out of the experiment. Jake spearheaded the design and construction of the new experiment, and I've learned a lot about designing and building experiments from working with him. I'm grateful for all of their hard work and dedication, which were instrumental for many of the results presented in this thesis. More recently, I've had the pleasure of working with Matt Miecnikowksi and Zhengkun Fu. I trust the experiment is in good hands with Jake and Matt, as they start to get the new system working.

Mike Martin, Matt Swallows, and Jan Hall were very helpful when I was setting up the cavity for the Raman lasers. The staff in the machine shop and electronics shop (especially Hans Green, Carl Sauer, and Terry Brown) were incredibly helpful at various points of the experiment, and the computing department (especially J.R. Raith) helped us with any computing issues we had. I would also like to thank Sara Campbell, Ben and Ruth Bloom, Xibo Zhang, Craig Benko, Bryce Bjork, Brian Lester, Adam Kaufman, Ross Hutson, Toby Bothwell, Wei Zhang, Matt Grau, Will Cairncross, Ed Marti, Shimon Kolkowitz, Tim Langen, Hao Wu, Dave Reens, Alejandra Collopy, Matt Hummon, Mark Yeo, Phil Makotyn, Dan Lobser, Yoav Sagi, Tara Drake, Ming-Guang Hu, Roman Chapurin, Cathy Klauss, Xin Xie, Kevin Cossel, Dan Gresh, Sebastian Blatt, Tom Allison, Arman Cingoz, Brian Sawyer, Travis Nicholson, Oliver Heckl, and all of the other members of the Jin, Ye, and Cornell groups with whom I've overlapped.

I had the pleasure of working and interacting with many great theoretical physicists at JILA and beyond, including Ana Maria Rey, John Bohn, Murray Holland, Paul Julienne, Svetlana Kotochigova, Michael Wall, Kaden Hazzard, Martin Gärttner, Arghavan Safavi, Bihui Zhu, Johannes Schachenmayer, Goulven Quéméner, Michael Foss-Feig, Stefan Natu, and Norman Yao. Thanks for being patient and answering my questions, however silly they may have been.

Rabin Paudel, Adam Reed, Bryce Bjork, and Karl Mayer are great friends, with whom I've

had many great discussions and enjoyed and brewed many beers. Going into the mountains helped me to maintain a healthy work-life balance. When I moved to Boulder, I never imagined that I would one day be running up mountains, biking centuries, and skiing double blacks. But I had a great group of people to do stuff with, and we constantly pushed each other to be our best and do increasingly harder things. In particular, I would like to thank Karl, Adam, Bryce, Carlos Pinilla, Paul Ackerman, Dan Palken, Adam Keith, Phoebe Tengdin, Brad Pelz, Dhruv Kedar, Scott Miller, and all of the other people who I've adventured in the outdoors with.

Finally, I would like to thank my family, who have constantly supported me throughout the years. Their sacrifices during the early years of my education helped pave the way to where I am today.

## Contents

**Chapter**


**1** Introduction 1

1.1 Contents . . . . . 4

**2** Apparatus and techniques 6

2.1 The vacuum system . . . . . 6

2.2 Laser systems . . . . . 7

2.2.1 MOT lasers . . . . . 7

2.2.2 Raman lasers and cavity . . . . . 10

2.2.3 Optical trap/lattice lasers . . . . . 22

2.3 Electric fields . . . . . 23

2.3.1 Electric-field problems . . . . . 23

2.4 Optical lattice techniques . . . . . 25

2.4.1 Band structure and eigenfunctions . . . . . 25

2.4.2 Dependence on beam parameters . . . . . 30

2.4.3 Avoiding superlattices . . . . . 31

2.4.4 Calibrating the lattice depths . . . . . 31

2.4.5 Band mapping . . . . . 34

2.4.6 Generating the lattice beams . . . . . 35

**3** Chemical reactions and the Zeno effect 38

3.1 Brief summary of molecule production . . . 40

3.2 Rotational states and driving rotational transitions . . . 41

3.3 Chemical reactions in 3D . . . 43

3.4 Suppressing chemical reactions in a 1D lattice . . . 45

3.5 Shutting off chemical reactions in a 3D lattice . . . 47

3.6 Long-lived Feshbach molecules and conversion of preformed pairs . . . 50

3.7 Quantum Zeno effect . . . 51

3.8 Conclusion . . . 57

**4** Observation of spin exchange 59

4.1 Deriving the dipolar Hamiltonian . . . 61

4.2 Anisotropic polarizability and differential light shifts . . . 71

4.3 Simple Ramsey sequence and some technical issues . . . 74

4.3.1 Effect of the inhomogeneous light shift . . . 77

4.3.2 Imaging both spin states . . . 78

4.3.3 Creating phase stable microwaves . . . 79

4.3.4 Experimentally measured Ramsey decays . . . 82

4.4 Initial experiments in the $\{|0,0\rangle, |1,-1\rangle\}$ manifold . . . 82

4.4.1 WAHUHA pulse sequence . . . 83

4.4.2 Robustness to imperfections . . . 88

4.5 Second set of experiments . . . 88

4.5.1 Contrast decay for the $|0,0\rangle \rightarrow |1,0\rangle$ transition . . . 88

4.5.2 Fitting to multiple frequencies . . . 89

4.5.3 Theory comparison . . . 91

4.6 Future ideas . . . 93

4.6.1 Simple simulation of spin transport . . . 93

4.6.2 Realizing additional terms in the Hamiltonian . . . . . 95

**5** Increasing the filling fraction 97

5.1 Target distributions: Rb Mott insulator and K band insulator . . . . . 101

5.1.1 Rb Mott insulator . . . . . 102

5.1.2 K band insulator . . . . . 104

5.1.3 Challenges of making a dual insulator . . . . . 106

5.2 Top imaging . . . . . 110

5.2.1 Calibrating the saturation intensity . . . . . 113

5.2.2 Fitting the atomic distributions . . . . . 115

5.3 Measuring the filling of the individual atomic gases . . . . . 117

5.3.1 Measuring the filling of the Rb Mott insulator . . . . . 117

5.3.2 Measuring the filling of the K band insulator . . . . . 120

5.3.3 Using inelastic loss to measure the K filling . . . . . 122

5.4 Studying the dual insulator . . . . . 123

5.5 Putting all of the ingredients together . . . . . 125

5.6 Conclusion and outlook . . . . . 131

**6** Studying doublons in the lattice 133

6.1 Experimental setup . . . . . 134

6.2 Effect of the *d*-wave resonance . . . . . 134

6.3 Detrimental effects due to tunneling . . . . . 140

6.4 Conclusions . . . . . 142

**7** Conclusions and future work 143

**Bibliography** 147

**Appendix**

**A** Deriving the dipolar Hamiltonian 159

# Tables

**Table**

2.1 Polarizabilities and lattice depths of K, Rb, and KRb at 1064 nm. . . . . 33

4.1 Coupling constants of the dipolar Hamiltonian . . . . . 68

# Figures

**Figure**


2.1 Rb laser system . . . . . 9

2.2 K laser system . . . . . 11

2.3 Energy levels and timing diagram for STIRAP . . . . . 12

2.4 Comparison of wavelength tuning of Littrow and Littman configurations for an Eagleyard 980 nm laser diode . . . . . 14

2.5 Optics layout for the Raman lasers . . . . . 17

2.6 Pictures and diagrams of the Raman laser cavity . . . . . 18

2.7 Scheme for bridging the frequency difference between the cavity modes and the STIRAP transitions . . . . . 19

2.8 Measuring the free spectral range of the cavity . . . . . 20

2.9 Ringdown measurements to measure the cavity finesse . . . . . 21

2.10 Beatnote of the down leg master laser with the Sr red MOT laser at 689 nm . . . . . 22

2.11 Electric-field problems . . . . . 26

2.12 Band structure in the lattice . . . . . 27

2.13 Bloch and Wannier functions . . . . . 29

2.14 Calculation of $J$ and $U$ for an isotropic 3D lattice . . . . . 29

2.15 Illustration of how we get superlattices . . . . . 32

2.16 Band mapping in the harmonic trap . . . . . 36

2.17 Different configurations for the optical trap and lattice beams . . . . . 37

3.1 Anisotropy of dipolar collisions in an applied DC electric field . . . . . 39
3.2 Chemical reactions in 3D . . . . . 44
3.3 Loss rate for a mixture of $|0, 0, -4, 1/2\rangle$ and $|1, -1, -4, 1/2\rangle$ molecules . . . . . 44
3.4 Chemical reactions in the 1D lattice . . . . . 46
3.5 Lifetime of ground-state molecules in the 3D lattice . . . . . 49
3.6 Going from 2D to 3D lattices . . . . . 49
3.7 Lifetime of Feshbach molecules after removing all unpaired atoms . . . . . 52
3.8 Experimental setup for studying the continuous quantum Zeno effect . . . . . 54
3.9 Lattice parameters for the Zeno experiment . . . . . 56
3.10 Extracting the filling fraction from the loss measurements . . . . . 56

4.1 Schematic of spin exchange . . . . . 59
4.2 Induced dipole moments of the $N = 0$ and $N = 1$ states . . . . . 64
4.3 Electric field dependence of $J_z$ and $J_\perp$ . . . . . 70
4.4 Diagram showing the anisotropic couplings in the lattice . . . . . 70
4.5 Polarizability of the $N = 0$ and $N = 1$ states at 1064 nm . . . . . 72
4.6 Differential light shifts vs. lattice depth . . . . . 75
4.7 Calculation of how exchange is suppressed by site-to-site energy shifts . . . . . 76
4.8 Timing diagram for Ramsey and spin echo sequences and typical Ramsey fringe . . . 76
4.9 Kinetics imaging for ground-state molecules . . . . . 80
4.10 Setup used to generate phase stable microwaves for driving rotational transitions . . 80
4.11 Typical Ramsey contrast decay for $|0, 0\rangle \rightarrow |1, -1\rangle$ and $|0, 0\rangle \rightarrow |1, 0\rangle$ transitions . . 81
4.12 Contrast decay for the $\{|0, 0\rangle, |1, -1\rangle\}$ manifold . . . . . 84
4.13 WAHUHA sequence . . . . . 85
4.14 A variant of the WAHUHA sequence where the inner $\pi$ pulse is about $\hat{y}$ instead of $\hat{x}$ 87
4.15 Looking at the effect of imperfect $\pi$ pulses and less magic traps on the contrast decay 87
4.16 Comparing contrast decay for $|\uparrow\rangle = |1, -1\rangle$ and $|\uparrow\rangle = |1, 0\rangle$ . . . . . 90

4.17 Comparing one- and three-frequency fits . . . . . 90
4.18 Theory comparsion for many-body dynamics . . . . . 92
4.19 Simulating spin transport in a randomly filled 2D array . . . . . 94

5.1 Ramping on and off the lattice causes very little heating for K, but significant heating for ground-state molecules . . . . . 100
5.2 Image of a Feshbach molecule cloud with a hole in the center due to the initial Rb density being too high . . . . . 100
5.3 Quantum synthesis for realizing high molecule fillings in the lattice . . . . . 101
5.4 Images showing the disappearance of the interference pattern in momentum space as we increase the lattice depth beyond the superfluid-to-Mott insulator transition . 103
5.5 Calculating densities of Fermi gases in the lattice in the limit of zero tunneling . . . 107
5.6 Comparing the densities of degenerate Bose and Fermi gases in a harmonic trap . . . 109
5.7 Issues with the side imaging . . . . . 111
5.8 Problems caused by the ITO plates . . . . . 112
5.9 New setup for top imaging . . . . . 114
5.10 Typical calibration of $I/I_{\mathrm{sat}}$ . . . . . 116
5.11 Calculated distributions of the Mott insulator for typical trap parameters . . . . . 119
5.12 Peak filling of the Rb Mott insulator . . . . . 121
5.13 Peak filling of K and K temperature vs. K number . . . . . 121
5.14 Band mapping of the K gas . . . . . 122
5.15 Hole in the K distribution after undergoing inelastic loss with Rb . . . . . 123
5.16 Using loss induced from spin-changing collisions to measure the K filling fraction . . 124
5.17 The dependence of the Mott insulator filling on interspecies interactions . . . . . 126
5.18 The Rb filling vs. interspecies interactions for different K temperatures . . . . . 127
5.19 Conversion efficiency of making Feshbach molecules vs. Rb number and *in situ* images of ground-state molecules . . . . . 129

5.20 The final molecule filling fraction for different lattice loading procedures . . . . . 129

6.1 Experimental scheme for studying the conversion of preformed pairs . . . . . 135

6.2 Effect of the $d$-wave resonance on molecule production. . . . . 137

6.3 Probability to be adiabatic with respect to the $s$-wave and $d$-wave Feshbach resonances in the lattice . . . . . 139

6.4 Conversion of doublons vs. interaction strength and lattice depth . . . . . 141

7.1 Pictures of KRb generation 2 . . . . . 145

# Chapter 1

# Introduction

One of the major thrusts of modern atomic, molecular, and optical (AMO) physics research is to use systems of cold atoms or molecules to create novel quantum systems that don't exist in nature. The scientific insights gained from studying these systems are useful on their own, but often can be applied to other areas of physics, such as condensed matter physics [1, 2]. AMO systems can be probed and manipulated in a straightforward and clean way. The quantum control of AMO systems has seen remarkable progress in the last few decades, and now experiments can control nearly all degrees of freedom, both internal and external, of the particles. This makes AMO systems ideal for simulating other quantum systems that are difficult to study otherwise [3, 4], and for making very precise measurements [5, 6, 7, 8]. The immense progress in controlling AMO systems really took off with the development of laser cooling [9, 10] and evaporative cooling [11], which led to the first realization of degenerate gases of bosons [12, 13, 14] and fermions [15]. More recently, quantum gas microscopes for bosons [16, 17] and fermions [18, 19, 20, 21] have been realized that can probe individual atoms in an optical lattice. Many other platforms, such as trapped ions [22] and superconducting qubits [23], are quickly building up the infrastructure to perform complex quantum simulations and computations.

Systems of cold neutral atoms are usually very dilute gases and normally weakly interacting. The strongly interacting regime is highly nontrivial and relevant to many interesting phenomena in condensed matter physics. There have been many recent experiments looking at the strongly interacting regime [24, 25, 26, 27, 28]. For alkali atoms, the main tool used to control the interaction

strength is the Fano-Feshbach resonance, which is reviewed nicely in Ref. [29]. Even with this tunability, the particles are still effectively pointlike and interact via isotropic contact interactions that are well parametrized by a quantity called the scattering length $a$. This doesn't mean that neutral atoms cannot be used to study interesting phenomena. For example, the Fermi-Hubbard model, which is a leading candidate for the underlying mechanism of high-$T_c$ superconductivity [30, 31], can be realized with cold atoms in optical lattices [32, 33]; however, one of the main issues with using cold atoms to study the Hubbard model is that the energy scales are weak and the timescales for observing interesting dynamics are relatively long [34, 35, 36]. Systems with long-range interactions open up the possibility of stronger interactions (and correspondingly faster timescales). In addition, systems with long-range interactions could give insight into different physics questions, such as how thermalization and localization work in an isolated quantum system with both disorder and long-range interactions [37], and how correlations spread in a many-body system with long-range interactions [38, 39] (which is relevant for understanding how quickly quantum information can propagate through a system [40]).

There are many ways to realize long-range interactions in the laboratory. Some examples include coupling to phonon modes in trapped ion systems [41], placing atoms in optical cavities [42], using highly excited Rydberg atoms [43], or integrating cold atoms with nanophotonic structures [44]. This thesis discusses long-range interactions that arise from dipole-dipole interactions, which originate from interacting electric or magnetic dipoles. For typical electric and magnetic dipole strengths, electric dipoles are stronger by a factor of $\sim 1/\alpha^2$, where $\alpha$ is the fine-structure constant. Highly magnetic atoms (such as Cr, Er, and Dy) are relatively easy to cool, and both degenerate Bose and Fermi gases of highly magnetic atoms have been produced [45, 46, 47, 48, 49, 50]. In contrast, polar molecules usually have stronger interactions but are more difficult to manipulate and cool [51, 52, 53, 54, 55, 56, 57].

There has been a lot of experimental work trying to directly cool polar molecules. Some common techniques for cooling molecules starting from room temperature include buffer gas cooling [58], Stark deceleration [59, 60, 61], and making a magneto-optical trap (MOT) of polar molecules

[56, 57]. In the case of the MOT, only certain diatomic molecules can be cooled [62]. There are some exotic techniques being employed to cool polyatomic molecules using Sisyphus cooling [63] or a centrifuge decelerator [64]. An alternative approach, which is the method we employ, is to take very cold atoms, in our case $^{40}$K and $^{87}$Rb, first create weakly bound molecules using a Feshbach resonance [65, 66], and then optically transfer the weakly bound molecules to the rovibrational ground state using Stimulated Raman Adiabatic Passage (STIRAP) [51]. This technique produces molecules with a phase space density that is several orders of magnitude higher than the other methods but restricts the possible molecules that can be produced to those molecules comprised of atoms that can be easily laser cooled and for which Feshbach resonances exist [51, 52, 53, 54, 55]. Practically speaking, this usually means bialkali mixtures, although some groups are using an alkaline earth atom in place of one of the alkalis. An alternative option to the Feshbach association is to use STIRAP or photoassociation to first transfer pairs of atoms on individual sites of an optical lattice into weakly bound molecules, and this has worked reasonably well in specific cases, particularly $Sr_2$ [67, 68]. However, for most of the physics that we want to study, the actual atomic species involved are not so important, as our main requirement is that the molecules have a sufficiently large dipole moment. Due mainly to our group's work over the past ten years, a common theme throughout this thesis is that most of the hard work is done in cooling the atoms, and the molecule production is the final step that usually works quite well (there are some caveats, which are discussed in Chapters 5 and 6).

After producing the molecules [51], it was found that KRb suffers from inelastic loss due to chemical reactions [69, 70]. In the next few years, work focused on using optical lattices to suppress this chemical loss [71, 72]. After stabilizing the gas in the 3D lattice, we embarked on a series of experiments looking at coherent manifestations of the dipole-dipole interaction. There have been many proposals for realizing lattice Hamiltonians with multiple rotational states [73, 74, 75, 76, 77, 78, 79, 80, 81, 82]. In particular, Ref. [83] predicted we should be able to see signatures of dipolar interactions even at relatively high entropies and low lattice fillings. By mapping the two lowest rotational states to a spin-1/2 system we realized an XY Hamiltonian, which is one of the first

ingredients necessary for studying quantum magnetism with polar molecules [84, 85]. Models of quantum magnetism, such as the XY model, are some of the simplest yet ubiquitous models that are computationally hard to handle and are impossible to simulate on a classical computer even for as few as 30 spins [38]. There are a host of other interesting phenomena that polar molecule experiments could potentially study, such as Wigner crystallization [86], $d$-wave superfluidity in optical lattices [87], and novel forms of spin-orbit coupling [88]. Open-shell polar molecules could potentially be used to engineer topologically ordered states that could enable topologically protected quantum memories [73, 89].

An important question is whether our experiments are actually doing quantum simulation. After all, the results of our spin-exchange work [84, 85] could be simulated reasonably well using a cluster expansion [85]. If our experiment could achieve better imaging resolution and we could measure spin correlations between individual lattice sites, we should be in a position to measure something that would be classically intractable to simulate. However, even to simulate the global quench experiment, the theory had to be refined and improved in order to converge quickly enough [85]. For our system of polar molecules, the theory and experiment build off of one another in a symbiotic way. The validity of the improved theoretical methods is checked by comparison with the experimental results. The theory can then be used to make further predictions. It is in this sense that our experiment is pushing the field forward and hopefully leading to bigger and better results. In general, most experiments claiming to be doing quantum simulations are still in the benchmarking stage, but benchmarking the results of small systems with theory is very important before attempting to study something really nontrivial.

## 1.1 Contents

In Chapter 2, I describe the apparatus and the upgrades and changes made since I've been at JILA, as well as some relevant experimental techniques. In Chapter 3, I discuss chemical reactions in KRb and how we are able to control them. As an application of the chemical reactions, we studied the continuous Zeno mechanism in a rotational mixture [90]. In Chapters 4 and 5, I present the

main results of this thesis. In Chapter 4, I discuss our work in realizing a spin-1/2 system with polar molecules and then engineering one of the basic ingredients of quantum magnetism, spin exchange interactions. We observed spin exchange between molecules pinned in a deep 3D optical lattice, even though the lattice fillings were quite dilute. A systematic study was undertaken that studied the density dependence, dependence on choice of excited state, and implementing more complex pulse sequences that disentangled isolated pairs. In Chapter 5, I document a detailed study of the molecular filling fractions we can obtain in the 3D optical lattice. By loading a Mott insulator of bosons and a band insulator of fermions into the optical lattice, we optimized the number of lattice sites that have one atom of each species. Combined with efficient magnetoassociation and optical state transfer, this led to significantly higher molecular filling fractions. The achieved filling fractions of $\sim 25\%$ should enable future studies of transport and entanglement propagation in a many-body system with long-range dipole-dipole interactions. In Chapter 6, I present some additional studies related to the molecule association in the 3D lattice. In particular, we observed tunneling dynamics that were strongly modified by strong attractive interspecies interactions, as well as effects due to a $d$-wave Feshbach resonance that's about 1 G above the $s$-wave resonance usually used to make molecules. In Chapter 7, I conclude and give an outlook to future work.

The work described in this thesis is published in several papers, and I am an author on several of them. In particular, Chapter 3 discusses work presented in Refs. [72, 90], Chapter 4 discusses work presented in Refs. [84, 85, 91], Chapter 5 is based on Ref. [92], and Chapter 6 follows Ref. [93].

# Chapter 2

# Apparatus and techniques

This chapter describes the ultracold molecule apparatus, with a particular emphasis on the components that were built or modified during my time at JILA. Most of my time here was spent doing experiments with the first generation apparatus, which was started by Josh Zirbel and Kang-Kuen Ni in 2003. Except for when we broke vacuum in 2012 to change the science cell in an attempt to solve the electric-field charging problem, the vacuum chamber itself wasn't really modified and there were no significant vacuum issues. However, many other things on the experiment (laser systems, electronics, etc.) have been modified. A few years ago we started thinking about building a new generation of the experiment to address many technical limitations of the first generation experiment. This effort was spearheaded by Jake Covey, and in October 2015, we switched to the second generation apparatus.

## 2.1 The vacuum system

Similar to many of the other quantum gas machines at JILA, our vacuum chamber consists of two parts separated by a gate valve: a higher pressure MOT chamber and a lower pressure science chamber. The vacuum lifetimes are a few seconds in the MOT chamber and a few hundred seconds in the science chamber, implying the pressure is about two orders of magnitude lower in the science chamber. In contrast, many other experiments have a single chamber utilizing an oven and an atomic beam fed from a Zeeman slower. In our experiment, atoms are transferred between the two chambers via a cart with coils that provide a strong quadrupole field (these are the same

coils that produce the quadrupole field for the MOT). There are two ion pumps, one for the MOT chamber and another for the science chamber, and there is also a titanium sublimation pump near the science cell. The gate valve between the two sides allows one to break vacuum on one side without affecting the other side.

## 2.2 Laser systems

Many lasers are required to cool and trap two atomic species, and then create molecules. The lasers can be divided into three categories: cooling lasers which we use for cooling and imaging K and Rb, Raman lasers for the STIRAP transfer to the ground-state, and the optical trap/lattice lasers.

### 2.2.1 MOT lasers

When I first came to the lab in 2010, the laser systems for trapping and cooling Rb and K were less robust than we would desire. Many of the lasers were old and the beam height was about 6 inches, which meant that beams had to be realigned quite often. The trapping light was derived from external cavity diode lasers (ECDLs), some of which weren't AR coated, and a slave laser was used for both K and Rb since the power of the master lasers wasn't sufficient to inject a tapered amplifier (TA). The K slave laser was actually a 780 nm diode that was cooled to -40°C. Also, the lasers were on the same table as the main experiment, so there were a lot of issues due to vibrations from the cart and shutters.

To make the system more robust, I decided to rebuild the cooling diode lasers from scratch. We decided to replace the ECDLs with distributed Bragg reflector (DBR) lasers from Photodigm. The K laser diodes have a maximum power of 60 mW, while the Rb laser diodes have a maximum power of 120 mW, so no slave lasers are required. Because the feedback is provided by a distributed Bragg grating integrated on the diode, there is no external cavity, and the mode-hop-free tuning range is significantly higher than that of an ECDL, typically $> 50\,\mathrm{GHz}$. The downside is that the linewidth is about 1 MHz, which is larger than an ECDL but adequate for cooling alkali atoms.

Because there is no external cavity, the laser is incredibly sensitive to optical feedback, and we need two optical isolators to provide at least 60 dB of isolation. The beam height is roughly 2 inches and the system rarely needs realignment.

The repump lasers for both K and Rb are locked to an absorption cell using frequency-modulation (FM) spectroscopy. A beam of a few hundred $\mu$W is phase modulated at around 20 MHz with an electro-optic modulator (EOM), and then split into a strong pump beam and weak probe beam. We then do standard saturated absorption spectroscopy. The error signal is obtained from demodulating the probe beam transmission with a phase shifted copy of the same tone used to drive the EOM. This technique is described in Ref. [94] and is similar to Pound-Drever-Hall (PDH) locking, which will be discussed later.

The schematic of the Rb laser system is shown in Fig. 2.1. We lock the repump laser to the $F = 1$ to $F' = 1/2$ crossover. This is a fairly weak transition, and we heat the Rb vapor cell to get a better signal-to-noise ratio (SNR). For both K and Rb, the trap lasers are frequency locked to the repump lasers using a frequency-to-voltage (F-V) converter. We chose this option because of the large servo bandwidth that would be necessary to phase lock the DBR lasers to each other. The frequency offset is controlled by an RF frequency derived from a voltage controlled oscillator (VCO). The F-V converter is set up so that a frequency of around 30 MHz corresponds to 0 V (the useful range of the device is about 0-70 MHz). We also find it useful to put a 50 MHz low pass filter on the input to the F-V converter.

For K, we lock the repump laser to a $^{39}$K absorption line since the absorption cell contains only the natural abundance of $^{40}$K, which is $\sim 0.01\%$, whereas it has about 93% $^{39}$K. Specifically, we lock to the $F = 2$ to $F' =$ all feature, since the hyperfine structure is not resolved in $^{39}$K. To shift the laser to the right frequency for $^{40}$K, we use a 345 MHz acousto-optic modulator (AOM). In the old experiment, we derived two additional beams from the repump laser, the high-field imaging light and the $|9/2, -5/2\rangle$ blast light. The high-field imaging, which is on the $|9/2, -9/2\rangle \rightarrow |11/2, -11/2\rangle$ cycling transition, is about 770 MHz lower in frequency at 550 G than at zero magnetic field, so it can be accessed from the repump laser. For the experiments described in Chapters 5 and 6, we

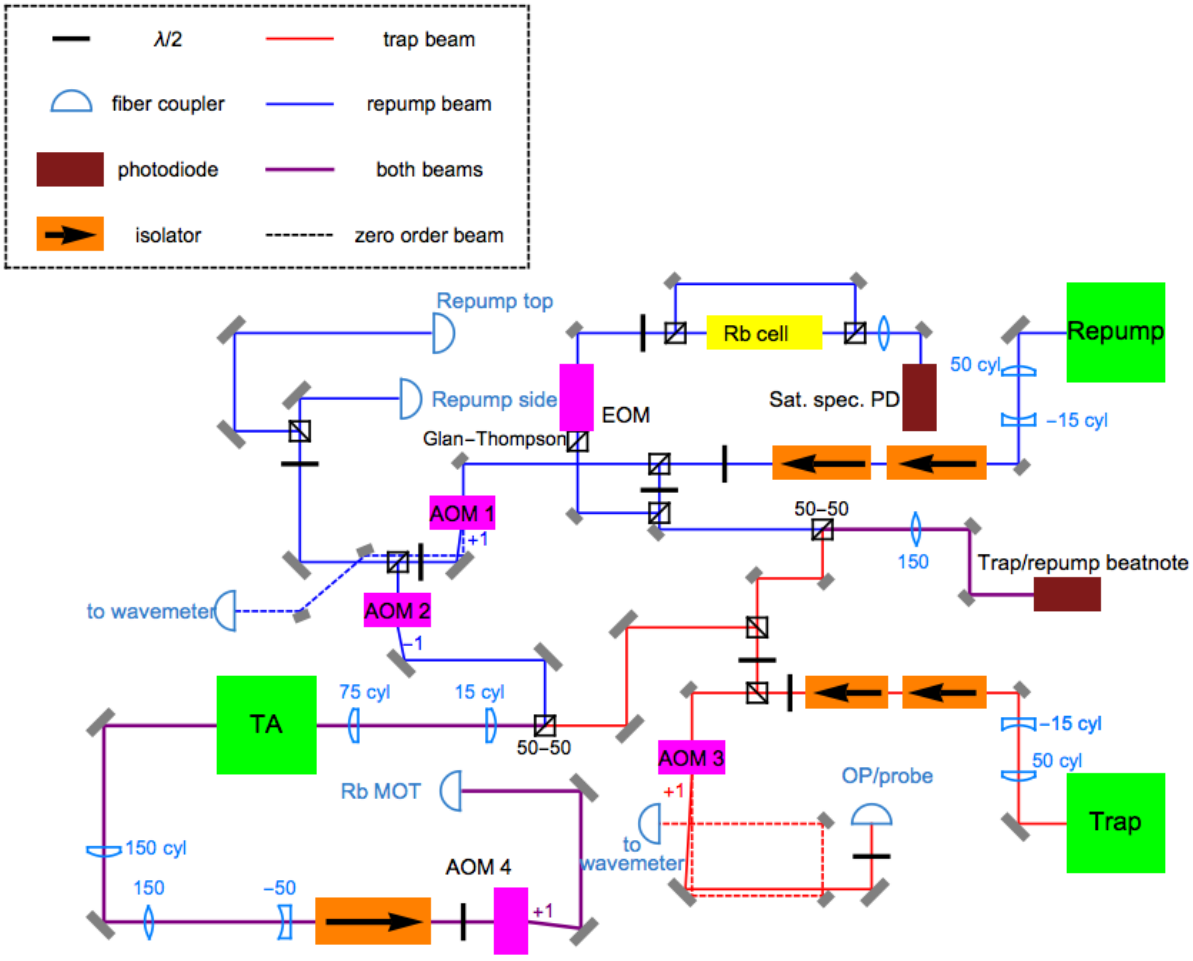


Figure 2.1: Rb laser system. AOM 1 shifts the frequency for the repump light used during optical pumping and high-field imaging, when it pumps atoms from the $F = 1$ manifold to the $F = 2$ manifold. AOM 2 undoes the frequency shift of AOM 1 and allows us to reduce the power of the repump light going to the MOT, which is useful during the CMOT and molasses stages. AOM 3 gives the frequency shift and switches the light for the Rb probe light, optical pumping, fluorescence pulse, and high-field imaging. To adjust the laser frequency for these different processes, the beatnote frequency between the trap and repump lasers is changed. AOM 4 is used to servo the total MOT intensity (which is mostly trap light). All beamsplitters are polarizing unless noted otherwise. The AOM orders are listed next to the beams after the AOM. All focal lengths are given in mm.

wanted to be able to image K at any magnetic field within 10-15 G of the Feshbach resonance. For this purpose, the original high-field imaging was insufficient since the frequency could only be tuned by a few MHz without requiring realignment. To solve this problem, we implemented an offset lock with a wider tuning range by switching to a VCO with larger bandwidth (part number ZX95-1300-S+ from Mini Circuits, which has a range 400-1300 MHz). With this expanded range for the offset lock, we were then able to derive the high-field imaging light from the trap laser. At one point, we used $^{41}$K instead of $^{40}$K. For this, we offset locked both DBR lasers to a master laser, which was an ECDL (this is the "third" laser in Fig. 2.2). In general this is the most flexible approach, and even though it requires one more laser, fewer AOMs (just 2 as opposed to 4 or 6) would be required.

### 2.2.2 Raman lasers and cavity

Stimulated Raman adiabatic passage (STIRAP) is used to transfer weakly bound Feshbach molecules to the ground state [95]. It's a Raman process, and the two colors we need (689 and 968 nm) are accessible with modern laser diode technology. The relevant energy levels are sketched in Fig. 2.3a. We start in the Feshbach state $|f\rangle$ and couple through a lossy excited state $|e\rangle$ (with decay rate $\gamma$) that has decent Franck-Condon factors with both the Feshbach state and the ground state $|g\rangle$. We apply two laser fields: the up leg (with Rabi frequency $\Omega_u$), which couples $|f\rangle$ and $|e\rangle$, and the down leg (with Rabi frequency $\Omega_d$), which couples $|g\rangle$ and $|e\rangle$. The goal of STIRAP is to coherently maintain the dark state $\cos\theta|f\rangle + \sin\theta|g\rangle$, where $\theta = \tan^{-1}\left(\frac{\Omega_u}{\Omega_d}\right)$. There are two relevant detunings, the single photon detuning $\Delta$ and the two-photon detuning $\delta$. We normally operate with $\Delta = \delta = 0$, but it's more imperative that $\delta$ be zero for efficient transfer. If we choose a pulse sequence where initially $\Omega_d/\Omega_u \gg 1$ and then adiabatically change the intensities so that at the end $\Omega_u/\Omega_d \gg 1$ (Fig. 2.3b), we can transfer most of the population from $|f\rangle$ to $|g\rangle$ without populating the lossy state $|e\rangle$. Experimentally, we define a pulse time $\tau$ as the time duration during which the intensity ramping occurs. For more details about STIRAP, see the thesis of Kang-Kuen Ni [96].

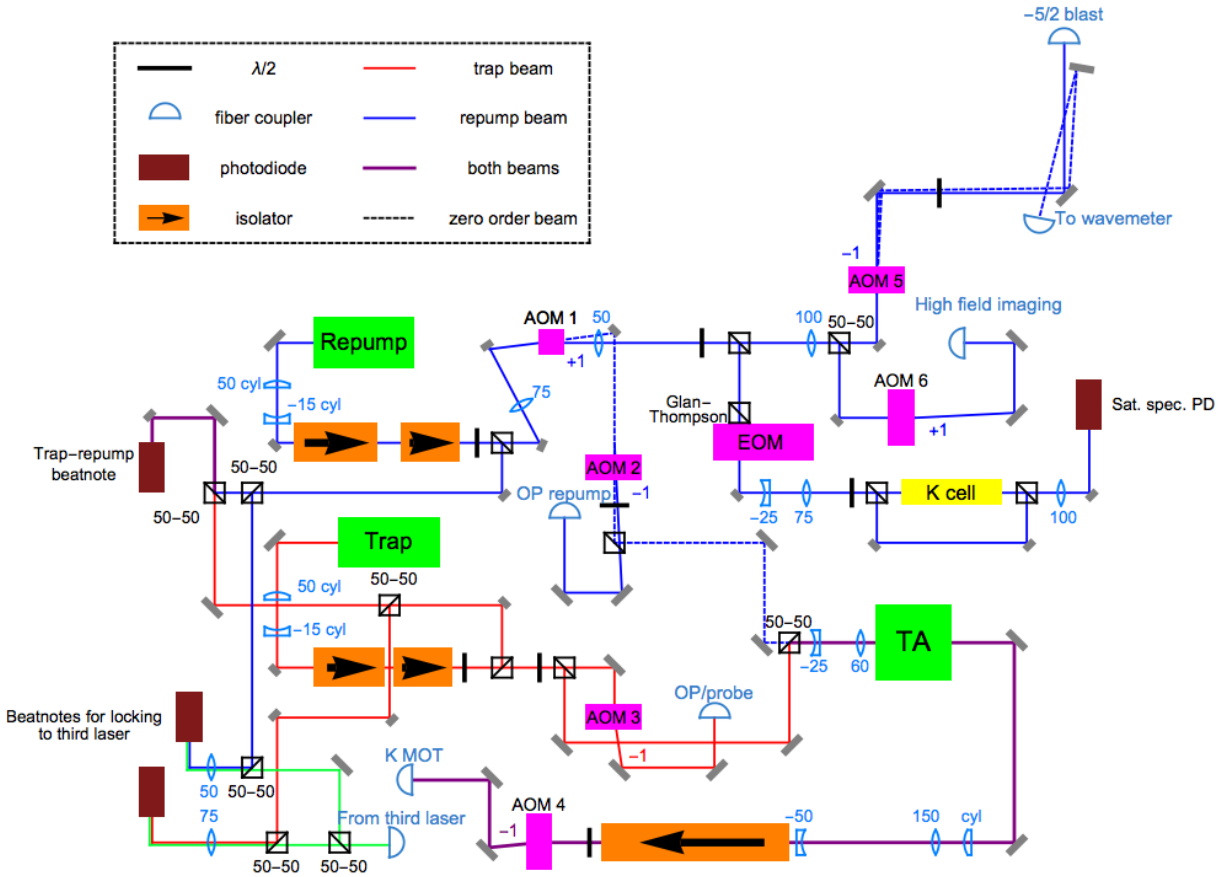


Figure 2.2: A schematic of the K laser system. Similar to the Rb system, there is a trap and repump laser, as well as a tapered amplifier. AOM 1 is at 345 MHz and is used to bridge the frequency difference between the $^{39}$K and $^{40}$K transitions (we lock the laser to one of the $^{39}$K transitions). AOM 2 is for the optical pumping repump. We also use this AOM to control the trap/repump power ratio for the MOT light. AOM 3 is for the probe and optical pumping beam. AOM 4 is for stabilizing the total power of the MOT. AOMs 5 and 6 provide the switch and frequency shift for the K $|9/2, -5/2\rangle \rightarrow |11/2, -5/2\rangle$ blast light and the K high-field imaging $|9/2, -9/2\rangle \rightarrow |11/2, -11/2\rangle$. All beamsplitters are polarizing unless noted otherwise. The third laser was an ECDL locked to one of the $^{39}$K transitions, which we used as a reference when trapping and cooling $^{41}$K.

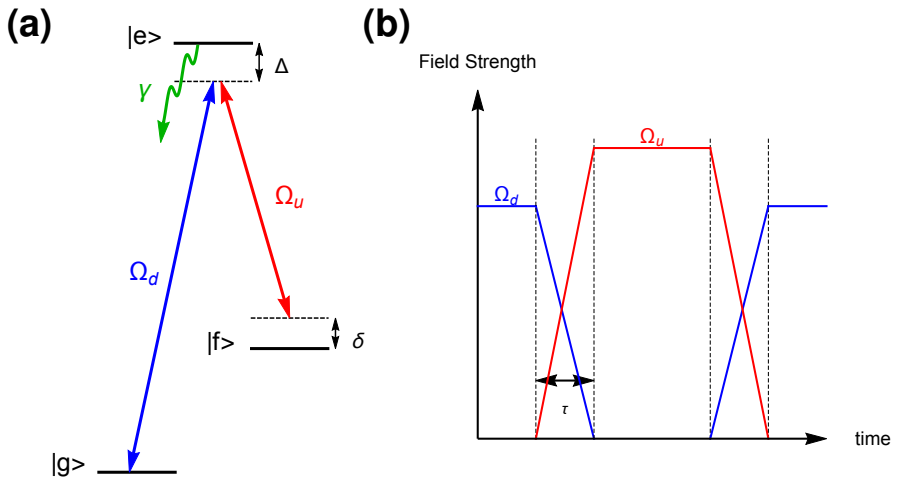


Figure 2.3: (a) The energy levels relevant for STIRAP are the Feshbach molecules $|f\rangle$, the lossy excited state $|e\rangle$ (with decay rate $\gamma$) and the ground state $|g\rangle$. Usually we set the single-photon detuning $\Delta = 0$ and we scan the two-photon detuning $\delta$ by adjusting the up leg double-pass AOM, driven at frequency $f_{\mathrm{DP}}$. (b) Timing diagram for STIRAP. Initially $\Omega_d \gg \Omega_u$. We then ramp $\Omega_d$ to 0 as we ramp $\Omega_u$ to its maximum value. Here a linear ramp in field strength is shown. In practice, we usually ramp the intensities linearly. The pulse time $\tau$ is the duration of the ramps. To STIRAP back to Feshbach molecules, we reverse the order of the ramps (start with $\Omega_d$ at zero, $\Omega_u$ at the maximum value, and then ramp $\Omega_d$ to the maximum value and $\Omega_u$ to zero).

To maintain the dark state and transfer a significant fraction of the population, it's necessary for the two laser fields to be phase stable during the pulse time $\tau$. More precisely, the transfer efficiency scales as $e^{-\pi^2\gamma/(\Omega_0^2\tau)-\eta\tau/2}$, where $\eta$ is the relative linewidth, $\tau$ is the pulse time, and $\Omega_0 = \sqrt{\Omega_{u,max}^2 + \Omega_{d,max}^2}$ [97]. For efficient STIRAP, we require $\eta\tau \ll 1$ and $\gamma/(\Omega_0^2\tau) \ll 1$. For us, $\gamma = 2\pi \times 6.7\,\mathrm{MHz}$ [96], $\Omega_0$ is typically $2\pi \times 6$ MHz, and $\tau$ is usually 6-10 $\mu$s. Plugging these in, the first factor is $\sim e^{-0.05} = 0.95$, and the relative linewidth should be less than 1 kHz in order to not be limited by the laser linewidth. In the work of Ref. [92], the one-way transfer efficiency was routinely 0.9-0.95 for cold, small samples.

To get a sense of the optical powers required for STIRAP, it's necessary to know both the transition dipole moments and the sizes of the beams. The beams are focused to roughly the same size as the optical trap beams ($200 \times 40\,\mu$m in the radial and vertical directions, respectively) to give roughly homogeneous coupling over the cloud while still getting a reasonably large intensity. The transition dipole moments are $0.005(2)\,ea_0$ for the up leg and $0.012(3)\,ea_0$ for the down leg [96]. These are substantially weaker than typical cycling transitions in alkali atoms ($\sim 1\,ea_0$). We want to achieve Rabi frequencies of a few MHz, which means we need powers in the range 20-100 mW. As a result, the power from the master lasers is insufficient, so we need some additional amplification. For the up leg, we use a laser diode operating at 968 nm. Currently, this is an Eagleyard AR-coated 980 nm laser diode in a Littrow configuration (see Fig. 2.4 for a discussion of how these lasers don't perform well in the Littman configuration) along with an Eagleyard 970 nm TA. For the down leg, we use an AR-coated laser diode operating at 689 nm (again in the Littrow configuration), along with a slave laser (HL6750MG), which is optically injected.

When I first came to the lab, we were stabilizing both of the Raman lasers to a Ti-sapphire frequency comb [98]. While the comb is useful for the initial spectroscopy, it can be a bit cumbersome on a daily basis. We stabilized both degrees of freedom of the comb, the repetition rate $f_{\mathrm{rep}}$ and the carrier offset frequency $f_{\mathrm{ceo}}$. To stabilize $f_{\mathrm{rep}}$, we locked one comb tooth to Jan Hall's 1064 nm stable laser, which was stabilized to an iodine cell. To stabilize $f_{\mathrm{ceo}}$, we frequency doubled the part of the comb around 1064 nm and beat it with the part of the comb at 532 nm. Thus, we needed

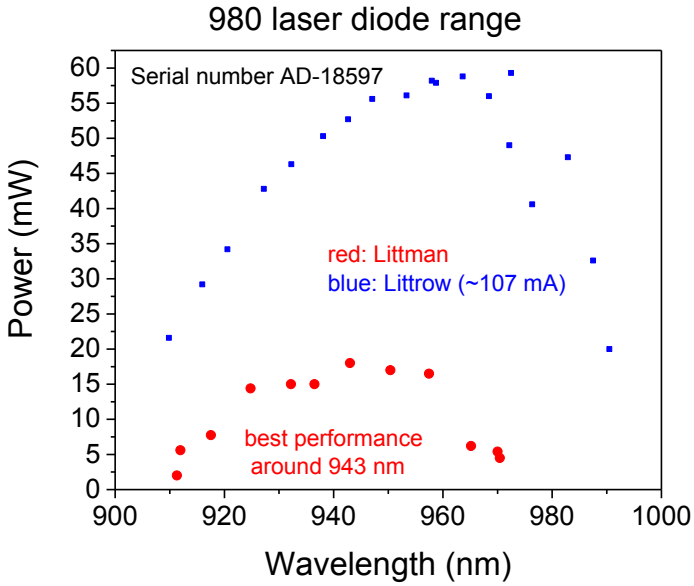


Figure 2.4: We could never get the Eagleyard laser diodes to work well in the Littman configuration. Here we compare the performance of an Eagleyard 980 nm AR-coated diode in the Littrow and Littman configurations. The power in the Littman configuration is lower (which is to be expected), but the wavelength tuning range is smaller and the peak wavelength is shorter, such that the laser doesn't work well at our desired wavelength of 968 nm.

an octave spanning comb from 532 to 1064 nm and also required sufficient optical spectrum at 690 and 970 nm to obtain strong beatnotes for locking the Raman lasers. In principle, by phase locking both lasers to the comb, the two lasers should be perfectly phase-locked to each other; however, the comb itself had a linewidth of about 1 kHz. Furthermore, the comb was located in a different room from the main experiment, with $\sim$ 25-meter fibers sending the light from the lasers to the comb and similar length BNC cables transmitting the error signal back to our room. We weren't canceling the phase noise induced by acoustic vibrations in the fibers, which could broaden each of the lasers, and the long cables meant a long time delay and correspondingly low servo bandwidth. This may have led to a mediocre relative linewidth. We would definitely see fluctuations in the transfer efficiency from day to day depending on how well the lasers were locked, and some days we spent the entire day getting the comb and lasers locked.

To make the experiment more reliable, we decided to replace the comb with a high finesse cavity. This system is much more robust and usually it takes less than 5 minutes every day to get the lasers locked well. Most other groups making ultracold polar molecules have followed our example and are using cavities for locking their Raman lasers. The cavity is comprised of a cylindrical piece of Zerodur (a glass-ceramic with very small coefficient of thermal expansion) with a bore through the center, and fused silica substrates optically contacted on the ends. One of the mirrors is flat and the other has a 50 cm radius of curvature, which ensures the transverse modes are not degenerate. A highly reflective coating at both 690 and 970 nm gives finesses of several $10^4$, which are measured via ringdown (Fig. 2.9). The coating was done by Advanced Thin Films, a company in Boulder. The cavity is housed inside of an aluminum box and pumped down to about $10^{-6}$ torr (see Fig. 2.6). We passively stabilize the temperature of this box to $\sim$ 10 mK, which gives day to day frequency drifts of roughly 100 kHz (inferred from scanning the two-photon detuning of STIRAP), which is less than the typical two-photon width of STIRAP of 500 kHz. We scan the STIRAP lineshape roughly once a day and rarely see any degradation in the transfer throughout the day due to the frequency shifting. When we moved the lab from JILA's S-wing to the new X-wing at the end of 2012, there seemed to be a small leak in the cavity chamber. Upon pumping down again, the cavity

seems to have slightly changed length or moved, since the resonant frequencies shifted by about 10 MHz.

We lock the lasers using standard PDH locking techniques [99, 100] to the $TEM_{0,0}$ modes. In both cases we fiber couple the lasers to the cavity platform to have a stable alignment and to get better mode matching into the $TEM_{0,0}$ modes. To achieve the highest possible servo bandwidth, we minimize the length of the cables from the current controller to the laser and from the servo to the current controller. We achieve servo bandwidths of 2-3 MHz for the down leg laser and 1.5-2 MHz for the up leg laser (the lower servo bandwidth in this case seems to arise from the laser diode itself since we could achieve higher servo bandwidths with different 970 nm laser diodes). This servo bandwidth is much larger than we achieved when locking the lasers to the comb and is comparable to the Rabi frequencies $\Omega_{u,max}$ and $\Omega_{d,max}$. For the down leg, we observed that the STIRAP efficiency was very sensitive to the servo gain. To avoid deleterious effects of the relaxation bumps of the laser (which occur at the servo bandwidth), we optically inject the 690 slave laser with the transmitted light from the cavity. Good spatial mode matching between the transmitted beam and the slave laser beam is important in order to be able to reliably inject the slave laser with less than 200 $\mu$W. In order to use the transmitted beam, it's very important to have an optical isolator after the cavity. Otherwise, a small amount of light from the slave laser is coupled into the cavity the wrong way and makes it all the way to the photodiode (PD 3 in Fig. 2.5). This light interferes with the normal reflection off of the cavity and writes noise on the error signal. For the up leg, we inject the TA with the unfiltered master light, as we didn't observe a similar sensitivity to the servo gain.

In general, there will be a frequency difference between the $TEM_{0,0}$ cavity modes and the transitions for STIRAP. The difference could be as large as $\nu_{\mathrm{FSR}}/2$, where the free spectral range $\nu_{\mathrm{FSR}} = c/2L$ is the spacing between longitudinal modes of the cavity ($c$ is the speed of light and $L$ is the cavity length). We heat the chamber to stabilize the temperature, but since it's ULE glass we don't get a large tuning range with temperature. To compensate for this frequency difference, we use two AOMs for both lasers (see Fig. 2.7). For the up leg, the STIRAP transition is about 200

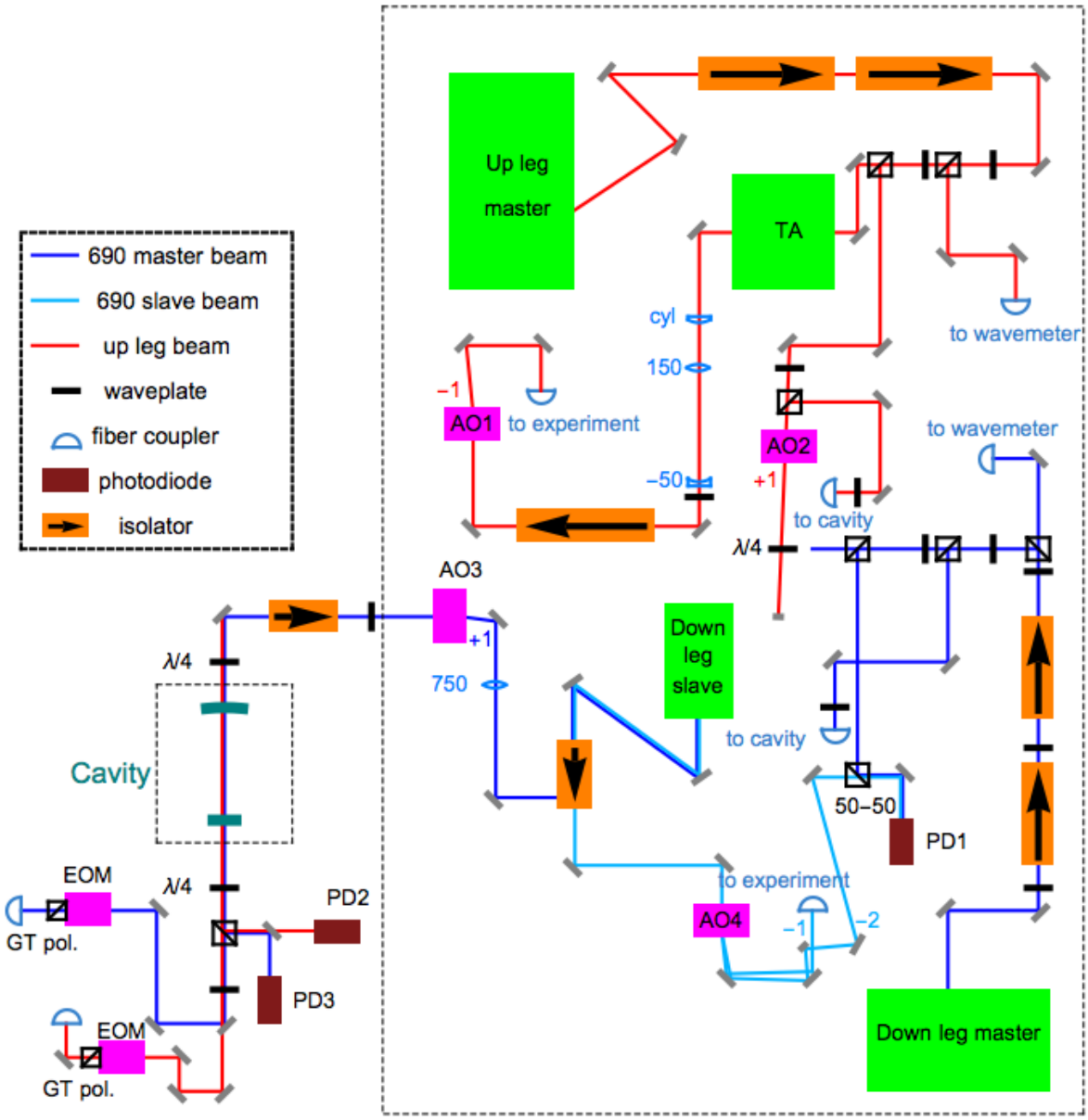


Figure 2.5: Layout for the Raman lasers. Both lasers are fiber coupled to the cavity platform. The frequency difference between the up leg STIRAP transition and the cavity mode is bridged by a double-pass AOM (AO2) and a single-pass AOM (AO1) of opposite orders, so that the total difference is $f_{\mathrm{SP}} + 2f_{\mathrm{DP}}$. For the down leg, two single-pass AOMs of opposite orders bridge the very small (less than 10 MHz) frequency difference between the cavity mode and the STIRAP line. We scan the two-photon detuning $\delta$ by changing $f_{\mathrm{DP}}$. PD1 is for the master-slave beatnote. PD2 is for PDH locking for the up leg, and PD3 is for PDH locking for the down leg. On the cavity platform, the two colors are combined/separated using dichroic mirrors. The 690 slave laser is injected by sending the transmitted light from the cavity through the isolator the "wrong" way.

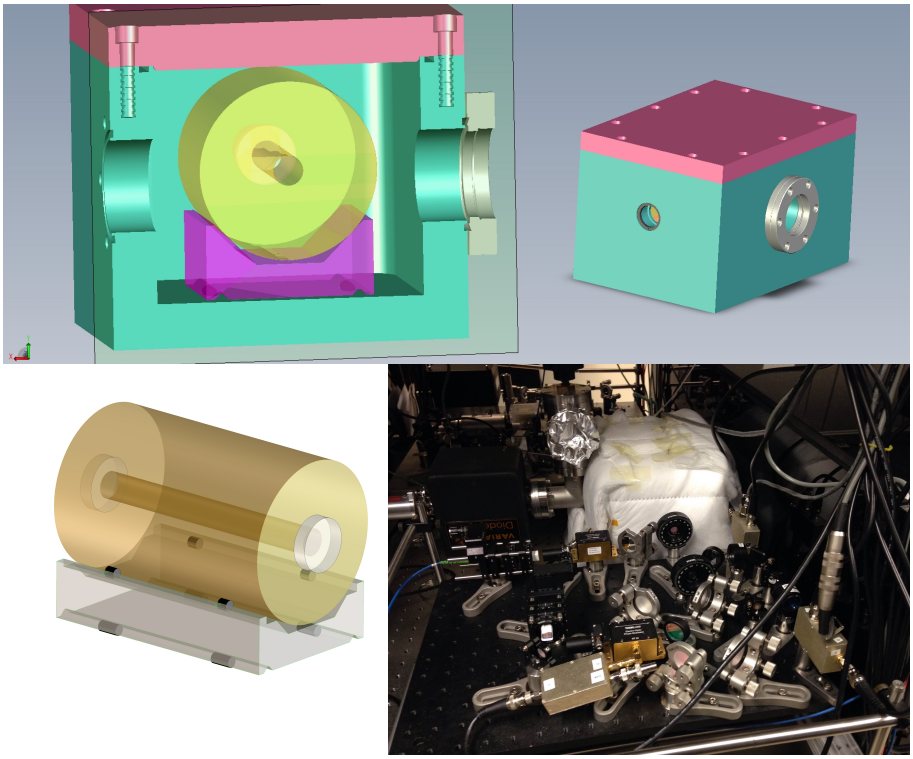

Figure 2.6: The cavity spacer is a cylindrical piece of zerodur, which is supported on top of another piece of ULE glass by four small oring pieces. This entire assembly sits inside of a vacuum chamber that is pumped down to $\sim 10^{-6}$ torr and temperature stabilized to $\sim$ 10 mK. The picture in the lower right shows how the chamber is currently installed in the lab. There are two layers of temperature control and a lot of insulation. The drawings are courtesy of Hans Green and the instrument shop.

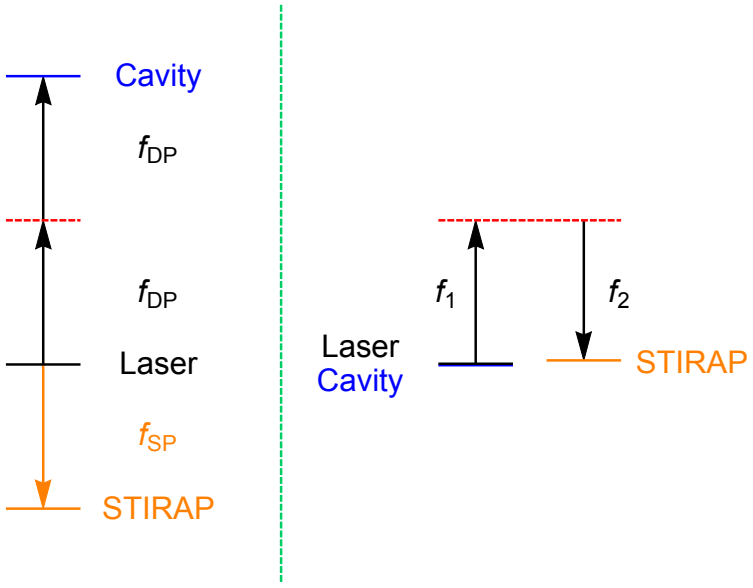


Figure 2.7: Left: Scheme for bridging the frequency difference between the cavity and up leg STIRAP line. Increasing the frequency of the double-pass AOM $f_{\mathrm{DP}}$ reduces the laser frequency. In Fig. 2.5, AOM 1 is driven at $f_{\mathrm{SP}}$ and AOM 2 is driven at $f_{\mathrm{DP}}$. Right: Similar diagram for the down leg. The STIRAP transition is within 10 MHz of the cavity mode. AOM 3 is driven at $f_1$ and AOM 4 is driven at $f_2$.

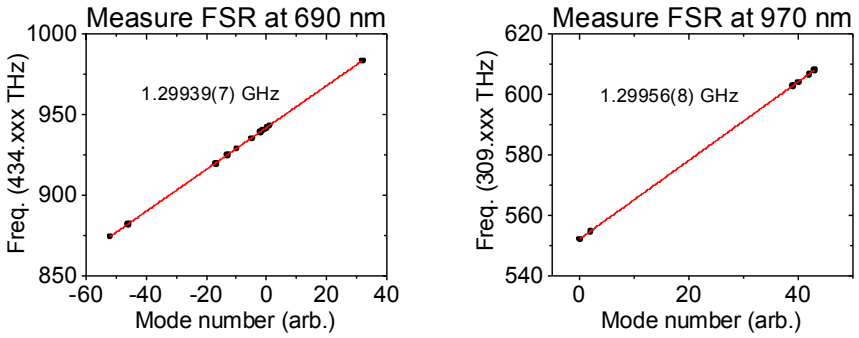


Figure 2.8: Position of many $\mathrm{TEM}_{0,0}$ modes, using our wavemeter to measure the frequency (to 8 digits). The measurements were taken on the same day to minimize any drifts of the wavemeter calibration. Fitting lines, we extract $\nu_{\mathrm{FSR}}$, which is around 1.3 GHz.

MHz lower than the closest cavity mode, and this difference can easily be bridged by double-pass and single-pass AOMs of opposite order. By scanning the RF frequency $f_{\mathrm{DP}}$ of the double-pass AOM, we scan the two-photon detuning $\delta$. For the down leg, the difference between the cavity mode and the STIRAP line is less than 10 MHz, so we use two single-pass AOMs of opposite order, one that deflects the transmitted light from the cavity to the slave laser and the other that switches the light to the main experiment.

To check the cavity is behaving as expected, I measured the FSR, the finesse, and the transmission on resonance. To measure the FSR of the cavity, I locked the laser to many different cavity modes and recorded the frequency using our wavemeter. Although our wavemeter is only accurate to about 100 MHz and only reads to the 10 MHz place (8 digits), on a given day the relative difference between two nearby frequencies should be known to $\sim$ 10 MHz. Fig. 2.8 shows these measurements for both colors, and the resulting $\nu_{\mathrm{FSR}} = 1.3$ GHz implies the cavity length is 11.5 cm.

A typical way to measure the finesse $\mathcal{F}$ of the cavity is to do a ringdown measurement, in which the incident light to the cavity is instantaneously shut off, which can be achieved by switching off an AOM. The light from the cavity will leave, but not all at once, since photons make roughly $\mathcal{F}$ roundtrips before exiting the cavity. The power leaving the cavity decays exponentially with a

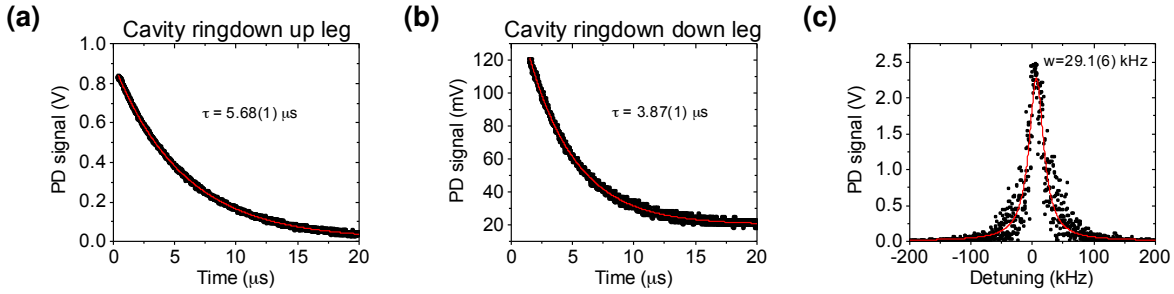


Figure 2.9: Ringdown measurements at 968 nm (a) and 689 nm (b). From the time constants we extract finesses of $4.6 \times 10^4$ and $3.2 \times 10^4$ at 968 and 689 nm, respectively. (c) The transmission of the up leg when it was locked to the comb. The FWHM $\kappa$ can be used as an independent measurement of the finesse, using $\mathcal{F} = \frac{\nu_{\mathrm{FSR}}}{\kappa}$. The result is $\mathcal{F} = 4.5 \times 10^4$, which is slightly lower than the finesse extracted from the ringdown measurement.

time constant given by

$$\tau = \frac{\mathcal{F}L}{\pi c} \rightarrow \mathcal{F} = 2\pi\tau\,\nu_{\mathrm{FSR}}. \tag{2.1}$$

This is shown in Fig. 2.9a for the up leg and Fig. 2.9b for the down leg. Alternatively, when the lasers were locked to the comb, I scanned the up leg across the cavity resonance (Fig. 2.9c). Then by measuring the transmission spectrum, we can obtain the cavity linewidth $\kappa$ through the equation $\mathcal{F} = \nu_{\mathrm{FSR}}/\kappa$. The two methods agree reasonably well, with the finesse extracted from the linewidth measurement slightly lower than the finesse extracted from the ringdown measurement.

Since we want to optically inject the down leg slave laser with the transmitted light from the cavity, we care about how much light is transmitted on resonance. I measured $P_t/P_{in} \approx 0.25$ for the down leg, which means we need to send more than 1 mW to the cavity in order to get enough transmitted light to inject the slave laser. The transmission for the up leg is about 0.35.

Going back to the condition stated earlier that the relative linewidth should be less than 1 kHz for efficient STIRAP transfer, we're interested in measuring the linewidth of our lasers. The most direct way to do this is to build two ostensibly identical systems and then beat them against each other. This is not really an option for us since we don't have the resources to build another complete cavity setup. A more indirect method is to use delayed self-heterodyne interferometry [101, 102], in which the laser is separated into two parts, one of which has a long delay (achieved

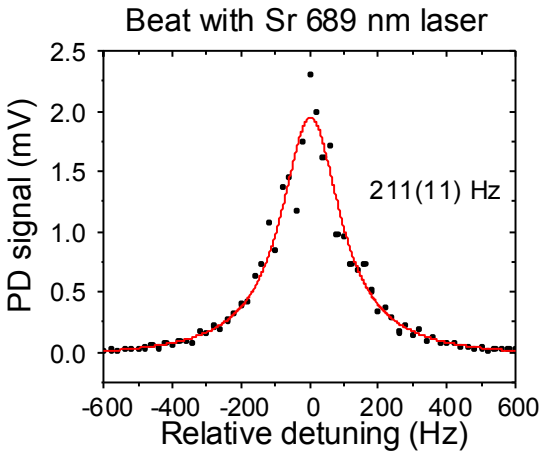


Figure 2.10: The average of 10 single sweeps on the spectrum analyzer with resolution bandwidth 30 Hz. Each time the beat frequency was subtracted. The fit is a Lorentzian.

by using a long optical fiber) and then creating a beatnote between the two paths. We only have a 1 km fiber available, which is not really sufficient to reliably measure sub-kHz linewidths.

Conveniently, the down leg transition is within 100 GHz of the Sr red MOT transition. So we decided to lock our laser to the nearest cavity mode to the Sr red MOT transition and beat our laser against the 689 nm Sr laser in the neighboring lab, which should have a linewidth $\ll 100$ Hz. Because the lasers are not referenced to each other, the beatnote frequency drifted over time, but averaging 10 single sweeps on the RF spectrum analyzer, we measure a relative linewidth of around 200 Hz (see Fig. 2.10). Since our two Raman lasers are locked to the same cavity, their relative linewidth should be at a similar level or even smaller, which is adequate for performing efficient STIRAP.

### 2.2.3 Optical trap/lattice lasers

For most of the work described in this thesis, the optical trap (OT) and lattice lasers are at 1064 nm. This is a convenient wavelength since high-power, low-noise lasers are commercially available, and the molecules have a long lifetime when exposed to 1064 nm light (1064 nm photons have a lower energy than necessary to excite to the bottom of the excited molecular potential [72]).

We used several different types of 1064 nm lasers for the OT and lattice during my time at JILA, including a Verdi-IR, an IPG fiber laser, and a Nufern fiber amplifier seeded by a Mephisto NPRO. This latter combination was chosen because the Mephisto has a relatively narrow linewidth ($\sim$ 1 kHz) and the Nufern fiber amplifier has low noise and a high gain (50 W for a 1-15 mW input). Towards the end of the generation 1 apparatus, we were using the Verdi-IR for just one of the OT beams. This is because the power of the Verdi-IR had deteriorated and so we couldn't reliably get all the power we needed for both OT beams, which is more than 1 W per beam at the beginning of the OT evaporation.

At one point the Mephisto laser that seeded our Nufern fiber amplifier became multimode, and this affected the lattice depths. We noticed this problem when we switched to using the Verdi for the seed laser, and all of the lattice depths increased, even though the power and polarization of the lattice beams didn't change. When using the Mephisto, a large fraction of the light was at a different frequency, and presumably the phase of the two lattices was different. Either way, there was likely some kind of superlattice and a large fraction of the light was not interfering, leading to a smaller lattice depth.

## 2.3 Electric fields

We want to apply large DC electric fields to polarize the molecules in the lab frame and induce dipole-dipole interactions. As will be discussed in Chapter 4, applying a DC electric field realizes Ising-type interactions between the two lowest rotational levels. We need to apply large fields (more than 10 kV/cm) to begin to saturate the dipole moment (see Fig. 4.2). Ideally, we want very flat fields without having to sacrifice optical access. To do this, we use electrodes with transparent indium-tin-oxide (ITO) coatings.

### 2.3.1 Electric-field problems

There were several limitations with the electric-field control in the old experiment. The layout and geometry of the electrodes was very similar to that described in the thesis of Kang-Kuen Ni

[96]. In short, the plates are arranged in a boxlike structure, with plates usually only on the top and bottom, similar to the setups depicted in Fig. 2.11a. In 2012, we were trying to use an electric-field gradient to tilt the 2D traps formed from a vertically oriented 1D optical lattice. After doing this for a while, we learned that there was a severe charging problem occurring in the glass walls forming our cell, where an electric field opposite in direction to our applied field would build up over time. We determined this charging field $E_{\mathrm{ch}}$ was in the opposite direction of the applied field by looking at the shift in the dark resonance with small applied electric fields of both polarities, and determining which direction of applied field would bring the transition closer to the zero field value (this was the same polarity used to get to the charged condition). The presence of $E_{\mathrm{ch}}$ manifested in two ways: (1) a shift in the two-photon detuning of STIRAP, and (2) a shift in the microwave transition frequency between the two lowest rotational states.

Since the ground-state is a strong-field seeking state, if we don't change the frequency of the down leg laser, the presence of an electric field means that in order for the STIRAP transfer to be on resonance, we have to adjust the two-photon detuning by decreasing the frequency of the up leg laser (by increasing $f_{\mathrm{DP}}$). When we were looking for charging we always did STIRAP with the applied field off, so the electric field present during STIRAP is the charging field $E_{\mathrm{ch}}$. We observed that running the experiment even just a few times (where the electric field was on for 500 ms or less out of a $\sim 60$ second total duration) would cause the STIRAP lineshape to shift by more than the two-photon linewidth (Fig. 2.11b). The maximum shifts we observed were 1-2 MHz, which imply $E_{\mathrm{ch}} = 500 - 1000$ V/cm. The charging problem was much more pronounced at higher applied fields. There was some hope that the field would be more stable at lower applied fields. To test this, we drove a microwave transition between the $N = 0$ and $N = 1$ states at a modest field of about 1 kV/cm. We saw that over a few hours, the frequency shifted, and the width of the feature became broader (Fig. 2.11c), which implies some uncontrolled charging field even at these low applied fields. From the magnitude of the shift, we inferred a shift of a few V/cm (out of 1 kV/cm) over the 1.5 hour experiment. We tried many things to get rid of this charging, such as applying blue light and heating the cell, but these didn't work. The charging on the cell would

relax over the time scale of $\sim 5$ hours (Fig. 2.11d).

## 2.4 Optical lattice techniques

Optical lattices have become a common tool in AMO physics. On a very naïve level, they're analogous to the lattice structure found in materials. One notable difference is that we don't usually have to worry about phonons in our system. The ability to tune the lattice strength and geometry and the ability to add disorder are the main features that make optical lattices so useful for AMO experiments, as most of these things cannot be controlled easily in solids. For us, optical lattices serve a very practical purpose, which is to shield the molecules from chemical loss (see Chapter 3). In this section, I briefly review the relevant aspects of lattice physics for our experiment.

### 2.4.1 Band structure and eigenfunctions

The eigenstates for particles in a periodic potential have the same periodicity as the lattice. Instead of the free-particle quadratic dispersion, only certain energy bands are allowed, and atoms occupy one of the allowed energy bands. The curvature of these bands determines the effective mass of the particles in the lattice. The calculation of the band structure is presented in many other places, including several theses [103, 104, 105]. Fig. 2.12a-c shows the dispersion for a few lattice depths. The lattice depth $U_0$ is expressed in units of the recoil energy $E_R = \frac{\hbar^2 k^2}{2m}$ by a dimensionless number $s = U_0/E_R$. In our case, we have a simple cubic lattice and $k = 2\pi/\lambda = \pi/a$, where $a$ is the lattice spacing.

The eigenstates, which are the Bloch wavefunctions $\phi_q^{(n)}(x)$, are given by

$$\phi_q^{(n)}(x) = e^{iqx/\hbar} u_q^{(n)}(x), \tag{2.2}$$

where $q$ is the quasimomentum (restricted to $-\pi/a$ to $\pi/a$ for the first Brillouin zone), $n$ is the band index, and $u_q^{(n)}(x)$ is a function with period $a$ [103]. The Bloch functions are a convenient basis for shallow lattices, since they are delocalized over the entire lattice, but in deep lattices the

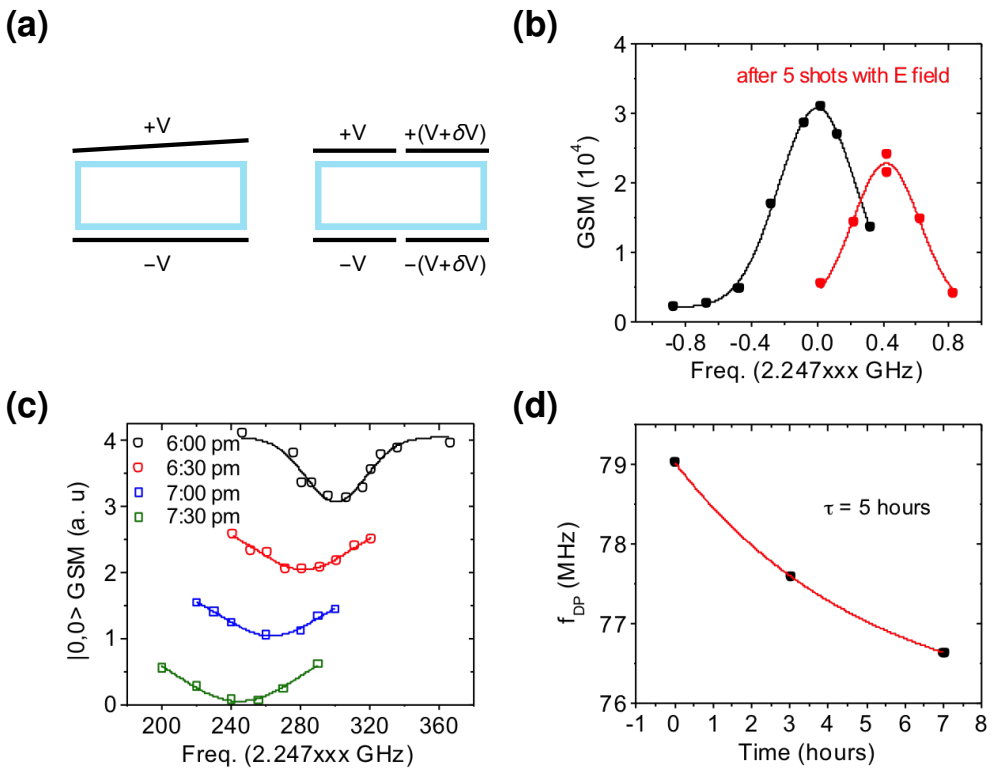


Figure 2.11: (a) Different configurations for applying electric-field gradients. A cross-section of the glass cell is indicated by the blue rectangle. We tried a configuration where one of the plates was tilted (left), and another configuration where the plates were flat but the electrical connection between the two sides was broken to allow independent voltages on the two sides (right). (b) The STIRAP lineshape would shift even though there was no applied field during STIRAP. After running the experiment for 5 shots the transition shifted by more than the two-photon linewidth (from the black curve to the red curve). (c) The microwave transition between the (molecular) $|0,0\rangle$ and $|1,0\rangle$ states also shifted. (d) The charging would dissipate in several hours, which we measured by periodically measuring the STIRAP resonance.

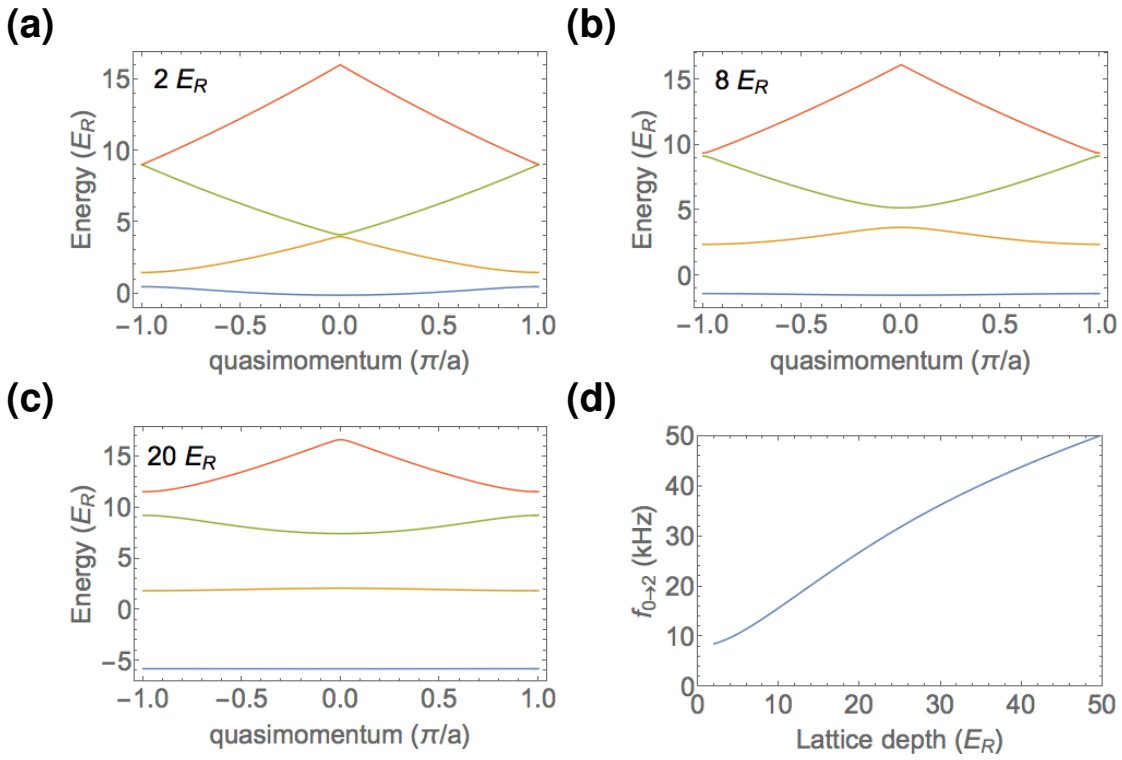


Figure 2.12: Dispersion relations for lattices of depths $2E_R$ (a), $8E_R$ (b), and $20E_R$ (c). (d) The transition frequency between bands 0 and 2 ($f_{0\to2} = E_{0\to2}/h$) at $q = 0$ vs. lattice depth. This frequency is measured by parametric heating.

Wannier functions are a more useful description. The Wannier function centered at site $x_j$ is [103]:

$$w_n(x - x_j) = \frac{1}{\sqrt{N}} \sum_q e^{-iqx_j/\hbar} \phi_q^{(n)}(x), \tag{2.3}$$

where $q$ is summed over the first Brillouin zone, and $N$ is a normalization factor. A decent approximation of the ground-band Wannier function in the limit of a deep lattice is a Gaussian of rms width $a/(\pi s^{1/4})$ [106]. Fig. 2.13 compares the densities of the Bloch functions and Wannier functions.

There are several relevant energy scales for atoms in the lattice, the tunneling $J$, the on-site interaction $U$ when there are two atoms on the same site, and the bandgap $\Delta$. We usually operate in a regime where $J, U \ll \Delta$ and the initial atomic temperatures are sufficiently low, so we usually consider only the lowest band.

$J$ and $U$ can be calculated from the Wannier functions by the following equations [103]:

$$J = \int w_n(x - x_i) \left( -\frac{\hbar^2}{2m} \frac{\partial^2}{\partial x^2} + V(x) \right) w_n(x - x_{i+1}) dx, \tag{2.4}$$

$$U = \frac{4\pi\hbar^2 a}{m} \int |w_j(\mathbf{r})|^4 d^3\mathbf{r}. \tag{2.5}$$

It was recently shown how dipole-dipole interactions modify these quantities [107].

$J$ can be calculated directly from the band structure calculation, since $J$ is 1/4 of the bandwidth of the ground band. An approximate functional form is given in Ref. [104] as

$$J/E_R = 1.39666\, s^{1.051}\, e^{-2.12104\sqrt{s}}. \tag{2.6}$$

An approximate formula for $U$ is given in Ref. [108] as

$$U/E_R = 5.97(a/\lambda)s^{0.88}, \tag{2.7}$$

where $a$ is the scattering length and $\lambda$ is the lattice wavelength. Fig. 2.14 shows $J$ for both Rb and K and $U_{\text{Rb-Rb}}$ at 1064 nm.

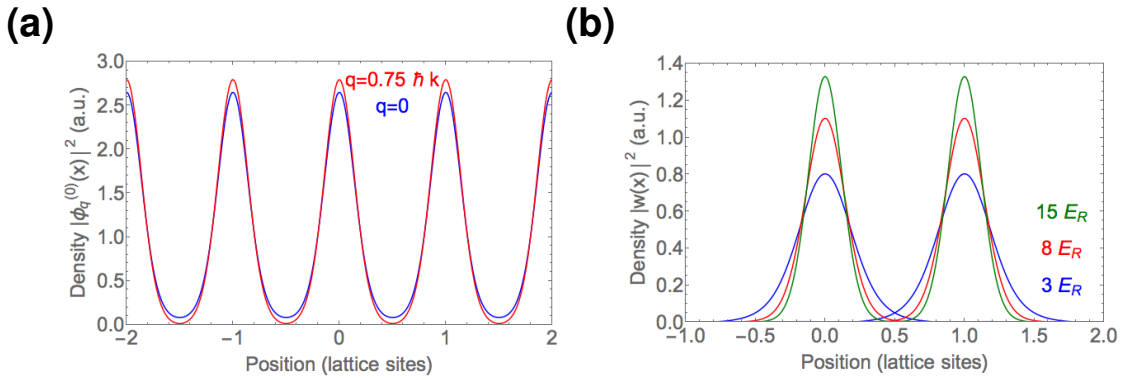


Figure 2.13: (a) Density $|\phi_q^{(0)}(x)|^2$ for Bloch functions in the lowest band, for $q = 0$ and $q = 0.75\hbar k$ and a lattice depth of 8 $E_R$. (b) Density $|w(x)|^2$ and $|w(x-a)|^2$ for different lattice depths. For deeper lattices, the Wannier function is more confined to one particular lattice site and the overlap with neighboring sites goes down, which leads to less tunneling.

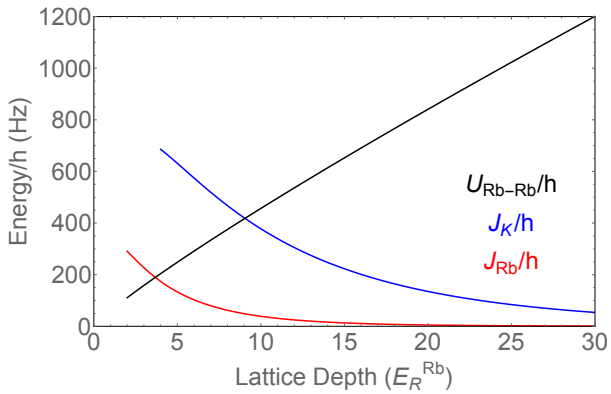


Figure 2.14: $J_{\mathrm{Rb}}$, $J_{\mathrm{K}}$, and $U_{\mathrm{Rb\text{-}Rb}}$ vs. the Rb lattice depth $E_R^{\mathrm{Rb}}$, calculated for an isotropic 3D lattice at 1064 nm, and using Eqs. 2.6 and 2.7. The tunneling for K takes into account that $s_{\mathrm{K}} = 0.4 s_{\mathrm{Rb}}$ at 1064 nm.

### 2.4.2 Dependence on beam parameters

We have a Gaussian beam of power $P$ and beam waists $W_x$ and $W_y$ that propagates along the $z$ direction. For simplicity, I assume that the retroreflection is the same size. To account for the intensity imbalance between the incoming and retroreflected beams (due to reflections and loss within optics), there is an attenuation factor $f$ for the retroreflected beam intensity ($f < 1$), which is a factor of $\sqrt{f}$ in the electric field amplitude. The peak intensity of one beam is

$$I_0 = \frac{2P}{\pi W_x W_y}. \tag{2.8}$$

The corresponding trap depth is $U_0 = \alpha I_0$, where $\alpha$ is the polarizability. The full dependence of $U$ is

$$\begin{aligned}
U(x,y,z) &= -U_0 |e^{ikz} + \sqrt{f} e^{-ikz}|^2 \, e^{-2x^2/(W_x^2)} \, e^{-2y^2/(W_y^2)} && (2.9)\\
&= -U_0 \left(1 + f + \sqrt{f}(e^{2ikz} + e^{-2ikz})\right) \, e^{-2x^2/(W_x^2)} \, e^{-2y^2/(W_y^2)} && (2.10)\\
&= -U_0 \left(1 + f - 2\sqrt{f} + 2\sqrt{f}(1 + \cos(2kz))\right) \, e^{-2x^2/(W_x^2)} \, e^{-2y^2/(W_y^2)} && (2.11)\\
&= -U_0 \left((1 - \sqrt{f})^2 + 4\sqrt{f}\cos^2(kz)\right) \, e^{-2x^2/(W_x^2)} \, e^{-2y^2/(W_y^2)}. && (2.12)
\end{aligned}$$

The trap frequencies are $\omega_i = \sqrt{\frac{1}{m}\frac{\partial^2 U}{\partial x_i^2}}|_{x=y=z=0}$, and the results are that

$$\omega_{x,y} = \sqrt{\frac{16U_0(1+\sqrt{f})^2}{4mW_{x,y}^2}} = \frac{1+\sqrt{f}}{2}\sqrt{\frac{16U_0}{mW_{x,y}^2}}, \tag{2.13}$$

and

$$\omega_z = \sqrt{\frac{8\sqrt{f}k^2U_0}{m}} = f^{1/4}\sqrt{\frac{8k^2U_0}{m}}. \tag{2.14}$$

Finally, the lattice depth $s = U_0/E_R$ is given by

$$s = \left(\frac{m\omega_z}{\hbar k^2}\right)^2 = \frac{8m}{\hbar^2 k^2} U_0 \sqrt{f}. \tag{2.15}$$

A relevant issue is whether attenuation in the beam path leads to unwanted harmonic confinement $\omega_{x,y}$ from the running-wave component. Using Eqs. 2.13-2.15, it can be shown that $\omega_r$ increases by a factor of $\frac{1+\sqrt{f}}{2f^{1/4}}$ when increasing the power to get the same lattice depth as when $f = 1$. An

example here clarifies this statement. If $f$ were 1, we would have some lattice strength $s_0$ with harmonic confinement $\omega_0$. Using the same incident power, if $f = 0.5$, we would have lattice depth $s_0/\sqrt{2}$ and harmonic confinement $\left(\frac{1}{2} + \frac{1}{2\sqrt{2}}\right)\omega_0 = 0.85\,\omega_0$. If we increase the power by a factor of $\sqrt{2}$, the lattice depth increases to $s_0$, and the harmonic confinement becomes $1.015\,\omega_0$. Thus we see that even for this fairly large attenuation the additional harmonic confinement (1.5%) of the running wave is almost negligible. In the experiment, $f$ is usually 0.6-0.8, so we don't have to worry about this.

### 2.4.3 Avoiding superlattices

Another thing we worry about is unwanted reflected beams interfering with the primary lattice beams and creating a superlattice. Fig. 2.15 shows the setup from the old chamber. There are four reflected beams that can hurt us, two from the incoming beam and two from the retroreflected beam. At normal incidence, each would be roughly 4% in intensity. This is problematic since the interference scales as $\sqrt{I_{in}I_r}$, which means each of these 4% reflections would produce a lattice that's 0.2 times the strength of the initial lattice (if there were perfect overlap of the beams). This suggests we can't propagate the beam normal to the cell. In principle, the superlattice should be stable if there's no relative motion between the cell and the retroreflecting mirror, but there would likely be a phase difference between the two lattices. This is bad, and we want to avoid it.

If we have beams with $I_0$ and $0.04I_0$ with the same waist, and we want the four possible reflections (Fig. 2.15) to give a lattice less than 0.01 times the strength of the regular lattice, the beams would need to be separated by about 2.5 beam waists. We typically use a 250 $\mu$m beam for the vertical lattice and the cell is 1 cm tall, so $\theta$ would need to be larger than about 4° to satisfy the above condition. Most recently the lattice beams were a little larger, so we chose 6° to be safe.

### 2.4.4 Calibrating the lattice depths

We regularly use two different methods to measure the lattice depth, parametric heating and Kapitza-Dirac scattering. Parametric heating, which consists of amplitude modulating the lattice

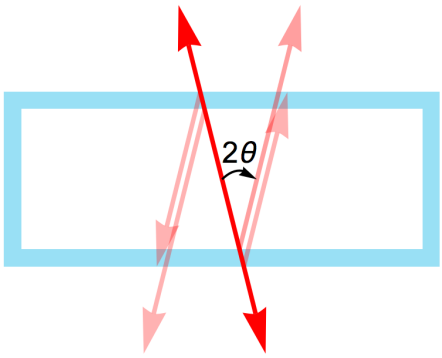


Figure 2.15: We get reflections off of the cell surfaces. The ones that could hurt us by interfering with the primary lattice beams are shown in light red (there are 4 total). For uncoated glass at normal incidence, each of these would give $\sim 4\%$ reflection. We tilt the beam at an angle $\theta$ with respect to normal. The atoms sit at the center, and we require the separation between the reflected beams and the desired lattice beams to be at least 2-3 beam waists to keep the superlattice depth below 1% of the primary lattice depth.

| Species | $\alpha_{1064}/h$ ($10^{-5}$ MHz/(W/cm$^2$)) | Relative lattice depth ($E_R^i$) |
|---|---|---|
| Rb | 3.2 | 1 |
| K | 2.8 | 0.40 |
| KRb | 5.5 | 2.48 |

Table 2.1: Polarizabilities and lattice depths of K, Rb, and KRb at 1064 nm.

beams and driving transitions that change the band index by 2, is discussed at length in Ref. [105]. Starting with atoms in the ground band, we measure $f_{0\to 2}$, corresponding to the energy difference between the ground band and the second excited band (see Fig. 2.12d). In Kapitza-Dirac scattering, the lattice is turned on for a short time $\tau$, which is typically less than 10 $\mu$s (which is faster than the lattice oscillation frequency). This diffracts the BEC into plane-wave components [109, 110]. Measuring the populations in the plane-wave components, one can extract the lattice depth. For short, strong pulses, the motion of the atoms during the pulse duration can be neglected, and the population in the $\pm 2n\hbar k$ component is approximately $J_n^2\left(\frac{sE_R\tau}{2\hbar}\right)$, where $J_n$ is the ordinary Bessel function of order $n$ [109]. This approximation is only valid for short times. We find it's relatively simple to find the shortest $\tau$ that minimizes the population of the $0\hbar k$ component. This occurs when the argument of $J_0$ is about 2.405, which leads to the condition $s\tau \approx 377\,\mu$s for Rb (solving the time-dependent Schrödinger equation exactly, this is true to within 2% for $s \geq 30$). We find that parametric heating and Kapitza-Dirac scattering give consistent answers for the lattice depth. Unless otherwise noted, the uncertainty in the lattice depth calibration is about 5%.

We measure the lattice depth for Rb and use our knowledge of the different mass and polarizability of K at 1064 nm to calculate the lattice depth for K. At 1064 nm, $\alpha_{\mathrm{Rb}}/\alpha_{\mathrm{K}} = 1.15$, which implies $\omega_{\mathrm{K}}/\omega_{\mathrm{Rb}} = 1.37$ [105]. The recoil energy is higher for K by a factor of $m_{\mathrm{Rb}}/m_{\mathrm{K}}$. Putting all of these factors together, $s_{\mathrm{K}} = 0.4\, s_{\mathrm{Rb}}$, so Rb can be well localized in the Mott insulating phase while K is still mobile. We do the same procedure for ground-state molecules; there, the conversion is $s_{\mathrm{KRb}}/s_{\mathrm{Rb}} = \frac{m_{\mathrm{KRb}}\alpha_{\mathrm{KRb}}}{m_{\mathrm{Rb}}\alpha_{\mathrm{Rb}}} \approx 2.48$. Note that it was by measuring parametric heating resonances that we measured the polarizability of molecules in both the $N = 0$ and $N = 1$ states (see Fig. 4.5) [91]. The results are summarized in Table 2.1.

### 2.4.5 Band mapping

Due to both finite temperature and nonadiabaticity in loading the lattices, we can have atoms and molecules populated in higher lattice bands. The standard way to detect particles in higher bands is via band mapping, whereby the lattice intensity is ramped to zero (instead of being instantaneously shut off) on a timescale fast compared to motion on a lattice site but slow enough to be adiabatic with respect to the band separation. This technique is described well in other places [98, 103, 105]. Here I only discuss a variant of the technique that we've recently implemented. We use a refocusing technique [111], where the lattices are ramped down in the same way, but the underlying harmonic trap is not turned off. Waiting a quarter trap period (of the harmonic trap), there is a one-to-one correspondence between the position of the atoms, given by the distribution function $n(\mathbf{x}, t)$, and the initial momentum, given by the distribution function $\Pi(\mathbf{p}, t)$:

$$n(\mathbf{x}, T/4) = \Pi(\mathbf{p}, 0), \tag{2.16}$$

where $\mathbf{p} = m\omega\mathbf{x}$. Note that in this case we are making a measurement in position space, whereas in normal band mapping, one makes a measurement in momentum space. In this case, the size of the first Brillouin zone is $2\hbar k/(m\omega_{\mathrm{hc}})$, where $\omega_{\mathrm{hc}}$ is the harmonic trap frequency. Ordinary band mapping requires a sufficiently long expansion such that the cloud is in momentum space, but the refocusing technique requires a shorter expansion time, such that the cloud is smaller and the OD and SNR are higher. When imaging from the top, we can fit the entire 2D distribution to the following functional form (similar to that in Ref. [98]):

$$
\begin{aligned}
&K + A\left[\mathrm{erf}\left(\frac{x - x_c - \Delta_x}{w_x}\right) - \mathrm{erf}\left(\frac{x - x_c + \Delta_x}{w_x}\right)\right] \times \left[\mathrm{erf}\left(\frac{y - y_c - \Delta_y}{w_y}\right) - \mathrm{erf}\left(\frac{y - y_c + \Delta_y}{w_y}\right)\right] \\
&+ B_1\left[\mathrm{erf}\left(\frac{x - x_c - \Delta_x}{w_x}\right) - \mathrm{erf}\left(\frac{x - x_c + \Delta_x}{w_x}\right)\right] \times \left[\mathrm{erf}\left(\frac{y - y_c + \Delta_y}{w_y}\right) - \mathrm{erf}\left(\frac{y - y_c + 2\Delta_y}{w_y}\right)\right] \\
&+ B_2\left[\mathrm{erf}\left(\frac{x - x_c - \Delta_x}{w_x}\right) - \mathrm{erf}\left(\frac{x - x_c + \Delta_x}{w_x}\right)\right] \times \left[\mathrm{erf}\left(\frac{y - y_c - 2\Delta_y}{w_y}\right) - \mathrm{erf}\left(\frac{y - y_c - \Delta_y}{w_y}\right)\right] \\
&+ C_1\left[\mathrm{erf}\left(\frac{x - x_c + \Delta_x}{w_x}\right) - \mathrm{erf}\left(\frac{x - x_c + 2\Delta_x}{w_x}\right)\right] \times \left[\mathrm{erf}\left(\frac{y - y_c - \Delta_y}{w_y}\right) - \mathrm{erf}\left(\frac{y - y_c + \Delta_y}{w_y}\right)\right] \\
&+ C_2\left[\mathrm{erf}\left(\frac{x - x_c - 2\Delta_x}{w_x}\right) - \mathrm{erf}\left(\frac{x - x_c - \Delta_x}{w_x}\right)\right] \times \left[\mathrm{erf}\left(\frac{y - y_c - \Delta_y}{w_y}\right) - \mathrm{erf}\left(\frac{y - y_c + \Delta_y}{w_y}\right)\right],
\end{aligned}
\tag{2.17}
$$

which includes an imaging offset $K$ and a contribution from the ground band and 4 additional regions corresponding to higher bands in $x$ and $y$ (see Fig. 2.16a). Since the probability of being excited along any given direction is small (usually $< 0.1$), multiply excited states will be ignored. $w_x$ and $w_y$ take into account imaging resolution and momentum smearing from not being perfectly adiabatic at the band edge (the momentum smearing seems to be the dominant effect). The center of the distribution is $(x_c, y_c)$ and the width of the Brillouin zone in $x\,(y)$ is $2\Delta_x\,(2\Delta_y)$. Ideally, these should be the same, but a different trap frequency along the two directions might cause slight differences in $\Delta_x$ and $\Delta_y$. We assume the higher-band population in $z$ is the same as in $x$ and $y$ and thus multiply the higher-band fraction measured for the $x$ and $y$ directions by 1.5 to account for those atoms excited along $z$. Thus, the fraction of atoms in higher bands is $\frac{1.5\,(B_1+B_2+C_1+C_2)}{2A+B_1+B_2+C_1+C_2}$.

### 2.4.6 Generating the lattice beams

The optical layout for the lattice beams changed since the original 3D lattice work [72]. Initially we were using the OT beams as the horizontal lattice beams. We would do the evaporation in the OT, load the vertical lattice, ramp the OTs to 0, open shutters to unblock the retroreflections, and then finally ramp on the horizontal lattices (see Fig. 2.17a). Eventually we wanted to be able to ramp the lattices independently of the dipole trap, so we made the polarization of the lattice beams orthogonal to the OT beams, sent in the lattice beams from the opposite side of the cell as

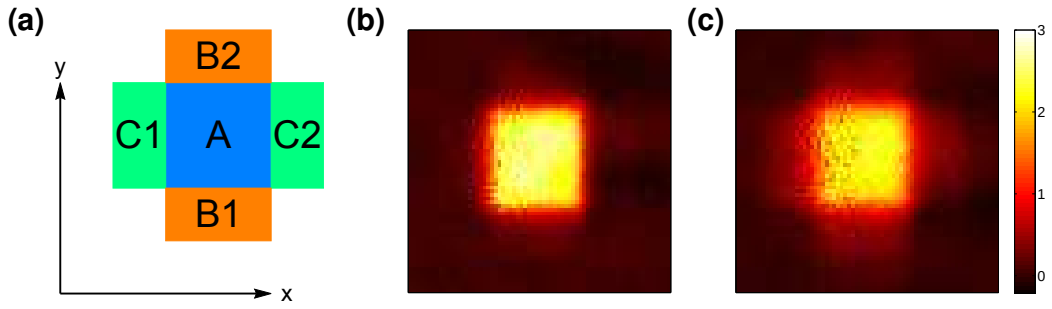


Figure 2.16: (a) A "map" that defines the different regions for band mapping when imaging such that excitations along two directions can be observed (see Eq. 2.17). (b) and (c) Typical images of band-mapped K from the experiment, using the refocusing technique, with lower (b) and higher (c) higher-band fraction. The OD is given by the color scale on the far right. These images come from Ref. [93].

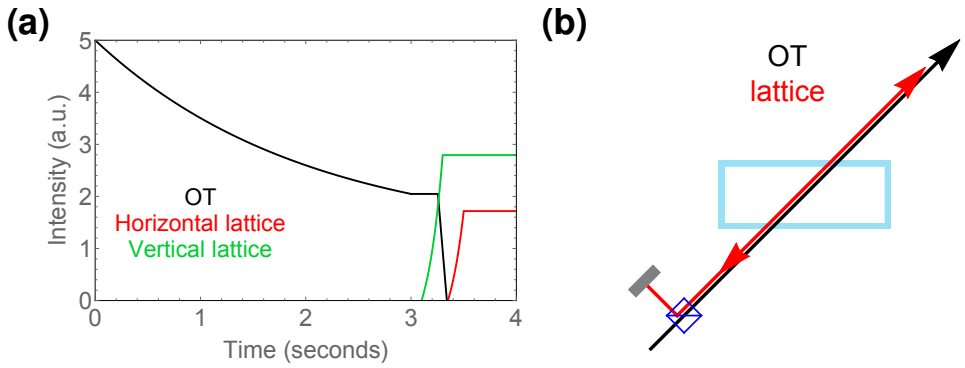


Figure 2.17: (a) Timing diagram for the initial lattice loading scheme, as used in Ref. [72]. We would ramp up the vertical lattice, ramp down the OTs, open the shutters, and then ramp up the horizontal lattice beams. (b) The most recent setup for the horizontal lattice beams and OT beams. The OT and lattice beams have orthogonal linear polarizations and the OT and lattice incoming beam propagate in opposite directions.

the OT beams, and then used a polarizing beamsplitter on the far side (on the incoming side for the OT) to separate the lattice beam from the optical trap (see Fig. 2.17b).

The typical OT beam size is 200 $\mu$m in the radial direction and 40 $\mu$m in the vertical direction. At one point, we made them even more oblate to reduce the radial harmonic confinement. After switching to separate horizontal lattice beams, the lattice beams were initially round (with a waist of 125-250 $\mu$m), and then oblate, with sizes $\sim 500 \times 100\,\mu$m in the radial and vertical directions, respectively. We wanted to make the horizontal lattice beams elliptical to better match the size of the cloud and have a lower harmonic confinement along the radial direction. The vertical lattice was round with a 200-300 $\mu$m waist, and most recently it was around 280 $\mu$m at the position of the atoms.

# Chapter 3

## Chemical reactions and the Zeno effect

One of the first observations made with ultracold KRb molecules in a 3D harmonic trap was that the molecules had a significantly shorter lifetime in the optical trap than the constituent K and Rb atoms [69]. Furthermore, upon applying a DC electric field, which is the simplest way to induce dipolar interactions between the molecules, the lifetime became much shorter [70]. This is a problem because it correlated strong interactions with strong inelastic losses, which makes it difficult to study dipolar interactions in a controlled way. Since the molecules were prepared in the lowest internal energy state with the thermal energy less than all other energy scales, no other states of the molecule were accessible. Therefore, it was concluded that exothermic chemical reactions are responsible for the loss, as the energy of $K_2$+$Rb_2$ is about 10 $cm^{-1}$ lower than the energy of 2 KRb, and the reaction 2KRb$\rightarrow$$K_2$+$Rb_2$ is barrierless [112]. The observations of chemical reactions in KRb signal a new epoch in the study of ultracold chemical reactions.

Fermionic $^{40}K^{87}Rb$ molecules prepared in the same internal quantum state collide in the partial-wave channel with $L = 1$ ($p$ wave), where $\hbar L$ is the quantized relative angular momentum. The projection of this angular momentum onto the quantization axis, $m_L$, determines the orientation in which the molecules collide: $m_L = 0$ corresponds to an attractive head-to-tail collision, while $m_L = \pm 1$ corresponds to a repulsive side-by-side collision. Distinguishable molecules can collide via $s$-wave collisions ($L$=0). In an applied DC electric field, the dipole-dipole interaction mixes states with different $L$, so the $L = 0$ channel becomes the lowest-energy adiabatic channel with even $L$, and the $L = 1$ channel becomes the lowest-energy adiabatic channel with odd $L$. This

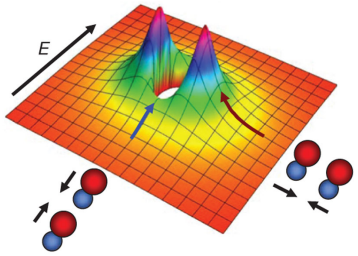


Figure 3.1: Cartoon illustrating the anisotropy of collisions in an applied DC electric field. The $p$-wave centrifugal barrier increases for repulsive side-by-side collisions (red arrow) and decreases for attractive head-to-tail collisions (blue arrow). Figure reproduced from Ref. [70].

odd-$L$ adiabatic channel has a centrifugal barrier. A simple model for the chemical reactions is that the molecules tunnel through the $p$-wave centrifugal barrier and then chemically react with unit probability (if the molecules are not in the lowest hyperfine state, another possibility is hyperfine-state changing collisions) [69]. In an electric field, the centrifugal barrier decreases for $m_L = 0$ (head-to-tail) collisions but increases for $m_L = \pm 1$ (side-by-side) collisions [70] (see Fig. 3.1). This suggests a natural strategy to stabilize the molecular gas in a strong electric field, which is to prevent the molecules from colliding head-to-tail. This can be accomplished by trapping the molecules in a 1D optical lattice, with the electric field perpendicular to the quasi-2D traps. In this geometry, the loss rate can be reduced by almost two orders of magnitude [71]. To completely shut off the chemical reactions, we can create the molecules in a 3D lattice. In the full 3D lattice, the molecules live for tens of seconds, independent of the electric field strength [72].

In the first part of this chapter, I briefly summarize the molecule production and chemical reactions in the harmonic trap and in optical lattices. Since a lot of this has been covered in other theses from our group, particularly those of Kang-Kuen Ni [96], Marcio de Miranda [98], and Brian Neyenhuis [105], I focus on the most important aspects. In the second part of the chapter, I describe our studies of the continuous Zeno effect. This occurs in a regime where the chemical reaction rate is the largest energy scale in the lattice, which occurs for chemical reactions on a single lattice site between distinguishable molecules in a rotational mixture (half in $N = 0$ and half in $N = 1$,

where $N$ is the molecule's principal rotational quantum number). The result of the Zeno effect is that, counterintuitively, the loss rate decreases as the chemical reaction rate increases. Much of this chapter follows Refs. [72] and [90], of which I am a coauthor.

## 3.1 Brief summary of molecule production

The experiment starts with magneto-optical traps (MOTs) of both $^{87}$Rb and $^{40}$K. After loading the MOTs for about 10 seconds, we do a compressed MOT stage, which gets the MOT to the correct position for loading into a magnetic quadrupole trap. We then have a molasses stage (where the magnetic field is completely shut off), which does sub-Doppler cooling. Finally, we use optical pumping to put the atoms in the magnetically trappable stretched states $|F, m_F\rangle = |2, 2\rangle$ for Rb and $|9/2, 9/2\rangle$ for K. We then load the atoms into the quadrupole trap and transfer the atoms to the science cell by a pair of moving coils. The evaporative cooling is done in a Ioffe-Pritchard (IP) trap by using $\sim 6.8$ GHz microwaves to transfer hot Rb atoms from the $|2, 2\rangle$ state to the $|1, 1\rangle$ state, which are not trapped. The K gas is sympathetically cooled by the Rb and remains thermalized with the Rb throughout the evaporation.

The $s$-wave Feshbach resonance that we use to create weakly bound Feshbach molecules occurs at a field of 546.6 Gauss between K in the $|9/2, -9/2\rangle$ state and Rb in the $|1, 1\rangle$ state [113]. These are both strong-field-seeking states so we can't trap them in a magnetic trap. Instead, we cool the atoms in the IP trap to about 1-2 $\mu$K and then load the atoms into a crossed-beam optical dipole trap at 1064 nm, which can trap all spin states. At this point, we ramp on a roughly homogeneous bias magnetic field to about 30 Gauss. About 300 ms after transferring into the dipole trap, we use an adiabatic rapid passage (ARP) to transfer K from the $|9/2, 9/2\rangle$ state to the $|9/2, -9/2\rangle$ state and use a microwave ARP at around 6.9 GHz to transfer Rb to the $|1, 1\rangle$ state. We then do further evaporation by reducing the intensity of the dipole trap beam over several seconds. After 3-4 seconds we produce a degenerate Fermi gas of K and a BEC of Rb. For optimal molecule production in the harmonic trap, we usually work with cold thermal gases ($T/T_c > 1$ for Rb) to maximize the phase-space overlap of the two species. For optimal molecule production in

the lattice, we use very small BECs and large, degenerate Fermi gases (see Chapter 5).

We ramp the magnetic field across the Feshbach resonance from high field to low field to adiabatically convert pairs of atoms to weakly bound Feshbach molecules (molecules in the least bound vibrational state). In a harmonic trap this is not very efficient, as we can only convert 10-20% of the minority species, but in the 3D lattice it is quite efficient (see Section 3.6 and Chapter 6). We use STIRAP to transfer the Feshbach molecules to the absolute ground state [51, 114]. When the molecules are in the ground state, we apply resonant light at 767 and 780 nm to remove the K and Rb atoms that didn't make molecules. This is necessary since the atoms can chemically react with the molecules. To image the molecules, we use STIRAP to bring the molecules back to the Feshbach molecule state and then dissociate the Feshbach molecules, either with light on the K cycling transition or by sweeping the magnetic field above the resonance. Either way, we then image K or Rb atoms on a cycling transition, but to image Rb we first have to do another microwave ARP to put the atoms in the $|2,2\rangle$ state.

## 3.2 Rotational states and driving rotational transitions

For $^1\Sigma$ molecules such as KRb, the rotational degree of freedom is instrumental in getting dipolar interactions, as successive rotational states have opposite parity. Transitions between rotational states are electric dipole transitions. Furthermore, the rotationally excited states are long-lived and we can easily couple to them using microwaves. As will be discussed in the next chapter, we can encode spin in the rotational degree of freedom and realize an XY coupling between molecules in the lattice. For studying chemical reactions, driving transitions to different rotational states is useful because it allows us to control the distinguishability of the molecules and to create molecules in the absolute hyperfine ground state. The energies of the excited rotational states are $E_N = hBN(N+1)$, where $B = 1.113950$ GHz is the rotational contstant [96]; however, higher-order terms break the degeneracy between different hyperfine states and different projections along the quantization axis. This section summarizes how we drive rotational transitions in the molecules and follows Ref. [115].

Although the ground-state molecules are a singlet ($X^1\Sigma^+$), there is still hyperfine structure arising from the nuclear magnetic moments of the K and Rb atoms. With nuclear spin quantum numbers $I^K = 4$ and $I^{\mathrm{Rb}} = 3/2$ for K and Rb, respectively, there are 36 hyperfine states for each rotational state $|N, m_N\rangle$, where $N$ is the principal rotational quantum number and $m_N$ is its projection onto the quantization axis. Thus, the states can be labeled by $|N, m_N, m_{\mathrm{K}}, m_{\mathrm{Rb}}\rangle$, where $m_{\mathrm{K}}$ is the nuclear spin projection for K, and $m_{\mathrm{Rb}}$ is the nuclear spin projection for Rb. $m_{\mathrm{K}}$ and $m_{\mathrm{Rb}}$ are good quantum numbers for magnetic fields larger than about 20 Gauss, where the linear Zeeman energy shift for each of the nuclear spins is much larger than the mutual coupling of the nuclear spins. At 550 Gauss, the splitting between states with $\Delta m_{\mathrm{Rb}} = \pm 1$ is about $h \times 760$ kHz, while the splitting between states with $\Delta m_{\mathrm{K}} = \pm 1$ is about $h \times 130$ kHz. In addition, there is a coupling between the nuclear electric quadrupole moments of the $^{40}$K and $^{87}$Rb nuclei and the electric-field gradients created by the molecules's electron cloud [115, 116]. This coupling breaks the degeneracy of states with the same $N$ but different $m_N$, and mixes states in the $N = 1$ manifold that have a constant sum $m_N + m_{\mathrm{Rb}}$ or $m_N + m_{\mathrm{K}}$. This leads to eigenstates of the form $|1, 0, m_{\mathrm{K}}, m_{\mathrm{Rb}} \pm 1\rangle + \delta|1, \pm 1, m_{\mathrm{K}}, m_{\mathrm{Rb}}\rangle$ or $|1, 0, m_{\mathrm{K}} \pm 1, m_{\mathrm{Rb}}\rangle + \delta|1, \pm 1, m_{\mathrm{K}}, m_{\mathrm{Rb}}\rangle$ and allows us to drive transitions that ultimately put the molecules in the absolute ground state $|0, 0, -4, 3/2\rangle$.

From selection rules and spectroscopic resolution, STIRAP populates a single hyperfine state of the ground rovibrational state, $|0, 0, -4, 1/2\rangle$ [96]. We then use a microwave signal to drive transitions to states in the $N = 1$ manifold. The microwave horn we use doesn't give us very much control over the microwave polarization, and we find we get much better coupling for $\sigma^{\pm}$ transitions than for $\pi$ transitions. To transfer molecules to the hyperfine ground state, we drive two microwave transitions, one of which changes $m_{\mathrm{Rb}}$. Specifically, we drive $|0, 0, -4, 1/2\rangle \rightarrow |1, 0, -4, 3/2\rangle + \delta|1, 1 - 4, 1/2\rangle \rightarrow |0, 0, -4, 3/2\rangle$ (note that these are $\sigma^+$ and $\pi$ transitions, respectively). For this particular intermediate state, $|\delta|^2 \approx 0.1$. Because $|\delta|^2 < 1$, for fixed microwave power, the Rabi frequency for a hyperfine-state changing transition is less than for a transition that doesn't change hyperfine state. For the spin-exchange work described in the next chapter, we drive the $|0, 0, -4, 1/2\rangle \rightarrow |1, 0, -4, 1/2\rangle$ and $|0, 0, -4, 1/2\rangle \rightarrow |1, -1, -4, 1/2\rangle$ transitions.

## 3.3 Chemical reactions in 3D

Chemical reactions of ultracold KRb molecules in the 3D harmonic trap depend on which state(s) the molecules are in, the temperature, and the applied electric field. There are three relevant cases: (1) indistinguishable molecules (spin-polarized), (2) a hyperfine mixture with both states in the $N = 0$ manifold, and (3) a hyperfine mixture with one state in the $N = 0$ manifold and one state in the $N = 1$ manifold. In the first two cases, the temperature and electric-field dependences were studied. The third case is relevant to the quantum Zeno work, where we have an incoherent mixture of $N = 0$ and $N = 1$ molecules.

The chemical reactions cause the number density of trapped molecules, $n$, to decrease according to

$$\frac{dn}{dt} = -\beta n^2 - \alpha n, \tag{3.1}$$

where $\beta$ is the two-body loss coefficient and $\alpha$ reflects a decrease in the density due to an increase in temperature [69]. Fig. 3.2a shows how $\beta$ depends on temperature for cases 1 and 2. For spin-polarized cases, the loss rate $\beta \propto T$, which is expected from the Bethe-Wigner threshold laws for $p$-wave collisions of indistinguishable fermions. For the hyperfine mixture, the molecules are distinguishable, $s$-wave collisions are allowed, and the loss has no significant temperature dependence. Another important conclusion from this data is that hyperfine changing collisions don't play a large role, since the loss rates are the same within experimental error for the $|0, 0, -4, 1/2\rangle$ state (for which hyperfine-state changing collisions are allowed in principle) and the $|0, 0, -4, 3/2\rangle$ state (for which there cannot be hyperfine-state changing collisions, as this is the hyperfine ground state). Fig. 3.2b shows that $\beta \propto d^6$ ($d$ is the induced dipole moment in the lab frame), consistent with a quantum threshold model [70]. Fig. 3.3 shows the loss of molecules in a mixture of $N = 0$ and $N = 1$ states, from which we extract $\beta = 9.0(4) \times 10^{-10}$ cm$^3$ s$^{-1}$, which is almost 5 times higher than for the $N = 0$ mixture [84]. To create an incoherent spin mixture, we applied a $\pi/2$ pulse on the $|0, 0, -4, 1/2\rangle \rightarrow |1, -1, -4, 1/2\rangle$ transition and waited 50 ms for any superpositions to decohere.

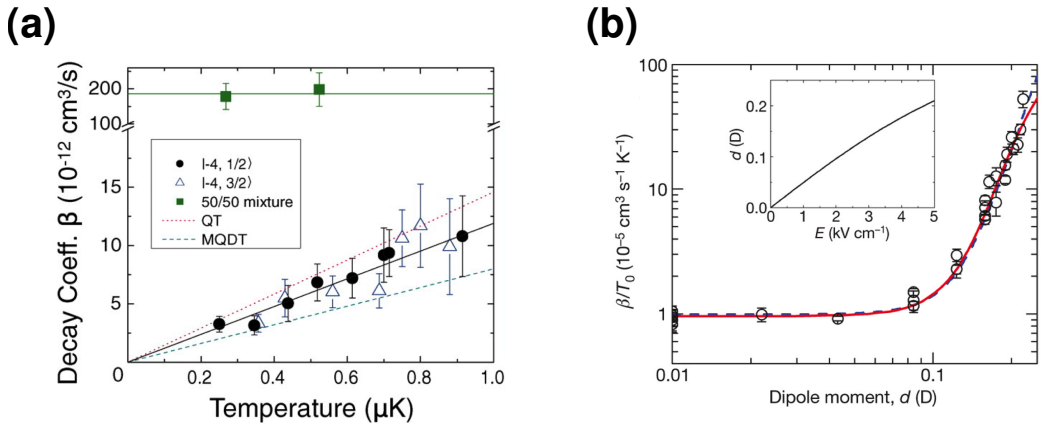


Figure 3.2: Chemical reactions in the 3D harmonic trap. (a) Chemical reaction rates at zero electric field for two different hyperfine states and a mixture. The loss rate $\beta$ is proportional to temperature for the spin-polarized case and is independent of temperature for the mixture. Figure reproduced from Ref. [69]. (b) The loss rate vs. induced dipole moment for a spin-polarized sample. $\beta \propto d^6$, which is consistent with a quantum threshold calculation [70]. Figure reproduced from Ref. [70].

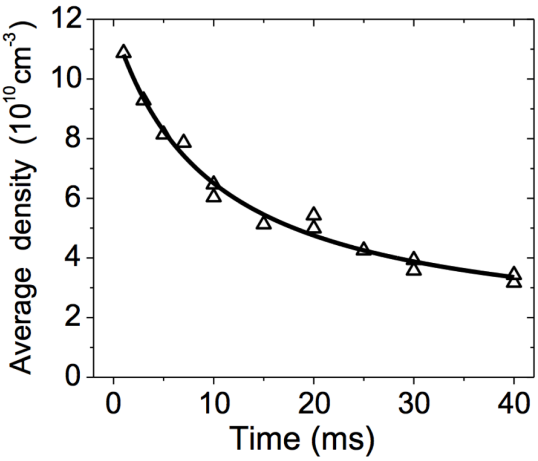


Figure 3.3: Decay of an incoherent mixture of rotational states $|0, 0, -4, 1/2\rangle$ and $|1, -1, -4, 1/2\rangle$. The extracted loss rate, $9.0(4) \times 10^{-10}$ cm$^3$ s$^{-1}$, is almost 5 times higher than for the mixture of two $N = 0$ hyperfine states ($|0, 0, -4, 1/2\rangle$ and $|0, 0, -4, 3/2\rangle$). Figure reproduced from Ref. [84].

In addition to reacting with themselves, the molecules can also react with the K and Rb atoms (K is worse for molecules in the ground hyperfine state, but both are bad for molecules in excited hyperfine states [96]). Thus, it's very important to remove all remaining atoms after making molecules, especially in cases where we convert a small fraction of one or both of the atomic species (this will be important for K in Chapter 5).

## 3.4 Suppressing chemical reactions in a 1D lattice

Because of the asymmetry between head-to-tail and side-by-side collisions, a natural strategy for stabilizing the gas against chemical reactions is to suppress the lossy head-to-tail collisions [71]. In particular, the lifetime should be enhanced in a 1D lattice geometry with the electric field oriented perpendicular to the pancake-shaped lattice sites. Here, the molecules are created in a vertically oriented lattice ($z$ direction) and an electric field is also applied along the $z$ direction. The lattice has a strong optical confinement with trap frequency $\omega_z$. For the applied electric field strengths, molecular temperatures, and harmonic confinements of Ref. [71], the experiments are performed in quasi-2D, and the combination of sufficiently tight optical confinement and Fermi statistics makes molecules preferentially collide in the side-by-side orientation. Chemical reactions are suppressed by the repulsive dipole-dipole interactions. In the quasi-2D geometry, $L$ is not a good quantum number to describe how molecules approach each other for intermolecular separations $\gg a_{\text{ho}}$ ($a_{\text{ho}} = \sqrt{\frac{\hbar}{m\omega_z}}$ is the harmonic oscillator length along $z$), and instead the relative motion is described by $m_L$. A quantum number $\nu$ labels which harmonic oscillator motional state (lattice band) a molecule is in. This quantum number acts as a new internal degree of freedom for molecules as they approach each other from long range. Fermionic molecules in the same internal state and same $\nu$ must collide with odd $m_L$ (side-by-side), whereas fermions in the same internal state but different $\nu$ collide with even $m_L$ (head-to-tail).

Again, there are three separate cases to consider (see Fig. 3.4a): (1) distinguishable molecules, (2) indistinguishable molecules in different bands, and (3) indistinguishable molecules in the same band. Similar to the 3D case, channel 1 leads to $s$-wave losses and should be avoided. Channel

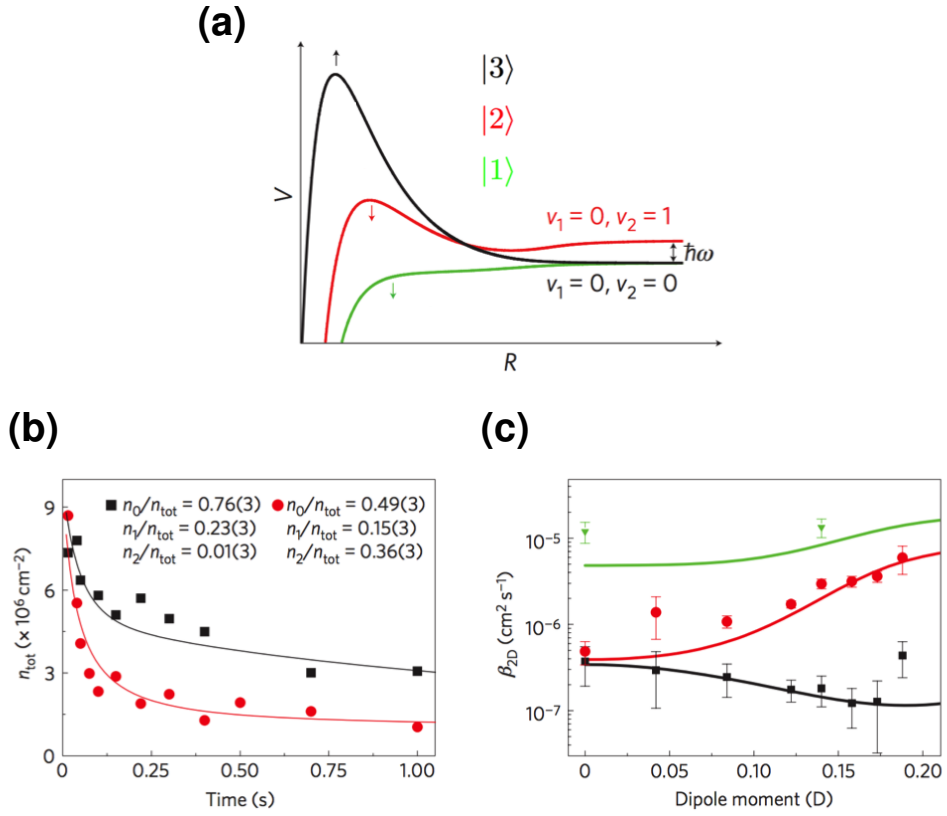


Figure 3.4: Chemical reactions in the 1D lattice. (a) The barrier for collision channel 1 (green, distinguishable molecules), 2 (red, indistinguishable molecules in different bands), and 3 (black, indistinguishable molecules in the same band). Channel 3 is the most desirable since it corresponds to repulsive side-by-side collisions. The arrows next to the curves indicate whether the barrier increases or decreases as the electric field increases. (b) Loss rates for two different initial band populations. The initial loss is faster when the initial higher band fraction is higher. (c) 2D decay coefficients $\beta_{2D}$ for the three cases depicted in (a). Figures reproduced from Ref. [71].

2 corresponds to head-to-tail collisions ($m_L = 0$), which are also undesirable. Channel 3 is the desirable scenario, and corresponds to $m_L = \pm 1$ (side-by-side collisions). In an applied electric field, dipole-dipole interactions cause the barrier for head-to-tail collisions to go down and the barrier for side-by-side collisions to go up. To control the fraction of molecules in excited bands and thus the relative importance of channels 2 and 3, parametric heating was used to promote molecules to higher bands. Fig. 3.4b shows the loss for two different initial conditions: for colder molecules, where about 75% of the molecules in the lowest band, and another case where parametric heating was used to heat the molecules to the second excited band. Fig. 3.4c shows the loss rate coefficient, $\beta_{2D}$, vs. induced dipole moment for the three cases depicted in panel a and clearly shows the loss rate is significantly less for channel 3. At an induced dipole moment of 0.174 D, the suppression is about a factor of 60.

It's worth noting that for very large applied electric fields and very strong optical confinements, repulsive dipole-dipole interactions can suppress chemical reactions, regardless of quantum statistics [71, 117, 118]. In this regime, the ratio of elastic to inelastic collisions should be favorable for evaporatively cooling the molecules [119], similar to pioneering work in dipolar Fermi gases of magnetic atoms [50]. However, Ref. [120] shows that for $d > 0.3$ D, the ratio of elastic to reactive collisions only really starts to significantly increase (beyond 100) for $\omega_z/(2\pi) > 100$ kHz, which is a significantly higher trap frequency than we have used so far.

## 3.5 Shutting off chemical reactions in a 3D lattice

The success in suppressing reactions in a 1D lattice motivated us to add lattices along the horizontal directions ($x$ and $y$) to create a 3D lattice [72]. Again, the strategy is to load the atoms into the lattice and then make molecules. In the 3D lattice, the molecules enjoy a long lifetime, as long as they are all in the lowest band, which for spin-polarized fermions trivially means there can't be more than one molecule per site. Furthermore, the lifetime is independent of electric field, and is actually limited by single-photon scattering from the lattice beams (the 1064 nm light is only about 30 nm detuned from the bottom of the excited molecular potential).

Fig. 3.5 shows a typical decay of ground-state molecules in a deep 3D lattice. After a fast initial loss, which could be due to collisions with dark molecules (those that didn't make it to the ground state), we observe a simple exponential decay of the molecules, with a $1/e$ lifetime of 16(2) seconds. These dark molecules could be $d$-wave molecules produced during the magnetoassociation in the lattice (see Chapter 6). The inset compares the lifetime at zero electric field with that for polarized molecules with an induced dipole moment of 0.17D, and we see no difference within experimental error.

To understand the loss mechanism, we first studied the crossover from vertically oriented tubes to an isotropic 3D lattice. Fig. 3.6 shows how the lifetime depends on the lattice depth in the vertical direction. For these experiments the horizontal lattices were 56 $E_R$. For just vertically oriented tubes (no lattice along $z$), the lifetime is about 1 second and decreases to about 0.1 seconds when the molecules are polarized to 0.17 D. Adding even a shallow lattice along $z$, the lifetime increases significantly (5 seconds for $s_z = 12$ and 20 seconds for $s_z = 20$), and even at 5 $E_R$ the lifetime doesn't significantly change in an applied electric field. Pauli blocking should lead to a rapid suppression of loss as the lattice is increased along $z$, but would do so more rapidly than we observe. This, combined with the insensitivity of the lifetime at 5 $E_R$ to the induced dipole moment, suggest that an incoherent process is responsible for the loss in this regime of strong horizontal and weak vertical lattices. A model that describes the loss well is that there is some heating rate that promotes molecules to higher bands, and then these higher band molecules can tunnel much faster and collide with other molecules at a rate much higher than the promotion rate. A heating rate $\sim 1 - 2\,E_R/\mathrm{s}$ matches the data well (red and blue curves in Fig. 3.6).

The lifetime reaches a maximum value of about 25(5) seconds for $s_z = 34$ (point b in Fig. 3.6) and then it starts to decrease. At large lattice depths, the lifetime becomes limited by off-resonant scattering from the lattice laser. The rich internal structure of the molecules makes it likely that upon absorbing a photon, the molecule won't return to the ground state. The lifetime depends on the total light intensity, which we verified by adding a running wave beam (points c and d in Fig. 3.6). Measuring this scattering rate allows us to measure the imaginary part of the polariz-

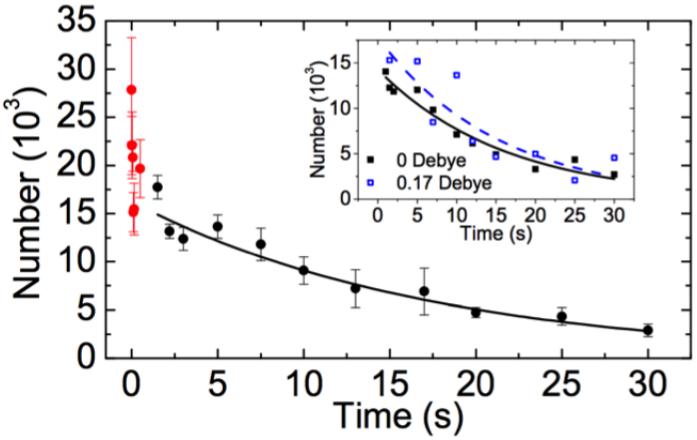


Figure 3.5: The lifetime of ground-state molecules in the 3D lattice, with $s_x = s_y = 56$ and $s_z = 70$ (the uncertainty in the lattice depths is at most 10%). After a fast initial loss of some of the molecules, the remaining molecules enjoy a long lifetime of $16.3 \pm 1.5$ seconds. The inset shows that the lifetime doesn't depend on electric field (these measurements were performed in an isotropic 50 $E_R$ lattice). Figure reproduced from Ref. [72].

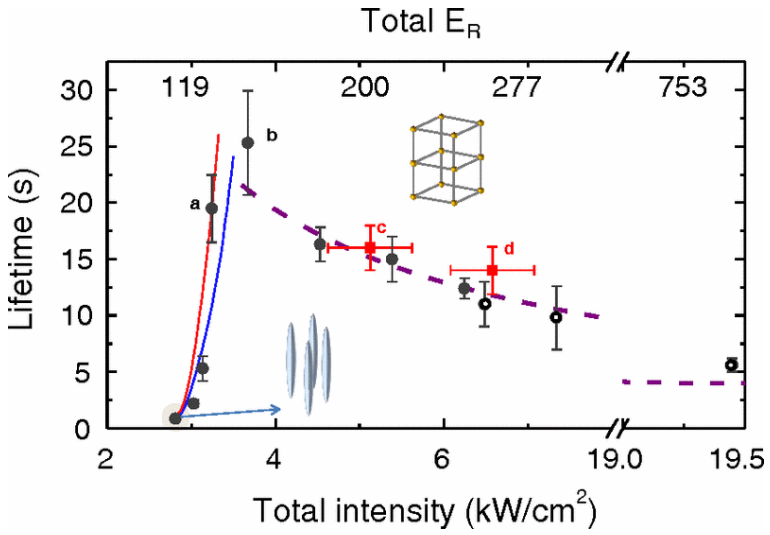


Figure 3.6: The lattice depth along the horizontal directions is fixed at 56 $E_R$, and the lattice depth along the vertical direction is gradually increased. This allows us to study the lifetime as we go from a 2D lattice to tubes with a small corrugation along the third direction to a full 3D lattice. For large $z$ lattice depths the lifetime becomes limited by off-resonant scattering. We can vary the intensity both by changing the $z$ lattice strength and by adding an additional running wave beam that increases the total intensity but doesn't increase the lattice depth. Figure reproduced from Ref. [72].

ability at 1064 nm to be $h \times 2.052(9) \times 10^{-12}$ MHz/(W/cm$^2$).

The achieved lifetimes of $\sim 10 - 20$ seconds are sufficient to realize a stable dipolar gas. As we will see in the next chapter, the exchange timescales for molecules in the lattice are as fast as 10 ms, so our lifetime provides ample opportunities to study interesting physics.

## 3.6 Long-lived Feshbach molecules and conversion of preformed pairs

Because Feshbach molecules are so weakly bound, it's difficult to cleanly remove all of the atoms that didn't get converted. This is especially problematic for K, where the light that we would use to remove the unpaired K atoms would kill the Feshbach molecules as well. Instead, we just "hide" the K in the $|9/2, -7/2\rangle$ state so we don't image them, but the atoms are still trapped. Furthermore, we typically convert only 10-20% of the minority species to Feshbach molecules, so the number of remaining atoms is significantly larger than the number of Feshbach molecules. These atoms can then collide with the Feshbach molecules and limit their lifetime. To verify this, we can use our ability to create ground-state molecules to more cleanly remove the unpaired atoms. If we then STIRAP the ground-state molecules back to the Feshbach state, we observe lifetimes $\sim 150$ ms in the dipole trap, significantly longer than the lifetime when "hiding" the atoms, which is less than 10 ms [114].

If we do the same procedure in the lattice, we find that the Feshbach molecules can live for up to 10 seconds (see Fig. 3.7). Varying the magnetic field after making molecules we can vary the size and binding energy of the Feshbach molecules. Similar to the ground-state molecules, we find that the lifetime is limited by off-resonant scattering. To explain the dependence on binding energy, we approximate the Feshbach molecule wavefunction $|f\rangle$ as

$$|f\rangle \approx \sqrt{Z}|C\rangle + \sqrt{1-Z}|O\rangle \tag{3.2}$$

where $|C\rangle$ is the closed-channel molecular wavefunction and $|O\rangle$ is the open-channel wave function for free atoms. $Z$ depends on the magnetic field and is 1 for $B \ll B_0$ (deeply bound molecules) and 0 for $B \gg B_0$ (free atoms), where $B_0$ is the location of the Feshbach resonance. The total

scattering rate is $Z\Gamma_{\rm mol} + (1-Z)\Gamma_{\rm atoms}$, where $\Gamma_{\rm mol}$ and $\Gamma_{\rm atoms}$ can be extracted from the lifetimes in the limiting cases, and $Z$ can be computed from a simple coupled-channel theory [29, 121]. The red fit curve in Fig. 3.7 has no free parameters and agrees well with the data.

By dissociating these long-lived Feshbach molecules to atoms, we can study the conversion of preformed pairs (lattice sites that have one K and one Rb atom). This is important because it allows us to understand how efficiently we can convert lattice sites with one K and one Rb atom to a Feshbach molecule. To do this we prepare a clean lattice of Feshbach molecules in the same way as described above. We then dissociate the Feshbach molecules by ramping the magnetic field above the resonance. At this point, we should have a lattice consisting of only preformed pairs. By then ramping $B$ to below the resonance to recreate molecules we can study how well we can convert these preformed pairs to Feshbach molecules. To measure the number of molecules, we apply an RF pulse which transfers free K atoms in the $|9/2, -9/2\rangle$ state to the $|9/2, -7/2\rangle$ state, but leaves Feshbach molecules unaffected. This renders the unpaired K atoms invisible during the subsequent molecule detection. We then dissociate the Feshbach molecules once again by ramping $B$ to above the resonance, and measure the number of K atoms with spin-selective resonant absorption imaging. We determine the conversion efficiency by dividing this molecule number by the total number of K atoms measured when we do not apply the RF pulse. In Ref. [72], we found a conversion of $87 \pm 13\%$. In Chapter 6, we investigate this issue in much further detail and confirm that in the ideal case of deep lattices and fast magnetic-field sweeps the conversion is near unity [93].

## 3.7 Quantum Zeno effect

As we've seen in the previous sections, the chemical reaction rate can be tuned over several orders of magnitude by changing the distinguishability of the molecular gas, the induced dipole moment, and the temperature. The highest two-body loss rate we observed is for the rotational mixture. In this case, the molecules are distinguishable, and there is no Pauli blocking and they can occupy the same site and chemically react. This onsite loss rate is very large and can be made to be larger than both the tunneling rate and the energy gap between different lattice bands. In

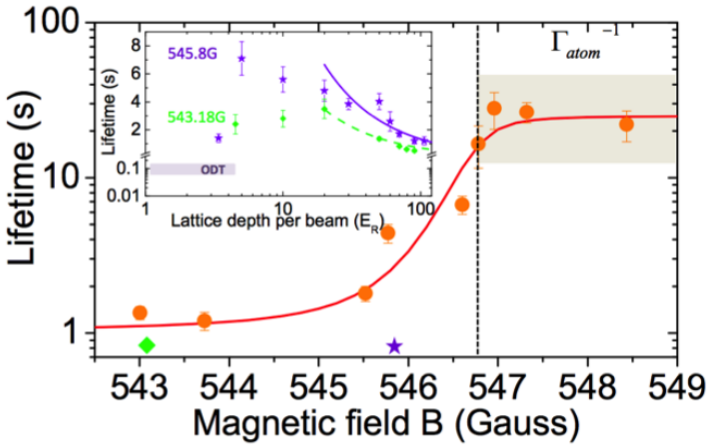


Figure 3.7: Using our ability to remove all unpaired atoms after making ground-state molecules, the lifetime of Feshbach molecules can be long. The lifetime depends on magnetic field because of the different admixture of open and closed channel contributions to the wave function, which depend on magnetic field. Above the resonance we have confinement-induced molecules, which don't exist in the absence of the lattice. Figure reproduced from Ref. [72].

this regime, tunneling onto an already occupied site is suppressed due to the continuous quantum Zeno effect, and as a result, the effective loss rate of the entire system decreases as the onsite loss rate increases. Some previous observations of the Zeno effect in AMO systems were reported in Refs. [122, 123]. It's worth noting here that the loss rates in the 3D lattice work [72], where we prepared a spin-polarized sample, were not large enough to be in the Zeno regime (at least for ground-band collisions). This section closely follows Ref. [90], of which I am an author.

Similar to the rotational mixture described above, we work with the $|0,0,-4,1/2\rangle$ and $|1,-1,-4,1/2\rangle$ states, which we map onto a spin-1/2 system ($|0,0\rangle \equiv |\downarrow\rangle$ and $|1,-1\rangle \equiv |\uparrow\rangle$). To see how the Zeno suppression comes about, consider just two lattice sites and take the initial state to be $|\uparrow,\downarrow\rangle$ (one particle in each well). The states that lead to loss are $|0,\uparrow\downarrow\rangle$ and $|\uparrow\downarrow,0\rangle$. To account for the loss we add an imaginary term $-i\hbar\Gamma_0/2$ to the energies of $|0,\uparrow\downarrow\rangle$ and $|\uparrow\downarrow,0\rangle$ (these two states also have a real energy shift $\Delta E$, which we assume to be small compared to $\hbar\Gamma_0$ [123, 124]). The system can be described by the following Hamiltonian, in the basis $|\uparrow,\downarrow\rangle$, $|\downarrow,\uparrow\rangle$, $|0,\uparrow\downarrow\rangle$, and $|\uparrow\downarrow,0\rangle$:

$$
\begin{array}{c}
\quad |\uparrow,\downarrow\rangle \quad |\downarrow,\uparrow\rangle \quad |0,\uparrow\downarrow\rangle \qquad |\uparrow\downarrow,0\rangle \\
H = \begin{pmatrix}
0 & 0 & -J & -J \\
0 & 0 & J & J \\
-J & J & \Delta E - \frac{i\hbar\Gamma_0}{2} & 0 \\
-J & J & 0 & \Delta E - \frac{i\hbar\Gamma_0}{2}
\end{pmatrix}.
\end{array}
\tag{3.3}
$$

Using second-order perturbation theory, the states $|\uparrow,\downarrow\rangle$ and $|\downarrow,\uparrow\rangle$ acquire an imaginary part to their energy, which in the limit that $\hbar\Gamma_0 \gg J, \Delta E$, is proportional to $\frac{J^2}{\hbar\Gamma_0}$. This implies that the states $|\uparrow,\downarrow\rangle$ and $|\downarrow,\uparrow\rangle$ decay at a rate proportional to $\frac{J^2}{\hbar^2\Gamma_0}$.

A schematic of the experimental setup is shown in Fig. 3.8. We used our standard preparation scheme to create $\sim 10^4$ ground-state molecules in a deep 3D lattice (along all three directions). Next, we applied a $\pi/2$ pulse on the $|0,0,-4,1/2\rangle \rightarrow |1,-1,-4,1/2\rangle$ transition and waited 50 ms to create an incoherent mixture. Then, we reduced the lattice depth along $y$ within 1 ms to allow

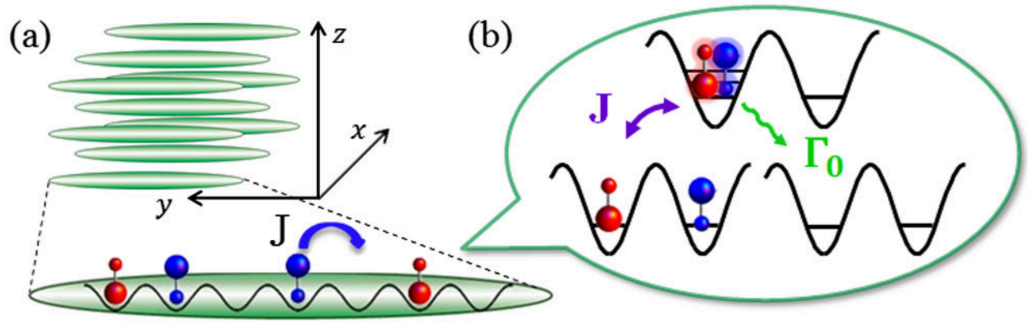


Figure 3.8: (a) Experimental setup for studying the continuous quantum Zeno effect. The molecules are held in a 3D lattice, with strong lattices along $x$ and $z$ and a weak lattice along $y$. This realizes a system of decoupled 1D tubes with a weak corrugation along the tubes. (b) The tunneling energy along the tube direction is $J$ and the onsite loss rate is $\Gamma_0$. Figure reproduced from Ref. [90].

tunneling along that direction (at a rate $J/h$), which realizes a system of decoupled tubes with weak corrugation along the tube. We held the molecules in the lattice for a variable hold time and then measured the number of $|\downarrow\rangle$ molecules.

When an $N = 0$ and $N = 1$ molecule encounter each other, there is no Pauli suppression preventing them from occupying the same site and their onsite loss rate due to chemical reactions $\Gamma_0$ is very large. In fact, we can have $\Gamma_0 > \omega_0 \gg \frac{J}{\hbar}$, where $\hbar\omega_0$ is the band separation and $J$ is the tunneling energy along the $y$ direction. The loss is this regime is governed by an effective loss rate

$$\Gamma_{\text{eff}} = \frac{2J^2}{\hbar^2\Gamma_0}. \tag{3.4}$$

The loss is two-body and the equation for the loss of either spin state is

$$\dot{N}_i(t) = -\frac{\kappa N_i(t)^2}{N_i(0)}, \tag{3.5}$$

where $i = |\uparrow\rangle$ or $|\downarrow\rangle$, $N_i(0)$ is the initial number of molecules in state $i$, and $\kappa = 4q\Gamma_{\text{eff}} g^{(2)}_{\downarrow\uparrow} n_\downarrow(0)$ (the master equation is needed to get the correct numerical prefactors). In the experiment we measure the population of molecules in $|\downarrow\rangle$, and $n_\downarrow(0)$ is the initial density, or filling fraction, of molecules in the $|\downarrow\rangle$ state, so that the total initial filling fraction is $2n_\downarrow(0)$. $q$ is the number of nearest neighbors, and $g^{(2)}_{\downarrow\uparrow} = \frac{\langle \hat{n}_i \hat{n}_j - 4\vec{S}_i \cdot \vec{S}_j \rangle}{\langle \hat{n}_i{}^2 \rangle}$ is the correlation function for the two spin states on neighboring sites $i$

and $j$ ($\hat{n}_i$ is the number operator on site $i$ and $\overrightarrow{S_i}$ is the spin-1/2 vector operator). Since we have an incoherent mixture, we assume $g^{(2)}_{\downarrow\uparrow} = 1$, but if our system were correlated such that $g^{(2)}_{\downarrow\uparrow} \neq 1$, we should be able to tell this by looking at the loss and comparing to an uncorrelated case. One goal of the experiment is to measure $\kappa$ for different values of $J$ and $\Gamma_0$ and verify the expected dependences from Eq. 3.4. Another goal is to get an idea of the filling fraction.

For our parameters, we likely occupy $\sim 1000 - 2000$ tubes with $\sim 6$ molecules/tube. Ultimately the small number of molecules per tube slows the loss down quite a bit for long hold times, and to account for this we only fit the loss until we lose 25% of the initial number. The typical transverse lattice strength is $40\,E_R$, while the lattice along the weak direction was varied between 5 and 16 $E_R$. We can adjust the lattice depths to tune over a wide range of $\Gamma_0$ and $J$ values (see Fig. 3.9). To change $J$, we primarily adjust the lattice depth along the $y$ direction. However, decreasing $J$ by reducing the lattice depth along $y$ causes $\Gamma_0$ to go down slightly since the onsite wavefunction size becomes slightly larger. So to reduce $J$ but keep $\Gamma_0$ fixed, we reduce $s_y$ and slightly increase $s_x$ and $s_z$. To change $\Gamma_0$ we need to change the size of the Wannier function, which we accomplish by changing the transverse lattice depths. Considering only the lowest band, $\Gamma_0$ is given by

$$\Gamma_0 = \beta^{(3D)} \int |w(\mathbf{r})|^4 d^3r, \tag{3.6}$$

where $w(\mathbf{r})$ is the (ground-band) Wannier function, and the rate coefficient $\beta^{(3D)}$ was measured in the harmonic trap to be $9.0(4) \times 10^{-10}$ cm$^3$ s$^{-1}$ (see Fig. 3.3).

Fig. 3.10a shows a typical loss curve. Here $s_y = 5$ and $s_x = s_z = 25$. The fit is the solution of Eq. 3.5. If we naïvely calculate the filling using Eq. 3.5, we get an answer that is much too high, something in the range of 30%, whereas we know that the filling is more like 5-10%. This is because we have neglected the effects of higher bands. Higher bands play a very important role because $\Gamma_0$ is on the same order of magnitude as the band gap. An admixture of higher bands causes the molecules to be less localized (since the onsite density is much lower for molecules in higher

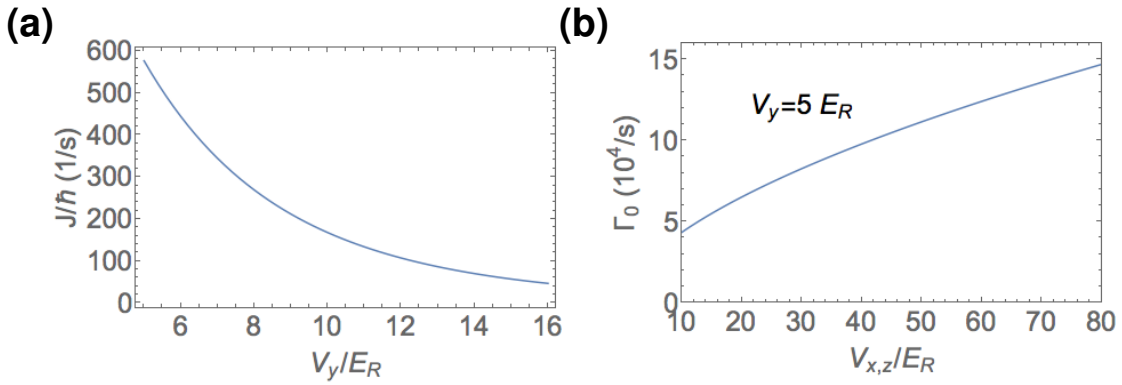


Figure 3.9: (a) Tunneling rate along the tube direction ($J/\hbar$) vs. lattice depth $V_y$ along the tube direction. In the experiment $V_y$ was varied between 5 and 16 $E_R$. (b) Onsite loss rate $\Gamma_0$ (considering only the lowest band) vs. $V_{x,z}$ ($V_x = V_z$) and $V_y = 5E_R$, calculated using Eqs. 3.6 and 2.7.

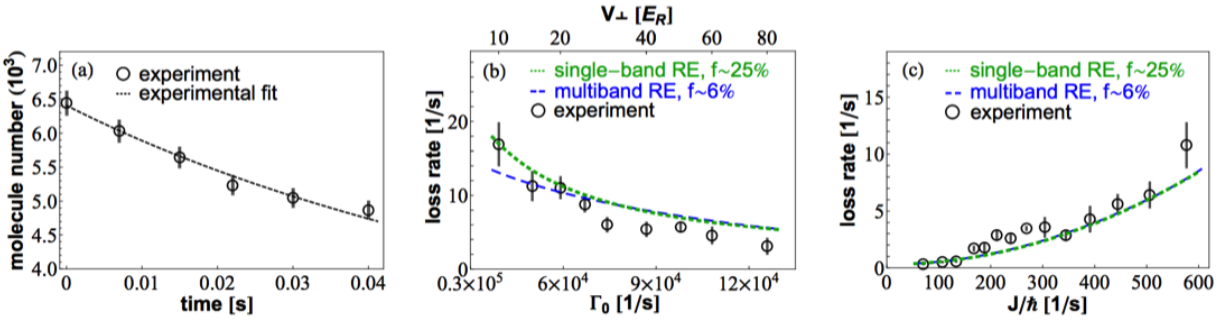


Figure 3.10: (a) Typical loss curve, with a fit to the rate equation (Eq. 3.5). (b) and (c) Comparison of the theory, considering both a single band (green) and multiple bands (blue). In both cases, the rate equation was used. The only difference is that in the case of multiple bands a renormalized $\widetilde{\Gamma_{\text{eff}}}$, which accounts for higher bands, is used. The multi-band theory fits the data with a much lower filling fraction than a single-band theory. Figure reproduced from Ref. [90].

bands) and hence the integral over $W$ is lower, which causes $\Gamma_0$ to be lower. This causes $\Gamma_{\text{eff}}$ to increase and reduces the filling fraction extracted from a measured value of $\kappa$. For our parameters, properly accounting for higher bands can increase $\Gamma_{\text{eff}}$ by about a factor of 5. Fig. 3.10b shows the dependence of $\kappa$ on $\Gamma_0$, and clearly shows the Zeno suppression. Fig. 3.10c shows that $\kappa$ depends roughly quadratically on $J/\hbar$. Panels b and c show that lattice fillings around 6% lead to the best agreement with the experiment.

## 3.8 Conclusion

This chapter described our efforts to understand, control, and finally shut off chemical reactions in KRb. It's widely viewed that chemical reactions are a disadvantage for studying quantum many-body physics with a system of molecules; however, we have shown that creating the molecules in the lattice completely avoids this problem. Our studies of the quantum Zeno effect show an interesting application of chemical reactions, which could be used to measure correlations between particles without relying on amazing imaging resolution. These experiments also informed us that the lattice fillings were quite low, less than 10%. Most of the rest of this thesis will focus on cases where the molecules are created and confined in a deep 3D lattice, so the chemical reactions are irrelevant and the lifetimes are long.

As an alternative way to avoid chemical reactions in ultracold molecular gases, a number of experiments are currently underway to produce gases of ultracold non-reactive molecules. However, it's not completely clear that other processes cannot occur in these "nonreactive" molecules that would limit the lifetime. For example, there are predictions for a three-body loss process whereby two nonreactive molecules form a transient complex which collides with a third molecule, leading to the loss of all three [125]; however, in reactive molecules like KRb, the chemical reactions make these loss processes unobservable [125].

Molecules in the lowest rotational state suffer from chemical reactions, and the situation only gets worse as the dipole moment is increased. However, collisions between molecules in mixed rotational states can be tuned via an applied electric field. In particular, Ref. [126] shows that the

ratio of elastic to quenching (reactive plus inelastic) collisions can be tuned by several orders of magnitude by using an electric field to make a second excited colliding channel cross the threshold of the incident channel. The specific cases considered were $|\tilde{1}, 0\rangle + |\tilde{1}, 0\rangle$ with either $|\tilde{0}, 0\rangle + |\tilde{2}, 0\rangle$ or $|\tilde{0}, 0\rangle + |\tilde{2}, \pm 1\rangle$, where $|\tilde{N}, m_N\rangle$ is the dressed state which asymptotically approaches $|N, m_N\rangle$ in the limit of zero electric field. These specific resonances occur around 12 kV/cm, which should be accessible in the second generation of our experiment.

# Chapter 4

## Observation of spin exchange

From the point of view of pursuing many-body physics mediated by long-range interactions, chemical reactions are a nuisance. Previous observations of effects caused by dipolar interactions in ultracold molecules involved inelastic collisions or chemical reactions [69, 70, 71]. In this chapter, I discuss a manifestation of coherent dipole-dipole interactions, where the molecules never actually come in contact with each other. It was proposed in Refs. [74, 82] that the molecules can behave as quantum magnets, and even at low lattice fillings, it should be possible to observe dipolar interactions [83]. In this scheme, we encode a spin-1/2 degree of freedom in two rotational states of the molecules, and the molecules can swap their spin orientation via a flip-flop process that can occur in principle over arbitrary distances. More specifically, the $N = 0$ and $N = 1$ rotational states have opposite parity, and by driving electric dipole transitions between them with microwaves, we realize an XY coupling, as depicted in Fig. 4.1. We probe these spin-exchange interactions using Ramsey spectroscopy [84]. This experiment can also be viewed as a global quench, as the initial $\pi/2$ pulse in our Ramsey sequence instantaneously turns on the interactions.

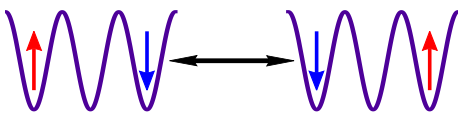

Figure 4.1: Spin exchange between molecules in $N = 0$, denoted by $\downarrow$ and $N = 1$, denoted by $\uparrow$. To emphasize the role that long-range interactions play, the exchange depicted here is between next-nearest neighbors.

There has been a lot of interest recently in quantum magnetism based on effective spin-1/2 systems. One of the appeals of quantum magnetic models is that although they appear very simple, they are actually very hard to solve with classical computers [34, 38]. In addition, quantum magnetic models are relevant to many classes of materials, including antiferromagnets, spin glasses, spin nematics, and unconventional superconductors [34]. Any experimental system with spin-spin couplings can engineer quantum magnetic models, including neutral atoms in optical lattices [35, 36, 46, 127], trapped ions [38, 39], NV centers [128], and Rydberg atoms [129]. Much of the work in this field was pioneered with neutral atoms in optical lattices. However, the contact interactions in cold atoms require wavefunction overlap, and effective spin-spin interactions are usually mediated by tunneling in a process called superexchange [130]. The resulting interactions are weak and limited to nearest neighbors, and very low temperatures are required for the interactions to manifest. Furthermore, the energy scale decreases exponentially as the lattice depth increases. In contrast, dipolar interactions give rise to spin-spin interactions that don't require tunneling, which enables coherent spin dynamics to persist in systems with high entropies and low lattice filling fractions, and in very deep lattices where the molecules are completely pinned. It's also worth noting that the dipolar interactions present in our system are different from the exchange interactions in electrons in metals. There, an effective spin-spin interaction arises from the combination of the spin-independent Coulomb interaction and the fermionic exchange symmetry of electrons, which is responsible for lifting the degeneracy between the singlet and triplet states.

This chapter is organized as follows. First, I describe how the molecules acquire a dipole moment and then give the expression for the dipolar Hamiltonian. Next, I discuss how the anisotropic polarizability of polar molecules affects the observation of dipole-dipole interactions. Then I describe how we used Ramsey spectroscopy (with a spin echo) to see dipolar effects in the lattice, and describe the various pieces of evidence that support that the dynamics of our system is governed by an XY Hamiltonian. Finally, I give an outlook of future experiments that could be done, which motivates the next chapter on increasing the lattice filling fraction. The discussion in this chapter closely follows Refs. [84] and [85], of which I am an author.

## 4.1 Deriving the dipolar Hamiltonian

An electric dipole moment only exists between quantum states of opposite parity. For polar molecules, the rotational states $|N, m_N\rangle$ are states of definite parity, and thus molecules in the $N = 0$ state have no dipole moment in the lab frame at zero electric field. In an electric field, the eigenstates become dressed states that are a superposition of many different rotational levels, and this gives a nonzero dipole moment in the lab frame. However, it takes a very large DC field to fully mix the rotational states and saturate the dipole moment. A field of more than 10 times the critical field $E_C = B/d$, where $B$ is the rotational constant and $d$ is the dipole moment, is required to get to 80% of the saturated dipole moment (see Fig. 4.2). For KRb, $E_C \sim 4$ kV/cm. Given the maximum DC field we could apply in the first generation of the experiment, as well as the instabilities described in Chapter 2, applying a DC field to study coherent dipole-dipole interactions is problematic. An alternative mechanism for getting dipolar interactions is to apply an AC electric field, which directly couples, on-resonance, two opposite parity rotational states. This is the technique discussed in this chapter for realizing strong dipole-dipole interactions in the lattice.

The classical dipole-dipole interaction between two dipoles $\mathbf{d_i}$ and $\mathbf{d_j}$ is

$$V_{dd} = \frac{\mathbf{d_i} \cdot \mathbf{d_j} - 3(\mathbf{d_i} \cdot \hat{\mathbf{r}}_{ij})(\mathbf{d_j} \cdot \hat{\mathbf{r}}_{ij})}{r_{ij}^3}, \tag{4.1}$$

where $r_{ij}$ is the distance between the dipoles and generally the dipoles are aligned along some quantization axis. For the rest of this section, I consider the case of molecules in a 3D square optical lattice with lattice spacing $a_{\text{lat}}$. The sites are labelled by $i$ and $j$, and $r_{ij}$ is in units of the lattice spacing.

The exchange process depicted in Fig. 4.1 is described by the Hamiltonian

$$H = \frac{1}{2} \sum_{i \neq j} V_{dd}(\mathbf{r_i} - \mathbf{r_j}) \left( \frac{J_\perp}{2} \left( \hat{S}_i^+ \hat{S}_j^- + \hat{S}_i^- \hat{S}_j^+ \right) \right), \tag{4.2}$$

where $V_{dd}(\mathbf{r_i} - \mathbf{r_j}) = \frac{1 - 3\cos^2\theta_{ij}}{r_{ij}^3}$, $\hat{S_i^+}$ and $\hat{S_i^-}$ are spin-1/2 raising and lowering operators on site $i$, and $J_\perp = k d_{\downarrow\uparrow}^2/(4\pi\epsilon_0 a_{\text{lat}}^3)$ ($k$ is a constant and $d_{\downarrow\uparrow}$ is the transition dipole moment between the

two states of our spin-1/2 system). In this section, I outline how to get Eq. 4.2 from Eq. 4.1. The derivations closely follow Ref. [34].

To understand how the dipoles can behave like quantum magnets, we would like to find the quantum analog of Eq. 4.1. To do this, it's useful to understand that the dipolar interaction is the result of the contraction of two rank-two tensors. One of these tensors acts on the molecules' internal states via the dipole operators, and the other acts on the orbital motion of two molecules (this is responsible for the angular dependence of Eq. 4.1) [34]. As a result, Eq. 4.1 can be expressed as a sum of terms that allow $q$ units of rotational angular momentum to be transferred to orbital angular momentum [34]. Appendix A shows that an equivalent way to write Eq. 4.1 is:

$$V_{dd} = -\frac{\sqrt{6}}{r_{ij}^3} \sum_{q=-2}^{q=2} (-1)^q C^2_{-q}(\theta,\phi) T^2_q(\mathbf{d_i}, \mathbf{d_j}), \tag{4.3}$$

where

$$C^k_q(\theta,\phi) = \sqrt{\frac{4\pi}{2k+1}} Y_{kq}(\theta,\phi), \tag{4.4}$$

and the $Y_{kq}(\theta,\phi)$'s are spherical harmonics [131]. The $T$'s are irreducible tensor operators:

$$T^2_{\pm 2} = \hat{d_i^{\pm}} \hat{d_j^{\pm}}. \tag{4.5}$$

$$T^2_{\pm 1} = \frac{\hat{d_i^0} \hat{d_j^{\pm}} + \hat{d_i^{\pm}} \hat{d_j^0}}{\sqrt{2}}. \tag{4.6}$$

$$T^2_0 = \frac{\hat{d_i^+} \hat{d_j^-} + \hat{d_i^-} \hat{d_j^+} + 2\hat{d_i^0} \hat{d_j^0}}{\sqrt{6}}. \tag{4.7}$$

Only the $q = 0$ term is relevant for this chapter, since the other terms don't conserve energy (see section 4.6.2 for more details). The $q = 0$ term of Eq. 4.3 is

$$V_{dd}^{q=0} = \frac{1 - 3\cos^2\theta_{ij}}{r_{ij}^3} \left( \hat{d_i^0} \hat{d_j^0} + \frac{\hat{d_i^+} \hat{d_j^-} + \hat{d_i^-} \hat{d_j^+}}{2} \right) \tag{4.8}$$

$$= V_{dd}(\mathbf{r_i} - \mathbf{r_j}) \left( \hat{d_i^0} \hat{d_j^0} + \frac{\hat{d_i^+} \hat{d_j^-} + \hat{d_i^-} \hat{d_j^+}}{2} \right). \tag{4.9}$$

The $\hat{d}$'s are spin-1/2 operators ($\hat{d^{\pm}}$ are analogous to the spin-1/2 raising and lowering operators, and $\hat{d^0}$ is equivalent to $\hat{d^z}$). In the basis of rotational states $|N, m_N\rangle$, the matrix elements of the

dipole operators $\hat{d}^p$, with $p = 0$ corresponding to $\hat{d}^0$, and $p = \pm 1$ corresponding to $\hat{d}^{\pm}$ are

$$\langle N, m_N|\hat{d}^p|N', m'_N\rangle = \mathcal{D}\sqrt{(2N+1)(2N'+1)}(-1)^{m_N} \begin{pmatrix} N & 1 & N' \\ -m_N & p & m'_N \end{pmatrix} \begin{pmatrix} N & 1 & N' \\ 0 & 0 & 0 \end{pmatrix}. \tag{4.10}$$

Here, $\mathcal{D}$ is the full dipole matrix element (which is 0.574 D for KRb), and the terms in parentheses are 3-$j$ symbols.

The Hamiltonian for the rotational states $|N, m_N\rangle$ consists of the rotational energy and the Stark effect.

$$\langle N, m_N|\hat{H}|N', m'_N\rangle = BN(N+1)\delta_{N,N'}\delta_{m_N,m_{N'}} - \langle N, m_N|\mathbf{d}\cdot\boldsymbol{\epsilon}|N', m'_N\rangle, \tag{4.11}$$

where $B$ is the rotational constant and the coupling of the dipole with an external electric field $\boldsymbol{\epsilon}$ is $-\mathbf{d}\cdot\boldsymbol{\epsilon}$. We take the electric field, of magnitude $\epsilon$, to be along the $z$ direction; thus, the second term of Eq. 4.11 involves the $p = 0$ component of Eq. 4.10.

$$\langle N, m_N|\hat{H}|N', m'_N\rangle = BN(N+1)\delta_{N,N'}\delta_{m_N,m_{N'}} - \epsilon\langle N, m_N|\hat{d}^0|N', m'_N\rangle. \tag{4.12}$$

The $p = 0$ term of Eq. 4.10 preserves the value of $m_N$ (if $m_N \neq m_{N'}$, then the first 3-$j$ symbol is zero). Thus, the eigenstates in an electric field can be expressed as $|\tilde{N}, m_N\rangle$, which are the states which adiabatically connect to the states $|N, m_N\rangle$ at zero electric field.

$$|\tilde{N}, m_N\rangle = \sum_{N'} c_{N'}|N', m_N\rangle. \tag{4.13}$$

By diagonalizing Eq. 4.12, we obtain the dressed state energies $E_{\tilde{N},m_N}$ and the coefficients $c_{N'}$. The induced dipole moment of state $|\tilde{N}, m_N\rangle$ is then $-\frac{\partial E_{\tilde{N},m_N}}{\partial\epsilon}$. Fig. 4.2 shows the induced dipole moments for the $|\tilde{0}, 0\rangle$, $|\tilde{1}, 0\rangle$, and $|\tilde{1}, \pm 1\rangle$ states vs. applied DC field.

For our mapping to a spin-1/2 system, we choose $|\downarrow\rangle \equiv |\tilde{0}, 0\rangle$ and $|\uparrow\rangle \equiv |\tilde{1}, 0\rangle$ or $|\tilde{\uparrow}\rangle \equiv |\tilde{1}, \pm 1\rangle$ (following the notation of Ref. [34]). The induced dipole moments are:

$$d_{\downarrow} \equiv \langle\tilde{0}, 0|\hat{d}^0|\tilde{0}, 0\rangle. \tag{4.14}$$

$$d_{\uparrow} \equiv \langle\tilde{1}, 0|\hat{d}^0|\tilde{1}, 0\rangle. \tag{4.15}$$

$$d_{\tilde{\uparrow}} \equiv \langle\tilde{1}, \pm 1|\hat{d}^0|\tilde{1}, \pm 1\rangle. \tag{4.16}$$

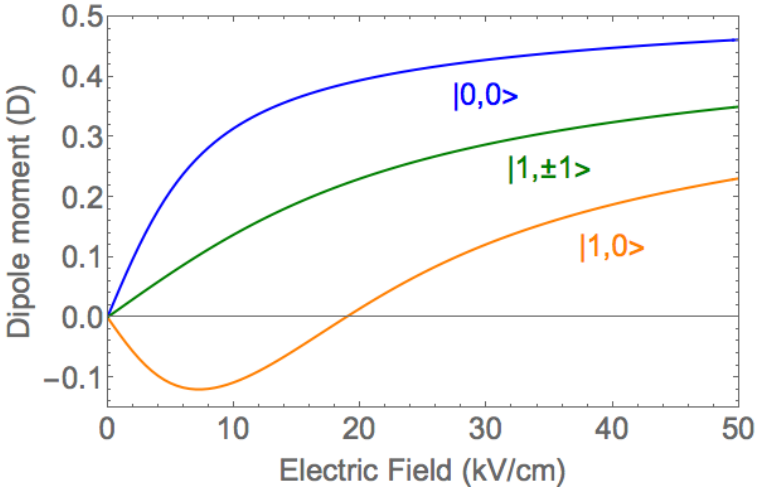


Figure 4.2: Induced dipole moments of the $|\tilde{0}, 0\rangle$ (blue), $|\tilde{1}, 0\rangle$ (orange), and $|\tilde{1}, \pm 1\rangle$ states (green). At a field of around 19 kV/cm, the dipole moment of the $|\tilde{1}, 0\rangle$ state changes sign. The lowest 20 rotational states were included in the calculation, which introduces an error of less than 1% in the limit of infinite electric field. The first generation of the experiment could access electric fields up to about 6 kV/cm.

For completeness, let's work out the expression for $d_\downarrow$. To do this, we use Eq. 4.13 to write

$$|\tilde{0},0\rangle = \sum_N c_N |N,0\rangle. \tag{4.17}$$

Then

$$d_\downarrow = \Big(\sum_{N'} c^*_{N'}\langle N',0|\Big)\hat{d}^0\Big(\sum_N c_N|N,0\rangle\Big) = \sum_{N,N'} c^*_{N'}c_N\langle N',0|\hat{d}^0|N,0\rangle. \tag{4.18}$$

For states with $m_N = 0$, the two 3-$j$ symbols in Eq. 4.10 are the same, and

$$\begin{pmatrix} N & 1 & N' \\ 0 & 0 & 0 \end{pmatrix} = (-1)^N\delta_{N,N'+1}\sqrt{\frac{N}{(2N+1)(2N'+1)}} + (-1)^{N'}\delta_{N,N'-1}\sqrt{\frac{N'}{(2N+1)(2N'+1)}}. \tag{4.19}$$

Then the sum in Eq. 4.18 becomes

$$d_\downarrow = 2\sum_{N=0}^{\infty} c^*_{N+1}c_N\langle N+1,0|\hat{d}^0|N,0\rangle, \tag{4.20}$$

which by Eqs. 4.10 and 4.19 becomes

$$d_\downarrow = 2\mathcal{D}\sum_{N=0}^{\infty} c^*_{N+1}c_N\frac{N+1}{\sqrt{(2N+1)(2N+3)}}. \tag{4.21}$$

We are also interested in the transition dipole moments between $|\downarrow\rangle$ and $|\uparrow\rangle$ or $|\tilde{\uparrow}\rangle$. Since $|\tilde{0},0\rangle$ and $|\tilde{1},0\rangle$ are coupled by $\hat{d}^0$, we have

$$d_{\downarrow\uparrow} \equiv \langle\tilde{1},0|\hat{d}^0|\tilde{0},0\rangle = \langle\tilde{0},0|\hat{d}^0|\tilde{1},0\rangle. \tag{4.22}$$

Again, it's useful to write out the full expression for this. If we let $|\tilde{0},0\rangle = \sum_N a_N|N,0\rangle$ and $|\tilde{1},0\rangle = \sum_N b_N|N,0\rangle$, then

$$\begin{aligned} d_{\downarrow\uparrow} &= \sum_{N=0}^{\infty}\Big(a^*_N b_{N+1}\langle N,0|\hat{d}^0|N+1,0\rangle + a_{N+1}b^*_N\langle N+1,0|\hat{d}^0|N,0\rangle\Big) &(4.23)\\ &= \mathcal{D}\sum_{N=0}^{\infty}(a^*_N b_{N+1} + a_{N+1}b^*_N)\frac{N+1}{\sqrt{(2N+1)(2N+3)}}. &(4.24)\end{aligned}$$

In contrast, $|\tilde{0},0\rangle$ and $|\tilde{1},\pm1\rangle$ are coupled by $\hat{d}^\pm$.

$$d_{\downarrow\tilde{\uparrow}} \equiv \langle\tilde{1},\pm1|\hat{d}^\pm|\tilde{0},0\rangle = -\langle\tilde{0},0|\hat{d}^\mp|\tilde{1},\pm1\rangle, \tag{4.25}$$

where the minus sign in the last equality comes from the $(-1)^{m_N}$ in Eq. 4.10.

With all of these definitions, we're now ready to proceed with turning Eq. 4.8 into something that looks like Eq. 4.2. First, let's consider the $\{|\tilde{0},0\rangle, |\tilde{1},0\rangle\}$ manifold. We project Eq. 4.8 onto the basis $\{|\uparrow_i\uparrow_j\rangle, |\uparrow_i\downarrow_j\rangle, |\downarrow_i\uparrow_j\rangle, |\downarrow_i\downarrow_j\rangle\}$ to get the Hamiltonian $\hat{H}_{ij}$ for two molecules on sites $i$ and $j$. Since the dipole-dipole interaction is a pairwise interaction, we can then sum over all pairs $i, j$ to get the full Hamiltonian for the system.

$$\hat{H}_{ij} = \sum_{\alpha,\beta} C_{\alpha\beta}|\alpha\rangle\langle\beta|, \tag{4.26}$$

where $C_{\alpha\beta} = \langle\alpha|V_{dd}^{q=0}|\beta\rangle$, and $|\alpha\rangle, |\beta\rangle \in \{|\uparrow_i\uparrow_j\rangle, |\uparrow_i\downarrow_j\rangle, |\downarrow_i\uparrow_j\rangle, |\downarrow_i\downarrow_j\rangle\}$. For example,

$$\langle\uparrow_i\uparrow_j |V_{dd}^{q=0}| \uparrow_i\uparrow_j\rangle = V_{dd}(\mathbf{r_i}-\mathbf{r_j})\langle\uparrow_i\uparrow_j |\hat{d_i^0}\hat{d_j^0}| \uparrow_i\uparrow_j\rangle = V_{dd}(\mathbf{r_i}-\mathbf{r_j})d_\uparrow^2, \tag{4.27}$$

since $\langle\uparrow_i\uparrow_j |\hat{d_i^0}\hat{d_j^0}| \uparrow_i\uparrow_j\rangle = \langle\uparrow_i |\hat{d_i^0}| \uparrow_i\rangle\langle\uparrow_j |\hat{d_j^0}| \uparrow_j\rangle = d_\uparrow^2$. Note that only the $\hat{d^0}$ terms of Eq. 4.8 contribute. Similarly,

$$\langle\uparrow_i\downarrow_j |V_{dd}^{q=0}| \downarrow_i\uparrow_j\rangle = V_{dd}(\mathbf{r_i}-\mathbf{r_j})\langle\uparrow_i\downarrow_j |\hat{d_i^0}\hat{d_j^0}| \downarrow_i\uparrow_j\rangle = V_{dd}(\mathbf{r_i}-\mathbf{r_j})d_{\downarrow\uparrow}^2, \tag{4.28}$$

since $\langle\uparrow_i\downarrow_j |\hat{d_i^0}\hat{d_j^0}| \downarrow_i\uparrow_j\rangle = \langle\uparrow_i |\hat{d_i^0}| \downarrow_i\rangle\langle\downarrow_j |\hat{d_j^0}| \uparrow_j\rangle = d_{\downarrow\uparrow}^2$ by Eq. 4.22. The result is a $4\times4$ matrix:

$$\hat{H}_{ij} = V_{dd}(\mathbf{r_i}-\mathbf{r_j}) \begin{array}{c} \begin{array}{cccc} |\uparrow\uparrow\rangle & |\uparrow\downarrow\rangle & |\downarrow\uparrow\rangle & |\downarrow\downarrow\rangle \end{array} \\ \begin{pmatrix} d_\uparrow^2 & 0 & 0 & 0 \\ 0 & d_\downarrow d_\uparrow & d_{\downarrow\uparrow}^2 & 0 \\ 0 & d_{\downarrow\uparrow}^2 & d_\downarrow d_\uparrow & 0 \\ 0 & 0 & 0 & d_\downarrow^2 \end{pmatrix} \end{array}. \tag{4.29}$$

For the $\{|\tilde{0},0\rangle, |\tilde{1},\pm1\rangle\}$ manifold, everything is the same except $d_\uparrow$ is replaced by $d_{\tilde{\uparrow}}$, and the flip-flop matrix elements are different.

$$\langle\tilde{\uparrow}_i\downarrow_j |V_{dd}^{q=0}| \downarrow_i\tilde{\uparrow}_j\rangle = V_{dd}(\mathbf{r_i}-\mathbf{r_j})\langle\tilde{\uparrow}_i\downarrow_j | \left(\frac{\hat{d_i^+}\hat{d_j^-} + \hat{d_i^-}\hat{d_j^+}}{2}\right) | \downarrow_i\tilde{\uparrow}_j\rangle = -\frac{V_{dd}(\mathbf{r_i}-\mathbf{r_j})}{2}d_{\downarrow\tilde{\uparrow}}^2. \tag{4.30}$$

To understand the origin of the factor of $-1/2$, consider $|\tilde{\uparrow}\rangle = |\tilde{1}, 1\rangle$. Then we have

$$\begin{aligned}
\frac{1}{2}\langle\tilde{\uparrow}_i \downarrow_j |\hat{d_i^+}\hat{d_j^-} + \hat{d_i^-}\hat{d_j^+}| \downarrow_i \tilde{\uparrow}_j\rangle &= \frac{1}{2}\langle\tilde{\uparrow}_i \downarrow_j |\hat{d_i^+}\hat{d_j^-}| \downarrow_i \tilde{\uparrow}_j\rangle + \frac{1}{2}\langle\tilde{\uparrow}_i \downarrow_j |\hat{d_i^-}\hat{d_j^+}| \downarrow_i \tilde{\uparrow}_j\rangle & (4.31)\\
&= \frac{1}{2}\langle\tilde{\uparrow}_i|\hat{d_i^+}| \downarrow_i\rangle\langle\downarrow_j |\hat{d_j^-}|\tilde{\uparrow}_i\rangle + \frac{1}{2}\langle\tilde{\uparrow}_i|\hat{d_i^-}| \downarrow_i\rangle\langle\downarrow_j |\hat{d_j^+}|\tilde{\uparrow}_i\rangle & (4.32)\\
&= \frac{1}{2}(d_{\downarrow\tilde{\uparrow}})(-d_{\downarrow\tilde{\uparrow}}) + 0 & (4.33)\\
&= \frac{-d^2_{\downarrow\tilde{\uparrow}}}{2}. & (4.34)
\end{aligned}$$

The answer is the same for the $|\tilde{1}, -1\rangle$ state. In this case, the $4 \times 4$ matrix is

$$\hat{H}_{ij} = V_{dd}(\mathbf{r_i} - \mathbf{r_j}) \begin{pmatrix} d^2_{\tilde{\uparrow}} & 0 & 0 & 0 \\ 0 & d_\downarrow d_{\tilde{\uparrow}} & \frac{-d^2_{\downarrow\tilde{\uparrow}}}{2} & 0 \\ 0 & \frac{-d^2_{\downarrow\tilde{\uparrow}}}{2} & d_\downarrow d_{\tilde{\uparrow}} & 0 \\ 0 & 0 & 0 & d^2_\downarrow \end{pmatrix}. \tag{4.35}$$

Now we want to write this in terms of spin operators $\hat{S^z_{i,j}}$, $\hat{S^+_{i,j}}$, and $\hat{S^-_{i,j}} = (\hat{S^+_{i,j}})^\dagger$. These operators have the commutation relations $[\hat{S^z_i}, \hat{S^\pm_j}] = \pm\delta_{ij}\hat{S^\pm_i}$ and can be represented as $4 \times 4$ matrices. A lot of algebra can be used to rewrite Eqs. 4.29 and 4.35 as

$$\hat{H}_{ij} = V_{dd}(\mathbf{r_i} - \mathbf{r_j}) \left( J_z \hat{S^z_i}\hat{S^z_j} + \frac{J_\perp}{2}\left(\hat{S^+_i}\hat{S^-_j} + \hat{S^-_i}\hat{S^+_j}\right) + W(\mathbb{1}_i\hat{S^z_j} + \hat{S^z_i}\mathbb{1}_j) + V\mathbb{1}_i\mathbb{1}_j \right), \tag{4.36}$$

where the $\mathbb{1}$'s are identity matrices, and the coupling constants are given in Table 4.1. The final step is to replace the identity matrices with the molecule density ($\mathbb{1}_k \to \hat{n}_k$, where $\hat{n}_k = 1$ if there is a molecule on site $k$, and 0 if there's not), and then sum over all lattice sites $i$ and $j$. The simplest way to do this is to sum over all $i$ and $j$ with $i \neq j$ and then multiply by $1/2$ to account for double counting. Finally, this gives us

$$\hat{H} = \frac{1}{2}\sum_{i\neq j} V_{dd}(\mathbf{r_i} - \mathbf{r_j}) \left( J_z \hat{S^z_i}\hat{S^z_j} + \frac{J_\perp}{2}\left(\hat{S^+_i}\hat{S^-_j} + \hat{S^-_i}\hat{S^+_j}\right) + W(\hat{n}_i\hat{S^z_j} + \hat{S^z_i}\hat{n}_j) + V\hat{n}_i\hat{n}_j \right). \tag{4.37}$$

Note that to get the coupling constants in SI units requires dividing by $4\pi\epsilon_0 a^3_{\text{lat}}$, where $\epsilon_0$ is the vacuum permittivity.

The first term, proportional to $J_z$, is the Ising term, which comes about because parallel and antiparallel spin configurations have different energies. At zero electric field, this term is zero since

| Parameter | Coupling $\{\|\tilde{0},0\rangle, \|\tilde{1},0\rangle\}$ | Coupling $\{\|\tilde{0},0\rangle, \|\tilde{1},\pm1\rangle\}$ |
|---|---|---|
| $J_z$ | $(d_\uparrow - d_\downarrow)^2$ | $(d_{\tilde{\uparrow}} - d_\downarrow)^2$ |
| $J_\perp$ | $2d_{\downarrow\uparrow}^2$ | $-d_{\downarrow\tilde{\uparrow}}^2$ |
| $W$ | $(d_\uparrow^2 - d_\downarrow^2)/2$ | $(d_{\tilde{\uparrow}}^2 - d_\downarrow^2)/2$ |
| $V$ | $(d_\uparrow + d_\downarrow)^2/4$ | $(d_{\tilde{\uparrow}} + d_\downarrow)^2/4$ |

Table 4.1: Coupling constants of the dipolar Hamiltonian, Eq. 4.37. To get the values in SI units, divide by $4\pi\epsilon_0 a_{\text{lat}}^3$.

both induced dipole moments are zero. The second term, proportional to $J_\perp$, can be rewritten as $J_\perp(\hat{S}_i^x\hat{S}_j^x + \hat{S}_i^y\hat{S}_j^y)$ and hence is referred to as the XY term. Physically, it gives rise to the flip-flop process depicted in Fig. 4.1. Fig. 4.3 plots $J_z$ and $J_\perp$ vs. applied electric field (for KRb in a 532 nm lattice spacing), and shows that we actually get the largest interactions, corresponding to an induced dipole moment of $\mathcal{D}/\sqrt{3}$, at zero electric field with a pure XY coupling ($J_z = 0, J_\perp \neq 0$). The XY term gets monotonically weaker as the electric field is increased. Second, any value of $J_z/J_\perp$ can be obtained in principle by tuning the electric field; however, it's not possible to independently control the strength of the total coupling. Third, $J_z$ has a maximum around 12 kV/cm.

The different signs for $J_\perp$ for the $\{|\tilde{0},0\rangle, |\tilde{1},0\rangle\}$ and $\{|\tilde{0},0\rangle, |\tilde{1},\pm1\rangle\}$ manifolds imply anti-ferromagnetic and ferromagnetic interactions, respectively. The term proportional to $W$ is the density-spin interaction, and in the limit of unit filling, it's a constant of motion and can be ignored. The term proportional to $V$ is the density-density interaction and is a constant for molecules pinned in a deep lattice. The experiments described in this chapter are performed at zero electric field, so $J_z = W = V = 0$, and the Hamiltonian simplifies to a long-range XY Hamiltonian:

$$H = \frac{1}{2}\sum_{i\neq j} V_{dd}(\mathbf{r_i} - \mathbf{r_j})\left(\frac{J_\perp}{2}\left(\hat{S}_i^+\hat{S}_j^- + \hat{S}_i^-\hat{S}_j^+\right)\right). \tag{4.38}$$

One additional complication in our experiment is that there is a site-to-site differential energy shift due to a residual inhomogeneous light shift arising from the molecules' anisotropic polarizability. This will be discussed more in the next section but it gives rise to an additional term in the

Hamiltonian $\sum_i h_i \hat{S}_i^z$. These site-to-site energy shifts suppress the exchange when $|h_i - h_j| > J_\perp V_{dd}(\mathbf{r_i} - \mathbf{r_j})$. Thus, the Hamiltonian we will study in this chapter is:

$$H = \frac{1}{2}\sum_{i \neq j} V_{dd}(\mathbf{r_i} - \mathbf{r_j}) \left( \frac{J_\perp}{2} \left( \hat{S}_i^+ \hat{S}_j^- + \hat{S}_i^- \hat{S}_j^+ \right) \right) + \sum_i h_i \hat{S}_i^z. \tag{4.39}$$

Since we're working at zero electric field all the tildes on the states will be dropped, and we will focus our attention on spin-1/2 systems formed from the $\{|0,0\rangle, |1,-1\rangle\}$ and $\{|0,0\rangle, |1,0\rangle\}$ manifolds.

The rate at which an isolated pair of molecules would swap from $|\uparrow_i\downarrow_j\rangle$ to $|\downarrow_i\uparrow_j\rangle$ (the exchange rate), is $\frac{J_\perp}{h} V_{dd}(\mathbf{r_i} - \mathbf{r_j})$. In the experiments of Refs. [84, 85], we measured the contrast of a Ramsey fringe, which depends on $\langle S_x \rangle$ and $\langle S_y \rangle$. These expectation values oscillate at a frequency of $\frac{J_\perp}{2h} V_{dd}(\mathbf{r_i} - \mathbf{r_j})$ [132]. This is because the populations in a spin-1/2 system undergoing coherent evolution (such as Rabi flopping) oscillate twice as fast as the wavefunction. For example, consider Rabi flopping at frequency $\Omega$. If the initial state is $|\downarrow\rangle$, then the state after a time $t$ is

$$\psi(t) = \cos\left(\frac{\Omega t}{2}\right)|\downarrow\rangle + \sin\left(\frac{\Omega t}{2}\right)|\uparrow\rangle. \tag{4.40}$$

After a $2\pi$ pulse, $\psi(2\pi/\Omega) = -|\downarrow\rangle$, and $|\langle\downarrow|\psi(2\pi/\Omega)\rangle|^2 = 1$, so the state has a minus sign but the population is the same. Thus, the population is periodic with a period of $2\pi$ but the state itself (which is what $\langle S_x \rangle$ depends on) is periodic with a period of $4\pi$.

The $V_{dd}$ factor gives the dependence on the distance between molecules and their orientation relative to the quantization axis, which for the experiments in this chapter is set by a magnetic field in the horizontal plane (see Fig. 4.4a). The maximum value of $\frac{J_\perp}{2h} V_{dd}(\mathbf{r_i} - \mathbf{r_j})$ is about 52 Hz for the $\{|0,0\rangle, |1,-1\rangle\}$ manifold [84] and 104 Hz for the $\{|0,0\rangle, |1,0\rangle\}$ manifold [85] (assuming a 532 nm lattice spacing). Hence, this is the dominant frequency component observed in the contrast decay. Fig. 4.4b shows the calculated spectrum of the contrast decay for the $\{|0,0\rangle, |1,-1\rangle\}$ manifold, which shows three pronounced oscillation frequencies on top of a broad, structured background [85]. Certain couplings are more pronounced: in particular, the head-to-tail orientation has strength -1 (with respect to the maximum possible coupling), and two couplings in the horizontal plane have strengths of $1/2$ and $1/\sqrt{2}$.

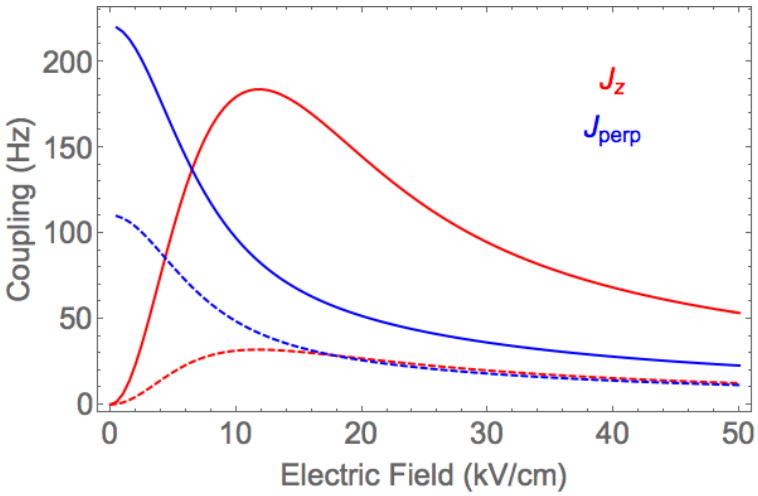


Figure 4.3: Magnitude of the coupling constants for the $\{|\tilde{0},0\rangle, |\tilde{1},0\rangle\}$ manifold (solid) and $\{|\tilde{0},0\rangle, |\tilde{1},\pm1\rangle\}$ manifolds (dashed), $J_z/h$ (red) and $J_\perp/h$ (blue), for a 532 nm lattice spacing. For these choices of states, we get the largest couplings at zero electric field. The lowest 20 rotational states were included in the calculation.

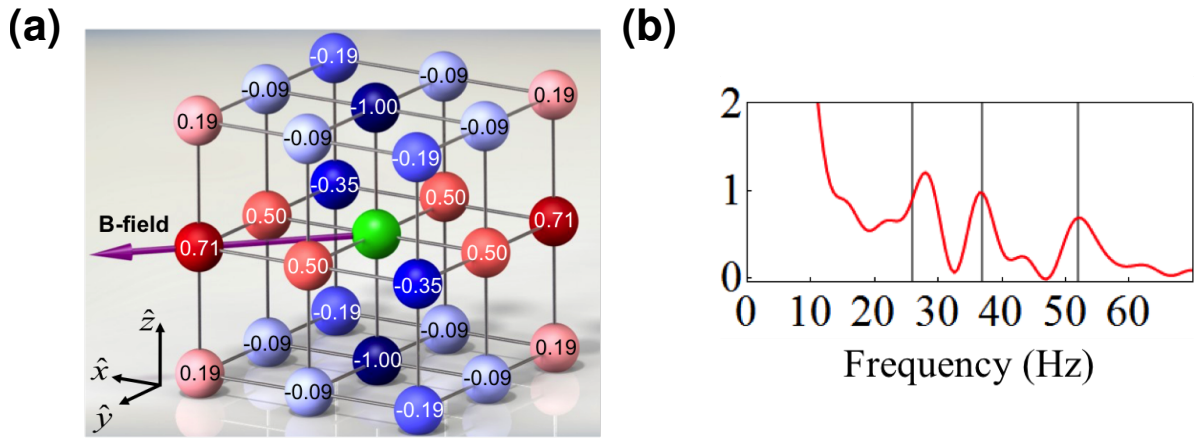


Figure 4.4: (a) Couplings between the molecule in green and its neighbors, normalized to the strongest coupling, which occurs for nearest neighbors along $\hat{z}$. There are three relatively well-pronounced couplings of magnitude 1, $1/\sqrt{2}$, and 0.5. Figure reproduced from Ref. [84]. (b) Calculated interaction spectrum for the $\{|0,0\rangle, |1,-1\rangle\}$ manifold. Pronounced interactions occur around 52 Hz, 37 Hz, and 26 Hz, corresponding to the interactions of magnitude 1, $1/\sqrt{2}$, and 0.5 in (a). Figure reproduced from from Ref. [85].

## 4.2 Anisotropic polarizability and differential light shifts

As I discussed in the last section, it takes a very large DC electric field to substantially polarize the molecules. Coupling the rotational states with an AC electric field is much more selective than with a DC field. Furthermore, for our choice of spin-1/2 system, we actually get the strongest interactions at zero electric field with just the spin-exchange terms. However, there were several issues we needed to address before we could actually see the spin-exchange interactions in the experiment. In particular, the anisotropic polarizability of the molecules creates a spread in transition frequencies between $|\uparrow\rangle$ and $|\downarrow\rangle$ across the cloud and leads to a rapid dephasing when probing the rotational coherence [91].

A well-established technique in precision spectroscopy is to match the shape of the trapping potentials for the two states of interest. For neutral atoms, it's usually possible to find some wavelength of light for which the polarizabilities of the two states are equal. A well-known example is the "magic wavelength" optical lattice for optical lattice clocks [133]. The polarizability of diatomic polar molecules is more complicated than atoms because the molecules can be polarized about different axes (in particular, parallel and perpendicular to the internuclear axis) [91]. For molecular states where the electron distribution is not spherically symmetric, the polarizability parallel and perpendicular to the molecular quantization axis can be significantly different. Although it would be possible, in principle, to find a magic wavelength for molecules, the large number of rovibrational states in the excited molecular potential make it difficult to find a suitable wavelength where the rate of off-resonant light scattering is tolerable [91]. However, there exist magic values of the electric field (for KRb this is about 12 kV/cm [134]), as well as magic angles [91], where the angle between the light polarization and the quantization axis is tuned to match the polarizabilities.

Ultimately we chose to find the magic angle, since a magic angle should exist even at zero electric field. Fig. 4.5 shows measurements of the real part of the polarizability at 1064 nm for the $|0,0\rangle$ state, as well as for the three $N = 1$ states [91]. For the experiments discussed in this chapter, we use both the $\{|0,0\rangle, |1,0\rangle\}$ manifolds and the $\{|0,0\rangle, |1,-1\rangle\}$ manifolds. The crossings

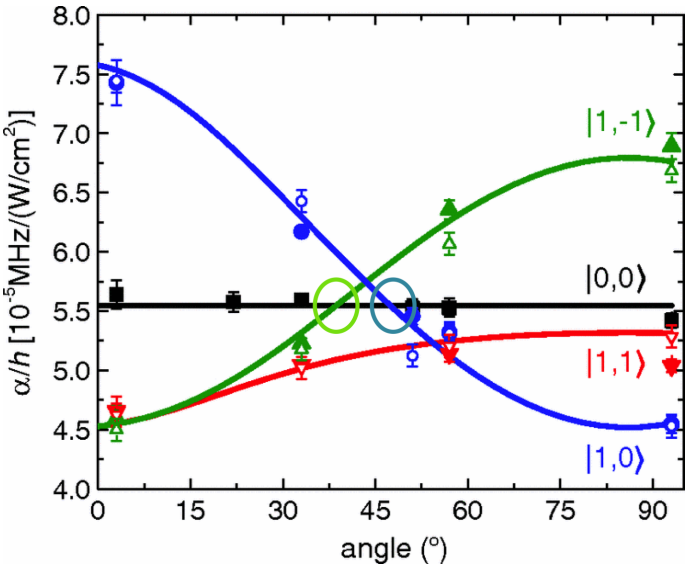


Figure 4.5: Real part of the polarizability at 1064 nm for the $|0,0\rangle$ (black), $|1,0\rangle$ (blue), $|1,1\rangle$ (red), and $|1,-1\rangle$ (green) states. This was measured in a 1D vertical lattice with peak intensity of 2.3 kW/cm$^2$, corresponding to a lattice depth of about 92 $E_R$ for the $|0,0\rangle$ molecules. Magic angles exist for the combinations $\{|0,0\rangle, |1,0\rangle\}$ and $\{|0,0\rangle, |1,-1\rangle\}$, and are indicated by the circles. Figure reproduced from Ref. [91].

for both states are indicated by the circles. Since the polarizabilities of the $|0,0\rangle$ and $|1,1\rangle$ states never cross, we chose to not use the $\{|0,0\rangle, |1,1\rangle\}$ manifold. In addition to depending on the angle between the light polarization and the quantization axis, the polarizability also depends on light intensity. The energies of the three $N = 1$ states can be found by diagonalizing the following $3 \times 3$ Hamiltonian:

$$H = \begin{array}{c} \begin{array}{ccc} |1,0\rangle & |1,-1\rangle & |1,1\rangle \end{array} \\ \begin{pmatrix} -\alpha_{11}I + \epsilon_1 & -\alpha_{12}I & -\alpha_{13}I \\ -\alpha_{12}I & -\alpha_{22}I + \epsilon_2 & -\alpha_{23}I \\ -\alpha_{13}I & -\alpha_{23}I & -\alpha_{33}I + \epsilon_3 \end{pmatrix} \end{array}. \tag{4.41}$$

The coefficients $\alpha_{ij}$ depend on the polarizabilities parallel to ($\alpha_\parallel$) and perpendicular to ($\alpha_\perp$) the quantization axis and on the angle $\theta$ between the quantization axis and the light polarization.

$$\alpha_{11} = \frac{\alpha_\parallel + 4\alpha_\perp}{5}\sin^2\theta + \frac{3\alpha_\parallel + 2\alpha_\perp}{5}\cos^2\theta. \tag{4.42}$$

$$\alpha_{22} = \alpha_{33} = \frac{2\alpha_\parallel + 3\alpha_\perp}{5}\sin^2\theta + \frac{\alpha_\parallel + 4\alpha_\perp}{5}\cos^2\theta. \tag{4.43}$$

$$\alpha_{12} = -\alpha_{13} = \sqrt{2}\frac{\alpha_\parallel - \alpha_\perp}{5}\sin\theta\cos\theta. \tag{4.44}$$

$$\alpha_{23} = \frac{1}{5}(\alpha_\perp - \alpha_\parallel)\sin^2\theta. \tag{4.45}$$

By doing a global fit to the data shown in Fig. 4.5, we extracted $\alpha_\parallel/h = 10.0(3)\times10^{-5}$ MHz/(W/cm$^2$) and $\alpha_\parallel/h = 3.3(1) \times 10^{-5}$ MHz/(W/cm$^2$).

A difference in polarizability between the two states also leads to a difference in the transition frequency compared to the bare transition frequency at zero light intensity. This differential light shift is plotted in Fig. 4.6a for light polarizations of $\{45°, -45°, 45°\}$ with respect to the magnetic field $\hat{B}$ (the quantization axis) along the $\hat{x}$, $\hat{y}$, and $\hat{z}$ directions (coordinate system defined in Fig. 4.4a). This is a convenient choice given that the horizontal lattice beams intersect the cell at roughly 45°, so if they're horizontally polarized then the polarizations already make an angle of 45° with respect to the magnetic field. A global differential light shift does not really cause a problem,

since a global uniform shift could be accounted for by simply shifting the microwave frequency. Instead, the problem arises because the lattice is formed from Gaussian laser beams, such that the molecules have a spread of positions, leading to a spread of differential light shifts.

We see that the differential light shift is quite small for the $\{|0,0\rangle, |1,-1\rangle\}$ manifold for lattice depths below 40 $E_R$; thus, we chose to do the initial experiments with this state. When using the $|1,0\rangle$ state, we had to put half waveplates before and after the cell for the horizontal lattices to get the linear polarizations correct (since for the $|1,0\rangle$ state, the magic angle is at about 52° [91]).

Another consequence of this inhomogeneous light shift is that it gives a site-to-site energy shift. In Ref. [84], we estimated the average site-to-site shift to be about 6 Hz (for nearest neighbors) by finding the standard deviation of differential light shifts across the cloud and dividing it by the characteristic size of the cloud. This means that the exchange interaction is suppressed over a few sites (see Fig. 4.7).

## 4.3 Simple Ramsey sequence and some technical issues

Ramsey spectroscopy is a powerful tool for studying decoherence in quantum systems. We're interested in using it to probe dipolar interactions in our experiment. In its simplest implementation, Ramsey spectroscopy consists of two $\pi/2$ pulses separated by some free evolution time $T$, as shown in Fig. 4.8a. We typically use microwave pulses that are resonant with the rotational transition. The experiment begins with all of the molecules in $|\downarrow\rangle$, which is the south pole of the Bloch sphere. The first $\pi/2$ pulse rotates the Bloch vector about the $\hat{y}$ axis from the south pole to the equator, which puts every molecule in a coherent superposition $(|\uparrow\rangle + |\downarrow\rangle)/\sqrt{2}$. After a free evolution time $T$, we apply another $\pi/2$ pulse with a phase $\phi$ relative to the first pulse, which rotates the Bloch vector about the axis $\hat{n} = \cos\phi\,\hat{y} + \sin\phi\,\hat{x}$. We then measure the number of molecules in $|\downarrow\rangle$ by doing STIRAP from the ground-state back to weakly bound Feshbach molecules, followed by our normal imaging of Feshbach molecules. By scanning $\phi$ at a fixed $T$, we obtain a fringe as shown in Fig. 4.8c. We fit the fringe to $\frac{N_{\rm tot}}{2}\big(1 + C\cos(\phi + \phi_0)\big)$, where $N_{\rm tot}$ is the total number of molecules and $C$ is the contrast ($0 \le C \le 1$). $\phi_0$ should be equal to $\pi$ if the microwave frequency

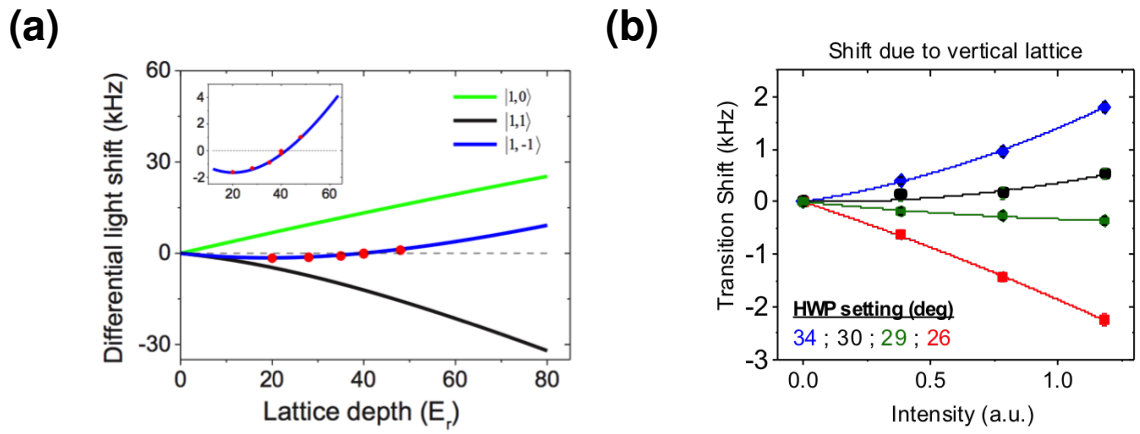


Figure 4.6: (a) The differential light shift for the three $N = 1$ states relative to the $N = 0$ state, for lattice polarizations of $\{45°, -45°, 45°\}$ with respect to the magnetic field $\hat{B}$ along the $\hat{x}$, $\hat{y}$, and $\hat{z}$ directions. For this beam configuration, the $|1, -1\rangle$ has the smallest differential light shift. This motivated us to use the $\{|0, 0\rangle, |1, -1\rangle\}$ manifold as our spin-1/2 system for the initial experiments in Ref. [84]. Note that the lattice depth is expressed in units of the recoil energy for the $|0, 0\rangle$ state. Figure reproduced from Ref. [84]. (b) Measured frequency shifts vs. lattice strength for different polarizations of the vertical lattice for the $|0, 0\rangle \rightarrow |1, 0\rangle$ transition. The angle of a half-waveplate before the cell was scanned, so the total range here corresponds to scanning the polarization by 16°. Here we could achieve even smaller differential light shifts, which led to longer Ramsey coherence times (see Fig. 4.11b).

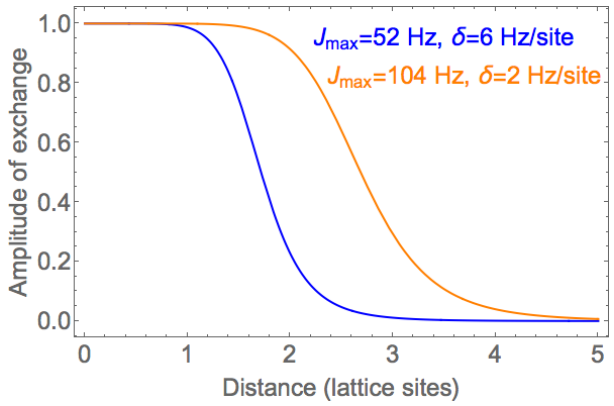


Figure 4.7: Because of the site-to-site energy offset, the exchange interaction is suppressed for molecules separated by more than one lattice site. Similar to off-resonant Rabi flopping, if the bare exchange rate is $J$ and the detuning is $\delta$, then the amplitude of the actual exchange is $\frac{J^2}{J^2+\delta^2}$. The plot shows this amplitude vs. distance between molecules, assuming $J = J_{\max}/|\Delta r|^3$ and $\delta = k|\Delta r|$, where $k$ is the shift per site, and $\Delta r$ is the distance between two molecules (in lattice sites). Two cases are plotted: $J_{\max} = 52$ Hz and $\delta = 6$ Hz/site (blue), relevant for the work in Ref. [84] and $J_{\max} = 104$ Hz and $\delta = 2$ Hz/site (orange), relevant for the work in Ref. [85], where we used the $\{|0,0\rangle, |1,0\rangle\}$ manifold. The 2 Hz is an estimate based on the fact that the coherence times could be $\sim 3$ times longer for the $\{|0,0\rangle, |1,0\rangle\}$ manifold.

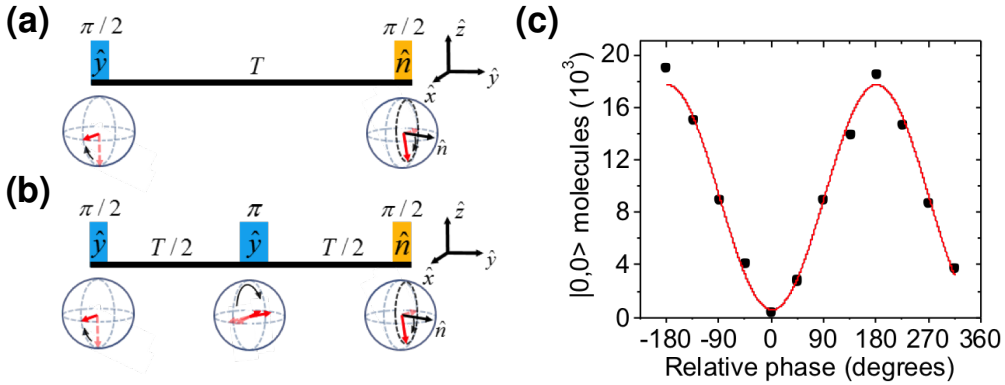


Figure 4.8: Timing diagrams and Bloch vector representation for a simple Ramsey sequence (a) and a spin echo sequence (b). Figure reproduced from Ref. [84]. (c) Typical Ramsey fringe using the DDS to program the phase offset of the final pulse. After the initial $\pi/2$ pulse, we wait a time $T$. We then apply a phase-shifted $\pi/2$ pulse and measure the number of molecules in $|\downarrow\rangle \equiv |0,0\rangle$ vs. the phase of the final pulse.

is exactly on resonance. Measuring the contrast of this fringe then determines the amount of spin coherence left in the system after time $T$. The contrast can be less than 1 for a variety of reasons, including single-particle dephasing and interaction effects.

Before getting to the experimental results, it's useful to discuss a few technical issues. First, we would like to understand the role of the inhomogeneous light shift described in the previous section. This will lead us to constraints on the pulse strengths that we should use. A quick calculation using the expected inhomogeneous light shifts tells us the coherence times we should expect for the simple two-pulse Ramsey sequence. Finally, I discuss the system we use to generate microwave pulses with programmable phase delay and discuss the prospects for imaging both spin states.

### 4.3.1 Effect of the inhomogeneous light shift

Several constraints determine the Rabi frequency $\Omega$ we should use (the time for a $\pi$ pulse is $\frac{\pi}{\Omega}$). For these experiments, we used square pulses, but it's worth noting that many groups use pulse shaping to mitigate some of the following issues. First, there is a finite energy splitting between the three different $N = 1$ substates, and we want to isolate one of them as our $|\uparrow\rangle$ of a spin-1/2 system. Let's call the smallest splitting $\Delta$. Clearly $\Omega$ must be less than $\Delta$ so we avoid populating other states. However, we need the $\pi$ pulse to be broad enough spectrally in order to overcome any differential light shifts in the sample, which cause an energy spread $\sigma$ and set a lower limit on the Rabi frequency.

The relationship between the energy spread $\sigma$ and the Ramsey coherence time $\tau_c$ depends on the shape of the distribution of frequency deviations $\delta$, $f(\delta)$. Let's assume that the frequency deviations have a Gaussian distribution, so $f(\delta) = e^{-\delta^2/(2\sigma^2)}$. Then taking the Fourier transform, $F(t) = \sigma e^{-\sigma^2 t^2/2} = \sigma e^{-t^2/(2\tau_c^2)}$, with the Ramsey coherence time $\tau_c = \frac{1}{\sigma}$. Another way to get the relationship between $\sigma$ and $\tau_c$ is to actually calculate the Ramsey fringe as a function of time. To do this, all we need to do is to calculate the probability that each particle is in $|\downarrow\rangle$ or $|\uparrow\rangle$ at the end of the sequence as a function of the dark time $T$ and the phase $\phi$ of the final pulse, and then

average over all of the particles. The Rabi frequency is $\Omega$. For a particle with frequency deviation $\delta_i$, there is an effective Rabi frequency $\Omega_{\text{eff},i} = \sqrt{\Omega^2 + \delta_i^2}$, and thus the pulses are not exactly $\pi/2$ pulses. As a function of the phase $\phi$ of the final pulse,

$$P(T,\phi) = \frac{\Omega^2}{\Omega_{\text{eff},i}^2} \sin^2\left(\frac{\pi}{4}\frac{\Omega_{\text{eff},i}}{\Omega}\right)\Big(1 + \cos(\delta_i T + \phi)\Big), \tag{4.46}$$

where $P = 0(1)$ corresponds to $|\downarrow\rangle(|\uparrow\rangle)$ and the first two factors account for the tipping angle not being exactly $\pi/2$. The contrast is the amplitude of the average of all of these oscillations, which is

$$C(T,\phi) = \left\langle \frac{\Omega^2}{\Omega_{\text{eff},i}^2} \sin^2\left(\frac{\pi}{4}\frac{\Omega_{\text{eff},i}}{\Omega}\right)\Big(1 + \cos(\delta_i T + \phi)\Big)\right\rangle. \tag{4.47}$$

Going through this prescription, one finds that the contrast has a Gaussian decay with $\tau_c \approx \frac{1}{\sigma}$ (assuming $\Omega \gg \sigma$). If $f(\delta)$ were Lorentzian, then the decay would be approximately exponential.

Thus, we require

$$\frac{1}{\tau_c} \ll \Omega \ll \Delta, \tag{4.48}$$

where all frequencies are angular frequencies. This tells us there's some minimum tolerable Ramsey coherence time; otherwise, we wouldn't be able to satisfy both inequalities in Eq. 4.48. For the $|1,-1\rangle$ state, $\Delta \approx 2\pi \times 60$ kHz, and the typical energy spreads are a few hundred Hz, calculated by converting the size of the cloud to a distribution of intensities, and then to a distribution of frequencies. This leads to Ramsey coherence times a little less than 1 ms. In practice, Rabi frequencies around a few kHz work well and allow us to achieve $\pi$ pulse fidelities $> 99\%$. For most of the work in Ref. [84], we use $\pi$ pulses of $\sim 180\,\mu$s duration, corresponding to a Rabi frequency of $\sim 2\pi \times 2.6$ kHz. Experimentally, we examined the robustness of the experiment to having a larger inhomogeneous light shift (which corresponds to having a shorter Ramsey coherence time) and to imperfect pulses, and we found the dynamics to be rather insensitive to such imperfections (Section 4.4.2).

### 4.3.2 Imaging both spin states

To read out the spin evolution after the Ramsey sequence, we need the excitation fraction, $N_\uparrow/N_{\text{tot}}$ or $N_\downarrow/N_{\text{tot}}$, where $N_{\text{tot}} = N_\uparrow + N_\downarrow$ is the total number. Normally, we measure the number

of $|\downarrow\rangle$ molecules, $N_\downarrow$, at the end of the sequence. Assuming that the total molecule number is stable, this gives a measurement of the excitation fraction. Normalization via the measurement of the total molecule number would allow us to remove technical noise, but requires that we image both spin states. To achieve this, we STIRAP back the $N = 0$ molecules, image the resulting atoms, do a $\pi$ pulse to transfer the $N = 1$ molecules to $N = 0$, and then repeat STIRAP back and imaging. The only problem with this is that during the first STIRAP pulse, the down leg laser is on for about 5 $\mu$s, and this is enough to kill about 20-25% of the molecules in the $N = 1$ state (see Fig. 4.9), presumably by exciting molecules in the $N = 1$ state to an excited electronic and rotational state. The fraction $\eta$ of $N = 1$ molecules that remain can be calibrated, as shown in Fig. 4.9b. However, we never consistently saw a significant improvement in the SNR of the Ramsey fringes using this technique and thus we ended up not using it. This could be because the calibration itself requires many shots to get a small uncertainty and any drifts in laser power could change $\eta$. In the future, we may be able to use a more spectrally selective STIRAP transfer (with improved coherence) to achieve this goal.

### 4.3.3 Creating phase stable microwaves

It's desirable to have precise and fast control of the microwave phase, especially for more complex pulse sequences. For the simple Ramsey and spin echo sequences, we only need two phases, since all we care about is the phase of the final pulse relative to the initial pulse(s). To accomplish this, we initially used two Agilent signal generators (which were both referenced to the same 10 MHz oscillator), and changed the phase of one of them by hand. In this scheme, one of the generators was used for the first pulse(s) and the other was used for the final pulse. There may have been a more efficient way to do this, but ultimately we decided to pursue other options. To do more complicated sequences such as the WAHUHA sequence (section 4.4.1), we need four distinct phases and we need to be able to switch between them relatively quickly (less than 1 ms).

Initially we tried an analog solution, which was an analog phase shifter from Mini Circuits (part JSPHS-2484+). A control voltage shifts the phase, but also affects the amplitude. To account

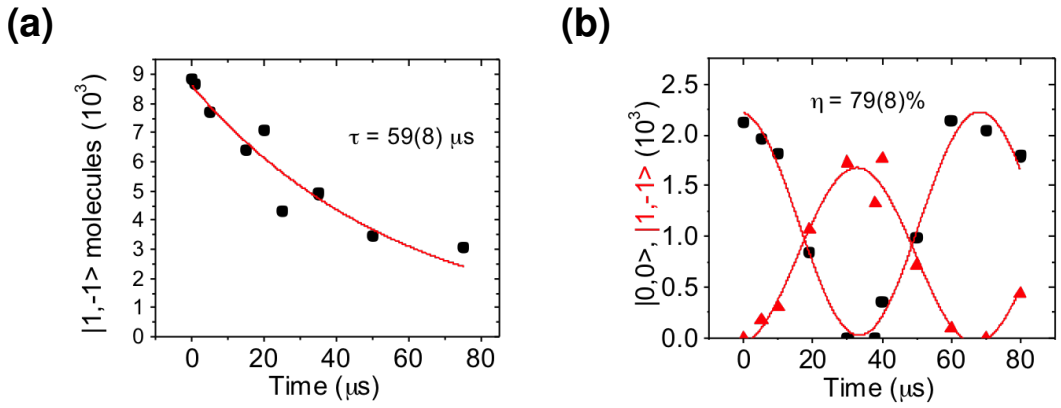


Figure 4.9: Imaging both spin states. We first do STIRAP back and image the molecules that were in $|\downarrow\rangle = |0,0\rangle$. Next, we apply a $\pi$ pulse, which transfers $|\uparrow\rangle$ to $|\downarrow\rangle$. Then we STIRAP back and image a second time. The only problem with this is that there's some loss of the $N = 1$ molecules during the imaging of the $N = 0$ molecules. (a) The loss of $|\uparrow\rangle = |1,-1\rangle$ molecules vs. pulse time of the down leg laser. (b) Starting with all molecules in $|0,0\rangle$, we perform a Rabi experiment. This allows us to normalize this loss by fitting both components to sine functions. For this dataset, the fraction of $|1,-1\rangle$ molecules lost is 21(8)%. More data would be required to reduce the error.

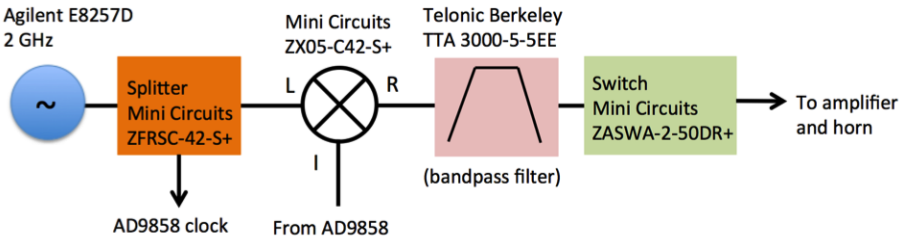


Figure 4.10: System used to generate microwaves with arbitrary phase control. An Agilent E8257D signal generator, which is referenced to a 10 MHz Wenzel oscillator, provides a 2 GHz tone. Half of the 2 GHz signal is sent to the DDS, where it is frequency divided by 2 and then used as the DDS clock; the other half is used as the local oscillator for the mixer. We program an AD9858 to put out an RF frequency of around 228 MHz. This goes to the IF port of the mixer. The output is $\sim$ 2.228 GHz, and we send this through a bandpass filter to get rid of the carrier and other unwanted frequency components before amplifying the signal and sending it to the horn. The mixing process maps the phase of the IF (which we can control with 14 bits of resolution) directly onto the phase of the microwave signal.

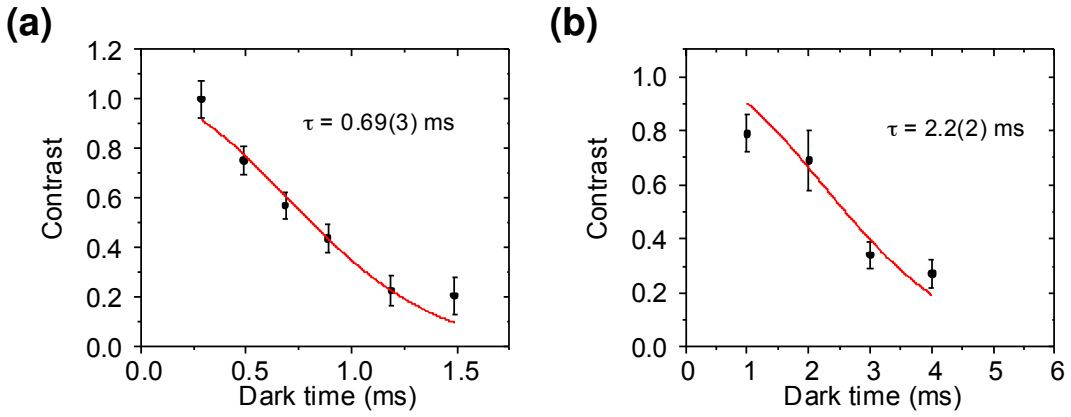


Figure 4.11: Typical Ramsey contrast decay for $|0,0\rangle \rightarrow |1,-1\rangle$ (a) and $|0,0\rangle \rightarrow |1,0\rangle$ transitions (b). We could achieve smaller inhomogeneous light shifts for the $|0,0\rangle \rightarrow |1,0\rangle$ transition, resulting in a longer Ramsey coherence time. The fitting function is $e^{-t^2/(2\tau^2)}$, which is the expected form if the energy spread has a Gaussian distribution.

for the amplitude variation as the phase changed, we used different pulse times depending on the phase we wanted. Ultimately, this was not flexible and efficient, so we decided a digital solution was better. Since it's hard to find an inexpensive DDS operating at 2.3 GHz (for this the clock would need to be more than 4.5 GHz), we decided to use a lower frequency DDS (at around 230 MHz) and mix it with a 2 GHz local oscillator to get the required frequency. We use an AD9858 from Analog devices, which has a maximum clock frequency of 2 GHz. The device can be programmed with four phase-frequency profiles, and it's feasible to switch between these profiles in $\ll 1\,\mu$s using two digital inputs. We use a 2 GHz signal from an Agilent synthesizer (E8257D) as both the local oscillator and also to clock the DDS (it's divided by 2 in the DDS so we end up with a 1 GHz clock). The mixer maps the phase of the RF directly onto the phase of the microwaves. After the mixer, we use a bandpass filter to filter out unwanted frequency components. A splitter, amplifier, and horn complete the setup, which is shown schematically in Fig. 4.10.

### 4.3.4 Experimentally measured Ramsey decays

Experimentally measured Ramsey decay curves are shown in Fig. 4.11. The data for the $|0,0\rangle \rightarrow |1,-1\rangle$ transition (a) was taken in a 40 $E_R$ deep lattice with the same lattice polarization configuration as in Fig. 4.6a. We find a Ramsey coherence time of around 700 $\mu$s. For the $|0,0\rangle \rightarrow |1,0\rangle$ transition (b), we can achieve a smaller differential AC Stark shift (Fig. 4.6b), and as a result the coherence time is longer (more than 2 ms). For these experiments the lattice depth was typically 20 $E_R$, although we could also achieve similar coherence times in deeper lattices. However, all of these coherence times are far too short to observe dipolar interactions, and we need to incorporate a spin echo to mitigate the single-particle dephasing.

## 4.4 Initial experiments in the $\{|0,0\rangle, |1,-1\rangle\}$ manifold

For the $|0,0\rangle \rightarrow |1,-1\rangle$ transition, the transition dipole moment $d_{\downarrow\uparrow}$ is $0.98\times\mathcal{D}/\sqrt{3}$, where the factor of 0.98 reflects an estimated 2% admixture of another hyperfine state. This gives $|J_\perp/(2h)| =$ 52 Hz, which implies that the dynamics occur on the tens of ms timescale. As we saw in the previous section, the Ramsey coherence time is limited by the inhomogenous light shift to less than 1 ms. This inhomogeneous light shift causes the Bloch vector for each molecule to precess at a slightly different rate. However, this rate is determined only by where the molecule sits and in principle it doesn't change throughout the experiment. By applying a spin echo pulse halfway through the free evolution (Fig. 4.8b) we can reverse this precession so that after a total time $T$, every molecule has no net precession from the inhomogeneous light shift. However, the spin echo has no impact on the dipolar interactions, and ideally any remaining dephasing should be due to interactions.

Typical contrast decay curves with the spin echo pulse are shown in Fig. 4.12. One of the most striking features of these curves is the oscillations on top of an overall decay. We attribute both the decay and the oscillations to dipolar interactions. We fit the contrast decay curves to an empirical function

$$C(T) = Ae^{-T/\tau} + B\cos^2(\pi f T) \tag{4.49}$$

to extract both a coherence time $\tau$ and oscillation frequency $f$. Low lattice fillings and the long-range interactions in the lattice both give rise to a spread of interaction energies, which lead to dephasing and loss of contrast. At very dilute fillings, the interaction energy spectrum can have a strong contribution from the strongest nearest-neighbor interaction (the vertically oriented interaction in Fig. 4.4). The oscillations can then arise from the beating of this particular frequency with the contribution from molecules with much smaller energy shifts.

One of the signatures of an interaction effect is the dependence on density. We reduce the density without changing the overall shape of the molecular distribution by holding the molecules in the lattice for a few seconds to allow molecules to be removed by single-particle loss [72]. The reduced density is proportional to the number of molecules remaining. The two curves shown in Fig. 4.12a show that the oscillation frequency is basically the same for different densities (also see Fig. 4.12c), but the coherence time becomes shorter for higher densities. We expect $\tau \propto 1/N$ because

$$\tau \propto \frac{1}{\langle E_{\mathrm{int}} \rangle} \propto \frac{\bar{R}^3}{J_\perp} \propto \frac{1}{J_\perp N}, \tag{4.50}$$

where $\bar{R}$ is the average interparticle spacing and the density $\rho = \bar{R}^{-3} \propto N$, given the way we reduce the density. Fig. 4.12b shows the coherence time vs. $N$ for many datasets and clearly shows a $1/N$ dependence.

### 4.4.1 WAHUHA pulse sequence

The spin-echo sequence, as well as more complicated pulse sequences, can be used for dynamical decoupling, which can remove dephasing and extend coherence times [135, 136, 137, 138]. One particular pulse sequence, named WAHUHA after its inventors, disentangles the dipole-dipole interactions of two particles [139]. The timing diagram is shown in Fig. 4.13a. The WAHUHA sequence swaps between eigenstates of the dipolar Hamiltonian, allowing for subsequent rephasing after a total dark time $T$. When we apply the multi-pulse sequence, the oscillations in the contrast are suppressed and the data fits well to a simple exponential decay (Fig. 4.13b). The inset shows the difference between the black points (WAHUHA sequence) and red points (spin echo), which

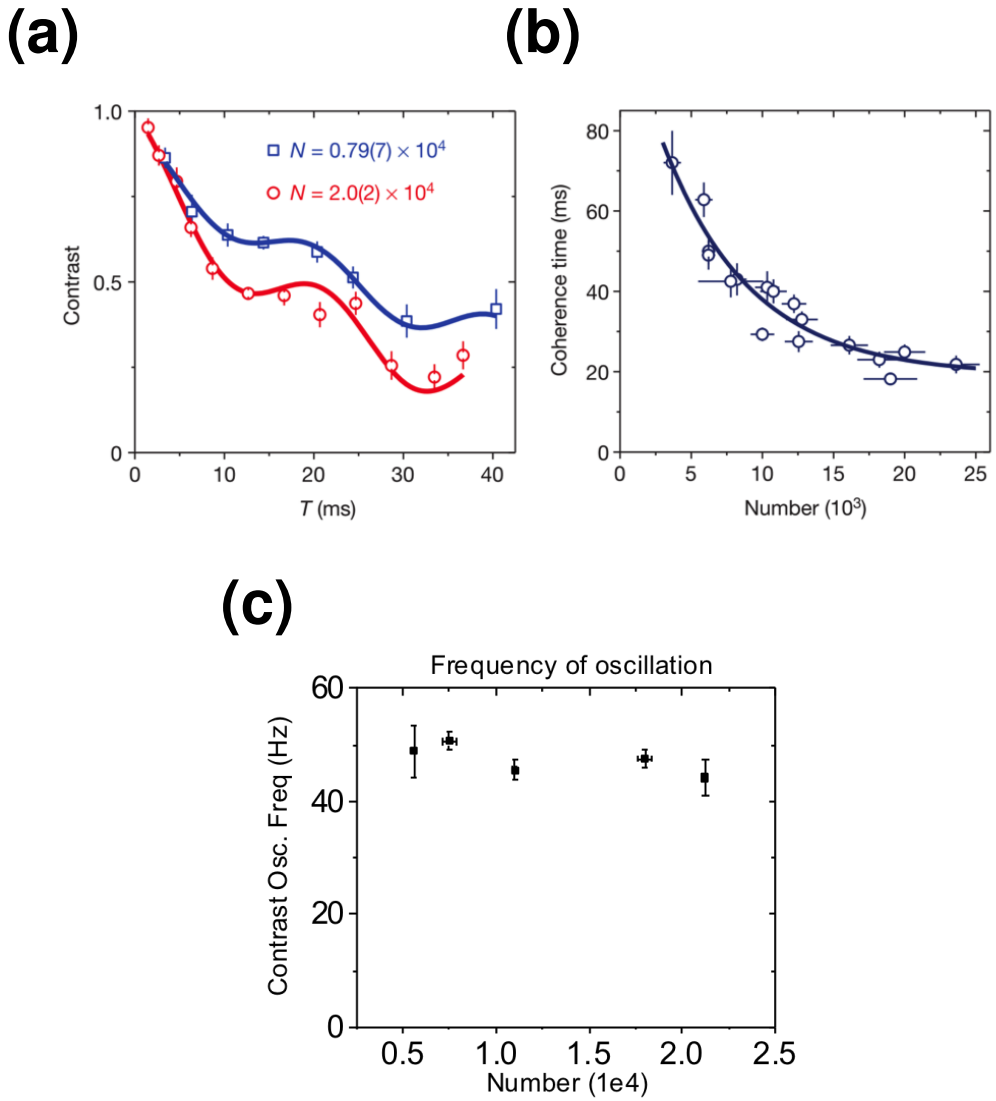


Figure 4.12: (a) Two contrast decay curves corresponding to different initial densities. The fit curves are Eq. 4.49. (b) All of the experimentally measured coherence times for a spin echo experiment on the $|0,0\rangle \rightarrow |1,-1\rangle$ transition. The fit is $C + A/N$, with $A$ and $C$ fit parameters. Figures reproduced from Ref. [84]. (c) Looking at typical datasets corresponding to different densities, we see the frequency obtained from fitting to Eq. 4.49 doesn't significantly change with density.

clearly shows that the oscillations are suppressed with the multi-pulse sequence.

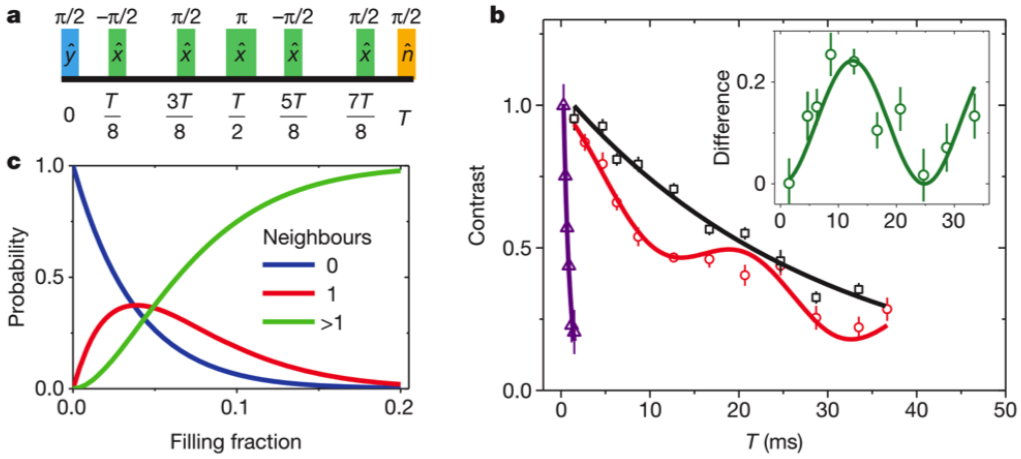


Figure 4.13: WAHUHA sequence: (a) The pulse sequence used for WAHUHA. The pulses about $\pm\hat{x}$ have a relative phase of $\pm 90°$ with respect to the initial pulse. (b) The contrast decay for a two-pulse Ramsey sequence (purple, same data as in Fig. 4.11a), spin echo (red), and WAHUHA (black). The inset (green points and curve) shows the difference between the red and black curves and highlights that the multi-pulse sequence largely suppresses the oscillations in the red data. (c) Number of nearest neighbors in the lattice vs. filling fraction. For fillings $< 0.05$, most of the molecules have 0 or 1 nearest neighbors. Figure reproduced from Ref. [84].

To understand how WAHUHA works, we examine the wavefunction for two molecules after each of the pulses. Initially, both molecules are in $|\downarrow\rangle$. The $\pi/2$ pulse puts each of them in a superposition of $|\uparrow\rangle$ and $|\downarrow\rangle$.

$$\psi(0) = \frac{1}{\sqrt{2}}(|\uparrow\rangle + |\downarrow\rangle) \otimes \frac{1}{\sqrt{2}}(|\uparrow\rangle + |\downarrow\rangle) = \frac{1}{2}(|\uparrow\uparrow\rangle + |\downarrow\downarrow\rangle + |\uparrow\downarrow\rangle + |\downarrow\uparrow\rangle). \tag{4.51}$$

The states $|\uparrow\uparrow\rangle$ and $|\downarrow\downarrow\rangle$ don't interact via the XY Hamiltonian, while $|\uparrow\downarrow\rangle$ and $|\downarrow\uparrow\rangle$ do. The three triplet states $|\uparrow\uparrow\rangle, |\downarrow\downarrow\rangle$, and $\frac{1}{\sqrt{2}}(|\uparrow\downarrow\rangle + |\downarrow\uparrow\rangle)$ are eigenstates with energy 0, 0, and $J_\perp/2$ respectively. A $(\pi/2)_x$ pulse converts between $|N\rangle = \frac{1}{\sqrt{2}}(|\uparrow\uparrow\rangle + |\downarrow\downarrow\rangle)$ and $|I\rangle = \frac{1}{\sqrt{2}}(|\uparrow\downarrow\rangle + |\downarrow\uparrow\rangle)$, so it basically acts as an echo between the noninteracting and interacting states. Thus we can rewrite Eq. 4.51 as

$$\psi(0) = \frac{1}{\sqrt{2}}(|N\rangle + |I\rangle). \tag{4.52}$$

After the first $T/8$ free evolution, $|N\rangle$ acquires no phase, while $|I\rangle$ acquires a phase $e^{-iJ_\perp T/(16\hbar)}$.

The first $-(\pi/2)_x$ pulse swaps this phase to $|N\rangle$ (there's also an additional factor of $-i$). Thus, the state after the second pulse is

$$\psi\left(\frac{T^+}{8}\right) = \frac{-i}{\sqrt{2}}\left(e^{-iJ_\perp T/(16\hbar)}|N\rangle + |I\rangle\right). \tag{4.53}$$

Immediately before the third pulse, the state is

$$\psi\left(\frac{3T^-}{8}\right) = \frac{-i}{\sqrt{2}}\left(e^{-iJ_\perp T/(16\hbar)}|N\rangle + |I\rangle e^{-iJ_\perp T/(8\hbar)}\right). \tag{4.54}$$

The $(\pi/2)_x$ swaps the phases again so

$$\psi\left(\frac{3T^+}{8}\right) = \frac{1}{\sqrt{2}}\left(e^{-iJ_\perp T/(8\hbar)}|N\rangle + e^{-iJ_\perp T/(16\hbar)}|I\rangle\right). \tag{4.55}$$

Finally in the evolution from $3T/8$ to $T/2$, $|I\rangle$ picks up another phase $e^{-iJ_\perp T/(16\hbar)}$. This means that the state after $T/2$ is

$$\psi\left(\frac{T}{2}\right) = \frac{1}{\sqrt{2}}e^{-iJ_\perp T/(8\hbar)}(|I\rangle + |N\rangle) = e^{-iJ_\perp T/(8\hbar)}\psi(0). \tag{4.56}$$

Thus apart from an overall phase, the state after half of the sequence is identical to the initial state. The pulses about $\hat{x}$ in the second half have the same effect, and the center $\pi$ pulse is still necessary for mitigating single-particle dephasing. It's worth noting that the WAHUHA sequence has no effect on dipole-dipole interactions beyond those that come from isolated pairs. As shown in Fig. 4.13c, for very dilute lattice fillings ($< 5\%$), most of the molecules have at most one neighbor; as a result, the multi-pulse sequence can have a large effect.

It's quite important that the echo pulse is a rotation about $\hat{x}$. Fig. 4.14 shows what happens when the echo pulse is about $\hat{y}$ instead of $\hat{x}$. In this case, the entanglement doesn't reverse at the end of the sequence, and the contrast decay is qualitatively very different from that in Fig. 4.13b. With the echo pulse about $\hat{x}$, the state immediately before the readout pulse is $-e^{-iJ_\perp T/(4\hbar)}\psi(0)$; however, when the echo pulse is about $\hat{y}$ it would be $e^{-iJ_\perp T/(4\hbar)}\left(\frac{|N\rangle - |I\rangle}{\sqrt{2}}\right)$, which cannot be expressed as a trivial multiple of the initial state.

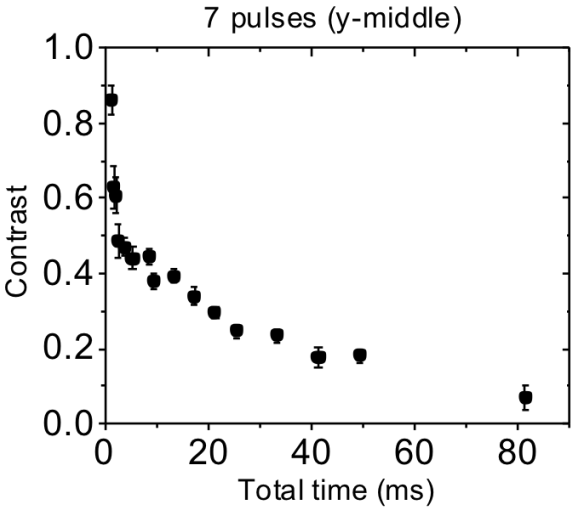


Figure 4.14: Same as WAHUHA, except the echo pulse in the middle is about $\hat{y}$ instead of $\hat{x}$. The contrast decay is qualitatively very different from that in Fig. 4.13b, as it decreases sharply at short times and then decays on a longer timescale.

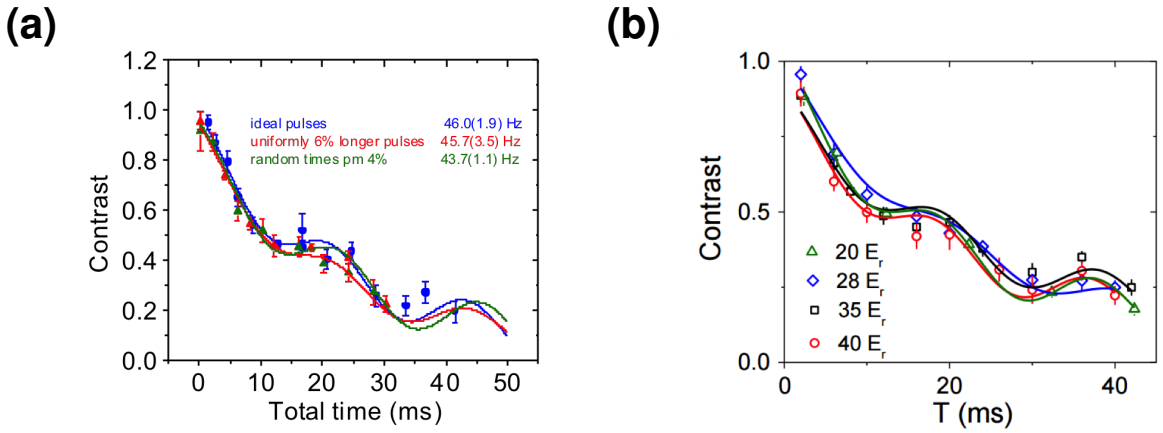


Figure 4.15: (a) Varying the duration of the echo pulse by up to 6% (so that it's 0.94-1.06 $\pi$), we see no significant effect on the coherence time or oscillation frequency. (b) Contrast decay for different lattice depths, which varies the spread of energies across the cloud. We don't observe any significant differences over the range 20-40 $E_R$. Figure reproduced from Ref. [84].

### 4.4.2 Robustness to imperfections

One natural question is how sensitive we are to various imperfections in the experiment. Earlier I stressed that we could achieve $> 99\%$ $\pi$-pulse fidelities. But is this actually necessary? To answer this question, we introduced pulse errors of up to 6%. As shown in Fig. 4.15a, we don't see any significant change in the contrast decay when the echo pulses aren't perfect. However, if we were to use a different initial tipping angle (other than $\pi/2$) then these pulse errors are more of an issue. We also looked at the effect of doing the experiment at different lattice depths (again using the same lattice polarizations as in Fig. 4.6a). This changes the magicness of the trap and the Ramsey coherence time. Fig. 4.15b shows that the oscillation frequency and coherence time are very similar over the range 20-40 $E_R$.

## 4.5 Second set of experiments

As was discussed in Section 4.1, $J_\perp$ is twice as large for the $\{|0,0\rangle, |1,0\rangle\}$ manifold. This gives us an easy way to change the strength of the interactions. In particular, the faster dynamics were useful to see that there were multiple frequency components present in the contrast decay. In addition, the observed dynamics for the faster interactions are basically identical to the slower interactions (except that time is rescaled), and this strongly suggests that processes other than interaction effects are negligible in the system's dynamics. Furthermore, the theoretical tools to describe the experiment had to be improved in order to explain our data, which exemplifies how the theory and experiment build off of one another in our system. The discussion in this section closely follows Ref. [85], of which I am an author.

### 4.5.1 Contrast decay for the $|0,0\rangle \rightarrow |1,0\rangle$ transition

The main experimental change when working with the $|1,0\rangle$ state is that we needed to add some additional waveplates to the horizontal lattice beams to get close to the magic angle (around 52 degrees for each beam). After doing this, we were able to achieve Ramsey coherence times longer

than 2 ms (Fig. 4.11b). We repeated the spin echo experiments following the same protocol outlined earlier. Typical contrast decay curves for $\sim 10^4$ molecules for both choices of $|\uparrow\rangle$ are shown in Fig. 4.16a. Larger couplings are observed for $|\uparrow\rangle = |1,0\rangle$ and the faster spin dynamics makes the experiment less sensitive to technical limitations. Fig. 4.16b compares the contrast decay for the two choices of $|\uparrow\rangle$ when time is rescaled by a factor of two for the $|1,-1\rangle$ data. This highlights that the dipole-dipole interactions are responsible for the observed dynamics and that other possible contributions play a negligible role in the decay.

### 4.5.2 Fitting to multiple frequencies

For the $|1,-1\rangle$ data, we fit to the sum of a single frequency oscillation and an exponential decay (Eq. 4.49). The low sampling rate makes it difficult to fit to more frequencies. Furthermore, as shown in Fig. 4.7, for the $|1,-1\rangle$ state the exchange is suppressed even at molecular spacings of 1.5-2 $a_{\mathrm{lat}}$, which could suppress some of the strong couplings on the diagonal. However, looking at Fig. 4.4, there should be other pronounced frequency components in the data. Since the timescales are faster for the $|1,0\rangle$ state, we tried fitting the contrast decay to three frequencies, with the functional form

$$C(T) = Ae^{-T/\tau} + B_1\cos^2(\pi f T) + B_2\cos^2(\pi f T/\sqrt{2}) + B_3\cos^2(\pi f T/2). \tag{4.57}$$

These three frequencies are the three dominant interactions as shown in Fig. 4.4a, and are predicted to give rise to observable frequency components in the contrast decay. The spacing between the couplings gets increasingly smaller at lower frequencies, and this is responsible for the overall decay. We see better agreement with the three frequency fit (Fig. 4.17). We see that the reduced $\chi^2$ is closer to 1 with the three frequency fit, with the lowest $\chi^2$ occurring for a frequency around 108 Hz, which is close to the expected value of 104 Hz from $J_\perp$.

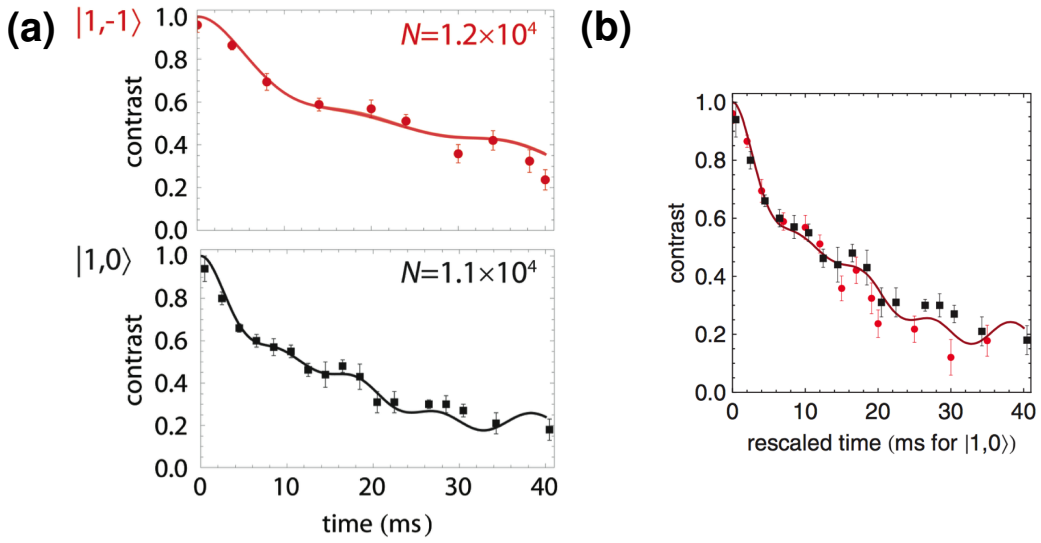


Figure 4.16: (a) Typical contrast decay curves for $|\uparrow\rangle = |1,-1\rangle$ (top) and $|\uparrow\rangle = |1,0\rangle$ (bottom) for roughly the same density ($\sim 1.2 \times 10^4$ molecules). The coherence time is clearly shorter for the $|1,0\rangle$ data, which is expected due to the stronger interactions. (b) Taking the two datasets from (a) and scaling the time axis for the $|1,-1\rangle$ data by a factor of two, we see that the curves collapse onto each other reasonably well, which highlights that dipolar interactions are responsible for the observed dynamics. Figures reproduced from Ref. [85].

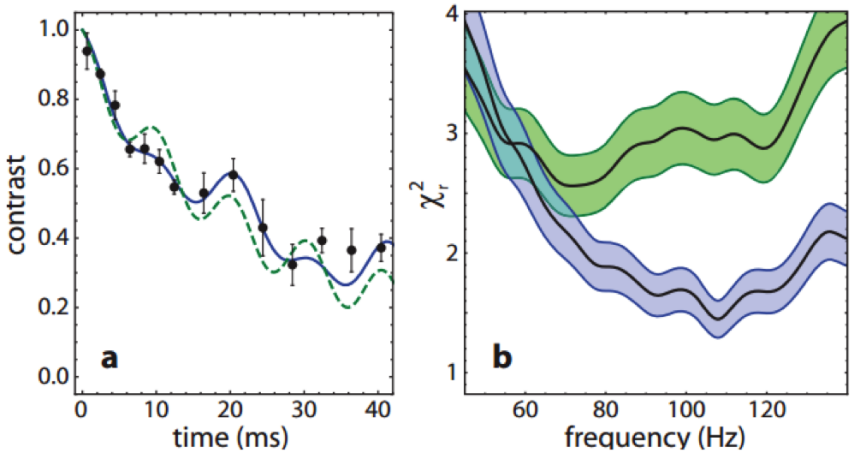


Figure 4.17: (a) Fitting a $|1,0\rangle$ contrast decay curve to Eq. 4.49 (1 frequency, dashed green) and Eq. 4.57 (3 frequencies, solid blue). (b) For this dataset, fitting to 3 frequencies yields a reduced $\chi^2$ closer to 1. For the 3 frequency fit, the best fit occurs for a frequency around 108 Hz, in good agreement with the expected value from $J_\perp$. Figure reproduced from Ref. [85].

### 4.5.3 Theory comparison

Our simple fitting functions, Eqs. 4.49 and 4.57, do a good job at extracting the coherence time and telling us about the dominant energies in the interaction spectrum. However, our theory colleagues can fit the data to a more sophisticated model. The basic idea, illustrated in Fig. 4.18a, is to use a cluster expansion, whereby the system of $\sim 10^4$ molecules is broken up into small clusters of $\sim 10$ molecules, and the dynamics within the clusters is computed exactly. The theoretical advance in Ref. [85] was to develop a "moving-average cluster expansion" (MACE), which is able to converge much faster than a discrete cluster expansion. The MACE builds an optimal cluster for each molecule $i$ by finding the set of largest couplings $V_{ij}$ to it. The expectation values $\langle S_i^x \rangle$ and $\langle S_i^y \rangle$ are computed exactly for each cluster, and the global Ramsey fringe contrast $C = 2\sqrt{\langle S_i^x \rangle^2 + \langle S_i^y \rangle^2}$ is calculated by summing these expectation values over all molecules. Details of the convergence of the algorithm are given in Ref. [85].

The theory was able to estimate the filling fraction by matching to the data in Fig. 4.16, and the result is that the filling is about 5% for that data. The molecular distribution was assumed to be a shell, given our expectation that the initial Rb density is high in the center and there will be many multiply occupied sites that do not produce molecules (this will be discussed more in depth in the next chapter). However, the theoretical decay curves are largely independent of the exact geometry in which the molecules are created. Another issue that the theory-experiment comparison can address is the role of long-range interactions in the experiment. In particular, it's interesting to see if the experimental data can be described accurately by only considering nearest neighbor interactions (or nearest and next-nearest neighbor interactions). As shown in Fig. 4.18b,c, the curves that only consider short-range interactions don't agree well with the experimental data, which says that long-range interactions are needed to explain the dynamics of our system.

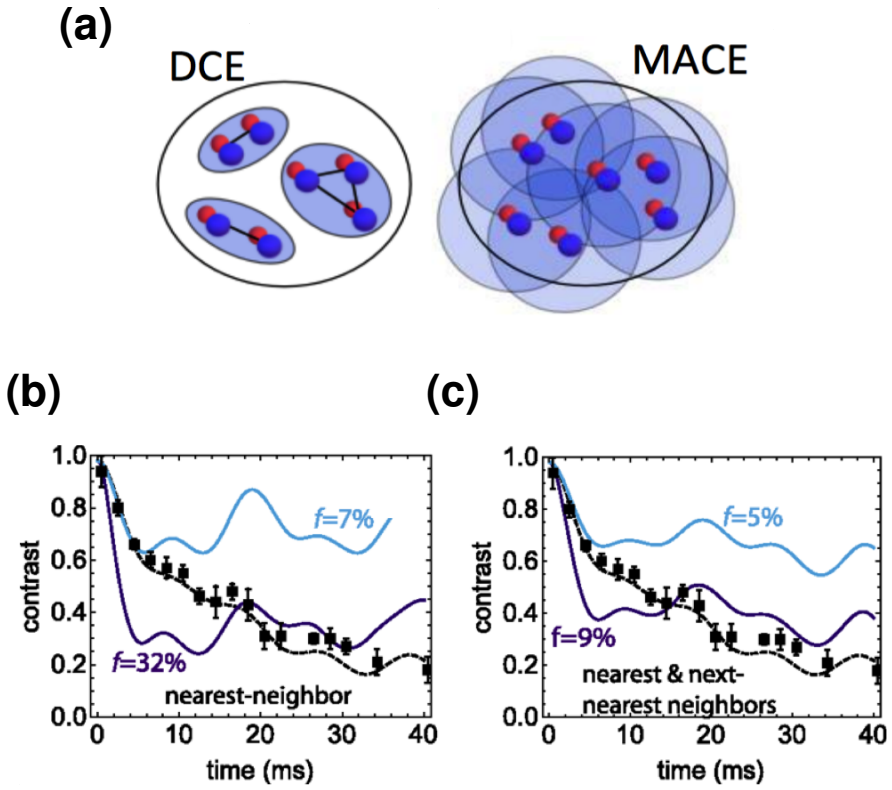


Figure 4.18: (a) Schematics of the discrete cluster expansion (DCE) and the moving-average cluster expansion (MACE). (b) and (c) Theoretically calculated contrast decay truncating the interactions at nearest-neighbor (b) and nearest and next-nearest neighbor (c). In both cases, the black points and dashed curve are the data and theory shown in Fig. 4.16 for $|\uparrow\rangle = |1,0\rangle$, and the purple and light blue solid curves are the predicted contrast decay curves for different filling fractions and truncated interactions. The disagreement of the short-ranged calculations with the data supports the claim that long-range interactions are present in the experiment. Figures reproduced from Ref. [85].

## 4.6 Future ideas

Our initial observations of spin-exchange are just the first step in studying quantum magnetism with polar molecules. The results of the theory comparison tell us that although we can see effects of long-range interactions in the experiment, the lattice fillings are low (less than 10% even for the highest densities). This is consistent with other methods for determining the filling, such as the losses in tubes [90] and direct imaging [84]. We would really like to increase the lattice filling so that we can study more complex dynamics, such as the buildup of entanglement and correlations, and the propagation of spin excitations. In the next chapter, we show that by tailoring the initial atomic distributions, we can achieve much higher lattice fillings.

### 4.6.1 Simple simulation of spin transport

To motivate why higher lattice fillings are important, it's useful to think about future experiments we would like to do. One example is to study spin transport. Here, the idea would be to create a small number of $|\uparrow\rangle$ molecules in a sea of $|\downarrow\rangle$ molecules. The molecules are pinned in the lattice and don't move, but the rotational excitations can move from site to site. Experimentally, we would want to see how these excitations propagate at different lattice fillings and electric fields, as well as in the presence of disorder, both from the finite filling fraction and from intentionally created disorder in the potential that the spin excitations see. This is intimately linked to the idea of many-body localization, where strong disorder could potentially localize these excitations [37]. This closely parallels work in trapped ions looking at the speed limit of the propagation of correlations in 1D chains of trapped ions [38, 39]. In our system, we could study these effects in 2 or 3 dimensions.

A naïve expectation is that the excitations will propagate faster for higher lattice fillings. To test this, I did a simple 2D simulation on a $15 \times 15$ grid. The center molecule is always $|\uparrow\rangle$ and the rest are $|\downarrow\rangle$, distributed randomly with filling $f$. I then compute the coupling matrix, calculate the wavefunction after some time $T$, and compute how far on average the excitation has moved. Note

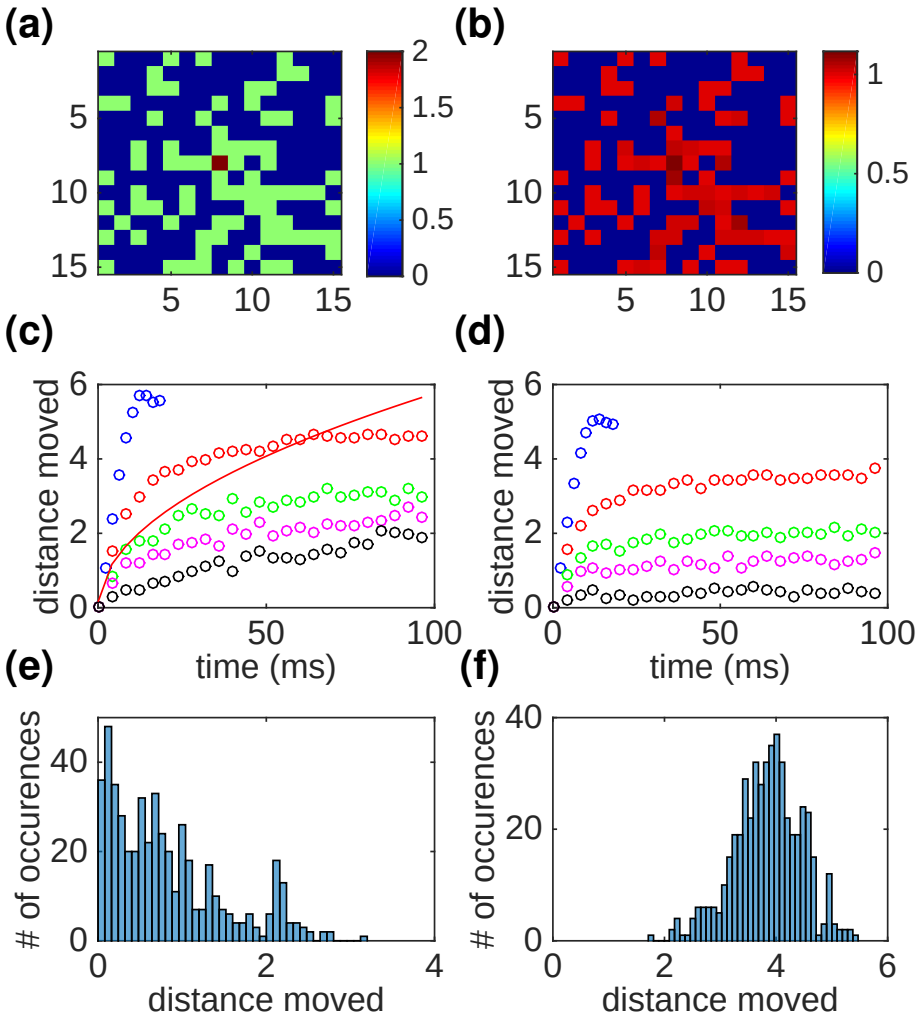


Figure 4.19: Simulation of spin transport. Dynamics in a single 2D plane (for example, the $xy$ plane of Fig. 4.4a) is considered for the coupling strengths for the $\{|0,0\rangle, |1,-1\rangle\}$ manifold. (a) Initial distribution with $f = 0.3$. The colorbar represents excitation: 0 is an empty site, 1 is $|\downarrow\rangle$, and 2 is $|\uparrow\rangle$. (b) Distribution after evolving for 50 ms. Note the change in colorbar. There is a finite probability of finding the excitation on any site. (c) Distance the excitation moves (in lattice sites), $\bar{R}$ (Eq. 4.58), vs. evolution time $T$ for $f = 1$ (blue), $f = 0.5$ (red), $f = 0.3$ (green), $f = 0.15$ (magenta), and $f = 0.05$ (black). The open circles are averages of 50 realizations (except for $f = 1$ where the dynamics is always the same), and the solid red curve is a fit to the $f = 0.5$ data, assuming diffusive transport ($\bar{R} \propto \sqrt{T}$). (d) Same as (c) except there is a site-to-site energy shift $3\,\mathrm{Hz} \times ((i-8)^2 + (j-8)^2)$ ($i$ and $j$ label the lattice sites along the two directions). (e) Histogram of $\bar{R}$ after 50 ms for $f = 0.05$. The simulation was repeated 500 times. (f) Same as (e) but for $f = 0.5$. Here there is a clear displacement from the center.

that since this is the one excitation subspace, this requires diagonalizing at most a $15^2 \times 15^2$ matrix, which is computationally easy. Fig. 4.19a shows a typical initial distribution for a 30% filling, while panel b shows the distribution after 50 ms. After 50 ms, the excitation has some probability to be on any site. The expected distance $\bar{R}$ (in lattice sites) is given by

$$\bar{R} = \sum_i p_i r_i, \tag{4.58}$$

where $p_i$ is the probability that the particle is on site $i$ and $r_i$ is the distance from the center site (in lattice sites). Panel c shows $\bar{R}$ vs. $T$ for different filling fractions, and panel d is the same but adding a site-to-site energy shift. Higher lattice fillings clearly lead to faster propagation. For fillings less than unity, the transport is not exactly diffusive (the red solid curve in panel c shows a fit of the red data to $\bar{R} \propto \sqrt{T}$) and there appears to be a saturation at longer times, which could be due to the finite system size. In the new experiment, we plan to have an imaging resolution of around 1 $\mu$m, which is about 2 lattice sites. We would want the excitation to propagate at least this far in order to detect that it moved.

For very dilute fillings the actual distribution is very different from one realization to the next, with some realizations having two particles close to each other (which will exchange quickly) and other realizations having only very small couplings. In the simulation this manifests as a very large standard deviation of the expected distance the excitation moved, which suggests that it would be difficult to get good statistics in the experiment for small lattice fillings. This is highlighted in panels e and f, which show histograms of the expected distance after 50 ms for both $f = 0.05$ (e) and $f = 0.5$ (f).

### 4.6.2 Realizing additional terms in the Hamiltonian

In addition to achieving higher lattice fillings, it would also be interesting to realize additional terms in the dipolar Hamiltonian (Eq. 4.3). As was shown earlier, the full dipolar Hamiltonian has more terms than just those in Eq. 4.8. In this chapter, I have so far focused on the $q = 0$ term. The $q = \pm 2$ terms are particularly interesting because they can be used to realize a novel form of

spin-orbit coupling [88]. Most realizations of spin-orbit coupling in cold atoms can be understood as a single-particle effect, with the coupling usually arising from Raman beams that couple hyperfine states, which generally means that spontaneous emission and heating are problematic. In contrast, the spin-orbit coupling described in Ref. [88] arises from interactions between the molecules and in principle shouldn't have any issues with spontaneous emission or heating.

The $q = \pm 2$ terms look like

$$V_{dd}^{q=\pm 2} = \frac{-3}{2r_{ij}^3}\left(\hat{d_i^+}\hat{d_j^+}e^{-2i\phi_{ij}} + \hat{d_i^-}\hat{d_j^-}e^{2i\phi_{ij}}\right)\sin^2\theta_{ij}, \tag{4.59}$$

and correspond to processes that transfer between rotational angular momentum and orbital angular momentum. This method of coupling the spin degree of freedom to the particles' orbital motion is similar to recent experiments in magnetic atoms [140, 141]. Because of the $\sin^2\theta$ term, Ref. [88] proposes to do the experiment in a single 2D layer, with $\theta = \pi/2$. The interactions occur with three states of the molecules and can drive the following process:

$$|1,-1\rangle + |0,0\rangle \rightarrow |0,0\rangle + |1,1\rangle. \tag{4.60}$$

As shown in Ref. [88], the strength of the coupling is $3J_\perp$, so in order for this to work, the energy difference between the $|1,1\rangle$ and $|1,-1\rangle$ states must be less than this. The easiest way to bring these states to degeneracy is to apply a large magnetic field of about 1260 G [88]. The second generation experiment will have the capability of reaching such large magnetic fields.

# Chapter 5

## Increasing the filling fraction

The last chapter described our observation of spin-exchange interactions for molecules pinned in a deep lattice; however, the lattice filling was quite dilute (less than 10%). This is consistent with the filling extracted from the measured loss rate of molecules confined in tubes and from direct imaging of the spatial extent of the cloud [84, 90]. The reason we could observe spin exchange at such low fillings is that there is a strong decoupling between spin and motion that makes the spin entropy the relevant quantity [83, 85]. Since we can easily initialize all of the molecules in the same quantum state, the spin entropy can be very low. This chapter addresses the question of why the filling was so low and presents a strategy that directly leads to a much higher lattice filling in our experiment.

Experimental imperfections, such as finite temperature, limit the filling fraction of cold atomic gases when they are loaded into optical lattices. Atomic Fermi gas experiments achieve fillings close to, but not exactly, unity [21, 142]. Exactly what filling fraction is required for polar molecule experiments depends on the experiment one wants to do. As shown in the simulations at the end of the previous chapter, the propagation of rotational excitations can occur at any density, but occurs much faster for higher fillings. Many other interesting proposals don't require unit filling. Fillings in the range 0.25-0.5 are sufficient for studying many-body localization [37], and the spin-orbit coupling discussed in the previous chapter can work even at fillings of $\sim 0.1$ [88]. However, even when an experiment is possible at low fillings, the SNR will almost surely be better at higher fillings.

One notion of sufficiently high filling is that the system is well connected, which means there is a reasonably efficient way to propagate information between any two parts of the system. Another way of saying this is that there has been a percolation in the system, which is defined as the filling at which an infinite cluster develops in an infinite system [143]. For an infinite 3D cubic lattice with nearest neighbor interactions, the percolation threshold occurs at a filling of around 0.3 [143], so this gives us a rough target. In our system, the exact critical filling will be different, and likely less than this, since we have long-range interactions and a finite system size.

There are two main approaches one might adopt to achieve higher fillings. The first is to try to directly cool the molecules and then load them adiabatically into the lattice, while the second is to start with two species of cold atom gases, optimize their loading into the lattice, and then make molecules, as proposed in Refs. [144, 145]. This second option has been demonstrated for $Rb_2$ Feshbach molecules, where the molecules were created out of a Mott insulator with two atoms per site [146].

The first option doesn't work very well for KRb because it's very difficult to cool the molecules in the presence of chemical reactions. There are proposals to evaporatively cool reactive polar molecules by using an electric-field gradient to remove hot molecules and the dipolar interactions to rethermalize [119]. Using universal dipolar scattering to evaporatively cool spin-polarized fermions was demonstrated beautifully for magnetic atoms, but there the ratio of good to bad collisions was very favorable [50]. For KRb, very large electric fields and harmonic confinements would be necessary in order to reach a favorable regime of good to bad collisions [119, 120]. In addition, we've also seen evidence that the molecular gas is heated a lot when loading and unloading the lattice. Doing the same experiment for K, we saw almost no heating (Fig. 5.1). This suggests problems in trying to adiabatically load molecules into the lattice. More experimental work would be required to determine the origin of this problem. In 2011-2012, we spent a lot of time trying to create colder molecules in the harmonic trap by using a species selective dipole trap around 790 nm, which affected K but not Rb and was useful for optimizing the overlap between the two species. However, ultimately the poor fractional conversion of the atom gases into Feshbach molecules limited the

temperature of the molecular gas to $T/T_F \sim 1$.

The second option benefits from the high conversion of preformed atomic pairs to Feshbach molecules, and the subsequent efficient optical transfer to the ground state. As shown in Ref. [72], the conversion of sites with one K and one Rb atom to molecules is nearly unity ($87 \pm 13\%$). This issue will be addressed further in Chapter 6, where we show that in the case of deep lattices and fast magnetic-field ramps, the conversion efficiency seems to be exactly 100%. Previous measurements of inelastic loss rates of Feshbach molecules with K and Rb atoms suggest that having multiple Rb atoms on a lattice site is detrimental to molecule production on that site [65, 69]. This motivated us to maximize the number of lattice sites that have one K and one Rb atom. The ideal states of the initial atomic gases are a bosonic Mott insulator (MI) with one atom per site and a fermionic band-insulator where the filling approaches unity at the center. If the temperature of the K gas is not sufficiently low, the number of K atoms will need to be much larger than the number of Rb atoms, so that we avoid multiple occupancies of Rb and so that the K density approaches one particle per site in the center of the lattice. Even in the harmonic trap, we see that if the Rb density is too high, this negatively affects the molecule production (Fig. 5.2).

Many of our previous attempts to increase the molecule filling looked at the final result as a function of many parameters (atom number, interspecies interactions, lattice depth, harmonic confinement, etc.) without seeing a significant dependence on these parameters. Since the molecule production involves several steps, we decided to systematically study each step individually before putting them all together. This ultimately led to a better understanding of the dependence of the molecular density on the parameters listed above and motivated a strategy to increase the density of molecules.

In Section 1, I give a brief theoretical discussion of the bosonic Mott insulator and fermionic band insulator, and then discuss the challenges of creating a dual insulator. In Section 2, I describe changes to the imaging system that were instrumental to the success of this study. In Section 3, I present measurements of the fillings of the individual atomic gases. In Section 4, I describe the effect of the insulators on each other and show it's optimal to turn off the interspecies interactions

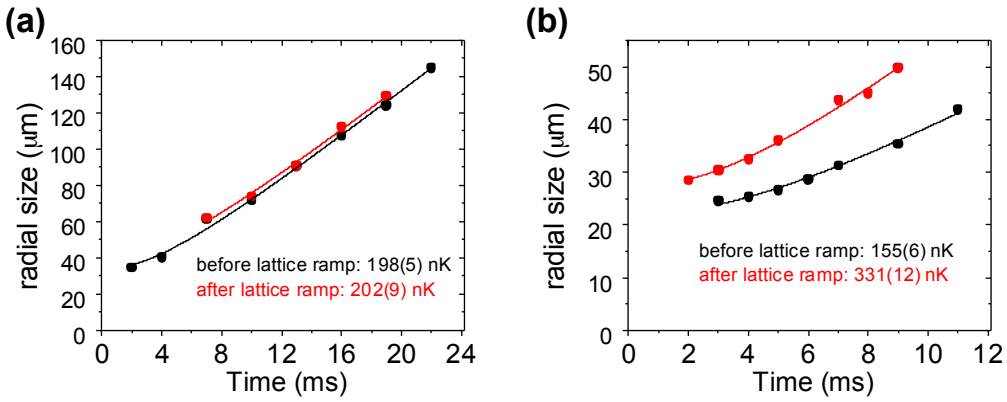


Figure 5.1: (a) Ramping up and down the vertical lattice in 200 ms and holding for 50 ms (total time 450 ms), the K gas is not significantly heated. We measure the temperature $T$ by fitting the radial size during a TOF expansion to $\sigma_r = \sqrt{\sigma_0^2 + \frac{k_B T}{m} t^2}$, where $\sigma_0$ is the *in situ* size and $m$ is the particle mass. (b) Repeating the same experiment for ground-state molecules, we see a lot of heating, which could mean we didn't load the lattice adiabatically. The exact origin of this problem is not very well understood.

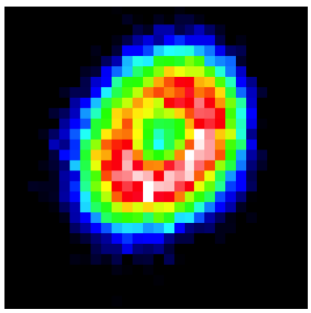

Figure 5.2: We see a hole in the center of the Feshbach molecule distribution when the Rb density is too high. This image was taken in the optical dipole trap.

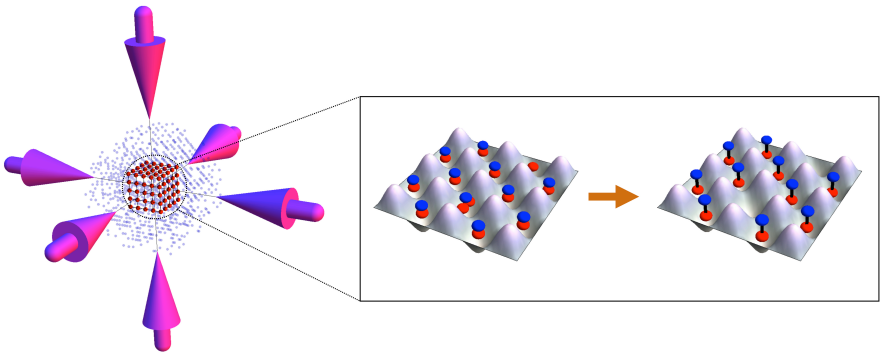

Figure 5.3: Quantum synthesis for realizing high molecule fillings in the lattice. Left: We load K (blue) and Rb (red) atoms into a 3D optical lattice, with many more K atoms. In the center of the lattice, we have a MI of Rb and band-insulator of K, each with a filling near unity. Right: Sites with one Rb and one K produce molecules with high probability, whereas sites with multiple Rb atoms or only a single atomic species don't produce molecules. Figure reproduced from Ref. [92].

by loading the lattice at $a_{\mathrm{KRb}} = 0$. In Section 5, I describe experiments that studied the conversion efficiency of Feshbach molecules vs. Rb number and show the final results of the improvement of the molecule filling fraction. In the best case, we achieve molecule fillings $> 25\%$. In Section 6, I conclude and give an outlook for future work. Most of the discussion of this chapter follows Ref. [92], of which I am the lead author.

## 5.1 Target distributions: Rb Mott insulator and K band insulator

Our strategy for realizing higher molecule fillings in the lattice relies on the precise experimental control that's available for manipulating the initial atomic quantum gas mixture in the 3D lattice. Specifically, we need to prepare low entropy states of both species and combine this with efficient molecule production at individual lattice sites. The combination of efficient magnetoassociation of preformed pairs [72] and efficient optical state transfer via STIRAP means the second step should work well; however, creating a low entropy state of both species with the optimal density of one particle per site is very challenging.

The basic scheme is illustrated in Fig. 5.3. By loading a nearly pure Rb BEC into a deep 3D lattice, we achieve a MI, where repulsive interactions between the Rb atoms drive a transition

to a state that has an integer number of particles per site. The initial BEC density should be sufficiently low that we end up with one atom per site. For spin-polarized K atoms, Pauli blocking prevents any site from having more than one K atom, assuming that all atoms are loaded into the lowest band. The initial K gas needs to be cold in order to load most of the atoms into the lowest band. The optimum case is a spin-polarized K band insulator with a filling $\sim 1$ atom per site in the center, which given our relatively high initial temperature, requires starting with a relatively large number of K atoms. In addition, we require that the Rb MI is well spatially overlapped with the center of the much larger K distribution and that the high filling of each species is preserved in the presence of the other.

### 5.1.1 Rb Mott insulator

Ultracold bosons in an optical lattice are well described by the Bose-Hubbard Hamiltonian [32, 103]:

$$H = -J \sum_{\langle i,j \rangle} \hat{a_i}^\dagger \hat{a_j} + \sum_i \frac{U}{2} \hat{n_i}(\hat{n_i} - 1) + \sum_i (V(\mathbf{r_i}) - \mu)\hat{n_i}, \tag{5.1}$$

where $\hat{a_i}^\dagger$ and $\hat{a_i}$ are bosonic creation and annihilation operators, and $\hat{n_i}$ is the number operator for site $i$. The first term represents tunneling at a rate $J$ between adjacent lattice sites (the sum is over neighboring sites $i$ and $j$), the second term is the onsite interaction energy (which is repulsive for Rb), and the third term represents the external harmonic confinement. The chemical potential $\mu$ sets the particle number.

In shallow lattices ($U/J \ll 1$), the atoms are delocalized over the entire lattice and there is a well-defined phase on each lattice site [147]. In this superfluid phase, the number of atoms on any site is uncertain and is given by a Poisson distribution. In momentum space, the superfluid displays an interference pattern with well-resolved peaks spaced by twice the lattice recoil momentum $2\hbar k$ (Fig. 5.4). For deep lattices ($U/J \gg 1$), the energy cost $U$ of having multiple occupancies suppresses number fluctuations. The result is a MI with Fock states on each lattice site. In the MI, the macroscopic phase on each lattice site has a maximum uncertainty and the interference pattern in

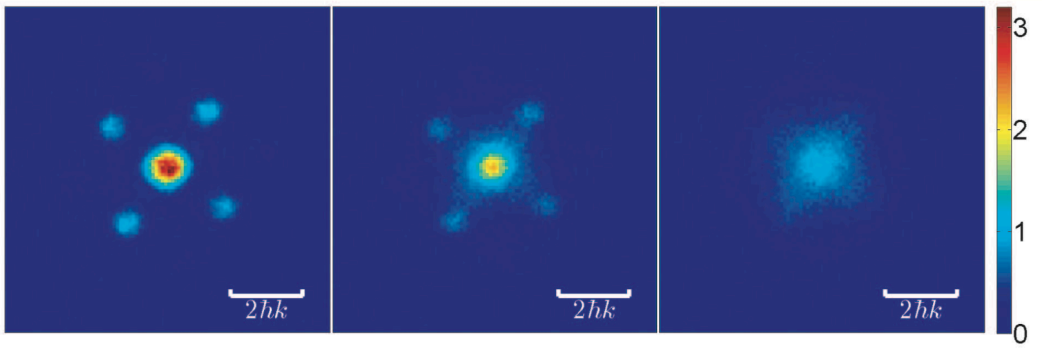


Figure 5.4: The superfluid-to-Mott insulator transition. The lattice depth is 12, 17, and 22 $E_R$ from left to right. The white bar shows twice the lattice recoil energy. The optical depth (OD) is displayed by the color scale. Figure reproduced from Ref. [92].

momentum space disappears (Fig. 5.4). The superfluid-Mott insulator transition was first observed in 2002 [147], and seen under a quantum gas microscope in 2010 [148, 149].

To gain an intuitive understanding, it's useful to consider the case of zero temperature and zero tunneling. In this case, the density of the MI depends on the ratio of the chemical potential to the interaction energy, $\mu/U$. Because of the additional harmonic confinement $V(\mathbf{r})$, the local chemical potential $\mu - V(\mathbf{r})$ determines the occupancy of a lattice site. Specifically, the occupancy of site $(i, j, k)$ is $\alpha$ if

$$(\alpha - 1) < \frac{\mu - V(i, j, k)}{U} \leq \alpha. \tag{5.2}$$

This condition allows for a self-consistent computation of the number of atoms for a given chemical potential, $N(\mu)$ [150]. In the thermodynamic limit, $\mu$ has a form very similar to the Thomas-Fermi (TF) result for a harmonic trap. It's useful to calculate this limit in order to understand how $\mu$ depends on $N$ and the harmonic trapping frequency. The calculation is outlined in Ref. [103]. Assuming a spherically symmetric distribution, the density $n(r)$ (in particles per lattice site) is given by

$$n(r) = \frac{\mu - \frac{1}{2}m\omega^2 r^2}{U}, \tag{5.3}$$

where $\omega$ is the underlying harmonic confinement of the lattice beams. The extent of the cloud,

$R_{\max}$, occurs when $\mu - \frac{1}{2}m\omega^2 R_{\max}^2 = 0$, which gives $R_{\max} = \sqrt{\frac{2\mu}{m\omega^2}}$ (to get this in number of lattice sites, divide by $a_{\text{lat}}$). Then $N$ is fixed by

$$N = \int_0^{R_{\max}/a_{\text{lat}}} n(r) d^3r = \int_0^{R_{\max}/a_{\text{lat}}} \frac{\mu - \frac{1}{2}m\omega^2 r^2}{U} 4\pi r^2 dr. \tag{5.4}$$

Doing the integral and solving for $\mu$ we obtain

$$\mu = \left( \frac{15\, U\, a_{\text{lat}}^3 m^{3/2}}{2^{9/2}\pi} \right)^{2/5} N^{2/5} \omega^{6/5}. \tag{5.5}$$

For different harmonic confinements along the three lattice directions, like we have in our experiment, $\omega$ is replaced by the geometric mean harmonic confinement $\bar{\omega}$. What's important about this expression is how $\mu$ scales with $N$ and $\bar{\omega}$: $\mu \propto N^{2/5}\bar{\omega}^{6/5}$. To have at most one atom per site, we require $\mu \leq U$. As shown in Fig. 2.14, a typical value of $U$ is $h \times 1$ kHz (for Rb in a 1064 nm lattice). For the harmonic confinements needed to overlap the species and achieve the required densities, the maximum $N$ we can have and still satisfy $\mu \leq U$ is a few thousand. But in general, we want to have as small of a harmonic confinement as possible in order to maximize the number of atoms $N$ in the $n = 1$ MI.

### 5.1.2 K band insulator

The fermionic analog to the bosonic superfluid and MI is the metal and fermionic MI, respectively. In the fermionic MI, strong repulsive interactions (onsite interaction $U$) between two spin components lead to a state with one particle per site. The fermionic nature of the particles combined with repulsive onsite interactions provides an ideal experimental setting to study fundamental questions related to strongly correlated electron systems [151]. The fermionic MI was first observed in 2008, with experimental signatures including a suppression of doubly occupied sites, a reduction of the compressibility, and the appearance of a gap in the excitation spectrum [151]. More recently, the fermionic Mott insulator was observed with imaging at the single-particle level [142]. If the chemical potential increases further ($\mu > U$), the state transitions to a band insulator, where there is one particle of each spin state per site [21, 152]. In our experiment, we

use spin-polarized fermionic $^{40}$K atoms in the $|9/2, -9/2\rangle$ state, so if the atoms are in the lowest band, there can be at most one atom per site. In this case, the state with one atom per site is a spin-polarized band-insulator.

The filling of fermions in optical lattices is more complicated to calculate than for bosons, and depends on an interplay between temperature, tunneling, and harmonic confinement. In contrast to the case of bosons, low temperature alone is not sufficient to guarantee unit filling, but we do require sufficiently low $T/T_F$. A few rough arguments tell us that large particle numbers and strong harmonic traps are going to be necessary to achieve a density $\sim 1$ particle per lattice site. Ref. [152] gives the following condition for a band insulator:

$$\frac{m\bar{\omega}^2\lambda^2}{8}\left(\frac{3N}{4\pi}\right)^{2/3} \gg 12J, \tag{5.6}$$

where $J$ is the tunneling energy, $\lambda$ is the lattice wavelength, and $\bar{\omega} = (\omega_r^2\omega_z)^{1/3}$ is the geometric mean harmonic confinement. The left hand side of Eq. 5.6 is the Fermi energy for noninteracting fermions in a deep 3D lattice [153], while the right side is the total tunneling bandwidth. Examining this condition at $10E_R^{\mathrm{K}}$ tells us that $N^{2/3}(\omega_r/(2\pi))^2 \gg 10^6$ Hz$^2$, which we roughly satisfy for $\omega_r = 2\pi \times 50$ Hz and $10^5$ atoms.

Another simple way to think about this is to calculate the partition function on each lattice site, assuming no tunneling. This calculation is outlined in Ref. [151] for a two-component gas. Although tunneling definitely plays a role in our experiment, the conclusions of this simple model give intuition that is useful for optimizing the K conditions. Each lattice site can have at most one particle, so the partition function for each site is

$$Z_i = 1 + \mathcal{Z}e^{-\beta\epsilon_i}. \tag{5.7}$$

The energy offset $\epsilon_i$ is due to the harmonic confinement ($\epsilon = 0$ at the center of the lattice), $\beta = 1/(k_BT)$ is the inverse temperature, and the fugacity is $\mathcal{Z} = e^{\beta\mu}$. $\mu$ is the chemical potential, which sets the number of particles. The probability that a site is occupied is $\mathcal{Z}e^{-\beta\epsilon_i}/Z_i$, so the peak filling is the probability that the central site is occupied, which is $\frac{\mathcal{Z}}{\mathcal{Z}+1}$. To find $\mu$, we require

that the total number of particles is $N$:

$$N = \sum_i \frac{\mathcal{Z} e^{-\beta \epsilon_i}}{Z_i}. \tag{5.8}$$

Fig. 5.5 shows results for small systems. We see that keeping the particle number fixed, the peak filling fraction increases when we reduce the temperature or increase the harmonic confinement. Increasing the number of atoms at fixed temperature and harmonic confinement also increases the peak filling.

### 5.1.3 Challenges of making a dual insulator

One of the main challenges of producing a dual Bose-Fermi insulator with one atom of each species per site is that there is generally a large mismatch in the size and spatial overlap of the two species, which comes from the different masses, polarizabilities, and quantum statistics. In this section we show that we need large harmonic confinement frequencies to support both species against gravity with a small differential sag and to achieve sufficiently high densities for K. We also briefly discuss challenges of evaporatively cooling the mixture to very cold temperatures. For the experiments described in this chapter, all optical potentials are at $\lambda$=1064 nm.

A lot of intuition about the constraints on the K and Rb distributions can be obtained from considering the densities in the optical trap. The distributions will change when loading the latices; however, in order to achieve a density of $\sim 1$ particle per lattice site ($6.6 \times 10^{12}$ cm$^{-3}$), we require a comparable density in the optical trap. The distribution of a sufficiently large BEC in a harmonic trap is given by a TF function, where the density has an inverted parabolic distribution and the cloud radius along an axis with harmonic confinement $\omega_i$ is

$$R_i = a_{\text{ho}}^{4/5} (15 N a_{\text{Rb,Rb}})^{1/5}, \tag{5.9}$$

where $a_{\text{ho}} = \sqrt{\frac{\hbar}{m\omega_i}}$ is the harmonic oscillator length and $a_{\text{Rb,Rb}} = 100\, a_0$ is the background scattering length [154]. For our typical trap frequencies for Rb of $\omega_r\,(\omega_z) = 2\pi \times 25\,(180)$ Hz and $10^5$ atoms, $R_x = R_y \approx 17$ $\mu$m, and $R_z \approx 2.3$ $\mu$m, which are quite small. For a degenerate Fermi gas,

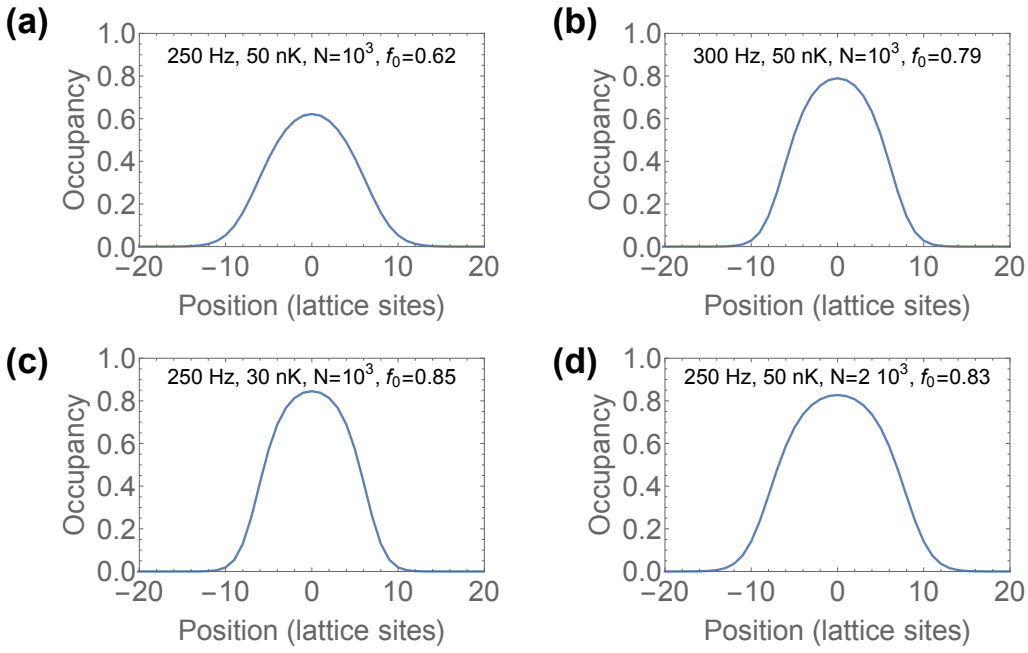


Figure 5.5: Calculating the density of spin-polarized fermions in the lattice in the zero tunneling limit for different temperatures and harmonic confinements. Here the trap is spherically symmetric and only a radial cut is shown. Comparing (a) and (b) we see that higher harmonic confinements give higher peak fillings. Comparing (a) and (c) we see that lower temperatures give higher peak fillings. Comparing (a) and (d) we see that more atoms give higher peak fillings.

the density is given by the Fermi-Dirac distribution:

$$n(\rho) = -\left(\frac{k_B m T}{2\pi\hbar^2}\right)^{3/2} Li_{3/2}(-\mathcal{Z}\exp(-m\omega_r^2\rho^2/(2k_B T))), \tag{5.10}$$

where $Li_{3/2}$ is a polylog function, $\mathcal{Z}$ is the fugacity, and $\rho^2 = x^2 + y^2 + \lambda^2 z^2$ is a scaled coordinate, where $\lambda = \omega_z/\omega_r$ characterizes the asymmetry of the trap [155]. The fugacity is related to $T/T_F$ by $Li_3(-\mathcal{Z}) = \frac{-1}{6(T/T_F)^3}$ [155]. Fig. 5.6a compares the density distributions of a pure BEC and a Fermi gas at $T/T_F = 0.25$ (each with $10^5$ atoms), and shows that the size of the Fermi gas is significantly larger. When optimizing the lattice loading to get one atom of each species per site, we would need to use a much smaller number of Rb atoms and the Rb cloud would be even smaller. Fig. 5.6b shows the peak density of K in the harmonic trap for different harmonic confinements, atom numbers, and temperatures. Like the simple model in the last section, there are several ways we can achieve high densities of K: increase the number of atoms, increase the trap frequencies, and use colder gases. Since we can only increase the number so much (perhaps to $3 \times 10^5$), and the scaling of density with harmonic confinement is much stronger, we choose to use relatively large harmonic confinement frequencies. For Rb, we're fighting the opposite battle. The typical BEC densities are very high, and as such, we have to go to small atom numbers.

We next briefly discuss the vertical overlap. Since the size of the K cloud is much larger than the BEC, we can tolerate a vertical offset of a few $\mu$m. K and Rb have different masses and polarizabilities at 1064 nm (see Table 2.1), so the two species have different trap frequencies ($\omega_{\mathrm{K}} = 1.37\,\omega_{\mathrm{Rb}}$). Consequently, there will be a differential gravitational sag $\Delta z = g\left(\frac{1}{\omega_{z,\mathrm{Rb}}^2} - \frac{1}{\omega_{z,\mathrm{K}}^2}\right) \approx \frac{0.27\,g}{\omega_{z,\mathrm{Rb}}^2}$, where $\omega_z$ is the vertical trap frequency. Clearly, $\Delta z$ becomes smaller as the vertical trap frequencies increase. For our normal optical trap frequencies of $\omega_r\,(\omega_z) = 2\pi \times (25)\,180$ Hz for Rb, the differential sag is about 2 $\mu$m, which is sufficiently small.

We want both gases to be as cold as possible. For Rb, this means a nearly pure BEC and for K it means a deeply degenerate Fermi gas. However, the way we do the evaporative cooling limits the temperature of K. In the optical trap, we evaporate the gases by lowering the intensity of the OT beams. However, Rb is heavier and has a smaller trap frequency, so it falls out of the trap first.

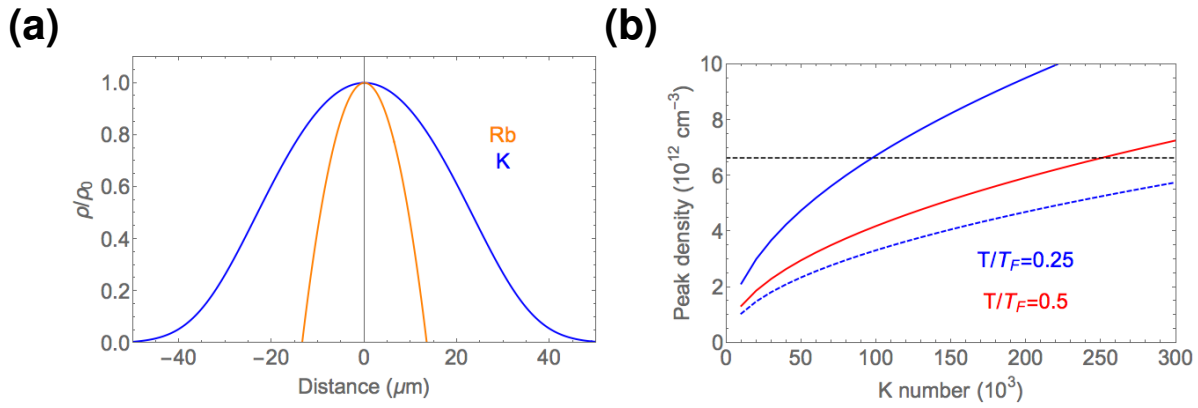


Figure 5.6: Comparing the densities of degenerate Bose and Fermi gases in a harmonic trap. (a) Comparison of a density cut along the radial direction for $10^5$ atoms for a K gas at $T/T_F = 0.25$ (blue) and a Rb BEC (orange) with a harmonic confinement $\omega_r\,(\omega_z) = 2\pi \times 51\,(290)$ Hz for K (the frequencies for Rb are 1.37 times less). This is the expected harmonic confinement of the optical trap plus lattice beams in the experiments of Ref. [92]. The density of each species is normalized to its peak density $\rho_0$. (b) Density of Fermi gases of $T = 0.25\,T_F$ (blue) and $T = 0.5\,T_F$ (red) in a 3D harmonic trap vs. atom number. The harmonic confinement is $\omega_r(\omega_z) = 2\pi \times 51(290)$ Hz (solid) and $2\pi \times 32(180)$ Hz (dashed). The density corresponding to one particle per lattice site is denoted by the dashed black line.

This means we do most of the cutting on Rb and we lose very few K atoms. We rely on collisions between K and Rb to thermalize the K. Once Rb condenses the K is no longer efficiently cooled since the BEC is much smaller than the Fermi gas. As a result, we observe that as the temperature drops, the K and Rb clouds are not in thermal equilibrium, with the K hotter. Experimentally we see that we can only reach temperatures of $T/T_F \approx 0.3$ (see Fig. 5.13).

To summarize, there is a huge compromise between the harmonic confinement and the densities of the atomic species. If we use a weak harmonic trap, the $n = 1$ MI will be larger but the K filling will be lower. If we use a much stronger trap, the size of the $n = 1$ MI will be very small but the density of K will be high. Ultimately we choose a harmonic confinement such that the K filling fraction saturates around $10^5$ atoms (see Section 5.3), and we have to live with the small Rb MIs (less than 5000 atoms).

## 5.2 Top imaging

Normally we would image the atoms from the side, using a probe beam that propagated through the entire chamber. This imaging direction is at 45° with respect to the principal axes defined by the OT and horizontal lattice beams. As a result, we were able to measure one radial size ($\sigma_r$) and the vertical size ($\sigma_z$). However, the imaging resolution was about 5 $\mu$m (Airy disk radius), which was sufficient for imaging in time-of-flight (TOF), but caused problems for imaging *in situ*, especially for very small clouds. As discussed in the previous section, the typical cloud radius of a BEC in the vertical direction is only a few $\mu$m, which is less than the imaging resolution. Measuring the filling of the atomic gases requires knowing the size along all three directions. Since $\sigma_z$ is less than the imaging resolution, we get no information about that direction. Thus, we were extracting all of the information from $\sigma_r$. Since the filling fraction scales like $1/\sigma_r^3$, any uncertainty in $\sigma_r$ contributes a larger fractional uncertainty to the measured filling fraction.

The bigger problem was that the system was unstable. The filling of the MI would change over time (over the course of a few hours) even if the lattice alignment didn't seem to change. Looking at the *in situ* distribution, we would sometimes see the cloud split into two parts (see

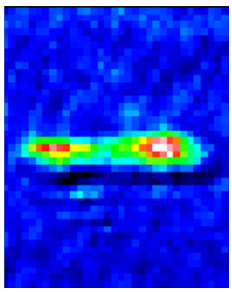

Figure 5.7: An image showing how the vertical lattice would split the cloud in two.

Fig. 5.7). To better understand the origin of this problem, and to see the cloud size along both radial directions, we decided to image the gas along the vertical direction. Once we set up the vertical imaging, we quickly understood the origin of these problems. It turns out that the ITO plates were probably vibrating when we ramped to high magnetic field. Because the plates were mechanically coupled to the coil assembly, this could have been due to mechanical forces arising from the changing current in the coils. This manifested as terrible fringes in the images caused by a relative motion of the probe beam between the shadow and light frames, which were separated by $\sim 500$ ms (see Fig. 5.8a). We determined that the magnetic-field ramps were problematic because if we waited at high field for a few seconds before imaging, the amplitude of the fringes was lower. The vibrations would also affect the vertical lattice, since the lattice beam also propagated through the ITO plates. This was likely what caused the cloud to sometimes split in half. Since we didn't need to apply electric fields, we decided to remove the ITO-coated glass from the region that the beams propagated through (we couldn't remove the whole plate since it was necessary to hold the microwave coil assembly together). This made the OD images much better (Fig. 5.8b) and the filling fraction of the atomic gases became much more robust, at least as far as we could tell from our detection. This also improved the stability of the vertical lattice.

A schematic of the top imaging setup can be seen in Fig. 5.9. For the objective, we used a single achromatic doublet from Edmund optics, with a focal length of 125 mm. In a test setup, we used this objective to image a 500 nm pinhole, which acts as a point source. This allowed us

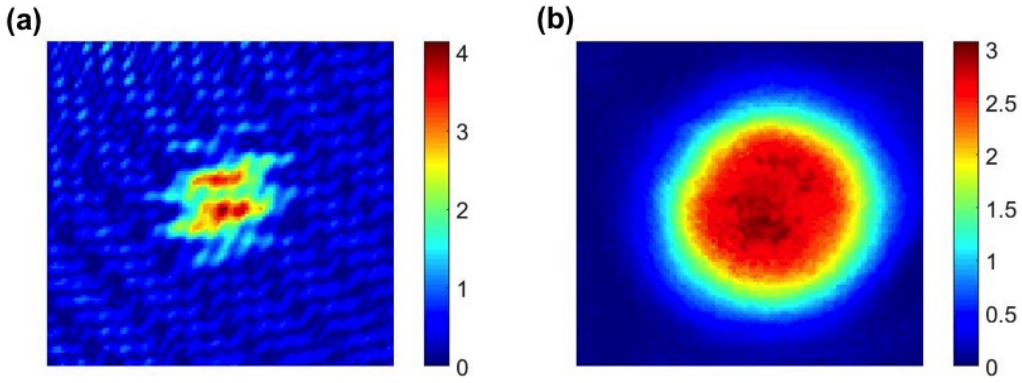


Figure 5.8: (a) OD image before we removed the ITO. The fringes between the shadow and light frames have an amplitude of about 1 OD. (b) Similar OD cloud after we removed the ITO plates. Removing the ITO made a huge difference, since the two clouds have a similar OD, and the SNR is much higher in (b).

to measure the imaging resolution to be 6.0(3) $\mu$m, which translates into a Gaussian rms width of 2.5(1) $\mu$m, or 4.7(2) lattice sites. The objective lens is not particularly well AR-coated (the reflection is 1-2% at 1064 nm). To avoid reflections that could create a superlattice, we decided to have separate beam paths for the lattice and probe beams. The probe beam propagates roughly vertically, while the lattice beam propagates at roughly 6° from vertical. The vertical lattice is not focused at the position of the atoms but rather at the retroreflecting mirror, which is a half mirror that sits above the objective lens without obstructing it.

### 5.2.1 Calibrating the saturation intensity

For reliably measuring the filling fractions of the atomic gases, it's necessary to be able to accurately measure the OD. In the past, we usually imaged dilute gases after a TOF expansion. For studying the filling fraction of the atomic insulators, we needed to image dense gases *in situ*. This introduces several systematic effects in the absorption imaging that need to be understood and characterized. Here I discuss the relevant aspects for our experiment, following the discussion from Rob Wild's PhD thesis [156].

We take three images, a shadow frame with the atoms, a light frame with the probe beam but no atoms, and a dark frame with no probe beam. These images are 2D arrays of "counts" on the CCD camera that we call $I_{\text{shadow}}$, $I_{\text{light}}$, and $I_{\text{dark}}$, respectively. The measured optical depth (OD) is then

$$OD_{\text{meas}} = \ln\left(\frac{I_{\text{light}} - I_{\text{dark}}}{I_{\text{shadow}} - I_{\text{dark}}}\right). \tag{5.11}$$

There are two main effects that give corrections to Eq. 5.11. The first is that there is a maximum OD we can measure ($\text{OD}_{\text{sat}}$) due to "bad" light, which can have the wrong polarization or frequency to be absorbed or could be light that scatters around the atoms. This "bad" light isn't absorbed and limits the contrast between the shadow and light frames. Ultimately, the dynamical range of the digital CCD camera also limits the maximum OD one can measure (a camera with $N$ bits can measure an OD up to $\ln(2^N)$) [156]. Applying the correction from $OD_{\text{sat}}$ gives a modified OD given

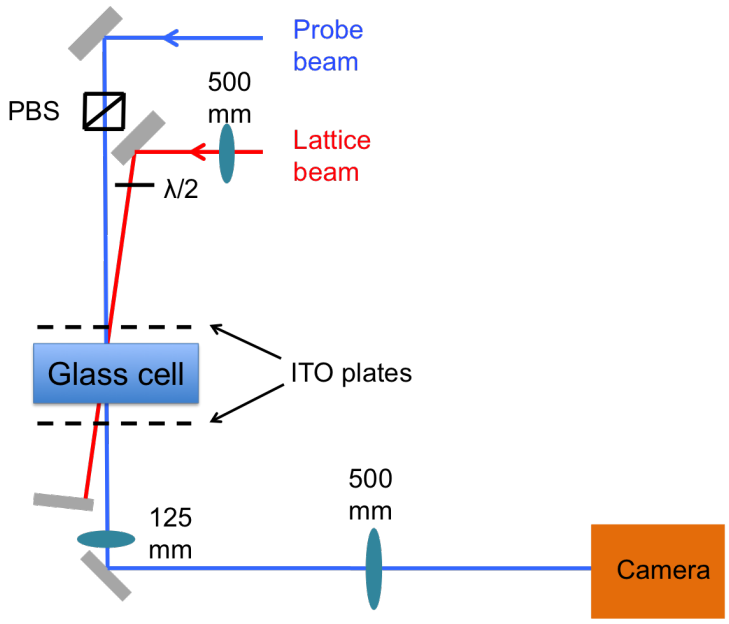


Figure 5.9: New setup for top imaging. The lattice beam is focused at a half mirror, which retroreflects the beam. The lens for the imaging beam sits below the half mirror. A PBS on the probe beam after the final mirror before the cell allows us to align the light polarization with the quantization axis, which is important for achieving a large $OD_{\mathrm{sat}}$. The position of the ITO plates is denoted by the black dashed lines above and below the glass cell. The region of glass on the ITO plates around where the probe beam and lattice beam go through was removed.

by [156]:

$$OD_{\mathrm{mod}} = \ln\left(\frac{1 - e^{-OD_{\mathrm{sat}}}}{e^{-OD_{\mathrm{meas}}} - e^{-OD_{\mathrm{sat}}}}\right). \tag{5.12}$$

There is also a correction due to imaging at finite intensity, which is a result of the probe beam saturating the transition. This gives the actual OD [156].

$$OD_{\mathrm{act}} = OD_{\mathrm{mod}} + (1 - e^{-OD_{\mathrm{mod}}})\frac{I}{I_{\mathrm{sat}}}. \tag{5.13}$$

Especially when doing absorption imaging of small clouds, we need to use short probe pulse durations so the atoms don't move significantly during the probe pulse. We find $\sim 10\,\mu$s is sufficiently short for our purposes. However, these short probe pulses are usually done at relatively high intensities. We can measure $OD_{\mathrm{sat}}$ by directly measuring very dense clouds, and we usually find $OD_{\mathrm{sat}} \sim 3.5 - 4$. To calibrate the intensity of our probe beam, we follow the procedure outlined in Ref. [156], where we image the same thermal cloud at different intensities and then fit to Eq. 5.13 (see Fig. 5.10).

### 5.2.2 Fitting the atomic distributions

When imaging from the top, we measure the two radial sides and compute the vertical size according to $\sigma_z = \sigma_r/A$, where $A$ is the aspect ratio. Using the side imaging, we measured $A = 6.4(1)$ for large thermal clouds in the combined potential of the OT and a 24 $E_R$ 3D lattice. We assume that $A$ is the same for small clouds in the lattice.

We fit the absorption images (after correcting the OD pixel by pixel) to obtain $\sigma_x$ and $\sigma_y$ ($\sigma_r = \sqrt{\sigma_x \sigma_y}$) and then fit to either a 2D Gaussian surface or a 2D TF surface to extract the peak density $\rho_0$. The Gaussian is

$$n_{\mathrm{Gauss}}(x, y) = \sqrt{2\pi}\sigma_z \rho_0 e^{-x^2/(2\sigma_x^2)} e^{-y^2/(2\sigma_y^2)}. \tag{5.14}$$

and the peak filling is

$$f_{\mathrm{Gauss}} = \frac{N(\lambda/2)^3}{(2\pi)^{3/2}\sigma_x\sigma_y\sigma_z} = \frac{NA(\lambda/2)^3}{(2\pi\sigma_x\sigma_y)^{3/2}}. \tag{5.15}$$

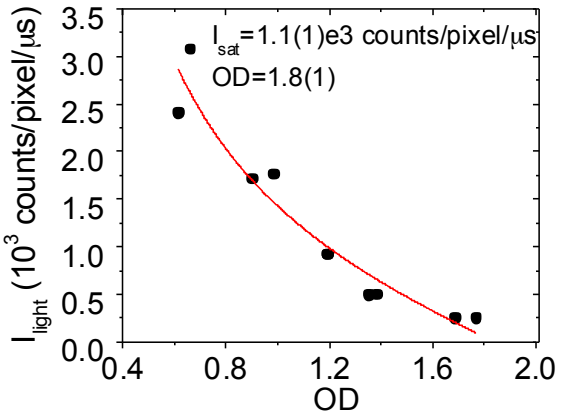


Figure 5.10: Typical calibration of $I/I_{\rm sat}$, following the procedure outlined in Ref. [156]. We image the same cloud with different intensities. The actual OD is the intersection of the curve with the $x$ axis, while the steepness of the curves tells us $I_{\rm sat}$ in counts/pixel/$\mu$s. As a measure of the intensity, we average the number of counts in the light frame around the location of the center of the atom cloud.

The 3D TF distribution is

$$n_{\mathrm{TF}}^{\mathrm{3D}}(x,y,z) = \rho_0 \left(1 - \left(\frac{x}{R_x}\right)^2 - \left(\frac{y}{R_y}\right)^2 - \left(\frac{z}{R_z}\right)^2\right). \tag{5.16}$$

Then integrating along $z$,

$$n_{\mathrm{TF}}^{\mathrm{2D}}(x,y) = \rho_0 \int_{-z_{\max}}^{z_{\max}} \left(1 - \left(\frac{x}{R_x}\right)^2 - \left(\frac{y}{R_y}\right)^2 - \left(\frac{z}{R_z}\right)^2\right) dz, \tag{5.17}$$

where $z_{\max} = R_z\sqrt{1 - \left(\frac{x}{R_x}\right)^2 - \left(\frac{y}{R_y}\right)^2}$. Doing the integral yields

$$n_{\mathrm{TF}}^{\mathrm{2D}}(x,y) = \frac{4\rho_0 R_z}{3}\left(1 - \left(\frac{x}{R_x}\right)^2 - \left(\frac{y}{R_y}\right)^2\right). \tag{5.18}$$

Integrating along $x$ and $y$ gives

$$N = \iint n_{\mathrm{TF}}^{\mathrm{2D}}(x,y)\, dx\, dy = \frac{8\pi}{15}\rho_0 R_x R_y R_z, \tag{5.19}$$

which can be inverted to give

$$f_{\mathrm{TF}} = \frac{15N(\lambda/2)^3}{8\pi R_x R_y R_z} = \frac{15NA(\lambda/2)^3}{8\pi (R_x R_y)^{3/2}}. \tag{5.20}$$

In both cases I used the fact that $\rho_0 = \frac{f}{(\lambda/2)^3}$ ($\lambda$ is the lattice wavelength), and $f$ represents the peak filling.

## 5.3 Measuring the filling of the individual atomic gases

In this section, we characterize the density of the individual atomic gases. This is an important step as fillings of $\sim 1$ particle per lattice site are necessary for our quantum synthesis scheme to be successful. We find good agreement with the conclusions from Section 1, namely that we need small number Rb clouds and large number K clouds to achieve densities $\sim 1$ particle per lattice site for each species at the trap center.

### 5.3.1 Measuring the filling of the Rb Mott insulator

Looking back at Eq. 5.5, we see that for our typical trap frequencies, the number of atoms in an $n = 1$ MI will be less than 5000. Given the aspect ratio of our trap, this implies a radial size of

about 10 $\mu$m, which is slightly less than twice the imaging resolution. For these small clouds, we begin to worry about the effect of the imaging resolution on the determination of the size of the cloud, and consequently on the determination of the filling fraction. Normally what one would do is to measure the point spread function of the imaging system and then deconvolve the images with this function. In our case, it's difficult for us to make such a small object (since a BEC of 5000 atoms is already very small and the size scales weakly with number), and also the magnification of the imaging system is such that the pixel size is not so different from the imaging resolution (this was chosen mainly due to space constraints). Instead, our approach is to model what we would expect the $n = 1$ MI to look like, given the finite imaging resolution and pixelation. We then fit the expected distribution the same way as we would fit the experimental data to obtain the filling fraction vs. number. We then compare the model's predicted filling fractions with the filling fractions measured in the experiment. Even though they're not useful for making molecules, we can also produce large MIs in the experiment, which should be much less sensitive to the effects of imaging resolution and pixelation, and we can benchmark the model by its agreement with these large clouds.

To be more specific, we calculate the expected distribution at $T = 0$ with no tunneling based on Ref. [150], using the expected trap frequencies for the combined OT and 3D lattice potential. The simulation begins by choosing a value of $\mu/U$ and then distributing the particles according to Eq. 5.2. Summing over the occupation of each site allows us to numerically find the relationship between $\mu$ and $N$. To compare with the experiment, we sum the number of atoms along the $z$ direction (following the experimental geometry where the probe beam integrates along $z$), and convolve the resulting 2D distribution with a Gaussian filter of rms width 4.5(5) lattice sites to account for the finite imaging resolution. To account for pixelation, every $6 \times 6$ group of lattice sites is mapped to one pixel (in the experiment, the pixel size is 3.2 $\mu$m $\approx 6a_{\mathrm{lat}}$). In the limit of large $\mu/U$, the density approaches a TF distribution; thus we fit both the experimental data and the distributions from the model to a TF distribution.

The distribution of a perfect MI of roughly $2.5 \times 10^3$ atoms with $\omega_r = 2\pi \times 38$ Hz and

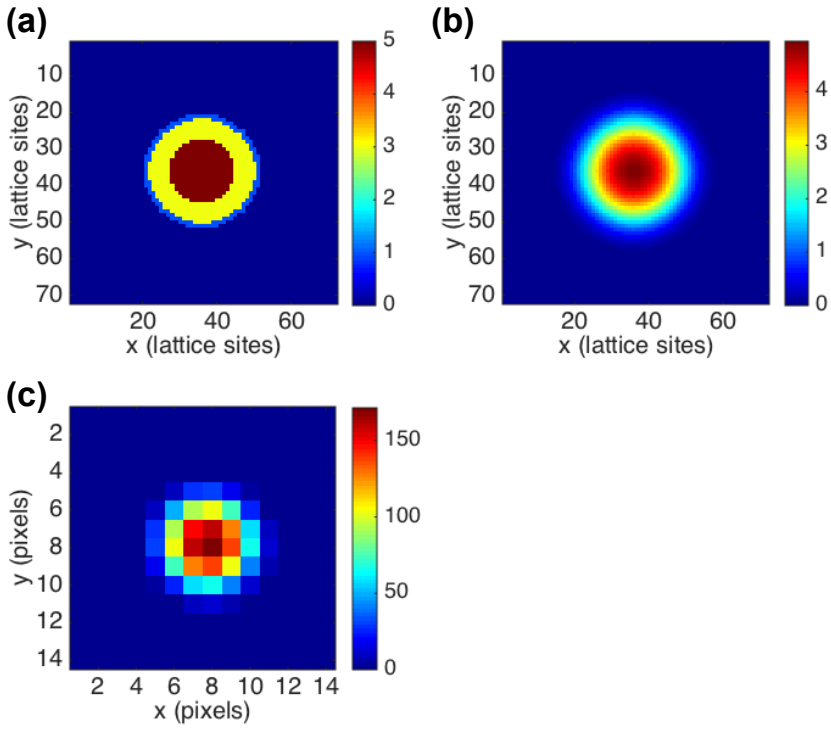


Figure 5.11: (a) 2D distribution of a perfect MI of $\sim 2.5 \times 10^3$ atoms after integrating along the $z$ direction. The colorbar represents the number of atoms. (b) Same distribution after convolving with a Gaussian filter of rms width 4 lattice sites. (c) Same distribution after binning every $6 \times 6$ sites into one pixel. This is what we would expect to see in the experimental images.

$A = 6.4$ is shown in Fig. 5.11a. Applying the Gaussian filter gives the distribution shown in panel b, and binning the distribution into pixels finally leads to the distribution shown in panel c. This is our best estimate of what the experimental distribution should look like. We then fit the model distribution to a 2D TF surface (Eq. 5.18) and extract $f_{\mathrm{TF}}$ according to Eq. 5.20, which is shown by the orange band in Fig. 5.12. The band reflects the experimental uncertainties in the trap frequencies ($\omega_r = 2\pi \times (38 \pm 2)$ Hz for Rb and $\omega_z = (6.4 \pm 0.1)\,\omega_r$) and imaging resolution. For the number of atoms, we use the number extracted from the fit, not the sum of the array (although these agree to within a few percent). Note that we do not subtract off the imaging resolution in any way. This leads to predicted fillings less than 1 for very small MIs. From the model, we can also compute the peak occupancy in the lattice, which is just $\mu/U$ promoted to the next largest integer. This is shown by the green curves in Fig. 5.12.

Experimentally, we fit the *in situ* images to a TF distribution and calculate $f_{\mathrm{TF}}$ according to Eq. 5.20. Fig. 5.12 shows the measured fillings over a range of Rb numbers of $2 \times 10^3$ to $\sim 10^5$. We find excellent agreement with the $T = 0$ model for large clouds, as expected because the imaging resolution and pixelation play less of a role; additionally, the production of larger BECs is much more robust. For smaller clouds, the agreement is also quite good, and we verify that the $n = 1$ MI occurs for small Rb numbers, less than about 5000 atoms.

### 5.3.2 Measuring the filling of the K band insulator

Fig. 5.13 shows the filling fraction for K measured for a $23E_R^{\mathrm{Rb}}$ lattice (which is only $9E_R^{\mathrm{K}}$), extracted from a Gaussian fit to the *in situ* distribution. Note that the distribution of cold fermions in the lattice is not necessarily given by Eq. 5.10. We choose a Gaussian distribution since it matches the observed density distribution well. We observe that the filling saturates to around 0.8 for K numbers $> 10^5$. At this point, the gas appears to be incompressible, since the peak filling no longer increases as we increase the number, which is indicative of the formation of a band insulator in the center of the lattice. We also see that the atoms nicely fill up the lowest Brillouin zone (Fig. 5.14), which we verify by taking band mapping images. We attribute the filling being less than 1 to finite

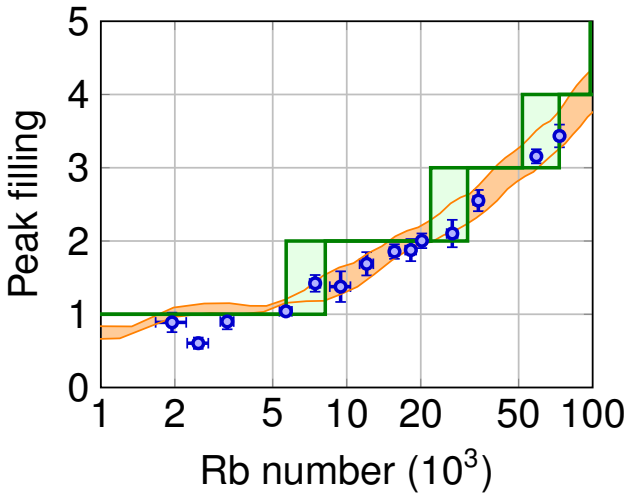


Figure 5.12: Peak filling of the Rb Mott insulator. For more than $5 \times 10^3$ atoms, the agreement with the $T = 0$ model is quite good. The orange band is a calculation of the filling extracted from $T = 0$ model, and the width reflects the uncertainty in the trap parameters. The green is the peak occupancy (restricted to be an integer) for the same distributions. Figure reproduced from Ref. [92].

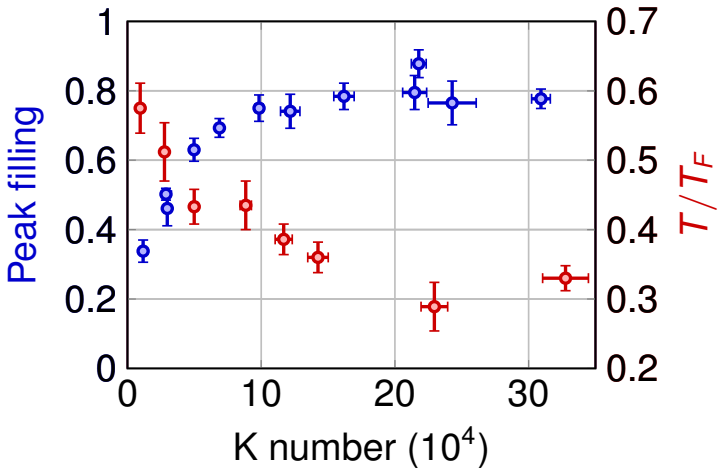


Figure 5.13: Peak filling of K vs. K number (blue points). For $N_K > 10^5$, the filling no longer significantly changes as we increase the number of atoms, which suggests the formation of an incompressible band insulator. The filling is less than 1, which we attribute to finite temperature. The red points show the measured $T/T_F$ of the K gas prior to loading the lattice. $T_F$ is calculated from the number of atoms and trap frequencies and $T$ is measured by measuring the temperature of a Rb thermal gas that's equilibrated with the K. Figure reproduced from Ref. [92].

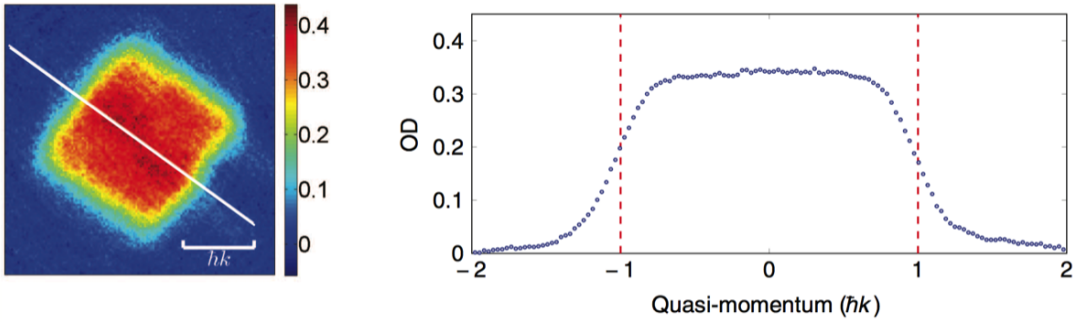


Figure 5.14: Left: Image of the K gas after 11.5 ms TOF, where the lattices were ramped off slowly to do band mapping. The colorbar shows the optical depth (OD). Right: A cut along the white line showing the distribution vs. quasimomentum (averaged along the other direction). This shows that most of the atoms are in the lowest band. Figure reproduced from Ref. [92].

temperature and tunneling, but experimental errors in the imaging procedure could also play a role. As discussed earlier, the temperature of the K gas is limited to $T/T_F \approx 0.3$ by the poor efficiency of the evaporative cooling once Rb condenses (see the red points in Fig. 5.13).

### 5.3.3 Using inelastic loss to measure the K filling

We can also measure the K filling fraction using an inelastic loss process. This work is described in Ref. [93]. The states normally used for making molecules are the $|1,1\rangle$ state for Rb and the $|9/2,-9/2\rangle$ state for K. These are the lowest energy states for both species and the mixture is stable. If we transfer Rb to the $|2,2\rangle$ state (which is $\sim 8$ GHz higher in energy at 550 G), the mixture is no longer stable and undergoes spin-changing collisions, which leads to loss of both species. At a collision energy of 1 $\mu$K, the calculated inelastic collision rate is $\beta = 6 \times 10^{12}$ cm$^3$/s [121], which corresponds to a loss timescale of $\sim 2$ ms in a 25 $E_R^{\mathrm{Rb}}$ lattice. Fig. 5.15 shows an *in situ* image of the K gas after transferring Rb to the $|2,2\rangle$ state. The hole in the center occurs where the K and Rb overlap and shows that the species are well overlapped.

Fig. 5.16a and b show typical loss curves for Rb after a 2.1 ms RF sweep that transfers Rb to the $|2,2\rangle$ state. The data show loss on two different timescales: a fast loss in a few ms, which we

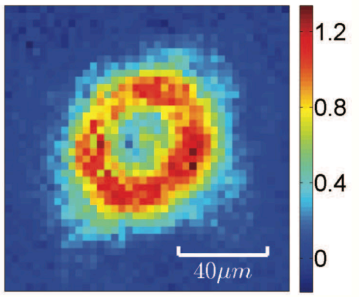


Figure 5.15: After transferring Rb to the $|2,2\rangle$ state, K and Rb undergo inelastic spin-changing collisions, leading to the loss of both species. This creates a hole in the center of the K distribution. Figure reproduced from Ref. [92].

attribute to loss on sites that initially have a K and Rb atom, followed by a slower decay, which we attribute to tunneling of atoms followed by inelastic loss once they get on the same site. The dashed lines are a fit to the sum of two exponential decays with different time constants. We can extract the fraction of Rb that is lost on the shorter timescale from these fits. Fig. 5.16c plots this fraction lost on the shorter timescale vs. Rb number. The solid curve shows the expected loss for a MI with temperature $T/J_{\mathrm{Rb}} = 15$ and total radial harmonic confinement $\omega_r = 2\pi \times 33$ Hz. The shaded band reflects a 10% uncertainty in the trap frequency and 30% uncertainty in the temperature. For small Rb numbers, we expect to have only one Rb per site, and the fraction lost should be equal to the K filling fraction (assuming no double occupancy of K). From the fit, we extract a K filling fraction of 77(2)%, which is in good agreement with the direct measurements shown in Fig. 5.13. For higher Rb numbers, multiple occupancies cause a reduction of the fractional loss, assuming that one Rb and one K are lost per inelastic collision.

## 5.4 Studying the dual insulator

In the last section, we showed that both atomic species can have fillings near unity. However, the optimal atom number for the two species is very different: less than $5 \times 10^3$ for Rb but more than $10^5$ for K. A natural concern is that the K will act as a heat bath and melt the Rb MI. There have been a few recent experiments looking at the effect of a bath of fermions on the superfluid-

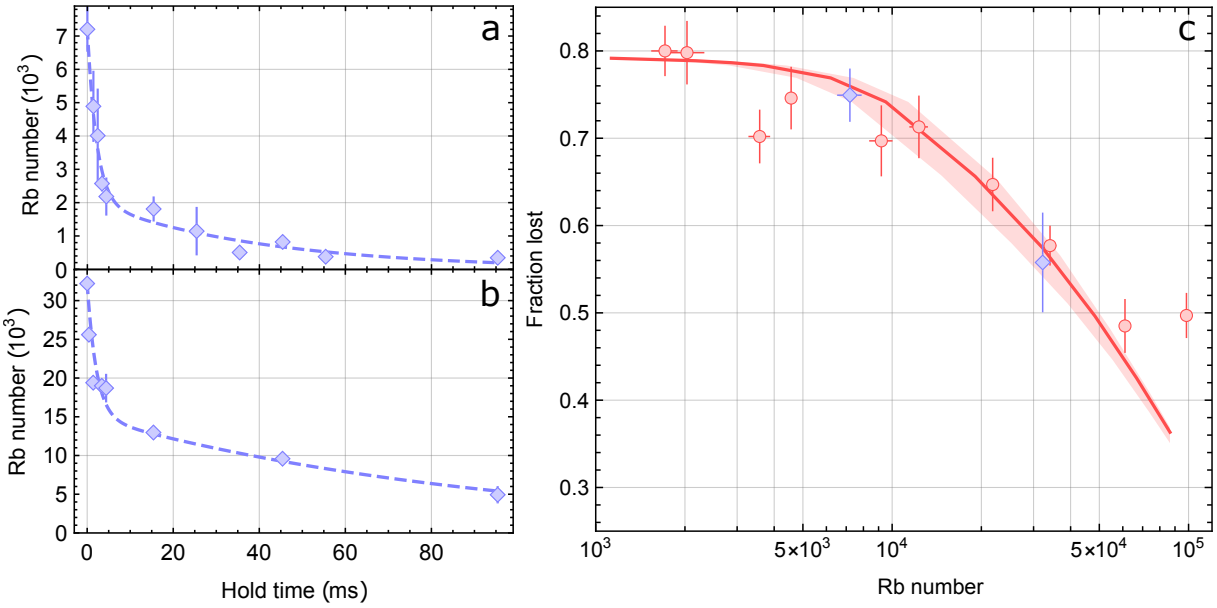


Figure 5.16: An alternative way to measure the filling fraction of K is to look at the loss of Rb induced by spin-changing collisions, in the limit of a small number of Rb atoms. The fits in (a) and (b) are double exponential fits, and the points in (c) are either the ratio of the coefficients of these two exponential fits (blue diamonds) or the fraction of atoms remaining after 8 ms (red circles). Figure reproduced from Ref. [93].

Mott insulator transition [157, 158]; however, these experiments focused on the visibility of the interference pattern, the lattice depth at which the coherence disappears, and the sharpness of the transition. We're more interested in the filling fraction of the Rb MI in the presence of a large bath of K.

When loading the dual insulator at low temperatures, one might expect that attractive interactions will enhance the overlap of the two species [145, 159]. However, for the relatively hot K temperatures in our system, we see that nonzero interspecies interactions detrimentally affect the Rb filling fraction (Fig. 5.17). However, at $a_{\mathrm{KRb}} = 0$, $f_{\mathrm{Rb}}$ is unaffected by the presence of K. We attribute the degradation in the filling when $a_{\mathrm{KRb}} \neq 0$ to the fact that the BEC fraction is significantly less than 1. To directly verify that heating from the K is playing a large role, we measured the dependence of filling on interaction strength for two K temperatures. The $f_{\mathrm{Rb}}$ dependence on $a_{\mathrm{KRb}}$ is more sensitive when the K gas is hotter (Fig. 5.18). However, at $a_{\mathrm{KRb}} = 0$, $f_{\mathrm{Rb}}$ is the same for the two cases. This highlights that the K and Rb distributions are basically independent at $a_{\mathrm{KRb}} = 0$.

## 5.5 Putting all of the ingredients together

The first step of molecule production is magnetoassociation, where we adiabatically sweep the magnetic field across the Feshbach resonance at $B_0 = 546.6$ G from high to low field. As shown in the previous section, we want to load the lattice at $a_{\mathrm{KRb}} = 0$ to preserve the filling of the MI. Loading the lattice at $a_{\mathrm{KRb}} = 0$, we would then first need to jump the magnetic field above the resonance so that we can initiate the magnetoassociation process. This jump should be diabatic to avoid promoting atoms to higher bands [160]. This effect will be discussed further in the next chapter. The high atomic densities on isolated lattice sites make it difficult to sweep the field fast enough. To circumvent this issue, we use an RF pulse to transfer K to the $|9/2, -7/2\rangle$ state, which doesn't experience the 546.6 G resonance. After ramping $B$ to 563 G, we transfer the K back to the $|9/2, -9/2\rangle$ state and then proceed with the magnetoassociation. The final sweep goes from 563 G to 545.6 G in 5 ms. We use STIRAP to transfer the Feshbach molecules

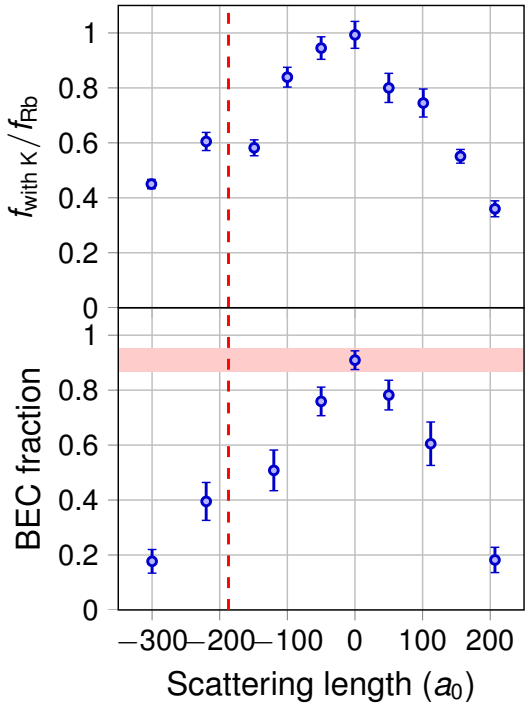


Figure 5.17: Top: $f_{\text{Rb}}$ vs. $a_{\text{KRb}}$. The filling is normalized to $f_{\text{Rb}}$ with Rb alone. For points below the resonance, the scattering length was ramped from around $-120\,a_0$ to the final value between 140 ms and 40 ms prior to loading the lattices. For points above the resonance, the evaporation was done above the resonance and the scattering length was ramped from around $-220\,a_0$ to the final value with the same timing. Away from $a_{\text{KRb}} = 0$, the filling degrades. Bottom: Initial BEC fraction vs. $a_{\text{KRb}}$, measured after holding in the OT for 150 ms. Away from $a_{\text{KRb}} = 0$, the BEC fraction is lower, likely from equilibrating with the hot K gas. The BEC fraction with Rb alone is denoted by the red shaded region. Figure reproduced from Ref. [92].

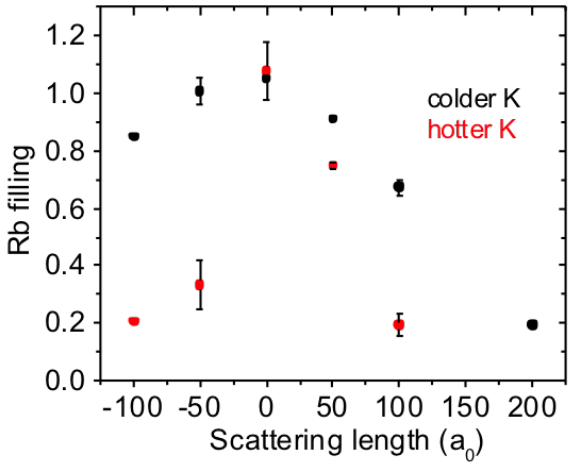


Figure 5.18: We looked at how the filling of Rb vs. interspecies interactions depends on the temperature of K. Here, the hot condition corresponds to $T/T_F \approx 0.7$ while the cold condition corresponds to $T/T_F \approx 0.3 - 0.4$. In the hotter case, $f_{\mathrm{Rb}}$ more strongly depends on $a_{\mathrm{KRb}}$, but at $a_{\mathrm{KRb}} = 0$ the filling is the same for both cases, which highlights that the densities of the two species are independent at $a_{\mathrm{KRb}} = 0$. Only data with $(6 - 10) \times 10^3$ Rb atoms are shown.

to the rovibrational ground-state. For these experiments, the typical one-way STIRAP efficiency is $89 \pm 4\%$. Once the molecules are in the ground state, we remove the unpaired K atoms with resonant light on the $|9/2, -9/2\rangle \rightarrow |11/2, -11/2\rangle$ cycling transition and we remove the Rb atoms with a series of adiabatic rapid passages to the $|2, 2\rangle$ state followed by pulses of resonant light on the $|2, 2\rangle \rightarrow |3, 3\rangle$ cycling transition. To detect the ground-state molecules, we STIRAP them back to Feshbach molecules, dissociate the Feshbach molecules by ramping $B$ back to 563 G in 1 ms, and finally image the resulting K atoms. We can also image the molecules by measuring the number of dissociated Rb, and the numbers agree within experimental uncertainty.

Since Rb is by far the minority species, we first looked at the number of Feshbach molecules produced vs. Rb number, since the best we can do is to convert all of the Rb to molecules. This is shown in Fig. 5.19a. Note that we only convert a very small fraction of the K to molecules (less than 5%). This makes the measurement challenging, since we can't completely remove the unpaired K atoms without also killing the Feshbach molecules. Rather, we just hide them in the $|9/2, -7/2\rangle$ state by using an RF pulse that can discriminate atoms from Feshbach molecules. The atoms in the $|9/2, -7/2\rangle$ state are invisible to the imaging (since the imaging light is 80 MHz detuned). Since we typically operate in lattices $\sim 10\, E_R^{\mathrm{K}}$, the K atoms are still mobile and can collide with the Feshbach molecules. Also, the RF pulse is only $\sim 99\%$ efficient, and the small background of K atoms in the $|9/2, -9/2\rangle$ state is not so much less than the number of molecules we create.

To directly see a positive effect of the spin flips, we did two experiments. In the first, we loaded the lattice at $a_{\mathrm{KRb}} = 0$ and compared the final filling of ground-state molecules with and without doing the spin flips. We observe that the filling is about 60% higher when we do the spin flips. In the second experiment, we compared the case of loading the lattice at $a_{\mathrm{KRb}} = 0$ and then doing the spin flips against a case where we loaded the lattice above the resonance (at around $a_{\mathrm{KRb}} = -220\, a_0$). This comparison is shown in Fig. 5.20 (note that the filling fraction of the ground-state molecules is plotted), where we see that for small Rb numbers there is a clear win to loading the lattice at $a_{\mathrm{KRb}} = 0$ and doing the spin flips.

We then imaged the ground-state molecules *in situ*, after holding in a $25 E_R^{\mathrm{Rb}}$ lattice for 40

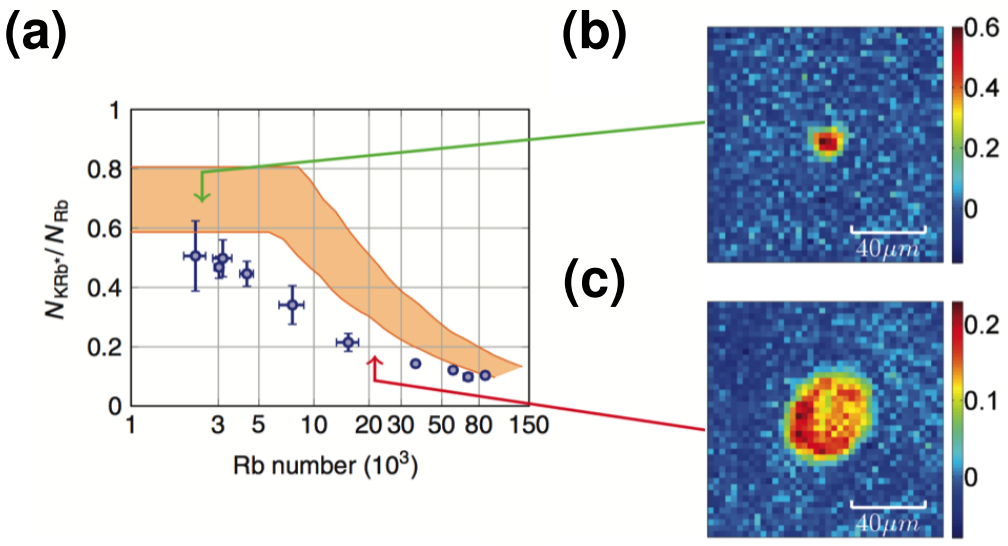


Figure 5.19: (a) Conversion efficiency of making Feshbach molecules vs. Rb number (Rb is the minority species). In the limit of small Rb number, the conversion is around 50%. The shaded band shows the predicted conversion, which is the product of the measured K filling fraction ($0.80 \pm 0.05$), the calculated fraction of Rb atoms on singly occupied sites (from our simple model), and the conversion efficiency of preformed pairs reported in Ref. [72] ($0.87 \pm 0.13$). (b) and (c) *In situ* images of the ground-state molecules after holding in the lattice for 40 ms, for high conversion (b, average of three images) and low conversion (c, average of seven images). The high conversion case corresponds to a filling of around 25% (see text for details). The scale bar is 40 $\mu$m. Figure reproduced from Ref. [92].

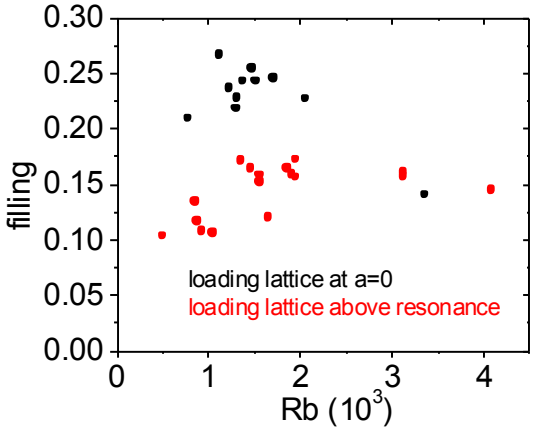


Figure 5.20: Filling of ground-state molecules vs. Rb number for two different lattice loading schemes. For small Rb numbers, loading the lattice at $a_{\mathrm{KRb}} = 0$ definitely leads to higher ground-state molecule fillings.

ms (Fig. 5.19b and c). Since the molecules are created within the confines of the Rb MI, we fit the images to a TF distribution. For the case of low conversion (c), the filling fraction is very low and there is a hole in the center of the molecular distribution. This is consistent with the central lattice sites containing multiple Rb atoms and not making molecules. This condition corresponds to starting with about $2.5 \times 10^4$ Rb atoms. When starting with about 2500 Rb atoms (b), we observe a much denser molecular sample. A TF fit yields $7.9(5) \times 10^2$ molecules with a TF radius of $12.0(2)\,\mu$m.

There are two ways we can extract the filling. One is to compute the filling directly from the TF fit. Doing this gives $f_{\mathrm{mol}} = 0.27(2)$. The other is to determine the filling by comparing the TF width of the molecular cloud to that of our simulated $T = 0$ Rb distribution and assume a uniform conversion of Rb into molecules. The molecules are best described by a distribution that corresponds to an initial Rb number of $3.2(4) \times 10^3$. Taking the ratio of the measured number of molecules to this number, we extract $f_{\mathrm{mol}} = 0.25(4)$, which is consistent with the result from direct fitting. From the product of the measured $f_{\mathrm{Rb}}$, $N_{\mathrm{KRb}^*}/N_{\mathrm{Rb}}$, and the STIRAP efficiency, one might expect $f_{\mathrm{mol}} = 0.35$. One possible explanation for the lower measured filling is molecular loss caused by the K atom removal.

As shown in Table 2.1, the different polarizability and mass of KRb means that a $25E_R^{\mathrm{Rb}}$ lattice corresponds to $62E_R^{\mathrm{KRb}}$. In such a deep lattice, the molecule tunneling rate is negligible. In this case, we can estimate the entropy per molecule from the filling fraction, with some assumption about the shape of the distribution. As shown in Ref. [161], the entropy per particle in a uniform lattice with average filling $f$ is

$$\frac{S}{N} = \frac{-k_B}{f}\big(f\ln(f) + (1-f)\ln(1-f)\big). \tag{5.21}$$

Our quantum synthesis approach likely leads to a molecular distribution that is much more homogeneous than if we were to adiabatically load a Fermi gas of molecules into the lattice. The K Fermi gas is roughly homogeneous within the confines of the Rb MI, and the entropy per particle in this region is roughly that of a uniformly filled lattice with $f = 80\%$, which is about $0.6\,k_B$. Applying

the same argument to the molecules with $f_{\mathrm{mol}} = 25\%$, we find the entropy per molecule is about $2.2\,k_B$. For comparision, the entropy associated with the lowest temperatures we have achieved in the harmonic trap ($T/T_F \approx 1$) is about $6\,k_B$ per molecule.

## 5.6 Conclusion and outlook

This chapter presented a detailed investigation of the molecule production in the 3D optical lattice. It was very important to diagnose each step in the molecule creation process in order to realize a significant increase in the final molecule filling fraction. In particular, it was very important to have a clear understanding of the appropriate sizes the Bose and Fermi gases should have in order to have roughly unit filling in the center of the lattice. Turning off the Bose-Fermi interactions when loading the lattice was also important. Finally, flipping K to a noninteracting spin state when crossing the resonance the wrong way was also a crucial step in maximizing the filling.

At the achieved filling fractions of $\sim 25\%$ the system should be reasonably well-connected, given our simple argument based on percolation theory. Additionally, given the results of the simulation in Section 4.6, the propagation of excitations at 25% filling should be reasonably fast. The number of molecules created at higher fillings is quite low, but is appropriately sized for quantum gas microscopy [16, 17]. There is no fundamental limit to our dual insulator approach, and I foresee filling fractions $> 50\%$ should be attainable in the new experiment. Two of the biggest issues that will likely need to be addressed in order to increase the filling further are that the K is too hot and the $n = 1$ MIs are small.

Colder K will help in many ways. We already see direct evidence of the K temperature on the Rb filling in the data of Fig. 5.18. Reducing the temperature at constant atom number and harmonic confinement leads to higher filling fractions. Having colder K should allow us to reduce the harmonic confinement and achieve larger $n = 1$ MIs. The temperatures we achieved in Ref. [92] seem to be limited by the evaporative cooling, and to get K colder while still having pure BECs, the evaporation strategy may need to be modified. One idea would be to transfer some of the K

to the $|9/2, -7/2\rangle$ state towards the end of the evaporation and allow the two spin components to thermalize with each other instead of with Rb (however, only one of the spin components is actually useful for making molecules).

In principle, there's not a huge problem with having to use such small Rb clouds, but producing them reliably in the presence of a huge K cloud is challenging. One way to make the Rb MI bigger is to have less harmonic confinement; however, to keep the K filling constant we would require colder K. Another option is to use a shorter wavelength lattice. The onsite interaction energy $U$ is proportional to $1/\lambda_L^3$, where $\lambda_L$ is the lattice wavelength (the dipolar interactions also get stronger by $1/\lambda_L^3$). This means that the chemical potential $\mu$ can be larger while still satisfying $\mu/U < 1$. The challenge is to find a wavelength that's favorable for K, Rb, and the ground-state molecules. For example, 532 nm would be nice, since high-power lasers are readily available, but we measured the lifetime of ground-state molecules to be quite short at that wavelength. Another choice we considered is 755 nm. At that wavelength, the size of the $n = 1$ MI can be more than an order of magnitude larger than at 1064 nm, and K and Rb feel the same lattice depth in units of their respective recoil energies. Experimentally, we observed that the lifetime of ground-state molecules is quite long at this wavelength; however, the real part of the polarizability is small and opposite in sign to the Rb and K (so the beam would be red-detuned for the molecules while being blue-detuned for both K and Rb), which is not so ideal. More work will be required in the future to determine whether shorter wavelength lattices offer advantages in molecule production.

# Chapter 6

## Studying doublons in the lattice

In the previous chapter, we devised a strategy to optimize the loading of the initial quantum gas mixture in the lattice. This led to a significant increase in the molecule filling fraction; however, the actual molecule production from preformed pairs was not examined that closely. In this chapter, we investigate the molecule production more thoroughly, to try to understand any effects that might limit molecule production. In particular, we want to isolate any effects that would cause preformed pairs to not make molecules. To do this, we leverage our capabilities in producing ground-state molecules and prepare a distribution where lattice sites are either empty or occupied by a doublon composed of an interacting K and Rb atom. This well-defined initial state allows us to address limitations in the molecule production process by measuring the efficiency at which these doublons are converted back to molecules, after varying the atomic tunneling rates, interspecies interactions, and adiabaticity of magnetic-field sweeps through a higher partial-wave Feshbach resonance.

There are two main ways that the doublons can fail to make molecules: the doublon makes something other than an $s$-wave molecule, or one of the atoms (especially the lighter K atom) tunnels off of the site before making a molecule. A $d$-wave resonance about 1 Gauss above the $s$-wave resonance can play a detrimental role in molecule production in the lattice. If we ramp across the $d$-wave resonance too slowly, it's very likely that we will make $d$-wave molecules (when sweeping from high to low field) or atoms with an excitation in the relative coordinate (when sweeping from low to high field). Because of the high onsite density in the lattice, the magnetic-field sweep rate necessary to be diabatic with respect to the $d$-wave resonance is not so different than our typical

sweep rate for making molecules. We show that in the limit of deep lattices and fast magnetic-field sweeps, we get near unity conversion of preformed pairs. We see that strong Bose-Fermi interactions hold the doublons together, even for weak lattices where the K would otherwise be very mobile; for weaker onsite interactions, we see evidence for K tunneling.

In Section 1, I discuss the preparation and measurement of doublons in the lattice. In Section 2, I describe our investigation of the role of the $d$-wave resonance on molecule production in the lattice. In Section 3, I discuss the interplay between tunneling and interactions. This chapter is based on Ref. [93], of which I am a coauthor.

## 6.1 Experimental setup

The experimental scheme for creating and studying a lattice of doublons is shown in Fig. 6.1. After making ground-state molecules in the lattice, we can cleanly remove the unpaired atoms, STIRAP back to Feshbach molecules, and then dissociate the Feshbach molecules by ramping the magnetic field above the resonance to a field $B_{\mathrm{hold}}$. This realizes a lattice where each site is either empty or occupied by a doublon comprised of a K and Rb atom. We then let the system evolve for some time $\tau$. To measure the doublon fraction after the evolution, we measure the conversion of preformed pairs to molecules, following the same protocol described in Section 3.6.

## 6.2 Effect of the $d$-wave resonance

In our normal magnetoassociation protocol, we start far above the resonance (by usually more than 10 Gauss), and then ramp below the $s$-wave resonance in a few ms. In doing this, we cross a narrow $d$-wave resonance that is located about 1 G above the 3 G-wide $s$-wave resonance. A schematic of the two resonances is shown in Fig. 6.2a. Normally, the $d$-wave resonance wouldn't play a role in the molecule production because it's so narrow; however, in the lattice, it can play a larger role since the onsite density is orders of magnitude higher than in a regular optical trap. Crossing the $d$-wave resonance too slowly from high to low $B$ field will produce $d$-wave molecules (Fig. 6.2b), which are not coupled to the ground state by the subsequent STIRAP pulses. Crossing

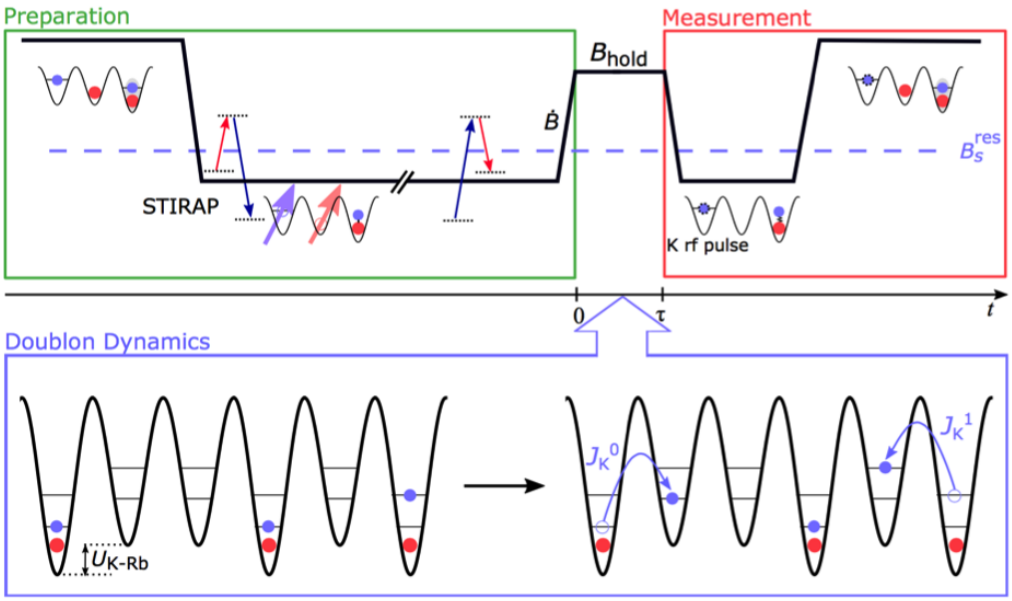


Figure 6.1: We start with a mixture of K (blue balls), Rb (red balls) and doublons (pair grouped with gray background) in a 3D lattice. We sweep the magnetic field across the $s$-wave Feshbach resonance at 546.6 G to create Feshbach molecules. These molecules are then transferred to the ro-vibrational ground state via STIRAP. We then remove the unpaired atoms with resonant light, reverse the STIRAP process to recreate Feshbach molecules, and then sweep the magnetic field above the resonance to dissociate the molecules and create a lattice of doublons. After holding for a time $\tau$, we measure the remaining doublon fraction by converting to Feshbach molecules again. To discriminate between Feshbach molecules and free K atoms, we use an RF pulse to transfer unpaired K atoms to the dark $|9/2, -7/2\rangle$ state (blue ball with dashed black edge). The bottom panel shows the possible dynamics during the hold time. Doublons have an energy shift due to the onsite interaction energy $U^0_{\text{K-Rb}}$. The K tunneling rates in the ground and first excited band are $J^0_{\text{K}}$ and $J^1_{\text{K}}$, respectively. Since Rb experiences a deeper lattice, the Rb tunneling rate is much slower and is irrelevant for the experiments discussed in this chapter. Figure reproduced from Ref. [93].

the $d$-wave resonance diabatically has no impact and is the desirable scenario. We seek to determine how fast we need to ramp the magnetic field across the $d$-wave resonance in order to be diabatic.

First, it is useful to understand the possible states we can have in the lattice system. These are shown in Fig. 6.2b. For simplicity, the states are illustrated for a harmonic potential where both species have the same trap frequency $\omega$. There are five relevant states: $s$-wave molecules ①, atoms in the ground band above both resonances ②, atoms with an excitation in the relative coordinate ③, free atoms below the resonance ④, and $d$-wave molecules ⑤. The ideal trajectory for making $s$-wave molecules is to follow the lower solid arrow from ② to ①. Being adiabatic with respect to the $d$-wave resonance would correspond to going from ① to ③ (if ramping from low to high field) or ② to ⑤ (if ramping from high to low field).

We investigate the $d$-wave resonance by varying the rate of the sweep, $\dot{B}$, that creates doublons, as well as $B_{\mathrm{hold}}$. For these experiments, the lattice depth is $30 - 35E_R$ (unless otherwise noted, the lattice depths are in units of the Rb recoil energy). We then measure the molecule conversion after $\tau = 1$ ms using a 16.8 G/ms sweep for the final association. Fig. 6.2c shows the measured conversion vs. $\dot{B}$ after sweeping from 545.6 G to 562.4 G. For the largest $\dot{B}$, the conversion is near unity. This high conversion fraction is crucial for creating molecules in the lattice at high filling.

Using a Landau-Zener formalism [162], we can fit this data to extract the width of the $d$-wave resonance. The probability to cross the resonance diabatically (and proceed to create $s$-wave Feshbach molecules) is $P_{\mathrm{dia}} = \exp(-A/|\dot{B}|)$, where $A$ depends on the on-site densities and on the parameters of the Feshbach resonance. We approximate the sites of the deep optical lattice as harmonic oscillators [162], so

$$A = \frac{4\sqrt{3}\omega_{\mathrm{HO}}|a_{\mathrm{bg}}\Delta_d|}{L_{\mathrm{HO}}}, \tag{6.1}$$

where $\omega_{\mathrm{HO}}$ is the harmonic trap frequency for the two atoms' relative motion, $L_{\mathrm{HO}} = \sqrt{\hbar/(\mu\omega_{\mathrm{HO}})}$ is the corresponding harmonic oscillator length, $\mu$ is the reduced mass, $\Delta_d$ is the width of the $d$-wave resonance, and $a_{\mathrm{bg}}$ is the background scattering length. We ignore the coupling between

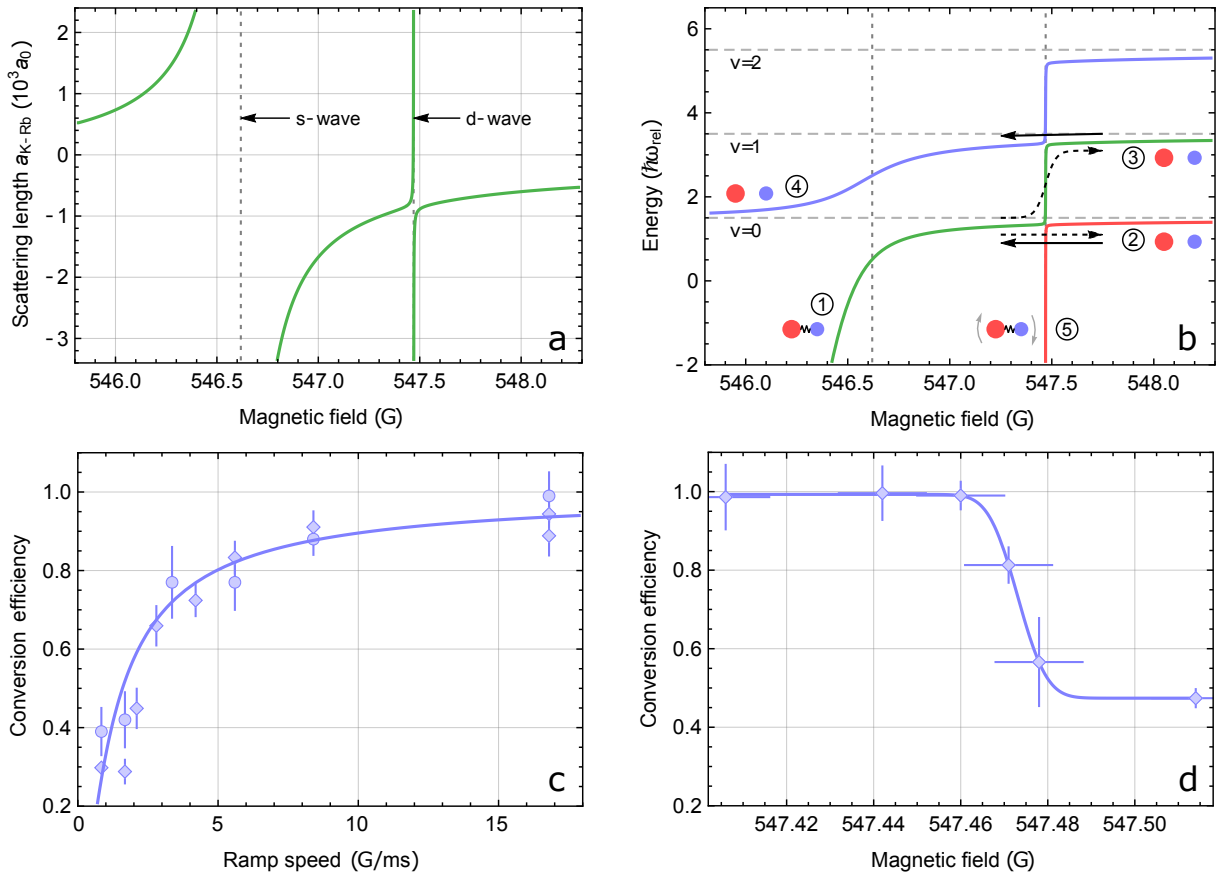


Figure 6.2: (a) The $s$-wave Feshbach resonance is used to create molecules. About 1 Gauss above the $s$-wave resonance there is a narrow $d$-wave resonance. (b) Pair states for K and Rb in a 1D lattice (we treat the 3D lattice as separable along the three directions). See the text for details. (c) Measurement of molecule conversion efficiency at 35 $E_R$ (circles) and 30 $E_R$ (diamonds), after ramping from 545.6 G to 562.4 G and varying $\dot{B}$. The data for 30 $E_R$ is exponentiated by $(35/30)^{3/4}$ to account for the expected dependence of $P_{\text{dia}}$ on lattice depth. The solid curve shows a fit to a Landau-Zener avoided crossing, which yields $|\Delta_d| = 9.3(7)$ mG. (d) The magnetic field at which the resonance occurs is determined by sweeping upwards to various fields at 1.8 G/ms and then downwards at 18 G/ms. By fitting to an error function, we determine the resonance is at 547.47(1) G in a 35 $E_R$ lattice. Figure adapted from Ref. [93].

the center of mass and relative coordinates and take $\omega_{\mathrm{HO}} = \sqrt{(m_{\mathrm{Rb}}\omega_{\mathrm{K}}^2 + m_{\mathrm{K}}\omega_{\mathrm{Rb}}^2)/(m_{\mathrm{Rb}} + m_{\mathrm{K}})}$. The scattering length depends on $B$ in the following way:

$$a(B) = a_{\mathrm{bg}}\left(1 - \frac{\Delta_s}{B - B_s^{\mathrm{res}}} - \frac{\Delta_d}{B - B_d^{\mathrm{res}}}\right). \tag{6.2}$$

Since $\Delta_d \ll \Delta_s$, this can be simplified near the $d$-wave resonance to

$$a(B) = a_{\mathrm{bg}}\left(1 - \frac{\Delta_s}{B_d^{\mathrm{res}} - B_s^{\mathrm{res}}} - \frac{\Delta_d}{B - B_d^{\mathrm{res}}}\right), \tag{6.3}$$

which can be approximated as

$$a(B) \approx a'_{\mathrm{bg}}\left(1 - \frac{\Delta'_d}{B - B_d^{\mathrm{res}}}\right), \tag{6.4}$$

where $a'_{\mathrm{bg}} = a_{\mathrm{bg}}\left(1 - \frac{\Delta_s}{B_d^{\mathrm{res}} - B_s^{\mathrm{res}}}\right)$ and $\Delta'_d = \frac{\Delta_d}{1 - \Delta_s/(B_d^{\mathrm{res}} - B_s^{\mathrm{res}})}$. We fit the data from Fig. 6.2c to $\exp(-A/|\dot{B}|)$, extract $A = 1.10(7)$ G/ms, and then get $\Delta_d = a'_{\mathrm{bg}}\Delta'_d/a_{\mathrm{bg}}$. The results are $\Delta'_d = -2.0(2)$ mG and $\Delta_d = -9.3(7)$ mG. For the $s$-wave resonance, $A$ is about 300 times larger. The probability to be adiabatic with respect to both resonances is shown in Fig. 6.3.

Fig. 6.2d shows the measured conversion vs. $B_{\mathrm{hold}}$ for a slow 1.8 G/ms sweep. From Fig. 6.2c, we see that this sweep rate corresponds to about a 50% probability to be diabatic. For $B_{\mathrm{hold}}$ below the $d$-wave resonance, we observe conversions near unity, but for $B_{\mathrm{hold}}$ above the $d$-wave resonance, we observe conversions $\sim 50\%$. By fitting the data to an error function, we extract the position of the resonance to be 547.47(1) G, in agreement with previous experiments that looked at atom loss [163, 164].

The precise determination of the width of the $d$-wave resonance enables us to determine its significance in molecule creation. In the work described in the previous chapter, we used $\dot{B} = 3.5$ G/ms for the molecule association, which gives a $\sim 70\%$ probability to be diabatic with respect to the $d$-wave resonance. This suggests we may have created a significant fraction of $d$-wave molecules that are dark to our detection, which may have limited the filling fractions we achieved. Future work will be necessary to confirm this hypothesis.

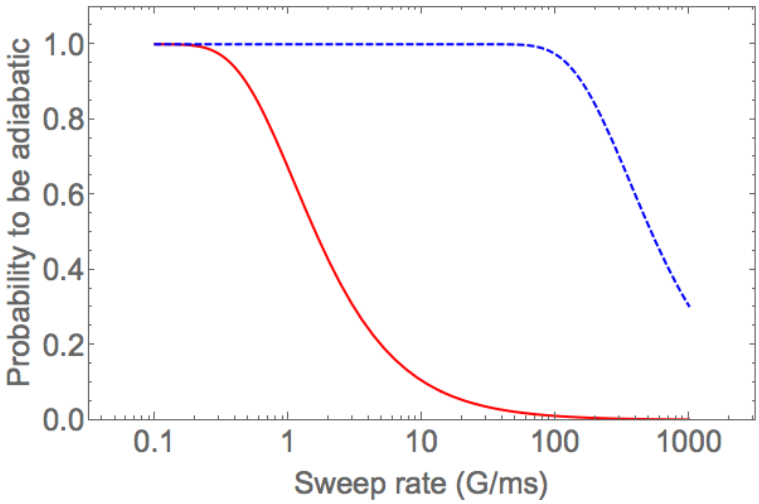


Figure 6.3: Probability to be adiabatic with respect to the $s$-wave (dashed blue) and $d$-wave (solid red) resonances in the lattice, using Eq. 6.1 with $\omega_{\mathrm{HO}} = 2\pi \times 30.4$ kHz (which corresponds to 35 $E_R$). For any experimentally accessible $\dot{B}$, we are adiabatic with respect to the $s$-wave resonance. For $\dot{B} > 20$ G/ms, the effect of the $d$-wave resonance is negligible. The timescales are different by about a factor of 300 between the two resonances.

## 6.3 Detrimental effects due to tunneling

In order to acheive high lattice fillings, we require not only a large fraction of sites that contain doublons, but also that these doublons are not lost due to tunneling or collisions before converting to molecules. By varying both the lattice depth and $B_{\mathrm{hold}}$, we can explore the interplay between tunneling and interactions. In our system, $s_{\mathrm{K}} = 0.4\, s_{\mathrm{Rb}}$ (recall $s = U_{\mathrm{lat}}/E_R$), so K tunnels faster than Rb. Fig. 6.4 shows the measured doublon fraction vs. lattice depth for different interaction strengths ($\tau = 1$ ms). For these experiments, the ramp time was fixed, so $\dot{B}$ depends on $B_{\mathrm{hold}}$ and ranges from 5 to 19 G/ms. The data are multiplied by a factor to account for these ramps not being perfectly diabatic with respect to the $d$-wave resonance.

We see that for deep lattices, the conversion is near unity for all interaction strengths, which is just trivial localization of the doublons (even resonant tunneling would be slow). For shallower lattices, the conversion is still high for very strong interactions ($a_{\mathrm{KRb}} = -1900\, a_0$), because the strong onsite interaction $U^0_{\text{K-Rb}}$ suppresses tunneling to empty sites, which are very far off-resonant. This modification of tunneling from interactions has been seen in other experiments, which studied the stability of repulsively interacting atom pairs [165] and the modification of tunneling of fermions due to interactions with bosons [166]. In our case, the interactions are attractive, but the sign doesn't really matter, as tunneling is off-resonant for either sign of the onsite interactions. For weaker interactions, the conversion decreases for shallower lattices, since the interactions are not strong enough to hold the doublons together.

The solid curves in Fig. 6.4 show the expected evolution of a single doublon in the lattice, which generally describes the data well. Here, only K tunneling is considered. For small doublon fractions, the solid curves start to disagree with the data, because there is a finite probability that the K will find another Rb partner. The dashed lines account for this by simulating the dynamics with a peak filling of 10%.

The relevance of this effect to molecule production is a little misleading, since this data was taken with a relatively dilute lattice (typically around 10% of the sites are initially occupied by

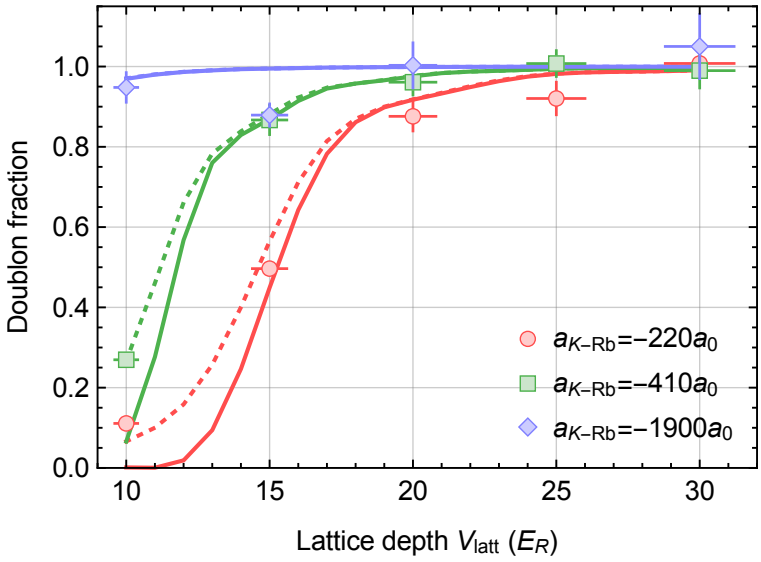


Figure 6.4: The remaining doublon fraction after a 1 ms hold in the lattice vs. lattice depth for different interaction strengths. For strong attractive interactions the conversion is high for any lattice depth, which is due to the doublons being held together by the strong onsite interactions. For weaker interactions, the conversion decreases for shallower lattices, which we attribute to the lighter K atoms tunneling. The solid curves show the expected evolution of a single doublon, while the dashed curves simulate the dynamics with a peak filling of 10%, which accounts for the possibility that the K will find another Rb atom after it tunnels. Figure reproduced from Ref. [93].

a doublon), and so the K have many sites to which they can tunnel. When we actually make molecules, the fillings of the atomic gases are much higher, and the K atoms have many fewer sites to which they can tunnel. However, the most important result of this study is that the conversion of preformed pairs is near unity, in the limit of fast magnetic-field sweeps and deep lattices.

## 6.4 Conclusions

In this chapter, we showed the important roles that tunneling, interspecies interactions, and magnetic-field sweep rates play in the conversion of doublons to molecules via magnetoassociation. Most importantly, we verified that we can get near unity conversion of preformed pairs, assuming we use sufficiently deep optical lattices and sufficiently fast magnetic-field sweeps. While we focused specifically on the $^{40}$K$^{87}$Rb mixture, our conclusions should be applicable to other heteronuclear systems, where narrow Feshbach resonances might exist in the vicinity of wider ones used for producing Feshbach molecules, and where the two species might have different mobilities in the lattice.

# Chapter 7

## Conclusions and future work

Over the last six years, the field of ultracold polar molecules has made immense strides. Our group has learned how to control and shut off the chemical reactions that make the bulk gas unstable, and that were initially viewed as a huge obstacle to studying quantum many-body physics with long-range dipolar interactions. With the chemical reactions under control, we learned how to induce and probe coherent long-range interactions between the molecules, which should lead to many interesting future experiments using polar molecules to study quantum magnetic models. More recently, our work in increasing the filling fraction shows that it's possible to use many of the tools of modern AMO physics to assemble heteronuclear molecules from the ground up. Other groups around the world have also succeeding in producing ground-state molecules [52, 53, 54, 55], and this will hopefully enable the field to progress even faster.

However, despite all of the successes of our experiment, there is much room for improvement. For example, our quantum synthesis scheme was able to produce molecules at $\sim 25\%$ filling, but future improvements based on the considerations discussed in Chapter 5 will be needed to increase the filling further and make the production of such dense samples more robust. The dream is that making dense samples of ultracold molecules in optical lattices would become routine, much like how the production of BECs of alkali atoms has become much more robust over the last 20 years. To do this, the importance of improving the technical capabilities of the experiments cannot be stressed enough. The dense molecular clouds described in Chapter 5 are very small, and better imaging resolution will be required to probe and manipulate them more precisely. Being able to

apply large, stable electric fields will make even richer physics accessible.

To this end, we recently installed a second generation KRb apparatus. The salient features are outlined in Fig. 7.1. The two main technical improvements are better electric field control and better imaging resolution. The glass cell has much more optical access and every window is nicely AR coated. The electric-field plates are now inside the vacuum chamber, with a combined ITO-AR coating such that there is no dielectric between the electrodes and the molecules. The plates will allow us to apply flat DC fields, while the four rods will enable us to apply field gradients both vertically and radially. A high numerical aperture (NA) objective will give us resolution around $\sim 1\,\mu$m, which is about 5 times better than in the first generation machine, and in principle we could get to $\sim 700$ nm with a higher NA objective. The ultimate goal would be to create a quantum gas microscope that can observe the dynamics of polar molecules at the single lattice site level.

Most likely, the first set of experiments in the new apparatus will highlight its improved technical capabilities. By applying a vertical electric-field gradient, it should be possible to perform manipulations of a single 2D layer of the lattice. This is because the molecules in each layer would experience a different electric field and hence different Stark shift, so the $N = 0 \rightarrow N = 1$ transition would be different in frequency in each layer and we could use microwaves to spectroscopically manipulate only molecules in a desired layer. This could be useful as a simple implementation of the excitation propagation experiment outlined in Section 4.6. If we can flip just a single layer to $|\uparrow\rangle$, then we could study the propagation of these spin excitations to other layers. The same manipulation that created the initial distribution could be used to read out the final distribution. We would either look for fewer $|\uparrow\rangle$ molecules in the starting layer or shift the microwave frequency to detect $|\uparrow\rangle$ molecules in other layers.

With the improved imaging capabilities, the experiments should be able to more precisely measure the spin dynamics. I think the trend of the experiment and theory building off of one another will continue. Similar to the work in Ref. [85] where the cluster expansion was greatly improved, as the experiment provides us means for more precisely probing and manipulating the molecules, we should be in a position to help validate other theoretical tools and methods. The

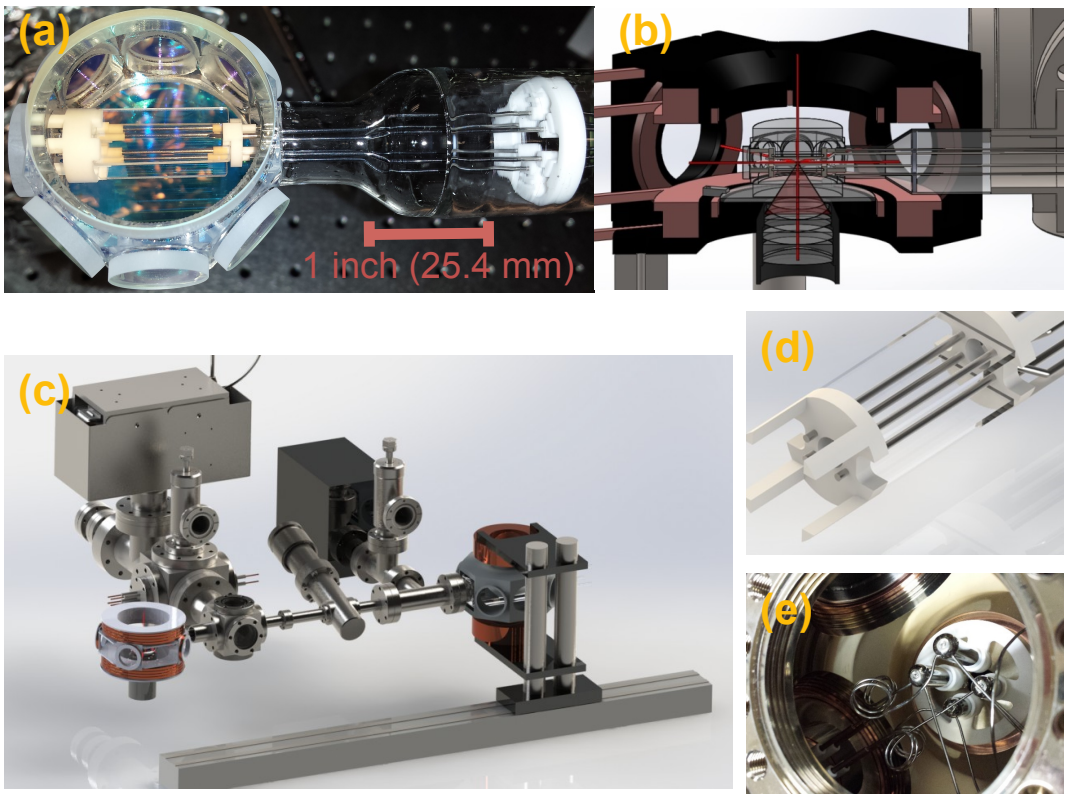


Figure 7.1: (a) A picture of the new science cell. There are two flat plates for applying DC fields and four rods for applying gradients. The entire structure is inside of a glass cell made by Precision Glassblowing and is held together by macor pieces. (b) Sketch of the science cell with the high-NA objective below it. (c) Sketch of the entire chamber. Similar to the first generation experiment, the MOT cell and science cell are separated by $\sim$ 1 m, with a gate valve in between. The main difference is that in the new chamber there is another cell before the science cell. The evaporative cooling will be done in this cell in a plugged quadrupole trap and then the atoms will be optically transported to the science cell. (d) Sketch of the electrode structure. (e) In-vacuum inductors and capacitors separate AC and DC on the rods and should enable us to couple microwaves onto the rods to drive rotational transitions.

future of polar molecule experiments looks bright, and I'm confident that the field will continue to progress in understanding and manipulating these interesting quantum many-body systems.

## Bibliography


[1] Immanuel Bloch, Jean Dalibard, and Sylvain Nascimbene. Quantum simulations with ultracold quantum gases. Nat. Phys., 8(4):267–276, 04 2012.

[2] Immanuel Bloch, Jean Dalibard, and Wilhelm Zwerger. Many-body physics with ultracold gases. Rev. Mod. Phys., 80:885–964, Jul 2008.

[3] Richard P. Feynman. Simulating physics with computers. International Journal of Theoretical Physics, 21(6):467–488, 1982.

[4] Seth Lloyd. Universal Quantum Simulators. Science, 273(5278):1073–1078, 1996.

[5] Rana X. Adhikari. Gravitational radiation detection with laser interferometry. Rev. Mod. Phys., 86:121–151, Feb 2014.

[6] Andrew D. Ludlow, Martin M. Boyd, Jun Ye, E. Peik, and P. O. Schmidt. Optical atomic clocks. Rev. Mod. Phys., 87:637–701, Jun 2015.

[7] Theodor W. Hänsch. Nobel Lecture: Passion for precision. Rev. Mod. Phys., 78:1297–1309, Nov 2006.

[8] Werner Bernreuther and Mahiko Suzuki. The electric dipole moment of the electron. Rev. Mod. Phys., 63:313–340, Apr 1991.

[9] D. J. Wineland, R. E. Drullinger, and F. L. Walls. Radiation-Pressure Cooling of Bound Resonant Absorbers. Phys. Rev. Lett., 40:1639–1642, Jun 1978.

[10] Paul D. Lett, Richard N. Watts, Christoph I. Westbrook, William D. Phillips, Phillip L. Gould, and Harold J. Metcalf. Observation of Atoms Laser Cooled below the Doppler Limit. Phys. Rev. Lett., 61:169–172, Jul 1988.

[11] Wolfgang Ketterle and N.J. Van Druten. In Benjamin Bederson and Herbert Walther, editors, Evaporative Cooling of Trapped Atoms, Advances In Atomic, Molecular, and Optical Physics, Vol. 37, pages 181 – 236. Academic Press, 1996.

[12] M. H. Anderson, J. R. Ensher, M. R. Matthews, C. E. Wieman, and E. A. Cornell. Observation of Bose-Einstein Condensation in a Dilute Atomic Vapor. Science, 269(5221):198–201, 1995.

[13] K. B. Davis, M. O. Mewes, M. R. Andrews, N. J. van Druten, D. S. Durfee, D. M. Kurn, and W. Ketterle. Bose-Einstein Condensation in a Gas of Sodium Atoms. Phys. Rev. Lett., 75:3969–3973, Nov 1995.

[14] C. C. Bradley, C. A. Sackett, J. J. Tollett, and R. G. Hulet. Evidence of Bose-Einstein Condensation in an Atomic Gas with Attractive Interactions. Phys. Rev. Lett., 75:1687–1690, Aug 1995.

[15] B. DeMarco and D. S. Jin. Onset of Fermi Degeneracy in a Trapped Atomic Gas. Science, 285(5434):1703–1706, 1999.

[16] Waseem S. Bakr, Jonathon I. Gillen, Amy Peng, Simon Fölling, and Markus Greiner. A quantum gas microscope for detecting single atoms in a Hubbard-regime optical lattice. Nature, 462(7269):74–77, 11 2009.

[17] Jacob F. Sherson, Christof Weitenberg, Manuel Endres, Marc Cheneau, Immanuel Bloch, and Stefan Kuhr. Single-atom-resolved fluorescence imaging of an atomic Mott insulator. Nature, 467(7311):68–72, 09 2010.

[18] Elmar Haller, James Hudson, Andrew Kelly, Dylan A. Cotta, Bruno Peaudecerf, Graham D. Bruce, and Stefan Kuhr. Single-atom imaging of fermions in a quantum-gas microscope. Nat Phys, 11(9):738–742, 09 2015.

[19] Lawrence W. Cheuk, Matthew A. Nichols, Melih Okan, Thomas Gersdorf, Vinay V. Ramasesh, Waseem S. Bakr, Thomas Lompe, and Martin W. Zwierlein. Quantum-Gas Microscope for Fermionic Atoms. Phys. Rev. Lett., 114:193001, May 2015.

[20] Maxwell F. Parsons, Florian Huber, Anton Mazurenko, Christie S. Chiu, Widagdo Setiawan, Katherine Wooley-Brown, Sebastian Blatt, and Markus Greiner. Site-Resolved Imaging of Fermionic $^6$Li in an Optical Lattice. Phys. Rev. Lett., 114:213002, May 2015.

[21] Ahmed Omran, Martin Boll, Timon A. Hilker, Katharina Kleinlein, Guillaume Salomon, Immanuel Bloch, and Christian Gross. Microscopic Observation of Pauli Blocking in Degenerate Fermionic Lattice Gases. Phys. Rev. Lett., 115:263001, Dec 2015.

[22] R. Blatt and C. F. Roos. Quantum simulations with trapped ions. Nat Phys, 8(4):277–284, 04 2012.

[23] M. H. Devoret and R. J. Schoelkopf. Superconducting Circuits for Quantum Information: An Outlook. Science, 339(6124):1169–1174, 2013.

[24] Markus Greiner, Cindy A. Regal, and Deborah S. Jin. Emergence of a molecular Bose-Einstein condensate from a Fermi gas. Nature, 426(6966):537–540, 12 2003.

[25] M. Bartenstein, A. Altmeyer, S. Riedl, S. Jochim, C. Chin, J. Hecker Denschlag, and R. Grimm. Crossover from a Molecular Bose-Einstein Condensate to a Degenerate Fermi Gas. Phys. Rev. Lett., 92:120401, Mar 2004.

[26] M. W. Zwierlein, J. R. Abo-Shaeer, A. Schirotzek, C. H. Schunck, and W. Ketterle. Vortices and superfluidity in a strongly interacting Fermi gas. Nature, 435(7045):1047–1051, 06 2005.

[27] C. Kohstall, M. Zaccanti, M. Jag, A. Trenkwalder, P. Massignan, G. M. Bruun, F. Schreck, and R. Grimm. Metastability and coherence of repulsive polarons in a strongly interacting Fermi mixture. Nature, 485(7400):615–618, 05 2012.

[28] P. Makotyn, C. E. Klauss, D. L. Goldberger, E. A. Cornell, and D. S. Jin. Universal dynamics of a degenerate unitary Bose gas. Nat Phys, 10(2):116–119, 02 2014.

[29] Cheng Chin, Rudolf Grimm, Paul Julienne, and Eite Tiesinga. Feshbach resonances in ultracold gases. Rev. Mod. Phys., 82:1225–1286, Apr 2010.

[30] P. W. Anderson. The Resonating Valence Bond State in $La_2CuO_4$ and Superconductivity. Science, 235(4793):1196–1198, 1987.

[31] Patrick A. Lee, Naoto Nagaosa, and Xiao-Gang Wen. Doping a Mott insulator: Physics of high-temperature superconductivity. Rev. Mod. Phys., 78:17–85, Jan 2006.

[32] D. Jaksch, C. Bruder, J. I. Cirac, C. W. Gardiner, and P. Zoller. Cold Bosonic Atoms in Optical Lattices. Phys. Rev. Lett., 81:3108–3111, Oct 1998.

[33] W. Hofstetter, J. I. Cirac, P. Zoller, E. Demler, and M. D. Lukin. High-Temperature Superfluidity of Fermionic Atoms in Optical Lattices. Phys. Rev. Lett., 89:220407, Nov 2002.

[34] M. L. Wall, K. R. A. Hazzard, and A. M. Rey. Quantum Magnetism with Ultracold Molecules. In From Atomic to Mesoscale, chapter 1, pages 3–37. World Scientific, 2015.

[35] Daniel Greif, Thomas Uehlinger, Gregor Jotzu, Leticia Tarruell, and Tilman Esslinger. Short-Range Quantum Magnetism of Ultracold Fermions in an Optical Lattice. Science, 340(6138):1307–1310, 2013.

[36] Russell A. Hart, Pedro M. Duarte, Tsung-Lin Yang, Xinxing Liu, Thereza Paiva, Ehsan Khatami, Richard T. Scalettar, Nandini Trivedi, David A. Huse, and Randall G. Hulet. Observation of antiferromagnetic correlations in the Hubbard model with ultracold atoms. Nature, 519(7542):211–214, 03 2015.

[37] N. Y. Yao, C. R. Laumann, S. Gopalakrishnan, M. Knap, M. Müller, E. A. Demler, and M. D. Lukin. Many-Body Localization in Dipolar Systems. Phys. Rev. Lett., 113:243002, Dec 2014.

[38] Philip Richerme, Zhe-Xuan Gong, Aaron Lee, Crystal Senko, Jacob Smith, Michael Foss-Feig, Spyridon Michalakis, Alexey V. Gorshkov, and Christopher Monroe. Non-local propagation of correlations in quantum systems with long-range interactions. Nature, 511(7508):198–201, 07 2014.

[39] P. Jurcevic, B. P. Lanyon, P. Hauke, C. Hempel, P. Zoller, R. Blatt, and C. F. Roos. Quasiparticle engineering and entanglement propagation in a quantum many-body system. Nature, 511(7508):202–205, 07 2014.

[40] Michael Foss-Feig, Zhe-Xuan Gong, Charles W. Clark, and Alexey V. Gorshkov. Nearly Linear Light Cones in Long-Range Interacting Quantum Systems. Phys. Rev. Lett., 114:157201, Apr 2015.

[41] D. Porras and J. I. Cirac. Effective Quantum Spin Systems with Trapped Ions. Phys. Rev. Lett., 92:207901, May 2004.

[42] Herbert Walther, Benjamin T H Varcoe, Berthold-Georg Englert, and Thomas Becker. Cavity quantum electrodynamics. Reports on Progress in Physics, 69(5):1325, 2006.

[43] Robert Löw, Hendrik Weimer, Johannes Nipper, Jonathan B Balewski, Björn Butscher, Hans Peter Büchler, and Tilman Pfau. An experimental and theoretical guide to strongly interacting Rydberg gases. Journal of Physics B: Atomic, Molecular and Optical Physics, 45(11):113001, 2012.

[44] J. S. Douglas, H. Habibian, C. L. Hung, A. V. Gorshkov, H. J. Kimble, and D. E. Chang. Quantum many-body models with cold atoms coupled to photonic crystals. Nat Photon, 9(5):326–331, 05 2015.

[45] T. Lahaye, J. Metz, B. Fröhlich, T. Koch, M. Meister, A. Griesmaier, T. Pfau, H. Saito, Y. Kawaguchi, and M. Ueda. *d*-Wave Collapse and Explosion of a Dipolar Bose-Einstein Condensate. Phys. Rev. Lett., 101:080401, Aug 2008.

[46] A. de Paz, A. Sharma, A. Chotia, E. Maréchal, J. H. Huckans, P. Pedri, L. Santos, O. Gorceix, L. Vernac, and B. Laburthe-Tolra. Nonequilibrium Quantum Magnetism in a Dipolar Lattice Gas. Phys. Rev. Lett., 111:185305, Oct 2013.

[47] Mingwu Lu, Nathaniel Q. Burdick, Seo Ho Youn, and Benjamin L. Lev. Strongly Dipolar Bose-Einstein Condensate of Dysprosium. Phys. Rev. Lett., 107:190401, Oct 2011.

[48] Mingwu Lu, Nathaniel Q. Burdick, and Benjamin L. Lev. Quantum Degenerate Dipolar Fermi Gas. Phys. Rev. Lett., 108:215301, May 2012.

[49] K. Aikawa, A. Frisch, M. Mark, S. Baier, A. Rietzler, R. Grimm, and F. Ferlaino. Bose-Einstein Condensation of Erbium. Phys. Rev. Lett., 108:210401, May 2012.

[50] K. Aikawa, A. Frisch, M. Mark, S. Baier, R. Grimm, and F. Ferlaino. Reaching Fermi Degeneracy via Universal Dipolar Scattering. Phys. Rev. Lett., 112:010404, Jan 2014.

[51] K.-K. Ni, S. Ospelkaus, M. H. G. de Miranda, A. Pe'er, B. Neyenhuis, J. J. Zirbel, S. Kotochigova, P. S. Julienne, D. S. Jin, and J. Ye. A High Phase-Space-Density Gas of Polar Molecules. Science, 322(5899):231–235, 2008.

[52] Jee Woo Park, Sebastian A. Will, and Martin W. Zwierlein. Ultracold Dipolar Gas of Fermionic $^{23}Na^{40}K$ Molecules in Their Absolute Ground State. Phys. Rev. Lett., 114:205302, May 2015.

[53] Tetsu Takekoshi, Lukas Reichsöllner, Andreas Schindewolf, Jeremy M. Hutson, C. Ruth Le Sueur, Olivier Dulieu, Francesca Ferlaino, Rudolf Grimm, and Hanns-Christoph Nägerl. Ultracold Dense Samples of Dipolar RbCs Molecules in the Rovibrational and Hyperfine Ground State. Phys. Rev. Lett., 113:205301, Nov 2014.

[54] Peter K. Molony, Philip D. Gregory, Zhonghua Ji, Bo Lu, Michael P. Köppinger, C. Ruth Le Sueur, Caroline L. Blackley, Jeremy M. Hutson, and Simon L. Cornish. Creation of Ultracold $^{87}Rb^{133}Cs$ Molecules in the Rovibrational Ground State. Phys. Rev. Lett., 113:255301, Dec 2014.

[55] M. Guo, B. Zhu, B. Lu, X. Ye, F. Wang, R. Vexiau, N. Bouloufa-Maafa, G. Quéméner, O. Dulieu, and D. Wang. Creation of a strongly dipolar gas of ultracold ground-state $^{23}Na^{87}Rb$ molecules. arXiv:1602.03947, February 2016.

[56] J. F. Barry, D. J. McCarron, E. B. Norrgard, M. H. Steinecker, and D. DeMille. Magneto-optical trapping of a diatomic molecule. Nature, 512(7514):286–289, 08 2014.

[57] Matthew T. Hummon, Mark Yeo, Benjamin K. Stuhl, Alejandra L. Collopy, Yong Xia, and Jun Ye. 2D Magneto-Optical Trapping of Diatomic Molecules. Phys. Rev. Lett., 110:143001, Apr 2013.

[58] Nicholas R. Hutzler, Hsin-I Lu, and John M. Doyle. The Buffer Gas Beam: An Intense, Cold, and Slow Source for Atoms and Molecules. Chemical Reviews, 112(9):4803–4827, 2012.

[59] Sebastiaan Y. T. van de Meerakker, Paul H. M. Smeets, Nicolas Vanhaecke, Rienk T. Jongma, and Gerard Meijer. Deceleration and Electrostatic Trapping of OH Radicals. Phys. Rev. Lett., 94:023004, Jan 2005.

[60] Brian C. Sawyer, Benjamin L. Lev, Eric R. Hudson, Benjamin K. Stuhl, Manuel Lara, John L. Bohn, and Jun Ye. Magnetoelectrostatic Trapping of Ground State OH Molecules. Phys. Rev. Lett., 98:253002, Jun 2007.

[61] Sebastiaan Y. T. van de Meerakker, Hendrick L. Bethlem, and Gerard Meijer. Taming molecular beams. Nat Phys, 4(8):595–602, 08 2008.

[62] Benjamin K. Stuhl, Brian C. Sawyer, Dajun Wang, and Jun Ye. Magneto-optical Trap for Polar Molecules. Phys. Rev. Lett., 101:243002, Dec 2008.

[63] Martin Zeppenfeld, Barbara G. U. Englert, Rosa Glockner, Alexander Prehn, Manuel Mielenz, Christian Sommer, Laurens D. van Buuren, Michael Motsch, and Gerhard Rempe. Sisyphus cooling of electrically trapped polyatomic molecules. Nature, 491(7425):570–573, 11 2012.

[64] S. Chervenkov, X. Wu, J. Bayerl, A. Rohlfes, T. Gantner, M. Zeppenfeld, and G. Rempe. Continuous Centrifuge Decelerator for Polar Molecules. Phys. Rev. Lett., 112:013001, Jan 2014.

[65] J. J. Zirbel, K.-K. Ni, S. Ospelkaus, J. P. D'Incao, C. E. Wieman, J. Ye, and D. S. Jin. Collisional Stability of Fermionic Feshbach Molecules. Phys. Rev. Lett., 100:143201, Apr 2008.

[66] C. Ospelkaus, S. Ospelkaus, L. Humbert, P. Ernst, K. Sengstock, and K. Bongs. Ultracold Heteronuclear Molecules in a 3D Optical Lattice. Phys. Rev. Lett., 97:120402, Sep 2006.

[67] Simon Stellmer, Benjamin Pasquiou, Rudolf Grimm, and Florian Schreck. Creation of Ultracold $Sr_2$ Molecules in the Electronic Ground State. Phys. Rev. Lett., 109:115302, Sep 2012.

[68] G. Reinaudi, C. B. Osborn, M. McDonald, S. Kotochigova, and T. Zelevinsky. Optical Production of Stable Ultracold $^{88}Sr_2$ Molecules. Phys. Rev. Lett., 109:115303, Sep 2012.

[69] S. Ospelkaus, K.-K. Ni, D. Wang, M. H. G. de Miranda, B. Neyenhuis, G. Quéméner, P. S. Julienne, J. L. Bohn, D. S. Jin, and J. Ye. Quantum-State Controlled Chemical Reactions of Ultracold Potassium-Rubidium Molecules. Science, 327(5967):853–857, 2010.

[70] K. K. Ni, S. Ospelkaus, D. Wang, G. Quéméner, B. Neyenhuis, M. H. G. de Miranda, J. L. Bohn, J. Ye, and D. S. Jin. Dipolar collisions of polar molecules in the quantum regime. Nature, 464(7293):1324–1328, 04 2010.

[71] M. H. G. de Miranda, A. Chotia, B. Neyenhuis, D. Wang, G. Quéméner, S. Ospelkaus, J. L. Bohn, J. Ye, and D. S. Jin. Controlling the quantum stereodynamics of ultracold bimolecular reactions. Nat. Phys., 7(6):502–507, 06 2011.

[72] Amodsen Chotia, Brian Neyenhuis, Steven A. Moses, Bo Yan, Jacob P. Covey, Michael Foss-Feig, Ana Maria Rey, Deborah S. Jin, and Jun Ye. Long-Lived Dipolar Molecules and Feshbach Molecules in a 3D Optical Lattice. Phys. Rev. Lett., 108:080405, Feb 2012.

[73] A. Micheli, G. K. Brennen, and P. Zoller. A toolbox for lattice-spin models with polar molecules. Nat. Phys., 2(5):341–347, 05 2006.

[74] Ryan Barnett, Dmitry Petrov, Mikhail Lukin, and Eugene Demler. Quantum Magnetism with Multicomponent Dipolar Molecules in an Optical Lattice. Phys. Rev. Lett., 96:190401, May 2006.

[75] M L Wall and L D Carr. Emergent timescales in entangled quantum dynamics of ultracold molecules in optical lattices. New Journal of Physics, 11(5):055027, 2009.

[76] J Schachenmayer, I Lesanovsky, A Micheli, and A J Daley. Dynamical crystal creation with polar molecules or Rydberg atoms in optical lattices. New Journal of Physics, 12(10):103044, 2010.

[77] Felipe Herrera, Marina Litinskaya, and Roman V. Krems. Tunable disorder in a crystal of cold polar molecules. Phys. Rev. A, 82:033428, Sep 2010.

[78] J Pérez-Ríos, F Herrera, and R V Krems. External field control of collective spin excitations in an optical lattice of $^2\Sigma$ molecules. New Journal of Physics, 12(10):103007, 2010.

[79] C Trefzger, M Alloing, C Menotti, F Dubin, and M Lewenstein. Quantum magnetism and counterflow supersolidity of up–down bosonic dipoles. New Journal of Physics, 12(9):093008, 2010.

[80] J. P. Kestner, Bin Wang, Jay D. Sau, and S. Das Sarma. Prediction of a gapless topological Haldane liquid phase in a one-dimensional cold polar molecular lattice. Phys. Rev. B, 83:174409, May 2011.

[81] Alexey V. Gorshkov, Salvatore R. Manmana, Gang Chen, Jun Ye, Eugene Demler, Mikhail D. Lukin, and Ana Maria Rey. Tunable Superfluidity and Quantum Magnetism with Ultracold Polar Molecules. Phys. Rev. Lett., 107:115301, Sep 2011.

[82] Alexey V. Gorshkov, Salvatore R. Manmana, Gang Chen, Eugene Demler, Mikhail D. Lukin, and Ana Maria Rey. Quantum magnetism with polar alkali-metal dimers. Phys. Rev. A, 84:033619, Sep 2011.

[83] Kaden R. A. Hazzard, Salvatore R. Manmana, Michael Foss-Feig, and Ana Maria Rey. Far-from-Equilibrium Quantum Magnetism with Ultracold Polar Molecules. Phys. Rev. Lett., 110:075301, Feb 2013.

[84] Bo Yan, Steven A. Moses, Bryce Gadway, Jacob P. Covey, Kaden R. A. Hazzard, Ana Maria Rey, Deborah S. Jin, and Jun Ye. Observation of dipolar spin-exchange interactions with lattice-confined polar molecules. Nature, 501(7468):521–525, 09 2013.

[85] Kaden R. A. Hazzard, Bryce Gadway, Michael Foss-Feig, Bo Yan, Steven A. Moses, Jacob P. Covey, Norman Y. Yao, Mikhail D. Lukin, Jun Ye, Deborah S. Jin, and Ana Maria Rey. Many-Body Dynamics of Dipolar Molecules in an Optical Lattice. Phys. Rev. Lett., 113:195302, Nov 2014.

[86] Michael Knap, Erez Berg, Martin Ganahl, and Eugene Demler. Clustered Wigner-crystal phases of cold polar molecules in arrays of one-dimensional tubes. Phys. Rev. B, 86:064501, Aug 2012.

[87] Kevin A. Kuns, Ana Maria Rey, and Alexey V. Gorshkov. *d*-wave superfluidity in optical lattices of ultracold polar molecules. Phys. Rev. A, 84:063639, Dec 2011.

[88] Sergey V. Syzranov, Michael L. Wall, Victor Gurarie, and Ana Maria Rey. Spin–orbital dynamics in a system of polar molecules. Nat. Commun., 5:5391, 11 2014.

[89] Piotr S. Żuchowski, J. Aldegunde, and Jeremy M. Hutson. Ultracold RbSr Molecules Can Be Formed by Magnetoassociation. Phys. Rev. Lett., 105:153201, Oct 2010.

[90] B. Zhu, B. Gadway, M. Foss-Feig, J. Schachenmayer, M. L. Wall, K. R. A. Hazzard, B. Yan, S. A. Moses, J. P. Covey, D. S. Jin, J. Ye, M. Holland, and A. M. Rey. Suppressing the Loss of Ultracold Molecules Via the Continuous Quantum Zeno Effect. Phys. Rev. Lett., 112:070404, Feb 2014.

[91] B. Neyenhuis, B. Yan, S. A. Moses, J. P. Covey, A. Chotia, A. Petrov, S. Kotochigova, J. Ye, and D. S. Jin. Anisotropic Polarizability of Ultracold Polar $^{40}$K$^{87}$Rb Molecules. Phys. Rev. Lett., 109:230403, Dec 2012.

[92] Steven A. Moses, Jacob P. Covey, Matthew T. Miecnikowski, Bo Yan, Bryce Gadway, Jun Ye, and Deborah S. Jin. Creation of a low-entropy quantum gas of polar molecules in an optical lattice. Science, 350(6261):659–662, 2015.

[93] J. P. Covey, S. A. Moses, M. Gärttner, A. Safavi-Naini, M. T. Miecnikowski, Z. Fu, J. Schachenmayer, P. S. Julienne, A. M. Rey, D. S. Jin, and J. Ye. Doublon dynamics and polar molecule production in an optical lattice. arXiv:1511.02225, November 2015.

[94] Gary C. Bjorklund. Frequency-modulation spectroscopy: a new method for measuring weak absorptions and dispersions. Opt. Lett., 5(1):15–17, Jan 1980.

[95] K. Bergmann, H. Theuer, and B. W. Shore. Coherent population transfer among quantum states of atoms and molecules. Rev. Mod. Phys., 70:1003–1025, Jul 1998.

[96] Kang-Kuen Ni. A Quantum Gas of Polar Molecules. PhD thesis, University of Colorado, Boulder, October 2009.

[97] K Aikawa, D Akamatsu, J Kobayashi, M Ueda, T Kishimoto, and S Inouye. Toward the production of quantum degenerate bosonic polar molecules, $^{41}$K$^{87}$Rb. New Journal of Physics, 11(5):055035, 2009.

[98] Marcio H. G. de Miranda. Control of dipolar collisions in the quantum regime. PhD thesis, University of Colorado, Boulder, November 2010.

[99] R.W.P. Drever, J.L. Hall, F.V. Kowalski, J. Hough, G.M. Ford, A.J. Munley, and H. Ward. Laser phase and frequency stabilization using an optical resonator. Applied Physics B, 31(2):97–105, 1983.

[100] Eric D. Black. An introduction to Pound-Drever-Hall laser frequency stabilization. American Journal of Physics, 69(1):79–87, 2001.

[101] T. Okoshi, K. Kikuchi, and A. Nakayama. Novel method for high resolution measurement of laser output spectrum. Electronics Letters, 16(16):630–631, July 1980.

[102] L. Richter, H.I. Mandelberg, M. Kruger, and P. McGrath. Linewidth determination from self-heterodyne measurements with subcoherence delay times. IEEE Journal of Quantum Electronics, 22(11):2070–2074, Nov 1986.

[103] Markus Greiner. Ultracold quantum gases in three-dimension optical lattice potentials. PhD thesis, Ludwig-Maximilians-Universität München, January 2003.

[104] Ana Maria Rey. Ultracold bosonic atoms in optical lattices. PhD thesis, University of Maryland, College Park, 2004.

[105] Brian Neyenhuis. Ultracold Polar KRb Molecules in Optical Lattices. PhD thesis, University of Colorado, Boulder, 2012.

[106] P. Pedri, L. Pitaevskii, S. Stringari, C. Fort, S. Burger, F. S. Cataliotti, P. Maddaloni, F. Minardi, and M. Inguscio. Expansion of a Coherent Array of Bose-Einstein Condensates. Phys. Rev. Lett., 87:220401, Nov 2001.

[107] S. Baier, M. J. Mark, D. Petter, K. Aikawa, L. Chomaz, Z. Cai, M. Baranov, P. Zoller, and F. Ferlaino. Extended Bose-Hubbard Models with Ultracold Magnetic Atoms. arXiv:1507.03500, July 2015.

[108] Fabrice Gerbier, Artur Widera, Simon Fölling, Olaf Mandel, Tatjana Gericke, and Immanuel Bloch. Interference pattern and visibility of a Mott insulator. Phys. Rev. A, 72:053606, Nov 2005.

[109] Yu. B. Ovchinnikov, J. H. Müller, M. R. Doery, E. J. D. Vredenbregt, K. Helmerson, S. L. Rolston, and W. D. Phillips. Diffraction of a Released Bose-Einstein Condensate by a Pulsed Standing Light Wave. Phys. Rev. Lett., 83:284–287, Jul 1999.

[110] Alexander D. Cronin, Jörg Schmiedmayer, and David E. Pritchard. Optics and interferometry with atoms and molecules. Rev. Mod. Phys., 81:1051–1129, Jul 2009.

[111] P. A. Murthy, D. Kedar, T. Lompe, M. Neidig, M. G. Ries, A. N. Wenz, G. Zürn, and S. Jochim. Matter-wave Fourier optics with a strongly interacting two-dimensional Fermi gas. Phys. Rev. A, 90:043611, Oct 2014.

[112] Jason N. Byrd, John A. Montgomery, and Robin Côté. Structure and thermochemistry of $K_2Rb$, $KRb_2$, and $K_2Rb_2$. Phys. Rev. A, 82:010502, Jul 2010.

[113] C. Klempt, T. Henninger, O. Topic, M. Scherer, L. Kattner, E. Tiemann, W. Ertmer, and J. J. Arlt. Radio-frequency association of heteronuclear Feshbach molecules. Phys. Rev. A, 78:061602, Dec 2008.

[114] S. Ospelkaus, A. Pe'er, K. K. Ni, J. J. Zirbel, B. Neyenhuis, S. Kotochigova, P. S. Julienne, J. Ye, and D. S. Jin. Efficient state transfer in an ultracold dense gas of heteronuclear molecules. Nat Phys, 4(8):622–626, 08 2008.

[115] S. Ospelkaus, K.-K. Ni, G. Quéméner, B. Neyenhuis, D. Wang, M. H. G. de Miranda, J. L. Bohn, J. Ye, and D. S. Jin. Controlling the Hyperfine State of Rovibronic Ground-State Polar Molecules. Phys. Rev. Lett., 104:030402, Jan 2010.

[116] J. Aldegunde, Hong Ran, and Jeremy M. Hutson. Manipulating ultracold polar molecules with microwave radiation: The influence of hyperfine structure. Phys. Rev. A, 80:043410, Oct 2009.

[117] H. P. Büchler, E. Demler, M. Lukin, A. Micheli, N. Prokof'ev, G. Pupillo, and P. Zoller. Strongly Correlated 2D Quantum Phases with Cold Polar Molecules: Controlling the Shape of the Interaction Potential. Phys. Rev. Lett., 98:060404, Feb 2007.

[118] A. Micheli, G. Pupillo, H. P. Büchler, and P. Zoller. Cold polar molecules in two-dimensional traps: Tailoring interactions with external fields for novel quantum phases. Phys. Rev. A, 76:043604, Oct 2007.

[119] Bihui Zhu, Goulven Quéméner, Ana M. Rey, and Murray J. Holland. Evaporative cooling of reactive polar molecules confined in a two-dimensional geometry. Phys. Rev. A, 88:063405, Dec 2013.

[120] Goulven Quéméner and John L. Bohn. Dynamics of ultracold molecules in confined geometry and electric field. Phys. Rev. A, 83:012705, Jan 2011.

[121] Paul S. Julienne. Ultracold molecules from ultracold atoms: a case study with the KRb molecule. Faraday Discuss., 142:361–388, 2009.

[122] Erik W. Streed, Jongchul Mun, Micah Boyd, Gretchen K. Campbell, Patrick Medley, Wolfgang Ketterle, and David E. Pritchard. Continuous and Pulsed Quantum Zeno Effect. Phys. Rev. Lett., 97:260402, Dec 2006.

[123] N. Syassen, D. M. Bauer, M. Lettner, T. Volz, D. Dietze, J. J. García-Ripoll, J. I. Cirac, G. Rempe, and S. Dürr. Strong Dissipation Inhibits Losses and Induces Correlations in Cold Molecular Gases. Science, 320(5881):1329–1331, 2008.

[124] Zbigniew Idziaszek and Paul S. Julienne. Universal rate constants for reactive collisions of ultracold molecules. Phys. Rev. Lett., 104:113202, Mar 2010.

[125] Michael Mayle, Goulven Quéméner, Brandon P. Ruzic, and John L. Bohn. Scattering of ultracold molecules in the highly resonant regime. Phys. Rev. A, 87:012709, Jan 2013.

[126] Gaoren Wang and Goulven Quéméner. Tuning ultracold collisions of excited rotational dipolar molecules. New Journal of Physics, 17(3):035015, 2015.

[127] Takeshi Fukuhara, Adrian Kantian, Manuel Endres, Marc Cheneau, Peter Schausz, Sebastian Hild, David Bellem, Ulrich Schollwock, Thierry Giamarchi, Christian Gross, Immanuel Bloch, and Stefan Kuhr. Quantum dynamics of a mobile spin impurity. Nat. Phys., 9(4):235–241, 04 2013.

[128] Jianming Cai, Alex Retzker, Fedor Jelezko, and Martin B. Plenio. A large-scale quantum simulator on a diamond surface at room temperature. Nat. Phys., 9(3):168–173, 03 2013.

[129] Sylvain Ravets, Henning Labuhn, Daniel Barredo, Lucas Beguin, Thierry Lahaye, and Antoine Browaeys. Coherent dipole-dipole coupling between two single Rydberg atoms at an electrically-tuned Forster resonance. Nat Phys, 10(12):914–917, 12 2014.

[130] S. Trotzky, P. Cheinet, S. Fölling, M. Feld, U. Schnorrberger, A. M. Rey, A. Polkovnikov, E. A. Demler, M. D. Lukin, and I. Bloch. Time-Resolved Observation and Control of Superexchange Interactions with Ultracold Atoms in Optical Lattices. Science, 319(5861):295–299, 2008.

[131] Salvatore R. Manmana, E. M. Stoudenmire, Kaden R. A. Hazzard, Ana Maria Rey, and Alexey V. Gorshkov. Topological phases in ultracold polar-molecule quantum magnets. Phys. Rev. B, 87:081106, Feb 2013.

[132] Kaden Hazzard. Private communication.

[133] Jun Ye, H. J. Kimble, and Hidetoshi Katori. Quantum State Engineering and Precision Metrology Using State-Insensitive Light Traps. Science, 320(5884):1734–1738, 2008.

[134] Svetlana Kotochigova and David DeMille. Electric-field-dependent dynamic polarizability and state-insensitive conditions for optical trapping of diatomic polar molecules. Phys. Rev. A, 82:063421, Dec 2010.

[135] M. Bishof, X. Zhang, M. J. Martin, and Jun Ye. Optical Spectrum Analyzer with Quantum-Limited Noise Floor. Phys. Rev. Lett., 111:093604, Aug 2013.

[136] Michael J. Biercuk, Hermann Uys, Aaron P. VanDevender, Nobuyasu Shiga, Wayne M. Itano, and John J. Bollinger. Optimized dynamical decoupling in a model quantum memory. Nature, 458(7241):996–1000, 04 2009.

[137] Ashok Ajoy, Gonzalo A. Álvarez, and Dieter Suter. Optimal pulse spacing for dynamical decoupling in the presence of a purely dephasing spin bath. Phys. Rev. A, 83:032303, Mar 2011.

[138] P. C. Maurer, G. Kucsko, C. Latta, L. Jiang, N. Y. Yao, S. D. Bennett, F. Pastawski, D. Hunger, N. Chisholm, M. Markham, D. J. Twitchen, J. I. Cirac, and M. D. Lukin. Room-Temperature Quantum Bit Memory Exceeding One Second. Science, 336(6086):1283–1286, 2012.

[139] J. S. Waugh, L. M. Huber, and U. Haeberlen. Approach to High-Resolution nmr in Solids. Phys. Rev. Lett., 20:180–182, Jan 1968.

[140] M. Fattori, T. Koch, S. Goetz, A. Griesmaier, S. Hensler, J. Stuhler, and T. Pfau. Demagnetization cooling of a gas. Nat Phys, 2(11):765–768, 11 2006.

[141] A. de Paz, A. Chotia, E. Maréchal, P. Pedri, L. Vernac, O. Gorceix, and B. Laburthe-Tolra. Resonant demagnetization of a dipolar Bose-Einstein condensate in a three-dimensional optical lattice. Phys. Rev. A, 87:051609, May 2013.

[142] Daniel Greif, Maxwell F. Parsons, Anton Mazurenko, Christie S. Chiu, Sebastian Blatt, Florian Huber, Geoffrey Ji, and Markus Greiner. Site-resolved imaging of a fermionic Mott insulator. Science, 351(6276):953–957, 2016.

[143] Dietrich Stauffer and Ammon Aharon. Introduction to Percolation Theory: Revised Second Edition. Taylor and Francis, London, 1994.

[144] B. Damski, L. Santos, E. Tiemann, M. Lewenstein, S. Kotochigova, P. Julienne, and P. Zoller. Creation of a Dipolar Superfluid in Optical Lattices. Phys. Rev. Lett., 90:110401, Mar 2003.

[145] J. K. Freericks, M. M. Maśka, Anzi Hu, Thomas M. Hanna, C. J. Williams, P. S. Julienne, and R. Lemański. Improving the efficiency of ultracold dipolar molecule formation by first loading onto an optical lattice. Phys. Rev. A, 81:011605, Jan 2010.

[146] T. Volz, N. Syassen, D. M. Bauer, E. Hansis, S. Dürr, and G. Rempe. Preparation of a quantum state with one molecule at each site of an optical lattice. Nat Phys, 2(10):692–695, 10 2006.

[147] Markus Greiner, Olaf Mandel, Tilman Esslinger, Theodor W. Hansch, and Immanuel Bloch. Quantum phase transition from a superfluid to a Mott insulator in a gas of ultracold atoms. Nature, 415(6867):39–44, 01 2002.

[148] W. S. Bakr, A. Peng, M. E. Tai, R. Ma, J. Simon, J. I. Gillen, S. Fölling, L. Pollet, and M. Greiner. Probing the Superfluid-to-Mott Insulator Transition at the Single-Atom Level. Science, 329(5991):547–550, 2010.

[149] Jacob F. Sherson, Christof Weitenberg, Manuel Endres, Marc Cheneau, Immanuel Bloch, and Stefan Kuhr. Single-atom-resolved fluorescence imaging of an atomic Mott insulator. Nature, 467(7311):68–72, 09 2010.

[150] B. DeMarco, C. Lannert, S. Vishveshwara, and T.-C. Wei. Structure and stability of Mott-insulator shells of bosons trapped in an optical lattice. Phys. Rev. A, 71:063601, Jun 2005.

[151] Robert Jördens, Niels Strohmaier, Kenneth Günter, Henning Moritz, and Tilman Esslinger. A Mott insulator of fermionic atoms in an optical lattice. Nature, 455(7210):204–207, 09 2008.

[152] U. Schneider, L. Hackermüller, S. Will, Th. Best, I. Bloch, T. A. Costi, R. W. Helmes, D. Rasch, and A. Rosch. Metallic and Insulating Phases of Repulsively Interacting Fermions in a 3D Optical Lattice. Science, 322(5907):1520–1525, 2008.

[153] Michael Köhl. Thermometry of fermionic atoms in an optical lattice. Phys. Rev. A, 73:031601, Mar 2006.

[154] C. J. Petcock and H. Smith. Bose-Einstein Condensation in Dilute Gases, Second Edition. Cambridge University Press, Cambridge, UK, 2008.

[155] Brian DeMarco. Quantum Behavior of an Atomic Fermi Gas. PhD thesis, University of Colorado, Boulder, 2001.

[156] Robert Johannes Wild. Contact Measurements on a Strongly Interacting Bose Gas. PhD thesis, University of Colorado, Boulder, 2012.

[157] S. Ospelkaus, C. Ospelkaus, O. Wille, M. Succo, P. Ernst, K. Sengstock, and K. Bongs. Localization of Bosonic Atoms by Fermionic Impurities in a Three-Dimensional Optical Lattice. Phys. Rev. Lett., 96:180403, May 2006.

[158] Th. Best, S. Will, U. Schneider, L. Hackermüller, D. van Oosten, I. Bloch, and D.-S. Lühmann. Role of Interactions in $^{87}$Rb-$^{40}$K Bose-Fermi Mixtures in a 3D Optical Lattice. Phys. Rev. Lett., 102:030408, Jan 2009.

[159] Seiji Sugawa, Kensuke Inaba, Shintaro Taie, Rekishu Yamazaki, Makoto Yamashita, and Yoshiro Takahashi. Interaction and filling-induced quantum phases of dual Mott insulators of bosons and fermions. Nat. Phys., 7(8):642–648, 08 2011.

[160] Michael Köhl, Henning Moritz, Thilo Stöferle, Kenneth Günter, and Tilman Esslinger. Fermionic Atoms in a Three Dimensional Optical Lattice: Observing Fermi Surfaces, Dynamics, and Interactions. Phys. Rev. Lett., 94:080403, Mar 2005.

[161] Dmitry Budker, Derek Kimball, and David Demille. Atomic Physics: An Exploration through Problems and Solutions, Second Edition. Oxford University Press, Oxford, 2008.

[162] F. H. Mies, E. Tiesinga, and P. S. Julienne. Manipulation of Feshbach resonances in ultracold atomic collisions using time-dependent magnetic fields. Phys. Rev. A, 61:022721, Jan 2000.

[163] M. Zaccanti, C. D'Errico, F. Ferlaino, G. Roati, M. Inguscio, and G. Modugno. Control of the interaction in a Fermi-Bose mixture. Phys. Rev. A, 74:041605, Oct 2006.

[164] Ruth S. Bloom, Ming-Guang Hu, Tyler D. Cumby, and Deborah S. Jin. Tests of Universal Three-Body Physics in an Ultracold Bose-Fermi Mixture. Phys. Rev. Lett., 111:105301, Sep 2013.

[165] K. Winkler, G. Thalhammer, F. Lang, R. Grimm, J. Hecker Denschlag, A. J. Daley, A. Kantian, H. P. Büchler, and P. Zoller. Repulsively bound atom pairs in an optical lattice. Nature, 441(7311):853–856, 06 2006.

[166] J. Heinze, S. Götze, J. S. Krauser, B. Hundt, N. Fläschner, D.-S. Lühmann, C. Becker, and K. Sengstock. Multiband Spectroscopy of Ultracold Fermions: Observation of Reduced Tunneling in Attractive Bose-Fermi Mixtures. Phys. Rev. Lett., 107:135303, Sep 2011.

[167] John M. Brown and Alan Carrington. Rotational Spectroscopy of Diatomic Molecules. Cambridge University Press, Cambridge, UK, 2003.

# Appendix A

## Deriving the dipolar Hamiltonian

Here I show how to connect the classical and quantum expressions for the dipole operator, which are useful in understanding the Hamiltonian presented in Chapter 4. The derivations in this section come mainly from Refs. [34, 167].

Recall the classical dipole-dipole interaction

$$V_{dd} = \frac{\mathbf{d_1} \cdot \mathbf{d_2} - 3(\mathbf{d_1} \cdot \hat{\mathbf{r}}_{12})(\mathbf{d_2} \cdot \hat{\mathbf{r}}_{12})}{r_{12}^3}. \tag{A.1}$$

To get the quantum analog of this expression, we need to replace the classical dipole $d$ with an operator $\hat{d}$. It turns out that the familiar angular dependence $(1 - 3\cos^2\theta)$ from Eq. 4.1 represents just one term in the full expression for the dipole-dipole interaction, and to get the full angular dependence it is necessary to decompose the dipole operator into irreducible tensor components. This decomposition yields a sum of terms corresponding to $q$ units of angular momentum being exchanged between rotational and orbital angular momentum [34].

The result is that

$$V_{dd} = -\frac{\sqrt{6}}{r_{12}^3} \sum_{q=-2}^{q=2} (-1)^q C_{-q}^2(\theta, \phi) T_q^2(\mathbf{d_1}, \mathbf{d_2}), \tag{A.2}$$

where

$$C_q^k(\theta, \phi) = \sqrt{\frac{4\pi}{2k+1}} Y_{kq}(\theta, \phi) \tag{A.3}$$

and $Y_{kq}(\theta, \phi)$ is a normal spherical harmonic. The $T$'s are irreducible tensor operators [131]:

$$T_{\pm 2}^2 = \hat{d_1^{\pm}} \hat{d_2^{\pm}}, \tag{A.4}$$

$$T^2_{\pm 1} = \frac{\hat{d^0_1}\hat{d^\pm_2} + \hat{d^\pm_1}\hat{d^0_2}}{\sqrt{2}}, \tag{A.5}$$

$$T^2_0 = \frac{\hat{d^+_1}\hat{d^-_2} + \hat{d^-_1}\hat{d^+_2} + 2\hat{d^0_1}\hat{d^0_2}}{\sqrt{6}}. \tag{A.6}$$

From now on, I will omit the hats to denote operators since every $d$ will be understood to be an operator. We will also need the following relationships between the Cartesian and tensor forms:

$$d^\pm = \mp\frac{d_x \pm i d_y}{\sqrt{2}}, \tag{A.7}$$

$$d^0 = d_z. \tag{A.8}$$

To make things simple, we'll put one dipole at the origin and the other at the point $(x, y, z)$, with the electric field in the $z$ direction. Then $r_{12} = r$, and the polar angle $\theta$ and azimuthal angle $\phi$ are defined in the usual way ($z = r\cos\theta$, $x = r\sin\theta\cos\phi$, and $y = r\sin\theta\sin\phi$, where $r = \sqrt{x^2 + y^2 + z^2}$).

For completeness, the $C$'s are given by

$$C^2_{\pm 2} = \frac{\sqrt{6}}{4}\sin^2\theta e^{\pm 2i\phi}, \tag{A.9}$$

$$C^2_{\pm 1} = \mp\frac{\sqrt{6}}{2}\sin\theta\cos\theta e^{\pm i\phi}, \tag{A.10}$$

$$C^2_0 = \frac{1}{2}(3\cos^2\theta - 1). \tag{A.11}$$

Then Eq. A.2 becomes

$$V_{dd} = -\frac{\sqrt{6}}{r^3}\left(\frac{\sqrt{6}}{4}\sin^2\theta(e^{2i\phi}d^+_1 d^+_2 + e^{-2i\phi}d^-_1 d^-_2) + \frac{\sin\theta\cos\theta}{2\sqrt{2}}(e^{i\phi}(d^0_1 d^-_2 + d^-_1 d^0_2) - e^{-i\phi}(d^0_1 d^+_2 + d^+_1 d^0_2)) + \frac{3\cos^2\theta - 1}{12}(d^+_1 d^-_2 + d^-_1 d^+_2 + 2d^0_1 d^0_2)\right). \tag{A.12}$$

After using Eqs. A.7 and A.8 and simplifying, we obtain

$$V_{dd} = -\frac{6}{r^3}\left(\frac{1}{4}\sin^2\theta\big((d_{1x}d_{2x} - d_{1y}d_{2y})\cos(2\phi) + (d_{1y}d_{2x} + d_{1x}d_{2y})\sin(2\phi)\big) + \frac{\sin\theta\cos\theta}{2}\big((d_{1z}d_{2x} + d_{1x}d_{2z})\cos\phi + (d_{1z}d_{2y} + d_{1y}d_{2z})\sin\phi\big) + \frac{3\cos^2\theta - 1}{12}\big(2d_{1z}d_{2z} - d_{1x}d_{2x} - d_{1y}d_{2y}\big)\right). \tag{A.13}$$

Substituting $\sin\phi = \frac{y}{\sqrt{x^2+y^2}}$, $\cos\phi = \frac{x}{\sqrt{x^2+y^2}}$, $\sin(2\phi) = \frac{2xy}{x^2+y^2}$, and $\cos(2\phi) = \frac{x^2-y^2}{x^2+y^2}$ we get

$$V_{dd} = -\frac{6}{r^3}\Bigg(\frac{x^2-y^2}{4r^2}(d_{1x}d_{2x} - d_{1y}d_{2y}) + \frac{xy}{2r^2}(d_{1y}d_{2x} + d_{1x}d_{2y}) + \frac{xz}{2r^2}(d_{1z}d_{2x} + d_{1x}d_{2z}) + \frac{yz}{2r^2}(d_{1z}d_{2y} + d_{1x}d_{2y}) + \frac{3\cos^2\theta - 1}{12}(2d_{1z}d_{2z} - d_{1x}d_{2x} - d_{1y}d_{2y})\Bigg). \quad \text{(A.14)}$$

$$V_{dd} = \frac{1}{r^3}\Bigg(d_{1x}d_{2x}(1 - \frac{3x^2}{r^2}) + d_{1y}d_{2y}(1 - \frac{3y^2}{r^2}) + d_{1z}d_{2z}(1 - \frac{3z^2}{r^2}) - \frac{3xy}{r^2}(d_{1y}d_{2x} + d_{1x}d_{2y}) - \frac{3xz}{r^2}(d_{1z}d_{2x} + d_{1x}d_{2z}) - \frac{3yz}{r^2}(d_{1z}d_{2y} + d_{1x}d_{2y})\Bigg). \quad \text{(A.15)}$$

$$V_{dd} = \frac{1}{r^3}\Big(d_{1x}d_{2x} + d_{1y}d_{2y} + d_{1z}d_{2z}\Big) - \frac{3}{r^5}\Bigg(d_{1x}d_{2x}x^2 + d_{1y}d_{2y}y^2 + d_{1z}d_{2z}z^2 + xy(d_{1y}d_{2x} + d_{1x}d_{2y}) + xz(d_{1z}d_{2x} + d_{1x}d_{2z}) + yz(d_{1z}d_{2y} + d_{1x}d_{2y})\Bigg). \quad \text{(A.16)}$$

$$V_{dd} = \frac{\mathbf{d_1}\cdot\mathbf{d_2}}{r^3} - 3\frac{(\mathbf{d_1}\cdot\hat{\mathbf{r}})(\mathbf{d_2}\cdot\hat{\mathbf{r}})}{r^3}. \quad \text{(A.17)}$$